Multi-Scale Analysis of the Spatial Distribution of Soil Organic Carbon Stocks in Permafrost-Affected Soils in West Greenland

Dissertation

der Mathematisch-Naturwissenschaftlichen Fakultät
der Eberhard Karls Universität Tübingen
zur Erlangung des Grades eines
Doktors der Naturwissenschaften
(Dr. rer. nat.)

vorgelegt von
Philipp Gries
aus Bietigheim-Bissingen

Tübingen
2022

Gedruckt mit Genehmigung der Mathematisch-Naturwissenschaftlichen Fakultät der Eberhard Karls Universität Tübingen.

Tag der mündlichen Qualifikation:	11.10.2022
Dekan:	Prof. Dr. Thilo Stehle
1. Berichterstatter/-in:	Prof. Dr. Thomas Scholten
2. Berichterstatter/-in:	Prof. Dr. Volker Hochschild

Table of content

List of figures

List of tables

Abstract

Soils of the northern circumpolar region are a key organic carbon storage strained by global warming. Thawing of permafrost-affected soils from global warming increases greenhouse-gas emissions whose quantification is limited by sparse, uncertain and spatially diverse data of soil organic carbon stocks (SOCS) across the Arctic region, especially in Greenland. The accurate assessment of the effects of global warming requires better understanding of environmental interactions and feedbacks on SOCS which, however, vary spatially and across scales in Arctic environments.

Therefore, different scales were selected to identify scale-dependent effects of environmental factors and processes on the SOCS distribution in permafrost-affected soils in Arctic environments, exemplified by two study areas in West Greenland. Three controlling factors (vegetation, landscape, aspect) were used as representation of spatial varying environmental conditions to investigate the spatial SOCS distribution over short distances separately in both areas on the local scale and over a long distance between both areas on the regional scale. Further, the spatial SOCS distribution was analyzed using a set of multi-scale terrain and spatial features representing environmental processes acting parallel but differing in their intensity on the moraine, valley and catchment scale. The soil data set comprises of SOCS from 140 locations distributed over a study area at the coast and at the ice margin of West Greenland being characterized by oceanic and continental climate.

On the local scale, the SOCS distribution was best explained by vegetation and aspect as both reflect the importance of wind and solar radiation in both areas. Furthermore, aspect and curvature best mapped the SOCS distribution shaped by water-driven relocation processes on the moraine and valley scale in SISI and wind-induced processes acting parallel on the moraine, valley and catchment scale in RUSS. On the regional scale, differences in the SOCS distribution result from contrasting climate conditions between the coast and the ice margin which both are reflected by differences in the importance of relevant terrain features and scales and vegetation units between both study areas. Consequently, it is recommended to apply multi-scale terrain features in combination with vegetation to address scale-dependent soil-landscape interrelations being essential for spatial analysis of SOCS in West Greenland.

Zusammenfassung

Böden der nördlichen zirkumpolaren Region speichern einen Großteil des weltweiten organischen Bodenkohlenstoffs. Der Klimawandel fördert das Auftauen von Permafrost beeinflussten Böden und die damit verbundene Freisetzung von Treibhausgasen, deren Quantifizierung aufgrund der bestehenden Datendrunglage des organischen Bodenkohlenstoffvorrats (SOCS) für diese Region, insbesondere für Grönland, eine hohe Unsicherheiten aufweist. Die Höhe des SOCS ist abhängig von zahlreichen bodenbildenden Faktoren und Prozessen, die sowohl räumlich als auch skalenabhängig variieren.

Es wurden mehrere Skalen ausgewählt, um die skalenabhängige Auswirkungen von Umweltfaktoren und -prozessen auf die SOCS-Verteilung in Permafrostböden der Arktisregion am Beispiel von zwei Untersuchungsgebieten in Westgrönland zu ermitteln. Drei Kontrollfaktoren (Vegetation, Landschaft, Exposition) wurden zur Beschreibung räumlich variierender Umweltbedingungen verwendet, um die räumliche SOCS-Verteilung über kurze Entfernungen in beiden Gebieten auf der lokalen Skala und über große Entfernungen zwischen beiden Gebieten auf der regionalen Skala zu untersuchen. Darüber hinaus wurde die räumliche SOCS-Verteilung anhand einer Reihe von mehrskaligen Gelände- und Raummerkmalen analysiert, die verschiedene Umweltprozesse auf der Moränen-, Tal- und Einzugsgebietsskala repräsentieren. Der zugrunde liegende Datensatz umfasst SOCS-Werte von 140 Standorten, die über zwei Untersuchungsgebiete verteilt sind, die sich an der Küste (SISI) und am Eisrand (RUSS) in West Grönland befinden.

Auf lokaler Ebene wurde die SOCS-Verteilung am besten durch Vegetation und Exposition beschrieben, da beide die Bedeutung von Wind und Sonneneinstrahlung in beiden Gebieten widerspiegeln. Darüber hinaus ließen sich mit Exposition und Krümmung der Einfluss wasserbedingter Verlagerungsprozesse auf der Moränen- und Talskala in SISI und windinduzierter Prozesse auf allen drei Skalen in RUSS abbilden. Auf der regionalen Skala resultieren die Unterschiede in der SOCS-Verteilung aus den unterschiedlichen Klimabedingungen zwischen der Küste und dem Eisrand. Diese spiegeln sich sowohl in Unterschieden wichtiger Geländemerkmale, relevanter Prozessskalen und SOCS vergleichbarer Vegetationseinheiten zwischen beiden Gebieten wider. Schlußendlich empfielt sich Skalen bei Untersuchungen des SOCS einzubeziehen um die Genauigkeit von SOCS-Berechnungen zu verbessern.

List of publications and unpublished manuscripts

1. **Gries, P.**, Schmidt, K., Scholten, T., Kühn, P. (2020): Regional and local scale variations in soil organic carbon stocks in West Greenland. J. Plant Nutr. Soil Sci., 183, 292–305.

2. **Gries, P.,** Kühn, P., Scholten, T., Schmidt, K., (unpublished): Feature construction and machine learning for the spatial analysis of soil organic carbon stocks in West Greenland.

3. Behrens, T., Schmidt, K., Viscarra Rossel, R.A., **Gries, P.**, Scholten, T., MacMillan, R.A. (2018): Spatial modelling with Euclidean distance fields and machine learning. Eur. J. Soil. Sci., 69, 757–770.

4. Rentschler, T., **Gries, P.**, Behrens, T., Bruelheide, H., Kühn, P., Seitz, S., Shi, X., Trogisch, S., Scholten, T., Schmidt, K. (2019): Comparison of catchment scale 3D and 2.5D modelling of soil organic carbon stocks in Jiangxi Province, PR China. PLoS ONE 14(8): e0220881.

5. Rentschler, T., Werban, U., Ahner, M., Behrens, T., **Gries, P.**, Scholten, T., Teuber, S., Schmidt, K. (2020): 3D mapping of soil organic carbon content and soil moisture with multiple geophysical sensors and machine learning. Vadose zone journal 19, 1.

1 Introduction and objectives

Carbon storage and climate change

Worldwide, soils store up to 3000 Pg of carbon which is twice the amount of the biosphere and atmosphere combined (Lal, 2004; 2009; Köchy et al., 2015). A large portion of this total carbon is contained as organic carbon in permafrost-affected organic and mineral soils of the northern circumpolar permafrost region (Ping et al., 2015). In total, the amount of storage is approximately 1300 Pg of soil organic carbon (SOC; Tarnocai et al., 2009) whereof, the top 30 cm of the soil store 217 Pg and the first 100 cm 472 Pg (Hugelius et al., 2013; 2014).

This large SOC stock (SOCS) is sensitive to climate change as thawing of permafrost follows the increase in Arctic air temperatures which significantly exceeded the global average over the last decades (Biskaborn et al., 2019; IPCC, 2019). Consequently, permafrost-affected soils thaw to greater depth and longer period during the Arctic summer gradually intensify environmental interactions and feedbacks (Baumann et al., 2014; Westermann et al., 2015). Recent findings suggest microbial breakdown of organic carbon and thus the release of greenhouse gases into the atmosphere, which expedites climate change and related environmental impacts (Schuur et al., 2015; McGuire et al., 2018). Hence, the growing relevance of permafrost-affected soils over the last decades demands an assessment of the effects of global warming and greenhouse gas emissions on SOCS in permafrost-affected regions as precise as possible (van Huissteden and Dolman, 2012; Chadburn et al., 2017). However, the ability to quantify potential greenhouse gas release from thawing permafrost-affected soils in the northern circumpolar region is restricted by the uncertainty of the SOCS data due to several aspects (Wojcik et al., 2018).

Soil organic carbon stocks and data uncertainty

There is a high variety of approaches for taking soil samples, measuring soil characteristics and calculating soil properties being relevant for the calculating of SOCS which tend to be uncertain, e.g. bulk density (BD; Poeplau et al., 2017). On this account, suggestions of standardising procedural methods in soil science were developed to reduce uncertainty and to generate consistent soil data sets (Arrouays et al., 2014). Gaps in the underlying data are filled mathematically, which holds another potential for uncertainty (Hugelius et al., 2014). In addition to the

computational completion of single datasets, databases are expanded by artificial data in form of pseudo-observations to take the unequal SOCS distribution data across the Arctic into account (Hengl et al., 2017). However, such large-scale estimations, e.g. covering the whole Arctic region, are generalised representation of the spatial variation of soil information generated from polygon data (Jones et al., 2009; Hugelius et al., 2013; 2014) or raster data (Hengl. et al 2014; 2017; Poggio et al., 2021). Being potentially not representative for the undersampled areas of the northern circumpolar region due to limitations in quality and quantity of SOCS data, large-scale estimations differ significantly from various field measurements (Zubrzycki et al., 2014; Kühn and Henkner, 2019). Especially, the majority of studies is spread across Alaska, Canada and Siberia, which makes Greenland an underrepresented area (Tarnocai et al., 2009; Hugelius et al., 2013; 2014; Köchy et al., 2015; Ping et al., 2015).

Soil organic carbon stocks and environmental relationships

The SOCS distribution of the circumpolar region is related to vegetation varying spatially in species, growth height, density and thus biomass production being a key source of organic material for the formation of SOCS (CAVM Team, 2003). In addition to organic material on the terrain surface, the SOCS is built on plant roots of diverse characteristics within the topsoil (Joggáby and Jackson, 2000; Iversen et al., 2015). Vegetation patterns are linked to variations of the landscape which has been reshaped by periglacial processes since the last deglaciation which started around 10,000 years ago in West Greenland (Levy et al., 2012). Besides, the SOCS distribution in permafrost regions also depends on the intensity of accumulation and decomposition of SOC affected by specific site conditions (Elberling et al., 2004; Baumann et al., 2014). On the one hand, decomposition rates are high under warm and dry site conditions (Auslander et al., 2003) and, on the other hand, accumulation of organic material is high under cold and moist soil conditions (Hobbie et al., 2000). The Arctic region is characterized by such contrary conditions related to specific landforms and terrain features which represent various relocation processes as well as forms of deposits (Palmtag et al., 2018; Wojcik et al., 2019).

Overland and interflow relocates soil material including SOC downslope and thus effects the spatial SOCS distribution under humid climate conditions e.g. at the coast of West Greenland (Stäblein, 1977). Water is also important for predominant processes of Arctic environments for the horizontal and vertical transportation and mixing of soil

material by solifluction and cryoturbation respectively. Solifluction is characterized as slow movement of topsoil along inclined permafrost-affected landscape surfaces whereas the intensity of mixing and transport of soil material depends on the slope angle of the surface (Matsuoka, 2001; 2011). Additionally, sorting soil material horizontally and vertically, ice wedges are common in Arctic landscapes (Mackay, 1995) but rather occur on north-facing slopes in West Greenland (Henkner, et al. 2016). Being common for permafrost regions, cryoturbation significantly alters the vertical appearance of the soil by frequently running freeze and thaw cycles (Bockheim, 2007). Cryosols thereby formed are wide-spread and show high SOCS also in the subsoil (Jones et al., 2009). Furthermore, aeolian transport is typical relocation process of periglacial shaped landscapes (Brookfield, 2011). This results in alteration of topsoil texture and coverage of the prior land surface which forms paleosols with organic rich horizons in the subsoil, e.g. in the ice margin area of West Greenland (Müller et al., 2016). Altogether, distinctly affecting SOCS distribution of permafrost-affected soils, environmental controlling factors and processes however differ in their spatial extent and their intensity across scales.

Soil organic carbon stocks and spatial scale dependencies

On large scales, being limited in considering small scale effects on environmental factors and processes, estimations of the circumpolar region show little variation in SOCS and might to be considered as uncertain and not representative for Greenland (Hugelius et al., 2014). With smaller scales, spatial heterogeneity of SOCS becomes more apparent as controlling factors being considered in increasing resolution of the underlying data (Hengl., 2014; 2017; Poggio et al., 2021). On large scales, climate related environmental factors as precipitation and temperature control vegetation development and soil formation (Post et al., 1982) leading to regionally differing soils and soil-landscape-systems varying in SOCS across Greenland (CAVM Team, 2003; Jones et al., 2009). In West Greenland, Umbrisols and Cambisols are predominant and potentially hold higher SOCS than shallow soils in North and East Greenland (Kühn and Henkner, 2019).

On the regional scale, decreasing precipitation and temperature along the west coast of Greenland results in regionally differing soil types and vegetation turning from Cryosols and Histosols and prostrate vegetation on Thule Peninsula in the Northwest (Horwath Burnham and Sletten, 2010) to humus-rich Arctic brown soils and dwarf

shrub vegetation in the Southwest (Bradley-Cook and Virginia, 2016). There is also a distinct spatial trend in environmental conditions from the coast to the margin of the Greenland Ice Sheet (GrIS) in West Greenland. Shaped by differences in the Holocene deglaciation history (Levy et al., 2012) and climate conditions (Cappelen et al., 2001; Carstensen and Jørgensen, 2009), regionally specific landscapes vary in vegetal activity (CAVM Team, 2003) and permafrost thickness (Van Tatenhove and Olesen, 1994) between the coastal region at Sisimiut and the ice margin region at Kangerlussuaq in West Greenland on the regional scale. At the coast, oceanic climate conditions favour the accumulation of SOC under moist and cold soil conditions, while the production and decomposition of SOC benefits from warm continental climate at the ice margin (Stäblein 1977; Ozols and Broll, 2003; Bradley-Cook et al., 2016; Henkner et al., 2016; Petrenko et al.,2016). Acting over a long distance, teleconnected processes vary with predominant climate conditions and have a subordinate effect on the spatial distribution of soil characteristics in periglacial shaped landscapes (Behrens et al., 2019a). Aeolian processes are associated with SOCS distribution only at the ice margin in West Greenland (Henkner et al., 2016; Müller et al., 2016).

On the local scale, the spatial SOCS distribution is connected to location-specific characteristics and relocation processes in permafrost regions (Dörfer et al., 2013; Baumann et al., 2014; Patzner et al., 2020). Shaped by periglacial processes, such heterogeneous landscapes are characterized by a multitude of small-size geomorphological elements which can be described by representative landscape units (Palmtag et al., 2018; Wojcik et al., 2019). They also reflect different site conditions affecting plant growth and soil formation and thus the SOCS distribution on the local scale (Jobbágy and Jackson, 2000; Ozols and Broll, 2003; Bradley-Cook and Virginia, 2016; Henkner et al., 2016; Petrenko et al., 2016). Therefore, the SOCS is low on north-facing locations with colder microclimate than on south-facing locations with higher input of organic material which is represented by the aspect and vegetation respectively (Henkner et al. 2016). Soil characteristics vary vertically on small scales (Rentschler et al., 2019, 2020) and, however, are additionally affected by cryoturbation which spatially varies in the intensity with the terrain on the local scale at the coast of West Greenland (Stäblein, 1977).

Furthermore, environmental processes take place parallel on several environmental scales but differ in their role and intensity on soil characteristics. Common Arctic processes as cryoturbation and impeded drainage lead to higher SOCS on summits

and toeslopes than on backslopes and footslopes (Ramage et al., 2019). Interflow and hillwash relocate SOC downward along slopes of both small hills and valleys (Stäblein, 1977). On the hill scale, soil material is transported between small-scale geomorphological elements as from moraine crests to depressions but on the valley scale along the valley slope to moraine crests. In addition, material is moved by water and wind on the catchment scale depending on predominant environmental characteristics like sharply incised valleys being shaped by periglacial processes since the last deglaciation in West Greenland (Stäblein, 1977; Ozols and Broll, 2003; Willemse et al., 2003; Henriksen, 2008; Müller et al., 2016). Perspectival, comparable landscape characteristics show similar processes, however, affect the spatial SOCS distribution differently depending on the relevant scale which can be represented by multi-scale terrain features (Behrens et al., 2019b).

Soil organic carbon stocks and machine learning

Already, terrain features are successfully used as representatives for soil forming factors in digital soil mapping (Jenny, 1941; McBratney et al., 2003). Furthermore, environmental processes are related to landscape characteristics being represented by terrain features as well (Wilson and Gallant, 2000; Moran and Bui 2002). Over the last decades, a variety of extended and newly developed approaches as regression kriging (Hengl. et al., 2004) or geographically weighted regression (Fotheringham et al., 2002) were used to improve spatial estimations of soil information on different scales separately (Mishra and Riley, 2012; Hengl., 2014). Subsequently, increasing computing capacity advanced the development of machine learning techniques which nowadays are regarded as standard in soil-landscape analysis (Padarian et al., 2020; Taghizadeh-Mehrjardi et al., 2022).

Machine learning recently enabled interweaving the effects of multiple scales in soil data (e.g. Behrens et al. 2014, Behrens et al., 2018a). Such scale-dependent and spatial variation of soils results from multi-scale sources and interactions (Burrough, 1983), which can be detected by scale-related pattern recognition and contextual feature construction techniques such as the ConMap approach (Behrens et al., 2010), wavelet transformations (Biswas et al. 2013), Euclidean distance fields (EDF; Behrens et al., 2018b), a variogram based effective scale space (Karl and Maurer, 2010, Behrens et al., 2019b) and analyzing teleconnections in soil environmental systems (Behrens et al., 2019a). In addition, soil formation is dependent

on spatial scale-related processes which can be represented by multi-scale environmental features derived from feature construction and selection techniques such as generating soilscapes (Schmidt et al., 2010), hyper-scale digital soil mapping (Behrens et al., 2014) and a Gaussian scale space (Behrens et al., 2017). Among other soil information, reliable estimations of SOC were generated successfully by the application of machine learning techniques in different environmental systems at various scales (Grimm et al., 2008; Schmidt et al., 2014; Stumpf et al., 2018; Rentschler et al., 2019; 2020; Viscarra Rossel et al., 2019; Taghizadeh-Mehrjardi et al., 2020).

Random forests (RF) (Breiman, 2001) is frequently applied in soil science as being a robust machine learning technique unaffected by outliers and data gaps. Additionally, being a transparent method combined with the significant advantage of measuring the importance of environmental features (Kuhn, 2017), RF allows for an expert based interpretation in a pedological context concerning the role of single input features on the spatial variation of soil characteristics. Hence, machine learning techniques can increase the understanding of environmental controlling factors and associated spatial scale-dependent processes of soil formation on different scales in Arctic low mountain ranges with limited soil information, as in West Greenland.

Objectives

Objective of this thesis was to investigate the SOCS distribution of permafrost-affected soils in West Greenland. In this context, the role of controlling factors and relocation processes affecting the spatial variation of SOCS was observed. As interrelations of SOCS, controlling factors and relocation processes are scale-dependent and vary spatially, the investigations were allocated to two complementary scale approaches. First, this thesis focused on vegetation, landscape and aspect in form of defined units to describe the SOCS distribution over short distances on the local scale and over long distances on the regional scale within and between two study areas differing in climate conditions respectively (Gries et al., 2020). Second, spatial and multi-scale terrain features were applied to investigate the role of relocation processes related to frost change, water and wind acting parallel in varying intensity on the hill, valley and catchment scale on the SOCS distribution in two study areas separately (Gries et al., unpublished). Therefore, such spatial features were recreated to provide the integration of spatial-dependencies into machine-learning based digital soil mapping approaches (Behrens et al., 2018b). Further, the vertical distribution of SOC was

investigated (Rentschler et al., 2019; Gries et al., 2020, Rentschler et al., 2020). For this thesis, two study areas in West Greenland, showing comparable environmental conditions on the local scale and contrary climate conditions on the regional scale, were selected to ensure general conclusions and recommendations from ranking controlling factors and processes by comparing particular units and measuring the feature importance respectively.

The objectives of this thesis were to:

- investigate the role of environmental factors on the spatial and vertical SOCS distribution on the local and the regional scale in West Greenland (manuscript 1, 4, 5).
- investigate the role of relocation processes on the SOCS distribution acting on the hill, valley and catchment scale in West Greenland (manuscript 2, 3).

First, it was hypothesized that SOCS in West Greenland is higher in the amount and the spatial variation compared to existing large-scale estimations. Conjecturable, the SOCS decreases with warmer and drier environmental conditions towards the ice margin. Further, it was assumed that vegetation, landscape and aspect units are adequate representatives of heterogeneous environmental conditions on the local scale and of contrary climate conditions on the regional scale to describe the spatial SOCS distribution on both scales.

Second, it was hypothesised that the SOCS distribution is affected primarily by relocation processes on the hill scale due to heterogenous local terrain in both study areas. Further, it is assumed that relevant scales and important features differ between both study areas as presumably the SOCS distribution additionally depends on aeolian processes by katabatic winds at the ice margin.

2 Data and methods

To respond to the hypothesis and the objectives a wide spectrum of methods is required (Figure 1). To ensure an optimal representation of the environmental conditions of the study areas (Section 2.1), a stratified random sampling was applied (Section 2.2) for retrieving soil data (Section 2.3). Processing of environmental data and defining several scales (Section 2.4) are preconditioned for statistical and machine learning based analyses (2.5).

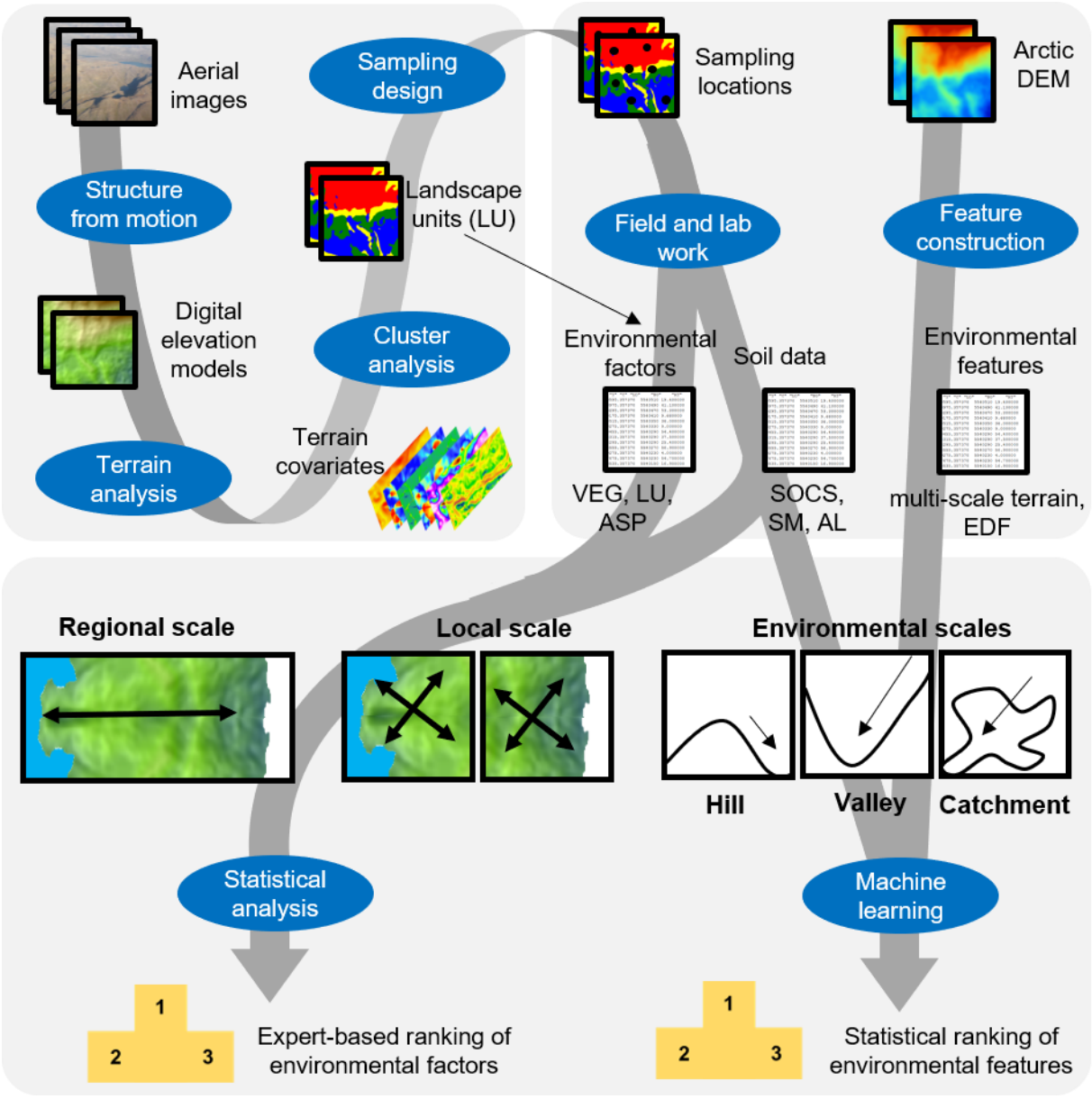

Figure 1: Methodical overview. Visualisation of the main methodical steps beginning with preprocessing steps required for an appropriate sampling scheme as basis for a comprehensive data set, consisting of soil and environmental data from field work and feature construction. The data set is analysed by statistical and machine learning techniques in consideration of two complementary scale approaches for a concluding ranking of environmental factors and features with regard to their potential to reflect the SOCS distribution.

2.1 Study areas

For this thesis, two study areas in West Greenland are selected (Fig. 2). The first one is located at the coast 4 km east of Sisimiut (SISI, 66° 57 N, 53° 33' W). The coastal region is characterized by oceanic climate conditions with coastal westerly winds, frequently occurring fog, a mean annual temperature (MAT) of –3.5 °C and a mean annual precipitation (MAP) of 383 mm (Cappelen et al., 2001; Carstensen and Jørgensen, 2009). SISI is 1.5 km^2 in size, located within a deep valley orientated northeast-southwest and has steep north- and south-facing slopes. To the north SISI is limited by steep slopes (> 30°) being characterized by thin soils and sparse vegetation cover. A small river defines the eastern boundary and crosses the study area to the southwest into a lake as the western boundary. In the south, steep north-facing slopes limit the study area, which is covered with adjacent depressions in smooth transition with slightly inclined slopes and moraines (Gries et al., 2020).

The second study area is 1.8 km^2 in size and located around two kilometres west of the Russell Glacier (RUSS, 67° 6' N, 50° 17' W) at the ice margin of the GrIS. This area is characterized by katabatic winds from the east and an Arctic continental climate with MAT of –5.7 °C and MAP of 149 mm (Cappelen et al., 2001; Carstensen and Jørgensen, 2009). RUSS is limited by lakes to the east and west and to the north and south by steep slopes of an east–west oriented valley. In north-south direction, different terminal moraines cross the valley which shows sand dunes occurring in the northeastern part formed by aeolian sediments from the outwash plains at the glacier foreland (cf. Müller et al., 2016).

Both study areas are covered by mountain vegetation on non-carbonate bedrock, i.e., mostly granite in SISI and gneiss in RUSS (CAVM Team, 2003; Henriksen, 2008). Vegetation cover is connected to geomorphology with sedges growing in flat areas. Mosses, lichens and prostrate dwarf shrubs cover steep slopes and ridges. Wind sheltered areas and slightly inclined slopes are covered by dwarf shrubs. The landscape has been reshaped by periglacial processes since the last deglaciation (Willemse et al., 2003; Henriksen, 2008), thus soil formation took place for around 10,000 years in SISI and 6,800 years in RUSS (Levy et al., 2012). Crests and the steep slopes of moraines are characterized by coarse substrate, thick active layer (> 200 cm) and less developed soils. Sandy substrate and warm and dry soil conditions are typical for wind sheltered locations of dunes and slightly inclined slopes showing partially

buried organic rich soils sometimes buried by aeolian sediments. Flat areas are covered by soils with thick organic horizons, silty substrate, high soil moisture and a thin active layer (~ 50 cm; Gries et al., 2020).

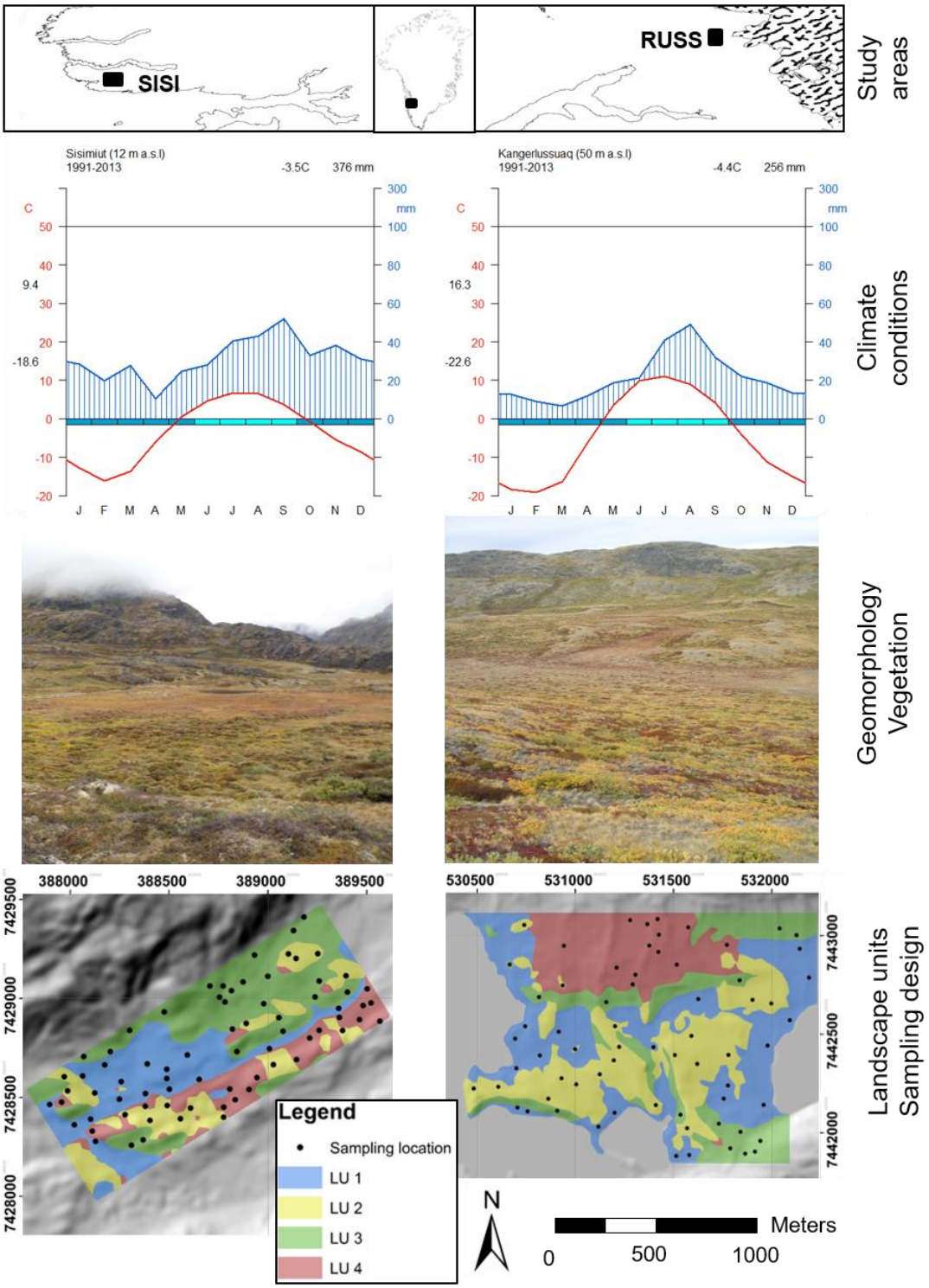

Figure 2: Study areas and sampling design. Overview of geographical locations of the study area close to Sisimiut at the coast (SISI, left) and nearby the Russell Glacier at the margin of the Greenland Ice Sheet of West Greenland (RUSS, right; geodata from © OpenStreetmap contributors), climate conditions (Cappelen et al., 2001; Guijarro, 2019), geomorphology and vegetation (Fotos: © J. Gries, Sept. 2015) and sampling design including landscape units and sampling locations (Maps from Gries et al., 2020, modified).

2.2 Sampling design and delineation of landscape units

As the landscape of both study areas is heterogenous, a sampling design adapted to the given environmental conditions is necessary to avoid under- or oversampling (Lohr, 2021). Therefore, both study areas are divided into homogenous landscape units (LU) according to the deglaciation history and geomorphology of the land surface (Fig. 1, Fig. 2).

In the first step, a set of local, regional and combined terrain covariates being relevant for the spatial distribution of SOCS (Tab. 1) is derived from a digital elevation model (DEM) using the *Terrain Analysis Toolbox* in SAGA GIS (version 2.2.2; Conrad et al., 2015). This DEM with a resolution of 5x5 m is computed from aerial images from the Geodetic Institute of Denmark using structure from motion and photogrammetry using VisualSFM (Wu, 2011; Wu et al., 2011; Smith et al., 2016).

In the second step, using the *stats package* in R (version 3.4.2; R Development Core Team, 2013), k-means cluster analysis for automated and unsupervised classification of the terrain covariates is applied to delineate the LU (Burrough et al., 2000; Schmidt et al., 2010). The result of the cluster analysis is the subdivision of the study areas into homogeneous classes showing high interclass variance and small intraclass variance (Webster and Beckett, 1968; Everitt, 1980). The selection of the number of clusters is based on a representation of the two study areas that is as structured and less fragmented as possible. The maximum number of LUs is set to k = 10 to address feasibility of the subsequent sampling design (Schmidt et al., 2010). For the determination of the optimal number of classes, the number of fragments and their perimeter per class is used. The optimal number of classes results from a low degree of fragmentation which is given at a small number of fragments and their perimeter. Visually, the intersection represents the optimal size of k which is both 3.68 and 4.34 for SISI and 4.18 for RUSS (Fig. 3). Finally, four classes are set for LUs (Gries et al., 2020).

In the third step, pairwise comparability of related LUs between both study areas is confirmed by a paired t-test of the terrain covariates of each LU (Tab. 1) using the *stats package* in R (version 3.4.2; R Development Core Team, 2013).

In the last step, according to surface percentage and fragmentation, 140 sampling points are proportionally allocated to the LUs and within each LU randomly distributed using *Create Random Points* in ArcGIS Desktop (version 10.3; ESRI, 2014; Fig. 2).

Table 1: Properties of landscape units. Comparison of landscape units (LU) adapted from main area distribution and descriptive statistics (mean ± SD) of terrain covariates, related to environmental processes and conditions affecting SOCS, including results of the t-test (significance level, α = 0.05) to verify the comparability of each LU between SISI and RUSS (from Gries et al., 2020, modified).

	Main area Distribution	p-vale	Study area	Terrain driven relocation processes				Insolation, wind pattern		Patterns of eroion or accumulation				Moisture
				Slope[1a]	FlowAcc[2b]	LS[3c]	RMB[4a]	CosA[1a]	SinA[1a]	ProCur[1a]	PlaCur[1a]	TCI[5d]	TPI[6e]	TWI[7f]
LU1	Depression	0.37	SISI	6.866 ± 4.128	7.706 ± 1.167	2.413 ± 1.637	- 0,485 ± 1.492	- 0.781 ± 0.289	- 0.042 ± 0.553	- 0.002 ± 0.002	- 0.013 ± 0.080	0.394 ± 0.098	- 3.114 ± 2.819	9.421 ± 2.077
			RUSS	3.136 ± 1.557	7.000 ± 1.535	0.899 ± 0.550	- 0.212 ± 1.364	- 0.328 ± 0.658	0.032 ± 0.678	- 0.001 ± 0.001	- 0.01 4± 0.059	0.655 ± 0.090	- 0.692 ± 0.451	10.086 ± 1.838
LU2	Crest	0.27	SISI	11.182 ± 8.882	4.561 ± 1.634	3.785 ± 3.547	- 0.487 ± 1.769	0.736 ± 0.322	0.317 ± 0.504	- 0.001 ± 0.005	0.001 ± 0.034	0.537 ± 0.149	0.168 ± 5.870	7.887 ± 1.601
			RUSS	3.436 ± 1.609	5.267 ± 0.889	0.746 ± 0.452	- 0.121 ± 1.398	- 0.186 ± 0.687	0.084 ± 0.698	0.001 ± 0.002	0.017 ± 0.067	0.761 ± 0.054	0.115 ± 0.412	8.237 ± 0.942
LU3	Plateau	0.19	SISI	13.418 ± 7.969	7.161 ± 1.128	4.748 ± 3.244	- 0.782 ± 1.648	- 0.762 ± 0.236	0.433 ± 0.420	- 0.001 ± 0.003	0.003 ± 0.033	0.652 ± 0.083	1.569 ± 5.596	7.686 ± 1.454
			RUSS	4.036 ± 1.581	6.273 ± 1.137	1.075 ± 0.52	- 0.07 6± 1.454	- 0.622 ± 0.415	- 0.122 ± 0.652	0.000 ± 0.001	0.001 ± 0.033	0.652 ± 0.083	1.569 ± 5.596	7.686 ± 1.454
LU4	Slope	0.20	SISI	12.074 ± 8.312	6.812 ± 0.999	4.154 ± 3.207	- 0.387 ± 1.670	0.542 ± 0.382	- 0.717 ± 0.215	0.061 ± 0.495	0.002 ± 0.039	0.538 ± 0.146	- 0.081 ± 7.222	7.949 ± 1.953
			RUSS	8.616 ± 1.882	6.215 ± 0.850	2.779 ± 0.848	- 0.299 ± 1.673	- 0.559 ± 0.663	0.061 ± 0.495	0.000 ± 0.002	- 0.001 ± 0.010	0.705 ± 0.079	- 0.081 ± 7.222	8.124 ± 0.917

[1]Zevenbergen and Thorne, 1987; [2]Freeman, 1991; [3]Moore et al., 1991; [4]Relative mass balance; Friedrich, 1996; [5]Topographic classification index for lowlands; Bock et al., 2007; [6]Topographic position index; Guisan et al., 1999; [7]Topographic wetness index; Beven and Kirkby, 1979. SAGA GIS tool box 'terrain analysis': [a]morphometry – slope [°], aspect [°], curvature [1/m]; [b]hydrology – flow accumulation (mass flux method) [log(n pixels)]; [c]hydrology – ls factor [dimensionless]; [d]hydrology – tci low [dimensionless]; [e]morphometry – topographic position index [dimensionless]; [f]hydrology – topographic wetness index [dimensionless].

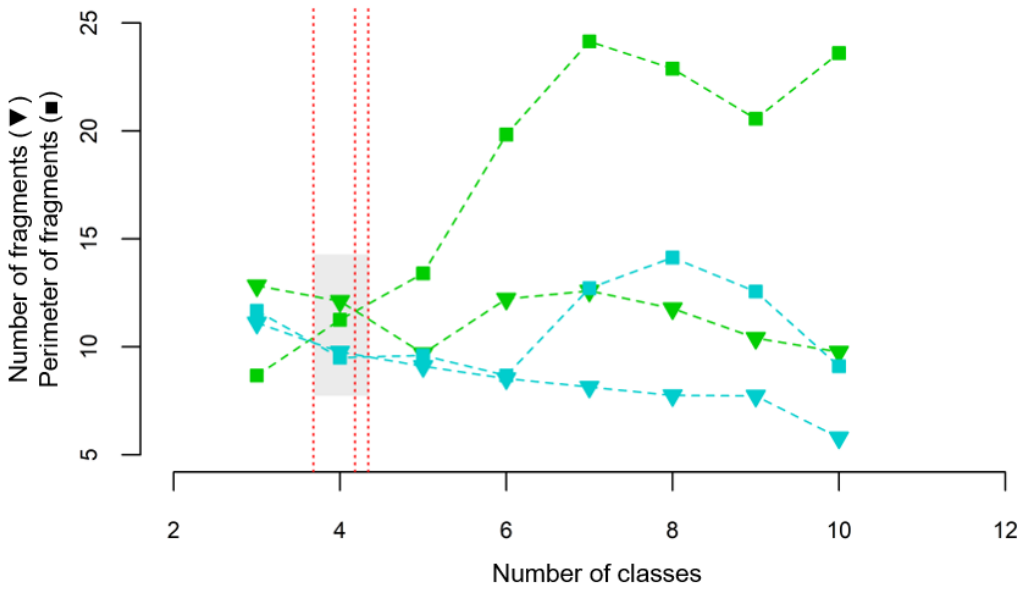

Figure 3: Number of landscape units. Comparing the fragmentation to the number of cluster classes to determine the optimal number of landscape units. The graphs represent the number (▼) and perimeter (■) of fragments as a function of the number of cluster classes subdividing SISI (blue) and RUSS (green) respectively. The optimal number of classes results from a low degree of fragmentation graphically expressed within the range (grey) of the intersections of corresponding graphs between 3.68 and 4.34 for SISI and RUSS (from Gries et al., 2020, modified).

2.3 Soil data

During the field work in the summer of 2016, soil, vegetation and landscape characteristics were recorded and soil samples were collected at 140 locations in total in both study areas. Soil moisture (SM) content [%] was measured within the top 5 cm using a HH2 Moisture Meter and Thetaprobe ML2 (Delta-T Devices, Cambridge, GB). The determination of the active layer (AL) thickness [cm] was done within the uppermost 200 cm while taking the soil samples. Dominant species and growth height were recorded as vegetation characteristics. The aspect was detected with a compass to specify the landscape at all sampling location.

Soil samples for SOC and BD were taken at four depth increments (0 – 25, 25 – 50, 50 – 100 and 100 – 200 cm) using a hand-driven, half-open Pürckhauer auger with a slot width of 18 mm for 0 – 100 cm and an extension with a slot width of 16 mm for 100 – 200 cm. Samples were only taken from the unfrozen ground. The first depth increment (D1) was set to 0 – 25 cm since a maximal thickness of the upper organic horizon of 25 cm was derived from a previous field survey in both study areas. The second depth increment (D2) was set to 25 – 50 cm to account for a minimum AL

thickness of about 50 cm under comparable landscape conditions in West Greenland (Bradley-Cook et al., 2016; Henkner et al., 2016). The third depth increment (D3) was set to 50 – 100 cm to address large amounts of SOC in the subsoil (Tarnocai et al., 2009; Hugelius et al., 2014). The fourth depth increment (D4) was set to 100 – 200 cm to consider soil heterogeneity due to cryoturbation (Ping et al., 1998).

At each sampling location, three soil cores were sampled for SOC analysis to ensure three replicates of each depth increment over the entire depth. The replicates of each depth increment were bulked to one sample. If frozen subsoil conditions or bedrock prevent sampling the entire depth increment, the SOCS of the not-sampled part was set to 0. Due to such subsoil conditions 140 samples were taken from D1, 138 samples from D2, 127 samples from D3, and 91 samples from D4 for SOCS. BD samples were collected from the middle of each depth increment (10 – 15, 35 – 40, 72.5 – 77.5, and 147.5 – 152.5 cm) from soil cores at 16 locations, covering all LUs (Gries et al., 2020).

Samples for SOC were dried at 40 °C, sieved (< 2 mm) and analyzed using an element analyzer (CN mode, Vario EL II, Elementar Analysesysteme GmbH, DE). Measurements below the detection limit (carbon: 0.2 %) were set to zero. The total carbon content equals SOC [%] as the carbonate content off all samples was zero according to the Scheibler test (Rothenhöfer et al., 2000). Samples for BD were dried at 105 °C to determine the $mass$ [g] gravimetrically to calculate the BD [g cm^{-3}] according to equation (1) and equation (2) and to define the mass proportion of the coarse fraction (CF; > 2 mm) [%] to calculate the SOCS [kg m^{-2}] according to equation (3; Scholten et al., 2017). Equation (2) is required to measure the volume of a sample (V_s) taken from a half-open Pürckhauer auger (Gries et al., 2020):

$$(1) \qquad BD = mass/V_s,$$

$$(2) \qquad V_s = V_c + 0.5 \times V_e = w \times h \times l + 0.5 \times (\pi \times a \times b \times l),$$

where V_s [cm^3] results from the volume of a cuboid V_c [cm^3] with height h and the half of an ellipse V_e [cm^3] with height b; a is the half of the slot width of the auger w and l is the depth of the BD samples; a, b, h, l, and w are given in cm.

$$(3) \qquad SOCS = SOC \times BD \times D \times (1 - CF),$$

where D [cm] is the thickness of the depth increments D1–D4. The actual depth was used for D if it was not possible to sample the entire depth increment due to subsoil conditions.

2.4 Environmental data and definition of scales

2.4.1 Vegetation, landscape and aspect units on the local and regional scale

Vegetation cover was classified by species and growth height according to Bliss (2000) into four vegetation units (VEG; Tab. 2): dwarf shrub heath tundra (VEG1), low shrub tundra (VEG2), tall shrub tundra (VEG3) and graminoid-moss tundra (VEG4). The LUs represent the spatial extend of homogenous landform elements of the land surface within the study areas (Tab. 1): depressions, flat and bankside areas (LU1), moraine crests, ridges and summits (LU2), plateau areas (LU3) and steep slopes (LU4). The aspect (ASP) was grouped to 8 classes according to the main (N, E, S, W) and ordinal directions (NE, SE, SW, NW).

In this scale approach, the role of spatially varying environmental conditions is represented by the above-mentioned controlling factors (VEG, LU, ASP) which are considered to explain the SOCS distribution at two different scales:

- The local scale focuses on the differences between the units of the controlling factors within each study area to explain the SOCS distribution over short distances.
- The regional scale focuses on the related units of each controlling factor between the two study areas to investigate differences of SOCS between the coast and the ice margin with different climatic conditions.

Table 2: Properties of vegetation units. Classification of vegetation based on species and growth height according to Bliss (2000) (from Gries et al., 2020, modified).

	Description	Main species	Growth height	Main area distribution	Surface conditions	Coverage (SISI / RUSS)
VEG1	Dwarf shrub heath tundra	*Betula nana, Dryas integrifolia*	5 – 20 cm	Crest	Dry	28 / 10
VEG2	Low shrub tundra	*Betula nana*	20 – 40 cm	Slope	Cold	38 / 39
VEG3	Tall shrub tundra	*Salix glauca*	> 40 cm	Gentle slope	Warm	4 / 18
VEG4	Graminoid-moss tundra	*Carex rariflora, Eriophorum angustifolium*	5 – 20 cm	Depression	Moist	30 / 33

2.4.2 Terrain and spatial features on the moraine, valley and catchment scale

Environmental factors and processes affecting the SOCS distribution are connected to landscape characteristics varying spatially and across different scales. As being a multi-scale hierarchical mapping approach combining terrain and spatial feature construction, contextual spatial modelling (CSM) allows for pedological multi-scale and spatial analyses (Behrens et al., 2018a; 2019b). Therefore, CSM was applied to construct terrain features using a hierarchical representation of the ArcticDEM (2x2 m, version 2.0, release 4; Porter et al., 2018) in the form of a Gaussian pyramid (Behrens et al., 2018a). First, the resolution of the ArcticDEM was halved stepwise using smoothing and scaling steps until no further scaling is possible (Burt and Adelson, 1983). This resulted in a sequence of 22 digital elevation models representing 22 different scales (Fig. 4). Second, all 22 DEMs were upsampled to the original resolution of 2 x 2 m to avoid any artefacts when combining gridded datasets of different cell sizes. Third, from all 22 resampled DEMs, the following terrain features were delineated based on the algorithms by Zevenbergen and Thorne (1987): elevation (Elev), steepest slope downslope (Slope), sine and cosine transformation of the aspect (sinAsp, cosAsp), average curvature (AvCurv), cross-sectional curvature (CrCurv) and longitudinal curvature (LoCurv).

To supplementary address spatial relationships within the data set, Euclidean distance fields (EDF) were used as spatial features (Behrens et al., 2018b). The EDFs are a representation of the distance to the edges (X01, Y01), corners (C1, C2, C3, C4) and the centre (CC) of an artificial grid surrounding the study areas. Being a collection of autocorrelated indicators of relative spatial position within the study area, EDFs allow to identify spatial non-linear relationships. EDFs are gridded datasets having the same resolution as the multi-scale terrain features whereas the pixel values correspond to the Euclidean distance to the respective edge, corner or centre of the bordering grid (Fig. 4). The inclusion of several reference points enables detecting spatially varying trends within the soil dataset and thus to consider for spatial non-stationarity (Behrens et al., 2018b). Multi-scale terrain and spatial features were constructed by the *CSM – contextual spatial modelling* software (version 17.08, BitMapping GmbH, DE).

In this scale approach, the SOCS distribution affected by environmental processes acting on different scales is considered. Such processes are linked to certain topographic conditions which can be represented by specific terrain features of

different scales (Wood, 1996). Therefore, the sequence of 22 scales which are the result of the multi-scale terrain feature construction is segmented into three environmental scales associated with key topographic conditions and related processes. The calculation basis for the subdivision is the resolution of the upsampled DEMs of the Gaussian pyramid and the maximum horizontal distance between key geomorphological elements of the periglacial landscape. The maximum horizontal distance is digitally determined based on expert knowledge in SAGA GIS (version 2.2.2; Conrad et al., 2015). All scales with a pixel size smaller than or equal to the maximum horizontal distance of the respective scale are combined (Fig. 4):

- The moraine scale deals with freeze-thaw processes as solifluction having an effect on the relocation of soil material along small-size geomorphologic elements such as moraines and small hills characterizing the heterogeneous terrain surface within the study areas. The maximum horizontal distance between ridge and footslope of moraines and small hills is 54 m and the moraine scale comprises the scales 1 – 10 with pixel sizes between 2 x 2 m to 48 x 48 m.
- The valley scale covers downslope processes, as interflow and hillwash, relocating soil components along the valley slopes into the study areas. The maximum horizontal distance of the slope segments potential for relocation is 145 m in both study areas and thus the valley scale comprises scales 11 – 14 with pixel sizes ranging from 64 x 64 m and 192 x 192 m.
- The catchment scale considers the catchment area of teleconnected processes, which result from the respective climate conditions in SISI and RUSS as wind direction and aeolian transport. Such processes take place over long distances being represented by the scales 15 – 22 with pixel sizes from 256 x 256 m to 3072 x 3072 m.

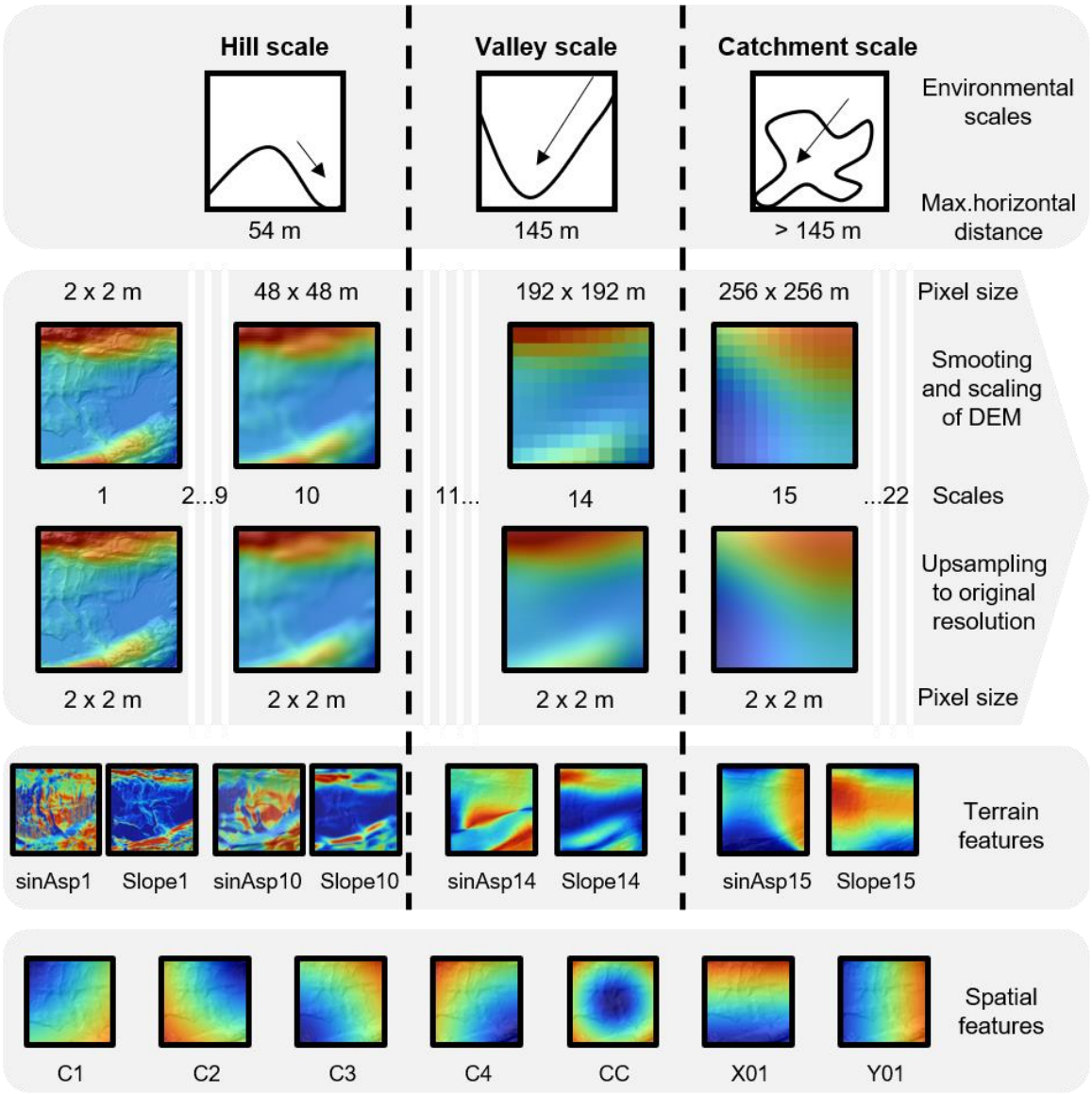

Figure 4: Environmental scales and feature construction. Definition of the moraine, valley and catchment scale according to the maximum horizontal distance of key geomorphological elements and corresponding pixel sizes of DEMs which result from sequenced smoothing and scaling steps. After resampling all DEMs to the original resolution (2 x 2 m), terrain features are delineated at overall 22 scales. Due to the smoothing and scaling and resampling steps, the representation of the landscape by the terrain features has changed which is exemplified by the sine of the aspect (sinAsp) and steepest slope downslope (Slope) at first and last scale of the moraine scale (1, 10), the last of the valley scale (14) and the first of the catchment scale (15) to demonstrate the trend in the delineation of the landscape at the respective environmental scale. The spatial features include the Euclidean distance fields (EDF) representing the distance to the upper left (C1), upper right (C2), lower left (C3) and lower right corner (C4), the centre (CC), the lower (X01) and left edge (Y01) of an artificial grid around the study area.

2.5 Data analyses, feature importance and spatial modelling

Statistical analyses of field and lab data and relationships between soil characteristics and environmental units are done with the statistical software R using the *stats package* (version 3.4.2; R Development Core Team, 2013).

The analyses of the importance of individual spatial features and terrain features of specific environmental scales was done using random forests (RF, Breiman, 2001) being – as a machine learning technique – highly suited to extract relationships within large and complex datasets for the spatial prediction of soil characteristics (Taghizadeh-Mehrjardi et al., 2022). The concept of RF is the aggregation of multiple Classification and Regression Trees (CART; Breiman, 1984) each build on randomly selected samples of the training data. The drawing of the samples bases on bootstrapping so that individual samples may be taken several times and others may be not considered in a single tree at all. The validation of the particular CART is done with the training data not being used. Besides, a random set of features is used for each split. By accounting for these random effects, RF is robust to outliers and offers higher model accuracy than CART. The specification of the optimum number of features at each split (*mtry*) is done by grid learning (cf. Schmidt et al., 2008) using the *caret package* (Kuhn, 2017) in R (R Development Core Team, 2013). The accuracy of the RF models is given by the coefficient of determination (R^2; equation 4) and the normalized root mean square error (nRMSE; equation 5) based on ten times repeated 10-fold cross-validation:

$$(4) \qquad R^2 = \left(\frac{\sum_{i=1}^{n}(y-\mu_y)(\hat{y}-\mu_{\hat{y}})}{\sqrt{\sum_{i=1}^{n}(y-\mu_y)^2}\sqrt{\sum_{i=1}^{n}(\hat{y}-\mu_{\hat{y}})^2}}\right)^2,$$

$$(5) \qquad nRMSE = \sqrt{\frac{1}{n}\sum_{i=1}^{n}(y_i-\hat{y}_i)^2}\Big/(y_{max}-y_{min}),$$

where y and $\hat{y}$ are the observed and predicted values and μ_y and $\mu_{\hat{y}}$ are the means of the observed and predicted values.

The advantage of RF is an integrated measurement of the feature importance in which the mean decrease in accuracy is calculated. Thereby, the values of each feature are permuted and the resulting decrease in the accuracy of the model is measured. The more important a feature is, the greater the decrease in accuracy (Kuhn, 2017).

The feature importance measurement is used to investigate the scale, spatial and regional dependencies of the SOCS distribution. The determination of dominant scales and features comprises the analyses of the feature importance to address the following dependencies:

- Scale dependencies of the SOCS distribution influenced by environmental processes acting parallelly on the moraine, valley and catchment scale are considered by this **area-specific approach** consisting of an ascending and a descending approach. The ascending approach ($SISI_{asc}$, $RUSS_{asc}$) primarily considers small scales and prevents the cover effect of large scales by stepwise adding scales in a sequence of RF models. The first RF model includes the terrain features of the first of 22 scales. The following RF model is extended by the terrain features of the next larger scale, and so on. The descending approach ($SISI_{desc}$, $RUSS_{desc}$) accounts for the effect of large scales and is processed in reverse order to the ascending one. The first RF model includes the terrain features of the last of 22 scales. The following RF model is extended by the terrain features of the next smaller scale, and so on. The ascending and descending approach are applied in each study area separately. For each area, one RF model is trained using all multi-scale terrain features to estimate the spatial distribution of SOCS in SISI ($SISI_{area\text{-}specific}$) and RUSS ($RUSS_{area\text{-}specific}$) separately.
- Spatial dependencies of the SOCS distribution are considered by additionally including spatial features into separate **spatial approache**s for SISI and RUSS ($SISI_{all}$, $RUSS_{all}$). These models allow for identifying spatial dependencies in the data set which might not covered by the terrain features.
- Regional dependencies of the SOCS distribution between SISI and RUSS are investigated by two regional-specific approaches. The **crosswise approach** ($SISI_{cross}$, $RUSS_{cross}$) examines regional dependencies by transferring models to regions differing in their environmental conditions. For SISI and RUSS, a RF model including terrain features from all scales is built separately and transferred to estimate the spatial SOCS distribution for the respective other study area. The **combined approach** ($COMB_{asc}$, $COMB_{desc}$) considers the impact of small and large scales on the spatial SOCS distribution in West Greenland from the coast to the ice margin. Therefore, as described above, ascending and descending sequences of RF models are trained on a merged dataset from both study areas. Finally, one RF model based on the merged data and all multi-scale terrain features ($COMB_{all}$) is used to estimate the SOCS in both areas.

3 Results and discussion of the manuscripts

3.1 SOCS distribution on the local and regional scale (manuscript 1, 4, 5)

3.1.1 Local scale SOCS distribution

In SISI, SOCS is lowest at all depth increments for dwarf shrub heath tundra (VEG1; Tab. 2; Fig. 5). As primarily covering north-west- and west-facing locations, growth of VEG1 is negatively affected by continuously blowing onshore winds and strong direct solar radiation. Consequently, low production but high decomposition rates of organic material results in low SOCS with VEG1 in coastal regions in West Greenland (Jensen et al., 2006). In SISI, SOCS distribution at the first depth increment is linked to heterogenous spatial variation in vegetation cover as the roots of most Arctic plants grow within the upper 25 – 30 cm (Iversen et al., 2015). Due to differences in rooting depth of the occurring species, the spatial varying vertical SOCS distribution follows non-linear trends (Rentschler et al., 2019). Further, downslope relocation processes transport organic material along steep slopes dominantly covered by VEG1 to flat areas and depressions covered by graminoid-moss tundra (VEG4; Gries et al., 2020). Such areas show highest SOCS at both 25 – 50 cm and 50 – 100 cm of depth due to dense rooting and the continuous accumulation of organic material forming thick organic layers at moist soil conditions with low decompositions rates at oceanic climate conditions (Stäblein, 1977; Jensen et al., 2006). The SOCS is high with low shrub tundra (VEG2) and tall shrub tundra (VEG3) due to similar processes of SOCS accumulation (Petrenko et al., 2016). Thus, the SOCS combined for VEG2 and VEG3 corresponds with 10.57 ± 6.33 kg m^{-2} in SISI to SOCS with 10.20 kg m^{-2} for comparable vegetation in coastal areas of West Greenland (Bradley-Cook and Virginia, 2016).

In RUSS, the general relationships between SOCS and VEG are similar to SISI. However, low precipitation rates and dry katabatic winds throughout the vegetation season negatively affect vegetation growth and biomass production on wind-exposed areas and additionally the accumulation of organic material into the soil at the ice margin area (Ozols and Broll, 2003). Therefore, the SOCS is lowest with 4.98 ± 4.03 kg m^{-2} at the first depth increment for VEG1 predominantly covering wind-exposed areas. The SOCS is highest with 10.88 ± 2.20 kg m^{-2} for VEG3 being 31 % higher than for VEG2 and VEG4 at 0 – 25 cm as leaf remains of *Salix glauca* – the

dominant species of VEG3 – contributes decisively to the accumulation of soil organic matter into the upper soil horizons (Ozols and Broll, 2003). Further, very dry soil conditions result in low decomposition rates and high SOCS with VEG2. In contrast, high soil moisture content also reduces decomposition rates in bankside areas and depressions in RUSS predominantly covered by VEG4. Soil moisture is connected to physical soil properties changing distinctly between soil horizons which results in high vertical variation of SOCS (Rentschler et al., 2020). In summary, the distribution of SOCS depends on the spatial variation of the vegetation cover and the portions in Arctic environments on the local scale (Elberling et al., 2008b; Horwath Burnham and Sletten, 2010; Palmtag et al., 2015; Siewert et al., 2015; Wojcik et al., 2019).

In both study areas, SOCS distribution is linked to the heterogenous periglacial landscape and the variety of associated processes. In SISI, the SOCS is highest with 10.82 ± 8.83 kg m^{-2} at 0 – 25 cm in plateau areas (LU3) which is about 40 % higher than in depressions, flat areas and bankside areas (LU1), moraine crests and ridges (LU2) and steep slopes (LU4) (Tab. 1, Fig. 6) due to dense shrub vegetation cover accompanied by fast incorporation of organic material and thus high accumulation rates into the soil (Ozols and Broll, 2003). Cryoturbation processes are characteristic for the coastal area in West Greenland (Stäblein, 1977; Jensen et al., 2006) which results from deep thawing of soils during the summer causing vertical relocation of SOC and thus high SOCS in the third and fourth depth increment at all landscape units in SISI. In addition, a low isolating effect of VEG1 fosters a thick active layer and vertical relocation of SOC causing SOCS being highest within 50 – 100 cm in LU4. High subsoil SOCS might also be caused by buried organic material by downslope relocation processes taking place along different topographic positions within the varying landscape (Palmtag et al., 2015; 2018; Wojcik et al., 2019). Such processes differ in their intensity causing SOCS varying more distinct between different topographic positions (Rentschler et al. 2019).

In RUSS, the spatially variation in SOCS is connected to cold and dry katabatic winds negatively affecting vegetation growth and increasing evapotranspiration at the ice margin (Ozols and Broll, 2003; Henkner et al., 2016). Therefore, particularly wind-exposed areas as east-facing upper slopes and moraine crests represented by LU2 show lowest SOCS within all depth increments. At the top depth increment, SOCS

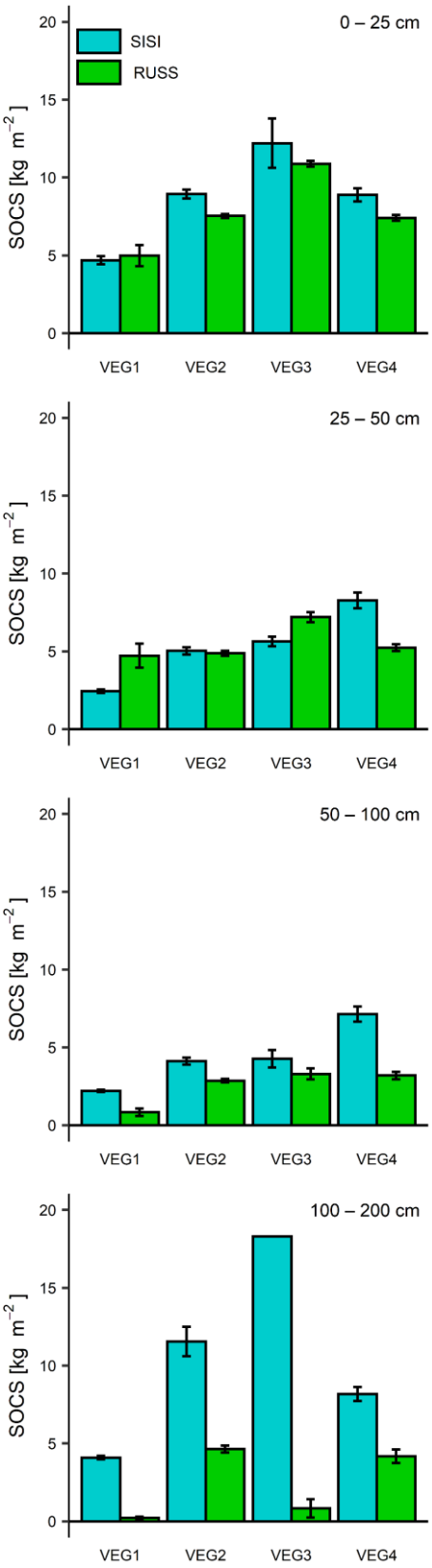

Figure 5: SOCS and vegetation. Variation in SOCS (mean, SD) by VEG in SISI (blue) and RUSS (green). Missing SD relates to n = 1 or SD > mean (from Gries et al., 2020, modified).

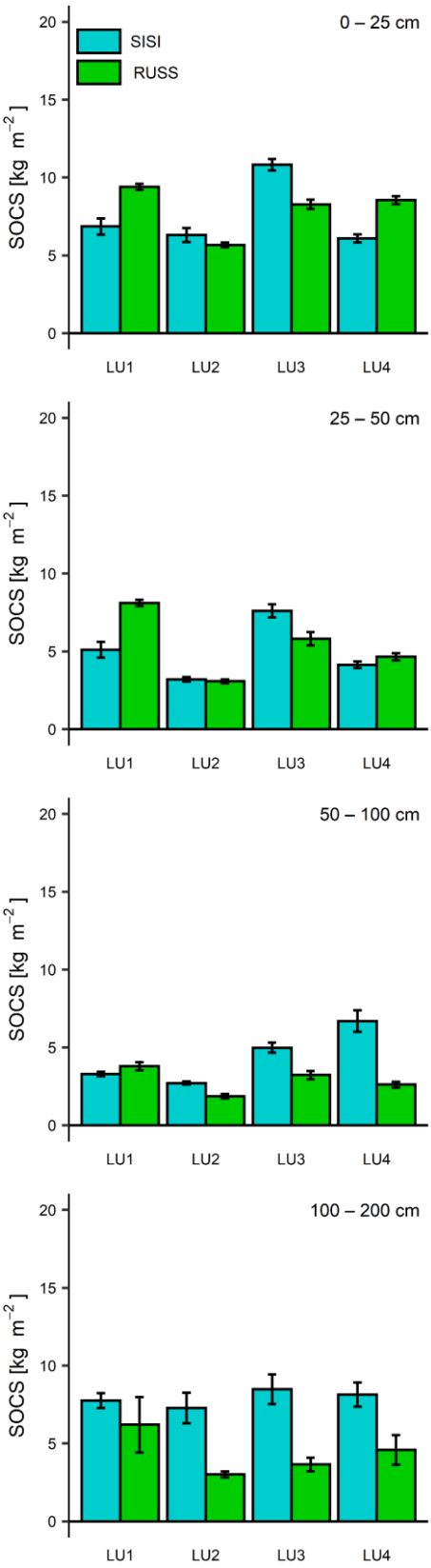

Figure 6: SOCS and landscape units. Variation in SOCS (mean, SD) by LU in SISI (blue) and RUSS (green). Missing SD relates to n = 1 or SD > mean (from Gries et al., 2020, modified).

with 5.66 ± 3.00 kg m^{-2} in LU2 in RUSS corresponds to SOCS on moraine crests and summits at 0 – 30 cm in the Umimmalissuaq valley at the ice margin with similar environmental conditions (Henkner et al., 2016). Terminal moraines are a characteristic geomorphological feature being transverse to the katabatic winds in RUSS. Consequences are a weakening of the katabatic winds and the creation of wind sheltered areas on leeside locations. Thus, favourable growing conditions results in high production of organic material and consequently in high SOCS at 0 – 25 cm in LU1, LU2 and LU4 (Fig. 6). Characterized by very moist to wet soil conditions with low decomposition rates of organic material, lake surroundings and depressions show highest SOCS at the first and second depth increment in LU1. Also, the SOCS is higher below 50 cm depth in LU1 than LU2, LU3 and LU4 which is connected to organic layers buried by lake sediments from fluctuating water levels during the Holocene (Willemse et al., 2003). Dry hillslope areas in LU4 show lower SOCS as organic material and sediments are relocated downslope (Palmtag et al., 2018) and decomposition rates are higher under warm and dry soil conditions (Elberling et al., 2004). This corresponds to findings by Rentschler et al. (2019) applying non-linear depth functions to express the high spatial variation in the vertical SOCS distribution across landscape positions. Finally, varying in their characteristics, LU also effect the distribution of SOCS on the local scale in both study areas.

There is a high variation in SOCS in both study areas linked to the aspect which reflects different (micro-)climate conditions. In SISI, the SOCS is with up to around 30 kg m^{-2} highest at 0 – 25 cm on south-facing locations (S, SE: Fig. 7) being characterized by high solar energy input and great water availability from an adjacent large catchment area in the north of the study area. These environmental conditions favour plant growth and limit decomposition of organic material under moist soil conditions. In contrast, the SOCS is lowest on average with < 5 kg m^{-2} within 0 – 25 cm on east-, west- and northwest-facing locations. East-facing locations show less solar energy input and thus less biomass production than south-facing locations due to often occurring fog until noon (Cappelen et al., 2001). Conversely, high solar energy input causes warm soil conditions, high decomposition rates (Elberling et al., 2004) and thus low SOCS on west- and north-west-facing locations in SISI (Gries et al., 2020).

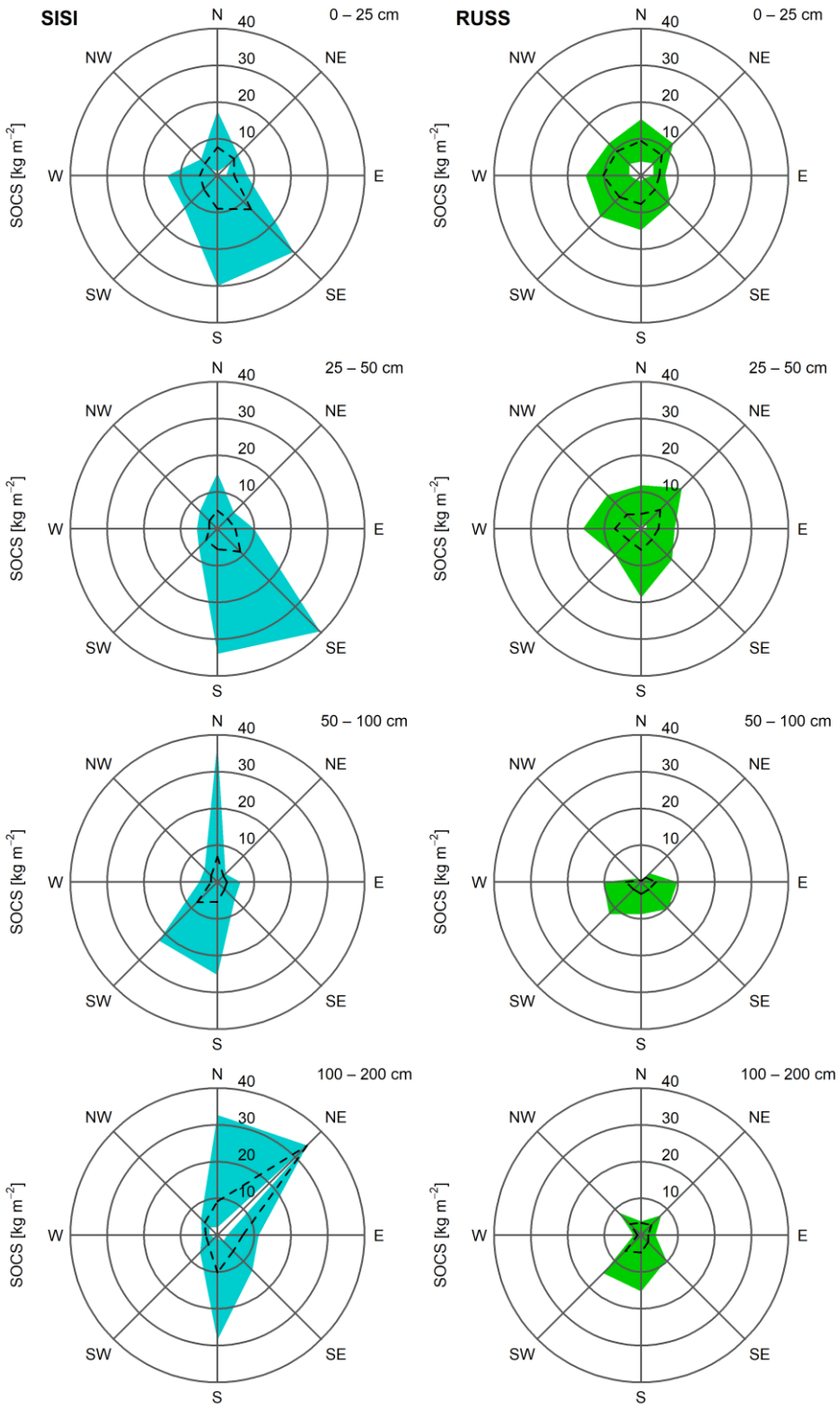

Figure 7: SOCS and aspect. Variation in SOCS (mean: dashed line) by ASP in SISI (blue) and RUSS (green) (from Gries et al., 2020, modified).

In RUSS, the SOCS is lowest with 4.95 ± 1.19 kg m^{-2} at 0 – 25 cm on east-facing locations, which is up to 15.17 kg m^{-2} lower than on west-facing locations where the SOCS is highest within 0 – 25 cm (Fig. 7). Both, east- and west-facing locations are affected by katabatic winds in RUSS. Production and input of organic material into the soil is limited on east- and south-east-facing locations by constantly blowing dry and cold winds from the Greenland Ice Sheet which results in low topsoil SOCS (Henkner et al., 2016). In contrast, shrub vegetation growth is favoured on leeside positions on west- and north-west-facing as well as on south- and south-west-facing locations having high SOCS (Ozols and Broll, 2003; Petrenko et al., 2016). Due to lower soil moisture, higher soil temperature and thus higher mineralisation rates on south-facing locations (SE, S, SW), the SOCS is with 7.16 ± 3.84 kg m^{-2} lower than on north-facing locations (NE, N, NW) with 8.91 ± 3.25 kg m^{-2} SOCS at 0 – 25 cm of depth. There are distinct similarities in SOCS in RUSS and the Umimmalissuaq valley being characterized by similar environmental conditions (Henkner et al., 2016). Topsoil SOCS on wind exposed crest positions in the Umimmalissuaq valley are comparable to east-facing locations in RUSS as both areas are affected by katabatic winds. The aspect affects microclimate on the land surface which results in varying topsoil depth and thus SOCS varying vertically with the aspect (Rentschler et al., 2019; 2020).

3.1.2 Regional scale SOCS distribution

On the regional scale, maximum SOCS is 47 – 68 % higher in SISI than in RUSS within all depth increments (Tab. 3) which can be explained by different landscape ages. Due to soil formation taking place 3000 years longer at the coast, soil could store more soil organic material than at the ice margin where the GrIS retreated 6.8 ka ago (Levy et al., 2012; Bradley-Cook and Virginia, 2016). Therefore, the SOCS differs distinctly in the range, which is with 7.85 ± 7.77 kg m^{-2} twice as large in SISI than with 7.86 ± 3.74 kg m^{-2} in RUSS at the first depth increment. This also applies to the second depth increment and is reflected in comparable mean SOCS and a higher value range in SISI than in RUSS. On average, within 50 – 100 cm and 100 – 200 cm, the SOCS is 36 % respectively 53 % higher in SISI than in RUSS, which is related to cryoturbation processes being characteristic for the coastal area but evident at the ice margin area in West Greenland (Stäblein, 1977; Petrenko et al., 2016; Gries et al., 2020).

Table 3: Descriptive statistics of soil characteristics in SISI and RUSS (values with "<" indicates the detection limit) (from Gries et al., 2020, modified).

	Depth [cm]	Min	Mean	± SD	Max	n	Study area
SOCS [kg m^{-2}]	0–25	0.34	7.85	± 7.77	30.05	74	SISI
	25–50	< 0.02	5.25	± 7.72	39.52	73	
	50–100	< 0.02	4.42	± 6.18	38.10	66	
	100–200	0.87	7.91	± 8.10	34.49	42	
SOC [%]	0–25	0.28	6.14	± 7.00	28.96	74	
	25–50	< 0.02	2.09	± 2.69	14.37	73	
	50–100	< 0.02	0.82	± 1.00	5.65	66	
	100–200	0.20	1.02	± 0.98	4.30	42	
BD [kg m^{-2}]	0–25	0.43	0.65	± 0.30	1.23	8	
	25–50	1.02	1.17	± 0.08	1.33	8	
	50–100	1.13	1.34	± 0.09	1.45	8	
	100–200	1.38	1.42	± 0.09	1.68	8	
SM [%]	0–5	0.70	26.80	± 23.48	92.60	74	
AL [cm]	< 200	4.00	70.00	± 42.70	144.00	17	
	> 200	–	–	–	–	57	
SOCS [kg m^{-2}]	0–25	1.01	7.86	± 3.74	15.79	66	RUSS
	25–50	0.58	5.41	± 4.24	18.75	65	
	50–100	< 0.02	2.82	± 3.13	12.32	56	
	100–200	< 0.02	3.74	± 3.97	15.33	33	
SOC [%]	0–25	0.46	3.23	± 1.45	6.27	66	
	25–50	0.20	2.41	± 2.05	9.44	65	
	50–100	< 0.02	0.97	± 1.30	7.29	56	
	100–200	< 0.02	0.54	± 0.67	3.47	33	
BD [kg m^{-2}]	0–25	0.84	0.97	± 0.08	1.10	8	
	25–50	0.82	1.12	± 0.18	1.39	8	
	50–100	0.83	0.99	± 0.30	1.40	8	
	100–200	1.06	1.24	± 0.22	1.75	8	
SM [%]	0–5	0.70	8.33	± 7.08	25.50	66	
AL [cm]	< 200	6.00	53.00	± 28.09	142.00	37	
	> 200	–	–	–	–	29	

The bioclimatic zonation of West Greenland indicates an increasing net annual production from the coast to the ice margin suggesting lower SOCS in SISI than RUSS (CAVM Team, 2003). However, this only applies for VEG1 where the SOCS (0 – 25 cm) is 6 % lower in SISI than in RUSS (Fig. 5). In contrast, the SOCS at 0 – 25 cm is 11 – 17 % higher for VEG2, VEG3 and VEG4 in SISI than in RUSS. Also, the SOCS is lower at the remaining depth increments in RUSS, except for VEG3, where SOCS at 25 – 50 cm is with 7.20 ± 3.93 kg m^{-2} higher in RUSS than in SISI (5.64 ± 0.93 kg m^{-2}). In General, differences in SOCS between SISI in RUSS are connected to differences in respective climate conditions. Oceanic climate provides better growing conditions at the coast than at the ice margin where dry climate restricts plant growth at the end of the growing season. Concurrently, decomposition rates of soil organic material increase with warmer and drier conditions in Greenland (Elberling et al., 2004; Jensen et al., 2006) resulting from decreasing mean annual precipitation and increasing mean summer temperatures from the coastal to the ice marginal area (Cappelen et al., 2001). The vertical variation in SOCS changes from the coast to the ice margin due to the influence of spatially varying SM conditions (Rentschler et al., 2020). In addition, decreasing topsoil SOCS with same vegetation cover from the coast towards the ice margin is linked to the deglaciation history in West Greenland (Bradley-Cook and Virginia, 2016). The interaction of these environmental conditions effects vegetation and thus SOCS differently in both study areas and results in higher SOCS in SISI than in RUSS within the same vegetation unit (Gries et al., 2020).

Although having the same landscape conditions, related LU show different SOCS between SISI and RUSS on the regional scale (Fig. 6) due to different climate conditions between the coast and the ice margin in West Greenland. In SISI, coastal climate is characterized by higher mean annual precipitation than at the ice margin showing continental climate conditions (Cappelen et al., 2001). Thus, relocation of SOC by overland flow is distinctly pronounced which results in 23 % higher SOCS at 0 – 25 cm in LU3 in SISI than in RUSS, where overland flow is restricted as a result of dry climate condition at the ice margin area. In SISI, the SOCS at 0 – 25 cm in LU2 is 10 % higher in SISI than RUSS due higher decomposition rates under drier and warmer soil conditions at the ice margin.

In both study areas, east-facing locations show lowest SOCS since the respective climate conditions restrict plant growth by low solar radiation due morning fog in SISI and high evapotranspiration rates due to katabatic winds in RUSS. As the coastal fog dissipates, solar radiation on south-east-facing locations increases, and with this biomass production which results in SOCS being 59 % higher in SISI than RUSS (Fig. 7), where south-east-facing locations are still affected by katabatic winds. In contrast, on west-facing locations, the SOCS is 54 % higher in RUSS than in SISI since plant growth is negatively affected by strong coastal west winds in SISI, but favoured on leeside positions of moraines in RUSS. In summary, under spatially varying environmental conditions, controlling factors affect the spatial distribution of SOCS in a different way on the regional scale.

In Greenland, there is a high spatial variation of SOCS across northern coastal regions. In Northeast Greenland, the SOCS at 0 – 50 cm is with 11.00 ± 1.5 kg m^{-2} at Zackenberg (Elberling et al., 2004) lower than in SISI with 13.18 ± 12.82 kg m^{-2} at 0 – 50 cm. In Northwest Greenland, the SOCS is with 6.7 kg m^{-2} at 0-100 cm on Thule peninsula (Horwath Burnham and Sletten, 2010) and with 6.7 kg m^{-2} at 0-60 cm on Disco Island (Jensen et al., 2006) also lower than in SISI. Differences in SOCS might be related to colder climate conditions in Northeast and Northwest Greenland. Variations in SOCS across northern coastal regions might also result from differences in vegetation cover and landscape pattern and related soil forming processes.

However, large scale estimations reflect such regional differences in SOCS to a limited extent since they are subject to uncertainty as basis datasets may contain data gaps filled mathematically or key soil characteristics for calculation SOCS can be uncertain (Tarnocai et al., 2009; Hugelius et al., 2014; Köchy et al., 2015; Ping et al., 2015). In addition, the underlying data might be not representative for various regions, which applies especially to Greenland (Hugelius et al., 2014; Köchy et al. 2015). Although, showing similar SOCS at the coast and the ice margin of West Greenland, large scale estimations differ significantly from SISI and RUSS in terms of the amount and value range of SOCS (Jones et al., 2009; Hugelius et al., 2014; Köchy et al., 2015). At the first depth increment, the mean SOCS in both study areas is distinctly higher and has six respectively three times the range than estimated SOCS with 0.1 – 5 kg m^{-2} within 0 – 30 cm (Hugelius et al., 2014). With focus on SOCS within 0 – 100 cm and

100 – 200 cm, differences in SOCS between SISI and RUSS are contrary to existing large-scale estimations showing no differences between the coast and the ice margin area. Within 0 – 100 cm, the SOCS is with 16.87 ± 14.79 kg m^{-2} in SISI and with 15.49 ± 8.75 kg m^{-2} in RUSS slightly higher than estimated SOCS with 9 – 15.9 kg m^{-2} by Jones et al. (2009) and with 5 – 15 kg m^{-2} by Hugelius et al. (2014) and around 30 % than estimated SOCS with 10 kg m^{-2} by Köchy et al. (2015). Within 100 – 200 cm, large range in SOCS in SISI (33.61 kg m^{-2}) and RUSS (15.33 kg m^{-2}) reflect the high spatial and vertical variation in SOCS in both study areas.

3.1.3 Role of controlling factors to describe the SOCS distribution

The results reflect the spatial variation in SOCS on both the local and the regional scale. The controlling factors being used (VEG, LU, ASP) have different capabilities to characterize the SOCS distribution on both scales. Therefore, the controlling factors are ranked according to their potential to address the spatial variation in SOCS: +++ high; ++ medium; + low. The expert-based ranking is based on the comparison of the potential of each unit to be unique according the used classification scheme. With a high potential, a specific range of the SOCS distribution within the study area is represented by a specific unit on the local scale and the ranking is also stable over both study areas on the regional scale (Tab. 4).

Vegetation units have a high (+++) potential to describe the spatial variation in SOCS by including to a certain extent insolation, geomorphology and wind on both the local and the regional scale. In SISI, similar topsoil SOCS for VEG2 and VEG4 is a result of fluvial relocated SOC. In RUSS, ASP reflects best the negative effect of katabatic winds being characteristic for continental climate at the ice margin. Further, the SOCS differs for all depth increments below 25 cm with VEG. Thus, VEG has a high potential (+++) to describe the variation in SOCS on the local scale. Showing similar pattern in the spatial distribution of SOCS, VEG points out different amounts of SOCS between SISI and RUSS on the regional scale. Therefore, VEG also have a high potential (+++) to describe the variation in SOCS on the regional scale.

However, landform and landscape classifications are well known approaches for analysis of the horizontal vertical distribution of SOCS (Palmtag et al., 2018; Siewert et al., 2016; Wojcik et al., 2019). In addition, such classifications are useful for

representing local patterns such as accumulation areas of additional SOC input (as in SISI) or convexly shaped moraines of limited SOCS (as in RUSS). Further, LUs reflect the effect of local climate conditions in both study areas. However, LUs have little potential (+) to capture the variation in SOCS at the local scale in this study. Although, reflecting similar geomorphologic features between SISI and RUSS, LUs consider the influence of different climatic conditions and thus the differences in SOCS of related LUs between the coast and the ice margin on the regional scale (++).

On both scales, ASP has high potential (+++) by representing great differences in site characteristics between east- and west-facing as well as north- and south-facing locations on the local scale and additionally by describing different climate conditions between the coast and the ice margin on the regional scale.

In general, corresponding to comparable studies applying landform classification approaches in Arctic environments (Elberling et al., 2008b; Henkner et al., 2016; Siewert et al., 2016; Palmtag et al., 2018; Wojcik et al., 2019), the results presented above demonstrates both ASP and LU additionally yielding relevant information for analysing and understanding the spatial distribution of SOCS in West Greenland. On the local scale, ASP and LU represent specific environmental conditions within the study areas and differences between the study areas on the regional scale as well. As LU has lowest potential to describe the distribution of SOCS on both scales, it is recommended to use vegetation and aspect for investigations on the SOCS distribution on the local and the regional scale (Gries et al., 2020). Further, both environmental controlling factors can be delineated from remote sensing data and digital elevation models with high resolution across large areas.

Table 4: Ranking of environmental units according to their potential (+++ high; ++ medium; + low) to describe the SOCS distribution on the local and regional scale (Gries et al., 2020).

	Local scale	Regional scale
VEG	+++	+++
LU	+	++
ASP	+++	+++

3.2 Scale and spatial SOCS dependencies (manuscript 2, 3)

3.2.1 Scale dependent SOCS distribution

The analysis of the area-specific approach shows distinct variations in the model accuracy of the sequenced RF models for SISI and RUSS (Fig. 8). In SISI, there is a decrease in the model accuracy from the moraine to the valley scale but a subsequent increase to the catchment scale for the ascending approach ($SISI_{asc}$). Both the ascending and the descending approach ($SISI_{desc}$) highlight the relevance of the moraine and catchment scale for the spatial SOCS distribution at the coast. This attest the SOCS distribution depending on small scale environmental conditions varying within the study area and being also influenced by oceanic climate conditions (Jensen et al., 2006; Bradley-Cook and Virginia, 2016; Gries et al., 2020). However, R^2 is 0.20 on average and very low for both $SISI_{asc}$ and $SISI_{desc}$ because the SOCS distribution is weakly connected to the terrain surface which has been reshaped by periglacial processes and SOC has been relocated since the deglaciation of the coastal region of West Greenland 10,000 years ago (Stäblein, 1977; Levy et al., 2012; Bradley-Cook and Virgina, 2016). In addition, since the beginning of soil formation, soil material was mixed and redistributed vertically by freeze and thaw cycles typically for permafrost-affected landscapes (Bockheim, 2007; Baumann et al., 2014).

In contrast, higher model accuracy in RUSS than in SISI suggests a stronger connection between SOCS and terrain as lower precipitation rates and landscape age have lower potential for reshaping the landscape and affecting soil formation at the ice margin. Therefore, the SOCS distribution is strongly connected to specific landscape elements at the ice margin in West Greenland (Gries et al., 2020). The increase in model accuracy on the moraine scale of the ascending and descending approach points out the importance of small-scale environmental conditions and processes to the spatial SOCS distribution at the ice margin. On the regional scale, differences in the model accuracy and important scales between SISI and RUSS confirm that controlling factors and processes affecting the SOCS distribution vary over long distances and with different climate conditions in West Greenland (Gries et al., 2020). Expressed by a function of soil forming factors, soils vary according to the variation in such factors including space (Jenny, 1941; McBratney at al., 2003). As soil-landscape

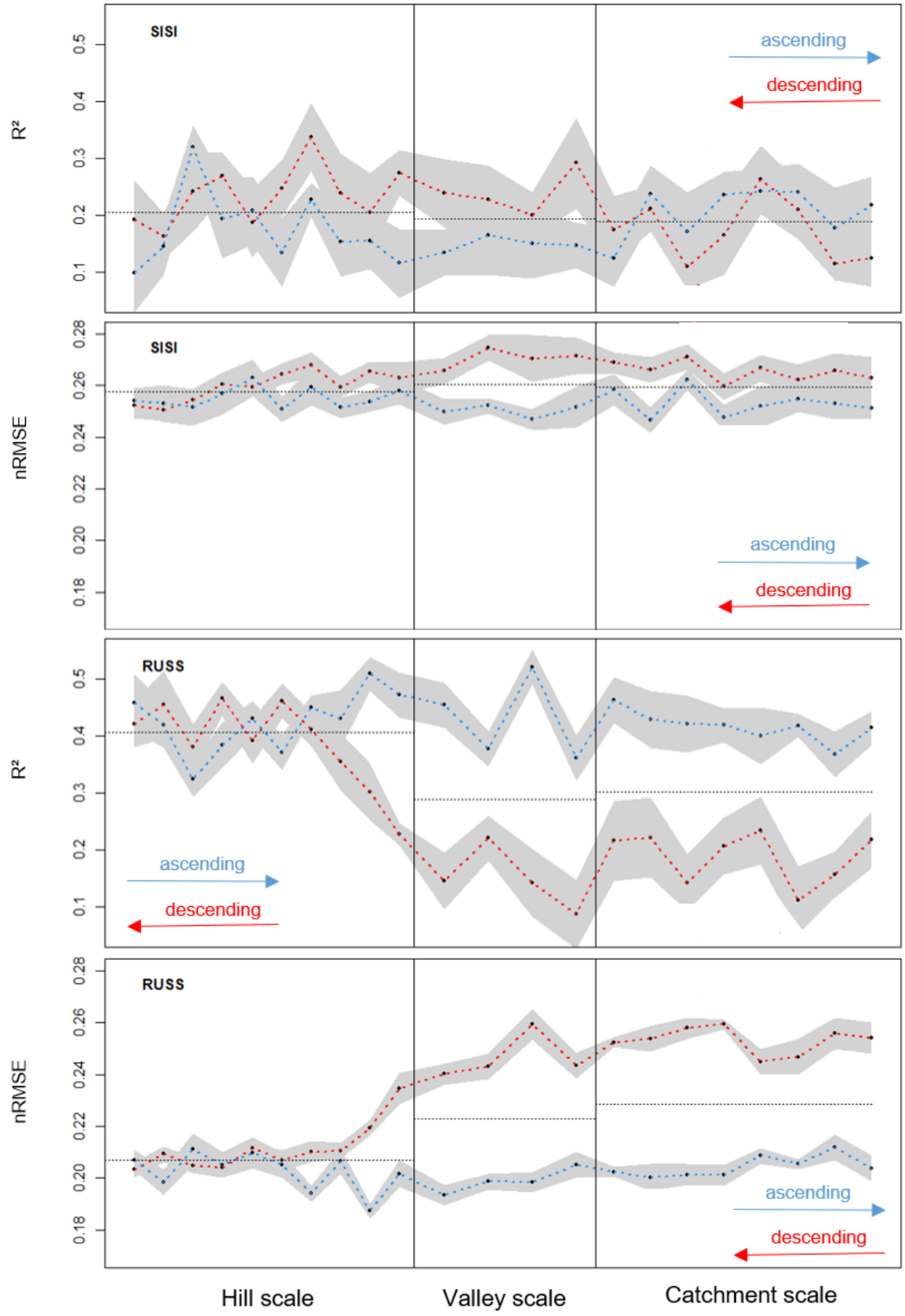

Figure 8: Variation in model accuracy across environmental scales. Mean variation in R² and nRMSE of the ascending (blue) and descending (red) sequence of RF models in SISI and RUSS across all single scales (black dots) which are grouped (vertical lines) to the hill scale (2 – 48 m), valley scale (64 – 192 m) and catchment scale (256 – 3072 m). Grey areas represent value range of the ten times repeated 10-fold cross-validation and the horizontal dotted lines the mean value of the validation of the respective environmental scale.

.

interrelations including environmental conditions and processes change across different scales, the estimation of the spatial SOCS distribution needs to respect the relevant scale (Viscarra Rossel et al., 2019).

The model accuracies vary over different scales since the importance of specific terrain features varies over different scales as well. Figure 9 shows the cumulative increase in feature importance of the terrain features across the environmental scales. The steeper the increase in feature importance within the moraine, valley or catchment scale the higher is the relevance of the respective environmental scale of the specific terrain feature. In SISI, the aspect is the most the important terrain feature on the moraine and the catchment scale and thus confirms its significance for the description of the SOCS distribution in West Greenland (Gries et al., 2020). The aspect also represents small-sized landscape elements as small hills on the moraine scale that affects microclimate, growing conditions and vegetation cover in West Greenland (Jensen et al., 2006; Horwarth Burnham et al., 2010; Henkner et al., 2016; Gries et al., 2020). On the catchment scale, the aspect represents the coastal climate that has a negative effect on plant growth in the form of coastal fog on eastern part and in form of strong coastal winds on the western part of SISI. Besides, curvature is a key terrain feature since addressing scale dependencies of the SCOS distribution in SISI on the moraine scale and the valley scale. Solifluction and erosion on valley slopes cause colluvial deposits at valley footslopes (Stäblein, 1977; Palmtag et al., 2015; Ramage et al., 2019) which results in high SOCS along the northern part of SISI (Stäblein, 1977; Gries et al., 2020). Downslope processes along moraine slopes result in high SOCS in depressions and accumulation areas within the study area (Gries et al., 2020).

In RUSS, curvature represents moraines slopes on the moraine scale and the valley slope on the valley scale and to both accompanied relocation processes. Moraines show downslope relocation processes, favour vegetation growth in wind protected areas and have a lasting effect on aeolian transport which results in high SOCS in depressions, on their western side and buried by aeolian deposits respectively (Henkner et al., 2016; Müller et al., 2016; Kühn and Henkner, 2019; Gries et al., 2020). Curvature generally is suitable to describe geomorphological pattern on various scales

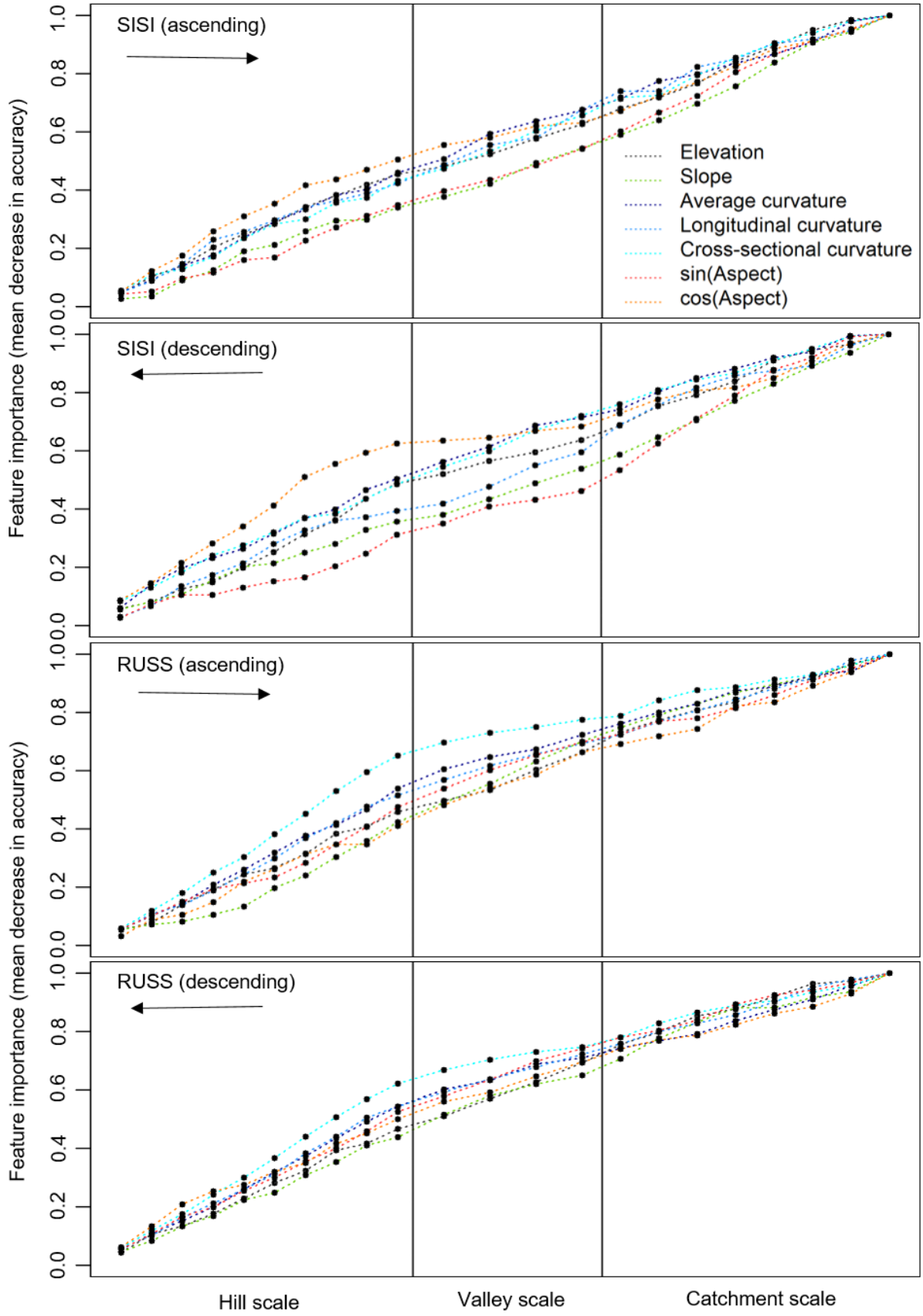

Figure 9: Cumulative importance of terrain features across environmental scales. The steeper the increase in cumulative feature importance of the ascending and descending RF sequences the higher is the relevance of the respective environmental scale. The black dots represent single scales being grouped to the hill (2 – 48 m), valley (64 – 192 m) and catchment scale (256 – 3072 m).

as small-scale landforms disappear and merge into large-scale generalised landforms when the scale enlarges (Wood, 1996). The highest moraine ridge significantly shapes the valley dividing it into a wind-exposed and a wind-protected part which causes lower SOCS on the east-facing than on the west-facing part as katabatic winds negatively affect vegetation growth on wind-exposed locations in the east of RUSS. The influence of the katabatic wind on the SOCS distribution is evident on all scales in different ways which can be captured by the aspect at the all three scales. On the moraine scale, the aspect reflects the SOCS distribution depending on vegetation growth affected by katabatic winds. On the valley scale, the aspect explains the SOCS distribution within the study area in the same way as the curvature on the valley scale. On the catchment scale, the aspect represents the spatial trend of increasing SOCS with increasing distance to the ice margin as a result of weakening influence of the katabatic winds related to aeolian transport and vegetation growth to the west (Henkner et al., 2016; Gries et al., 2020). Finally, reflecting wind as a soil forming factor not being used as predictor, the aspect is as proxy with high potential to capture and describe environmental factors and related processes on different scale levels which control the spatial distribution of soil properties in periglacial shaped landscape. In general, this confirms the relevance of considering multiple scale for the analysis of SOCS distribution to capture the effect of scale-dependent interactions between environmental conditions and the landscape towards the distribution of soils (Behrens et al., 2010; Kerry and Oliver, 2011).

3.2.2 Spatial dependent SOCS distribution

Spatial dependencies of the SOCS distribution are examined by comparing the importance of spatial features to terrain features with the spatial approaches for SISI and RUSS. The importance of the terrain and spatial features of both spatial approaches are given in Tab. 5 and Tab. 6. In SISI, the importance of spatial features is with an average of 2.02 ± 0.54 % higher than the mean importance of the terrain features (1.36 ± 1.61 %). Within the study area, SOCS slightly increase to the east as the effect of strong coastal winds on the vegetation, a key source of organic material, weakens with increasing distance to the coast. Further, the northeaster part of the study represents on the one hand a wind-sheltered area favouring biomass production and on the other hand the footslope of the valley with an additionally increase of

relocated material from the valley slopes which both generally results in high SOCS on the footslope (Stäblein, 1977; Ozols and Broll, 2003; Henkner et al., 2016; Palmtag et al., 2015; Ramage et al., 2019). This slight increase of SOCS from the west to the east in SISI is reflected by the spatial feature Y01, representing the Euclidean distance to the western boundary of the study area (Fig. 4). In addition, there is a spatial trend of decreasing SOCS to the south, which is reflected by the spatial feature X01 representing the Euclidean distance from the southern boundary of SISI. Cold soil conditions due to low solar energy input on the north-facing valley slope result in low SOCS in the south of SISI (Gries et al., 2020). The spatial approach ($SISI_{spatial}$) shows better validation results and comparable SOCS distribution than the non-spatial model approaches for SISI (Tab. 7; Fig. 10). This confirms that the SOCS distribution is weakly linked to the present land surface as coastal climate and landscape age foster relocations processes and highlights the relevance of EDFs as suitable spatial features to identify spatial dependencies of SOCS at the coast. However, the maximal importance of the terrain features is with 6.05 % for the sinAsp (18) at the catchment scale clearly higher than for the spatial features (2.61 %, Y01). The multi-scale terrain features consider small-scale variation of SOCS on the moraine and valley scale in addition to large-scale effects on the catchment scale as by the prominent EDFs.

In RUSS, the spatial feature importance is with 1.10 ± 2.14 % lower than for the terrain features 2.22 ± 3.46 %, as the spatial SOCS distribution is connected to local environmental controlling factors and thus varies over short distances with the local landscape. The variation of SOCS primarily results from soil-landscape interrelations on the moraine scale but additionally shows a subordinate increase in SOCS to the west. The negative effect of the katabatic winds decreases with increasing distance to the ice margin which is reflected by the aspect on the catchment scale and by the spatial feature Y01, both explaining increasing SOCS to the west in RUSS (Gries et al., 2020). The advantage of multi-scale terrain features covering both landscape-driven and spatial SOCS pattern within the study area is also reflected in the maximum feature importance of 15.57 % (Cross-sectional curvature at the moraine scale) being distinctly higher than for the EDFs with 4.48 % (C1). The spatial approach ($RUSS_{spatial}$) results in comparable validations results and predicted SOCS distribution in RUSS (Tab. 5; Fig. 11). This confirms that the SOCS distribution is linked to the present terrain at RUSS due the water-driven relocation of soil material is low due to low MAP at the ice margin.

Table 5: Importance of terrain and spatial features of the spatial approach for SISI ($SISI_{spatial}$).

Terrain features	Single scales																						Spatial features	
	1	2	3	4	5	6	7	8	9	10	11	12	13	14	15	16	17	18	19	20	21	22		
Elevation	1.88	2.19	3.16	-0.04	-0.44	1.05	0.32	0.78	1.35	1.39	2.15	0.6	0.5	2.58	3.2	4.14	3.19	4.23	-1.17	3.01	0.7	1.79	1.23	**X01**
Average curvature	1.53	0.91	2.37	1.16	2.18	3.05	2.29	2.55	1.62	1.59	0.33	3.55	2.79	2.03	0.38	-0.51	3.86	1.44	2.98	3.76	-0.23	-0.58	2.61	**Y01**
Slope	3.34	1.88	-0.68	-0.17	-0.8	-1.3	-1.47	-0.47	-0.77	0.38	0.98	3.01	3.48	1.17	1.14	0.98	-0.08	2.09	4.19	-0.91	1.7	2.83	2.43	**C1**
Cross-sectional curvature	0.51	1.57	2.64	1.56	1.59	1.86	0.3	1.45	0.48	-1.1	0.6	0.81	-0.39	1.98	2.7	1.4	2.76	3.66	3.06	0.7	1.54	0.41	1.65	**C2**
Longitudinal curvature	1.63	2.52	0.17	0.71	1.87	2.96	2.33	-1.8	-1.06	-2.2	0.81	-0.01	1.38	1.56	2.01	1.34	0.27	0.6	2.48	-3.55	2.17	-0.64	2.24	**C3**
cos(Aspect)	1.6	1.22	1.46	1.22	2.87	1.33	3.57	1.06	-1.28	-0.5	-1.6	-0.14	-0.29	0.47	1.84	3.04	0.19	1.87	2.72	3.78	3.18	1.3	2.46	**C4**
sin(Aspect)	-1.7	-0.72	0.61	0.84	-1.28	-1.06	-0.49	1.9	1.92	0.88	1.7	1.54	1.59	1.18	4.06	5.73	3.94	6.05	3.5	2.49	3.16	3.14	1.53	**CC**
	Hill scale										Valley scale				Catchment scale									

Table 6: Importance of terrain and spatial features of the spatial approach for RUSS ($RUSS_{spatial}$).

Terrain features	Single scales																						Spatial features	
	1	2	3	4	5	6	7	8	9	10	11	12	13	14	15	16	17	18	19	20	21	22		
Elevation	1.71	2.75	-0.06	2.34	2.76	2.29	1.36	1.16	2.25	0.98	0.55	3.14	3.48	4.85	3.44	-0.23	1.81	-0.14	-0.39	0.06	0.75	0.36	1.07	**X01**
Average curvature	1.77	-2.08	-1.58	-1.56	5.89	-1.67	-1.49	4.06	0.9	7.01	1.25	2.65	2.61	-1.59	-0.65	0.16	0.56	-2	-3.83	-3.16	-1.15	2.36	-0.58	**Y01**
Slope	-0.37	3.39	3.74	4.03	-1.56	6.24	4.95	-2.31	4.09	0.92	6.64	1.42	2.17	0.57	2.1	0.62	-1.72	-1.66	0.83	0.14	-2.12	3.96	4.48	**C1**
Cross-sectional curvature	7.33	8.46	7.39	9.38	10.14	12.67	15.57	12.48	9.65	2.11	3.35	2.84	1.63	-1.85	0.09	1.28	-0.11	-1.66	-0.97	-1.04	-0.9	2.82	-0.54	**C2**
Longitudinal curvature	2.68	3.5	4.72	3.3	4.89	6.87	8.96	8.57	4.93	1.85	3.56	1.44	1.9	1.3	-0.72	0.8	-1.49	0.1	2.2	3.53	-3.33	-0.34	1.08	**C3**
cos(Aspect)	0.74	-0.4	0.25	1.05	-1.2	2.1	1.58	0.28	-0.01	0.09	0.07	-0.88	-0.22	-0.83	-0.79	-2.27	-1.34	-1.8	-1.26	1.72	2.04	1.11	3.38	**C4**
sin(Aspect)	7.84	7.34	8.55	7.08	4.87	0.95	5.57	6.17	6.28	7.55	9.15	7.47	5.18	4.04	2.22	-0.2	0.24	1.69	1.97	3.8	2.92	1.54	-1.21	**CC**
	Hill scale										Valley scale				Catchment scale									

Table 7: Validation of the spatial SOCS predictions in SISI and RUSS.

Approach	SISI		RUSS	
	R^2	nRMSE	R^2	nRMSE
Area-specific	0.76	0.16	0.85	0.13
Spatial	0.84	0.15	0.87	0.11
Combined	0.64	0.21	0.88	0.12
Cross-transferred	0.00	0.26	0.02	0.58

3.2.3 Regional dependent SOCS distribution

The examination of regional dependencies is based on the estimation of the spatial SOCS distribution in both study areas by the area-specific, spatial, crosswise and combined approach using different training data sets and validation areas (Fig. 10; Fig. 11). The validation of the models results from the difference between the predicted and measured values and is expressed by nRMSE and R^2 (Tab. 7).

In SISI, the R^2 of the area-specific approach ($SISI_{area\text{-}specific}$) is with 0.76 higher than for the combined approach ($SISI_{combined}$). Relevant soil-landscape interrelationships at different scales are better depicted by $SISI_{area\text{-}specific}$, which minimizes differences between the observed and predicted values. With $SISI_{combined}$ strong scale-dependent soil-landscape interrelations at the ice margin may have been transmitted incorrectly from RUSS to SISI. This causes an underestimation of SOCS especially in the north-eastern part of SISI, where the SOCS is high due to relocation processes along the valley slope. This circumstance is characteristic for the coastal area showing higher precipitation and higher relocation rates than at the ice margin (Gries et al., 2020).

In contrast, slightly higher R^2 for $RUSS_{combined}$ (0.88) than $RUSS_{area\text{-}specific}$ (0.85) results from additional soil information from SISI. The combined dataset leads to an artificial expansion and thus better coverage of the range of the measured SOCS and a higher consistency of the predicted values in RUSS. The crosswise approaches ($SISI_{cross}$, $RUSS_{cross}$) cause highest nRMSE for SISI (0.26) and RUSS (0.58) and results in an underestimation and an overestimation of SOCS in SISI and RUSS respectively. Both,

$SISI_{cross}$ and $RUSS_{cross}$ extract scale-dependent soil-landscape interrelations being characteristic for the respective training dataset and study area which, however, have no validity in the respective other area. Also, $SISI_{spatial}$ shows best results of all model approaches pointing out that the SOCS distribution is less linked to the local terrain due to erosion processes and relocation of soil material which benefit from high precipitation rates under coastal climate conditions than at the ice magin where the the application of spatial features does not improve the prediction of SOCS in comparison to the non-spatial approaches of $RUSS_{area\text{-}specific}$ and $RUSS_{combined}$. This confirms regional differences of soil-landscape interrelations and SOCS related to contrary climatic conditions between the coast and the ice margin in West Greenland on the regional scale (Gries et al., 2020).

Distinct differences in relevant scales, important terrain features, biotic and abiotic controlling factors and climate conditions between SISI and RUSS and thus varying interactions between the coast and the ice margin contradict the requirements of spatial predictions: comparable environmental conditions in the training and validation area and balanced training data according to environmental controlling factors (Taghizadeh-Mehrjardi et al., 2020). On this basis, and considering these spatially varying and scale-dependent environmental interrelations, large scale estimations would be reliable and interpretable in a pedological context (Behrens et al., 2010; Viscarra Rossel et al., 2019). However, due to limited data and the mapped scales, the non-linear gradient in SOCS between the coast and the ice margin is not considered by large scale estimations which show no spatial variation in SOCS in West Greenland (Jones et al., 2009; Hugelius et al., 2013; 2014; Köchy et al., 2015).

Therefore, extrapolation and estimation of SOCS across large areas with spatially varying environmental conditions are subject to uncertainty. Mapping the uncertainty of soil information proves beneficial for the identification of underrepresented areas. Providing spatial uncertainty with the prediction of soil information, geo-statistical approaches are limited in representing non-linear relationships which can be detected within data sets by machine learning techniques (Behrens and Scholten, 2007). Stumpf et al. (2017) derived the spatial uncertainty of soil texture from RF on the catchment scale. Mapping the spatial uncertainty is also an element of large-scale estimations of various soil properties using machine learning (Poggio et al., 2021).

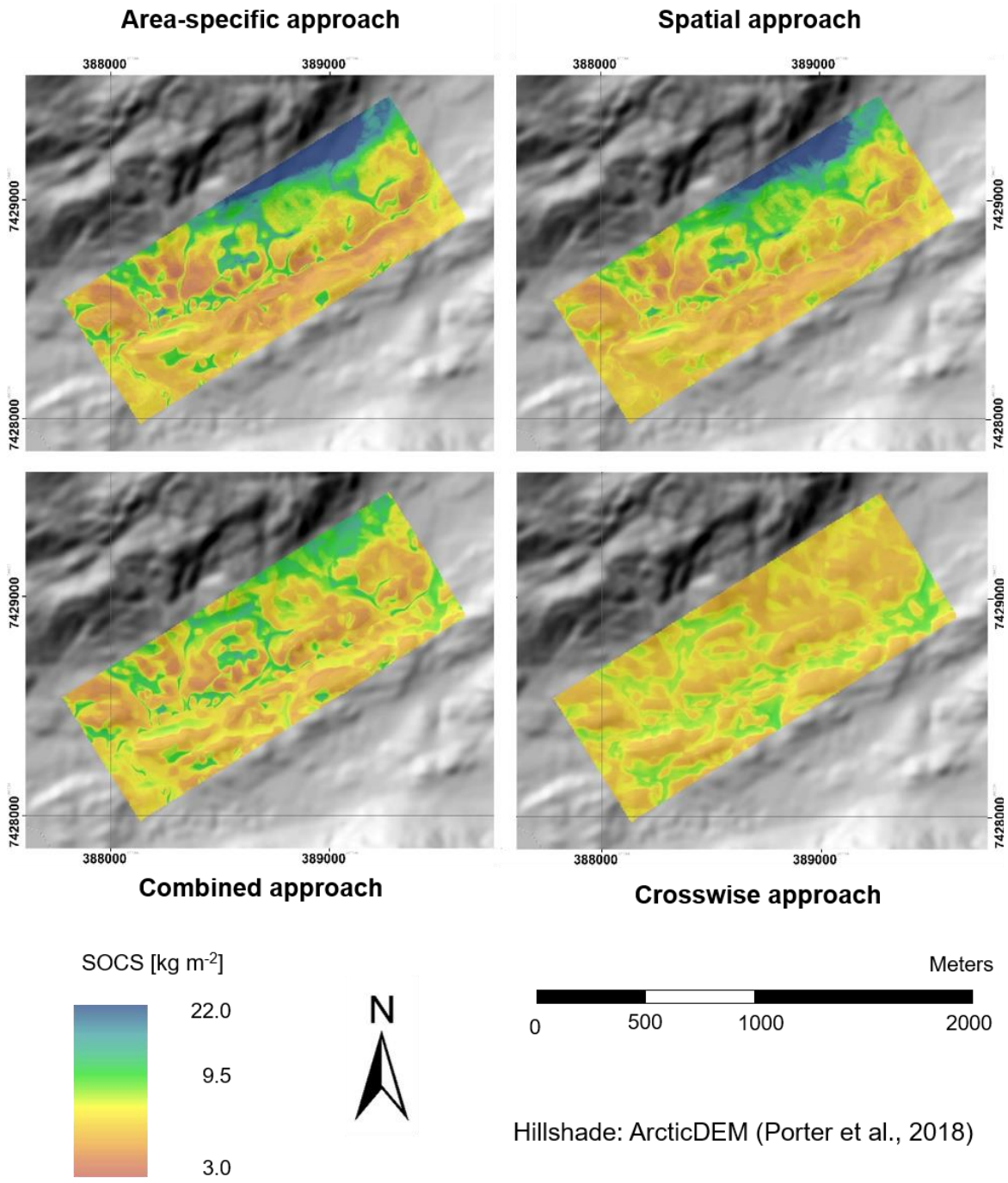

Figure 10: Prediction of the spatial SOCS distribution in SISI. The area-specific approaches uses multi-scale terrain features only. The spatial approach includes multi-scale and spatial features. The combined approach is based on a combined data set from SISI and RUSS and uses multi-scale terrain features to predict SOCS in SISI. The crosswise approach comprises a RF model trained with a data set from RUSS to predict SOCS in SISI.

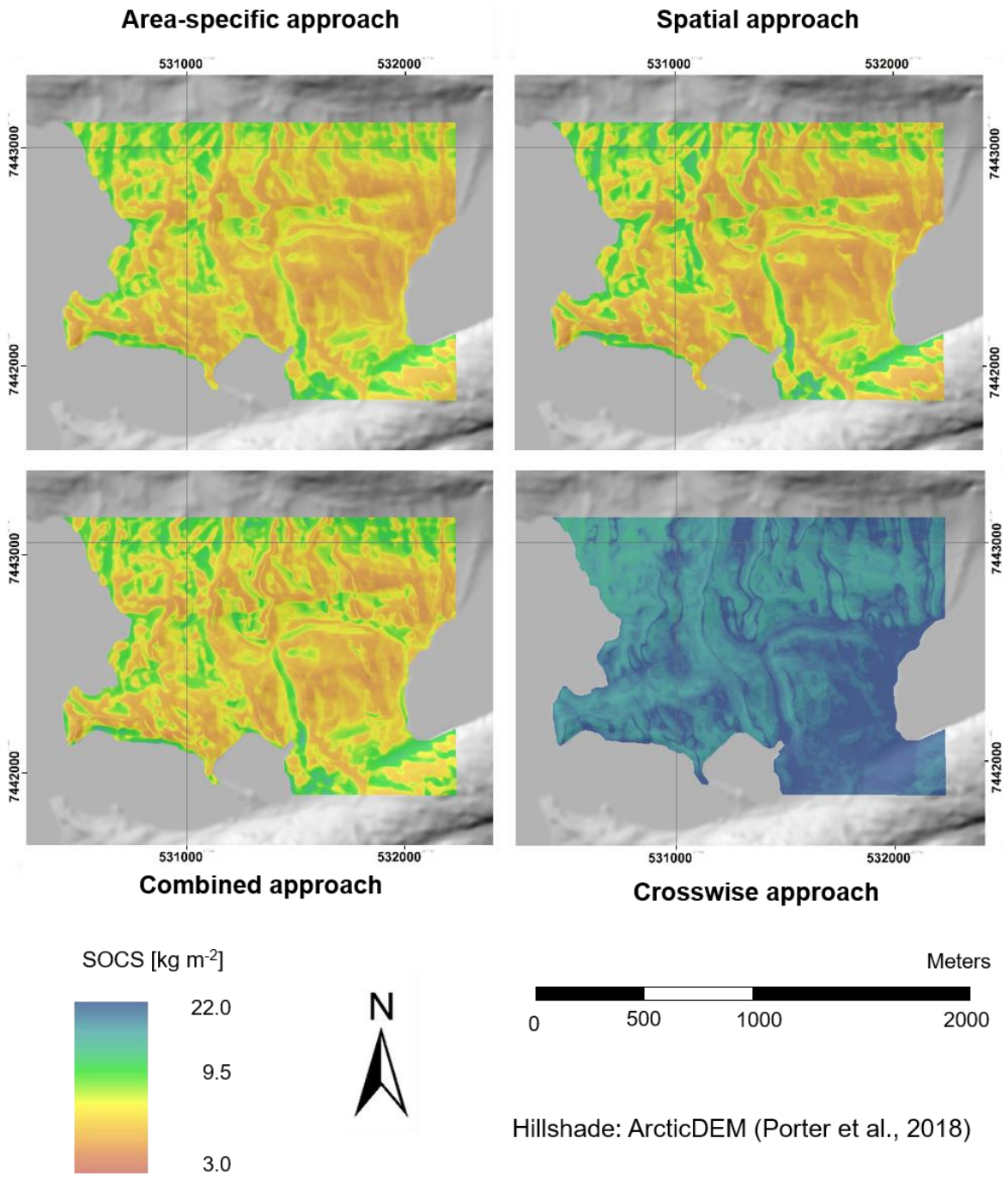

Figure 11: Prediction of spatial SOCS distribution in RUSS. The area-specific approaches uses multi-scale terrain features only. The spatial approach includes multi-scale and spatial features. The combined approach is based on a combined data set from SISI and RUSS and uses multi-scale terrain features to predict SOCS in RUSS. The crosswise approach comprises a RF model trained with a data set from SISI to predict SOCS in RUSS.

3.2.4 Role of environmental features to describe the SOCS distribution

The machine learning based approaches differ in revealing scale, spatial and regional dependencies of SOCS within and between SISI and RUSS which allows for ranking the area-specific, spatial and regional approach concerning the potential (high: +++; medium: ++; low: +; none: o) to describe the SOCS distribution over short distances on the local and large distances on the regional scale (Tab. 8). Due to the ascending and descending sequenced RF modelling, the area-specific approach is highly suitable to account for soil-landscape interrelationships varying across the moraine, valley and catchment scale as well as over space in SISI and RUSS on the local scale (+++). On the regional scale, differences in feature importance and relevant scales between the coast and the ice margin also show high potential of the area-specific approach (+++) to proof regional dependencies of SOCS related to different environmental conditions. Besides, allowing to consider spatial trends within the coastal and ice marginal study area by terrain features of the catchment scale, the area-specific approach has higher potential than the spatial approach. On the local scale, spatial features show low potential (+) to describe the SOCS distribution according to the heterogeneity of the landscape and variation of environmental conditions over short distances. However, contrary important spatial features between SISI and RUSS reflect contrary environmental conditions regarding wind systems and precipitation and thus medium potential on the regional scale (++). Regional dependencies are accentuated by the crosswise approach potentially suitable to point out differences in soil-landscape interrelations (++) between SISI and RUSS to some extent but not qualified to explain the spatial SOCS distribution in the other respective area on the local scale (o). The potential of the combined approach is low to account for scale dependencies on the local scale in SISI (+) as area-specific environmental relationships are disregarded. In contrast, the potential of the combined approach is high in RUSS (+++) as differences between the area-specific and combined approach are marginal according to the validation results.

Table 8: Ranking of model approaches according to their potential (+++ high; ++ medium; + low; o none) to describe the SOCS distribution on the local and regional scale.

	Local scale	Regional scale
Area-specific	+++	+++
Spatial	+	++
Crosswise	o	++
Combined	+	+++

4 Summary and outlook

Objective of this thesis was to investigate the SOCS distribution in permafrost-affected soils in West Greenland. To achieve this, soil and environmental data was collected at 140 sampling locations distributed according to a stratified random sampling design within two study areas. To consider contrary climate conditions, the study areas are located at the coast and the ice margin in West Greenland. The results confirm the hypothesis that the SOCS in West Greenland is higher in the amount and the spatial variation compared to existing large-scale estimations as environmental conditions and processes vary in their effect on different scales within and between both study areas. Such environmental conditions are successfully represented by the chosen environmental controlling factors (vegetation, landscape, aspect) in form of defined units to explain the spatial variation in SOCS over short distances within both study areas on the local scale and between the coastal and the ice marginal study area on the regional scale. Further, multi-scale terrain features allow to address environmental processes acting parallel on the moraine, valley and catchment scale but differ in the effect on the respective environmental scales on the local scale SOCS distribution.

On the local scale, the SOCS distribution is linked to spatial vegetation pattern in comparable ways within both study areas. Accordingly, the SOCS is highest with tall shrub tundra (VEG3) and low shrub tundra (VEG2) due to high biomass production favoured by the predominant occurrence under good growing conditions such as wind-protected locations with balanced solar energy input and sufficient water availability. In contrast, the SOCS is lowest with dwarf shrub tundra (VEG1) limited in growth by disfavour site conditions as unbalanced solar energy input, strong winds and insufficient water availability. Generally, the SOCS is higher with graminoid-moss tundra (VEG4) than with VEG1 in SISI and RUSS respectively due to lower decomposition rates under moist and cold soil conditions in depressions and bankside areas which corresponds to landscape unit LU1. However, landscape units show less potential than vegetation units to describe the spatial SOCS distribution. In both areas, the SOCS is similar for three of four LUs and thus the accentuation of SOCS of one LU is related to the respective climate conditions. So, the SOCS is highest in LU3 in SISI due to high water availability at the coast and the lowest in LU2 in RUSS due to strong katabatic winds at the ice margin. As an assemblage of multiple terrain features,

landscape units, however, show less potential in explaining the spatial variation in SOCS than a single terrain feature like the aspect. In both study areas, the aspect highlights the importance of solar energy input and predominant winds which causes low SOCS on east- and west-facing locations due to low solar energy input by morning fog and strong coastal winds in SISI and low SOCS on east-facing locations due to dry katabatic winds in RUSS on the local scale. Further, the application of multi-scale terrain features additionally highlights the advantage of an individual terrain feature over landscape units as sequenced RF models allow to measure the feature importance and thus to identify the relevant scale and to evaluate the role of related environmental processes on the SOCS distribution. In SISI, the aspect indicates the importance of downslope processes on the moraine scale and the role of wind related processes on the catchment scale being relevant for the spatial SOCS distribution at the coast as well. Further, the curvature highlights the effect of water-driven relocation processes on the valley scale which results in high SOCS along the northern boundary of the study area corresponding to LU3. Additionally, the spatial features describe spatial trends in the SOCS distribution at the coast that is less connected to the present terrain compared to the ice margin. In RUSS, katabatic winds are characteristic for the ice margin area and influence the SOCS distribution in different ways which is illustrated in detail by single terrain features of different scales. The aspect points out the negative effect of katabatic winds on the moraine scale which results in SOCS being lower on east-facing than on wind-sheltered west-facing locations in RUSS. This can be transferred to the valley scale, where in the west to the highest moraine ridge, illustrated by the curvature, the SOCS is higher than in the eastern and wind-exposed part of the study area. Further, the aspect reflects increasing SOCS with distance from the ice margin which results from decreasing strength of the katabatic winds on the catchment scale. These scale-dependent soil-landscape interrelations confirm the hypothesis that small-scale processes primarily affect the SOCS distribution on the one hand but on the other hand accentuate the importance to consider secondary large-scale processes in spatial analysis of SOCS.

On the regional scale, different soil-landscape interrelations between both study areas were inferred from differences in the range and in the amount of SOCS of corresponding units of the environmental controlling factors as well as differences in the importance and relevant scales of the terrain features and differences in related

environmental processes. A climatic gradient is expressed in opposing wind systems and decreasing amount of water over a long distance from the coast to the ice margin of West Greenland. Coastal climate causes cold and wet soil conditions fostering the accumulation of SOC whereas decomposition is favoured by the warm and dry continental climate at the ice margin. Furthermore, water shortage restricts plant growth especially at the end of the growing season at the ice margin and, thus, results in lower SOCS with related vegetation units in RUSS than SISI. Feature importance and relevant scales in SISI demonstrate the importance of relocation processes by water for SOCS at the coast. In contrast, a strong connection to the terrain and a subordinate role of respective scales and features indicate minor redistribution due to surface runoff at the ice margin. The aspect also captures the differenteffect of the role of solar energy input and wind direction on the SOCS between both study areas on the regional scale. Additionally, differences in relevant scales of the aspect between SISI and RUSS point out the multi-scale SOCS dependency on katabatic winds at the ice margin. Finally, by the comparison of environmental conditions and processes by unit, features and scales, it is recommended to combine a set of multi-scale terrain features with vegetation to examine the spatial SOCS distribution on various scales. Numerous software tools allow the derivation of multi-scale terrain features from DEMs and vegetation parameters from remote sensing data, which both are available in high resolution and over wide areas.

Future examinations and estimations of SOCS will benefit from new findings and recommendations as well as new soil data. With SOCS data from four depth increments at each of 140 locations and the analysis incorporating vegetation, climate and terrain conditions, this thesis is an important contribution to research of Arctic environments which will help to decrease uncertainty of large-scale estimations, especially in Greenland. This already applies to parts of this dataset which will be used in upscaling methods based on soil maps and also machine learning models for a global permafrost nitrogen stock estimation.

5 References

Arrouays, D., Grundy, M.G., Hartemink, A.E., Hempel, J.W., Heuvelink, G.B., Hong, S.Y., Lagacherie, P., Lelyk, G., McBratney, A.B., McKenzie, N.J., de Lourdes Mendonca-Santos, M., Minasny, B., Montanarella, L., Odeh, I.O., Sanchez, P.A., Thompson, J.A., and Zhang, G.-L. (2014): GlobalSoilMap: Toward a Fine-Resolution Global Grid of Soil Properties. Adv. Agron. 125, 93–134.

Auslander, M., Nevo, E., Inbar, M. (2003): The effects of slope orientation on plant growth, development instability and susceptibility to herbivores. J. Arid Environ. 55, 405–416.

Barbour, M. G. (2000): North American terrestrial vegetation. Cambridge University Press, Cambridge.

Baumann, F., Schmidt, K., Dörfer, C., He, J.-S., Scholten, T., Kühn, P. (2014): Pedogenesis, permafrost, substrate and topography: Plot and landscape scale interrelations of weathering processes on the central-eastern Tibetan Plateau. Geoderma 226-227, 300–316.

Behrens, T., MacMillan, R.A., Viscarra Rossel, R.A., Schmidt, K., Lee, J. (2019a): Teleconnections in spatial modelling. Geoderma, Volume 354, 113854.

Behrens, T., Viscarra Rossel, R. A., Kerry, R., MacMillan, R., Schmidt, K., Lee, J., Scholten, T., Zhu, A-X. (2019b): The relevant range of scales for multi-scale contextual spatial modelling. Sci. Rep. 9, 14800.

Behrens, T., Schmidt, K., MacMillan, R.A., Viscarra Rossel, R. (2018a): Multi-scale Digital Soil Mapping with deep learning. Sci Rep. 8, 15244.

Behrens, T., Schmidt, K., Viscarra Rossel, R.A., Gries, P., Scholten, T., MacMillan, R.A. (2018b): Spatial modelling with Euclidean distance fields and machine learning. Eur. J. Soil. Sci., 69, 757–770.

Behrens, T., Schmidt, K., MacMillan, R.A., Viscarra Rossel, R.A. (2017): Multiscale contextual spatial modelling with the Gaussian scale space. Geoderma 310, 128–137.

Behrens, T., Schmidt, K., Ramirez-Lopez, L., Gallant, J., Zhu, A-X., Scholten, T. (2014): Hyper-scale digital soil mapping and soil formation analysis. Geoderma 213, 578–588.

Behrens, T., Schmidt, K., Zhu, A.X. und Scholten, T. (2010): The ConMap approach for terrain-based digital soil mapping. Eur. J. Soil Sci. 61, 133–143.

Behrens, T., Scholten, T. (2006): A Comparison of Data Mining Approaches in Predictive Soil Mapping. In: Lagacherie, P., McBratney, A.B, Voltz, M. (eds.): Digital Soil Mapping. Developments in Soil Science 31, 353–617.

Beven, K.J., Kirkby, M.J. (1979): A physically based, variable contributing area model of basin hydrology. Hydrol. Sci. B. 24, 43–69.

Biskaborn, B.K., Smith, S.L., Noetzli, J., Matthes, H., Vieira, G., Streletskiy, D.A., Schoeneich, P., Romanovsky, V.E., Lewkowicz, A.G., Abramov, A., Allard, M., Boike, J., Cable, W.L., Christiansen, H.H., Delaloye, R., Diekmann, B., Drozdov, D., Etzelmüller, B., Grosse, G., Guglielmin, M., Ingeman-Nielsen, T., Isaksen, K., Ishikawa, M., Johansson, M., Johannsson, H., Joo, A., Kaverin, D., Kholodov, A., Konstaantinov, P., Kröger, T., Lambiel, C., Lanckman, J.-P., Luo, D., Malkova, G., Meiklejohn, I., Moskaalenko, N., Oliva, M., Phillips, M., Ramos, M., Sannel, A.B.K., Sergeev, D., Seybold, C., Skryabin, P., Vasiöiev, A., Wu, Q., Yoshikawa, K., Zheleznyak, M., Lantuit, H. (2019). Permafrost is warming at a global scale. Nat. Commun 10, 264.

Biswas, A., Cresswell, H., Viscarra Rossel, R., Si, B.C. (2013): Characterizing scale- and location-specific variation in non-linear soil systems using the wavelet transform. Eur. J. Soil Sci. 64, 706–715.

Bliss, L. C. (2000): Arctic tundra and polar desert biome. In: Barbour, M.G. (ed.): North American terrestrial vegetation. Cambridge University Press, Cambridge, pp. 1–40.

Bock, M., Böhner, J., Conrad, O., Köthe, R., Ringeler, A. (2007): XV. Methods for creating Functional Soil Database and applying Digital Soil Mapping to SAGA GIS. In: Hengl, T., Panagos, P., Jones, A., Toth, G. (eds.): Status and prospect of soil information in south-eastern Europe: soil databases, projects and applications. EUR 22646 EN Scientific and Technical Research series, Office for Official Publications of the European Communities, Luxemburg, p.149–162.

Bockheim, J.G. (2007): Importance of Cryoturbation in Redistributing Organic Carbon in Permafrost-Affected Soils. Soil. Sci. Soc. Am. J. 71, 1335–1342.

Breiman, L. (2001): Random Forests. Machine Learning, 45, 5–32.

Breiman, L., Friedman, J.H., Olshen, R.A., Stone, C.J. (1984): CART: Classification and Regression Trees. Wadsworth, Belmont, CA.

Bradley-Cook, J.I., Virginia, R.A. (2016): Soil carbon storage, respiration potential, and organic matter quality across an age and climate gradient in southwestern Greenland. Polar. Biol. 39, 1283–1295.

Bradley-Cook, J. I., Petrenko, C. L., Friedland, A. J., Virginia, R. A. (2016): Temperature sensitivity of mineral soil carbon decomposition in shrub and graminoid tundra, west Greenland. Clim. Chang. Responses 3, 1–15.

Brookfield, M.E. (2011) Aeolian processes and features in cool climates. In: Martini, I.P.., French, H.M., Perez Alberti, A. (eds): Ice-Marginal and Periglacial Processes and Sediments. Geological Society of London 354, London, 241–258.

Burrough, P.A., van Gaans, P.F. M., MacMillan, R.A. (2000): High-resolution landform classification using fuzzy k-means. Fuzzy Set. Syst. 113, 37–52.

Burrough, P.A. (1983): Multiscale sources of spatial variation in soil the application of fractal concepts to nested levels of soil variation. J. Soil Sci. 34, 577–597.

Burt, P., Adelson, E. (1983): The laplacian pyramid as a compact image code. IEEE Trans. Commun. 31, 532–540.

Cappelen, J., Jørgensen, B.V., Laursen, E.V., Stannius, L.S., Thomsen, R.S. (2001): The observed climate of Greenland, 1958–99 - with climatological standard normals, 1961–90. Technical Report 00–18. Danish Meteorological Institute Ministry of Transport and Energy, Copenhagen.

Carrivick, J.L., Smith, M.W., Quincey, D.J. (2016). Structure from Motion in the Geosciences. Wiley-Blackwell.

Carstensen, L.S., Jørgensen, B.V. (2009): Weather and climate data from Greenland 1958–2008: dataset available for research and educational purposes. Descriptions and documentation of observations of temperature, precipitation, wind, could cover, air pressure, humidity and depth of snow. Technical Report 09–11. Danish Meteorological Institute Ministry of Transport and Energy, Copenhagen.

Smith, M.W., Carrivick, J.L., Quincey, D.J. (2016): Structure from motion photogrammetry in physical geography. Prog. Phys. Geogr.: Earth Environ.40, 247–275.

CAVM Team (2003): Circum Arctic Vegetation Map. (1:7,500,000 scale), Conservation of Arctic Flora and Fauna (CAFF) Map No. 1. U.S. Fish and Wildlife Service, Anchorage, Alaska.

Chadburn, S.E, Burke, E.J., Cox, P.M., Friedlingstein, P., Hugelius, G., Westermann, S. (2017): An observation-based constraint on permafrost loss as a function of global warming. Nat. Clim. Change 7, 340–344.

Conrad, O., Bechtel, B., Bock, M., Dietrich, H., Fischer, E., Gerlitz, L., Wehberg, J., Wichmann, V., Böhner, J. (2015): System for Automated Geoscientific Analyses (SAGA) v. 2.1.4, Geosci. Model Dev., 8, 1991–2007.

Dörfer, C., Kühn, P., Baumann, F., He, J.-S., Scholten, T. (2013): Soil Organic Carbon Pools and Stocks in Permafrost-Affected Soils on the Tibetan Plateau. Plos One 8: e57024.

Elberling, B., Nordstroem, C., Groendahl, L., Soegaard, H., Friborg, T., Christensen, T.R., Stroem, L., Marchand, F., Nijs, I. (2008a): High-arctic soil CO2 and CH4 production controlled by temperature, water, freezing and snow, in: Meltofte, H. (ed.), High-Arctic Ecosystem Dynamics in a Changing, Vol. 40. Advances in ecological research, Elsevier, Amsterdam, Heidelberg, pp. 441–472.

Elberling, B., Tamstorf, M. P., Michelsen, A., Arndal, M. F., Sigsgaard, C., Illeris, L., Bay, C., Hansen, B. U., Christensen, T. R., Hansen, E. S., Jakobsen, B. H., Beyens, L. (2008b): Soil and plant community-characteristics and dynamics at Zackenberg, in: Meltofte, H. (ed.), High-Arctic Ecosystem Dynamics in a Changing, Vol. 40. Advances in ecological research, Elsevier, Amsterdam, Heidelberg, pp. 223–248.

Elberling, B., Jakobsen, B.H., Berg, P., Sondergaar, J., Sigsgaard, C. (2004): Influence of vegetation, temperature, and water content on soil carbon distribution and mineralization in four high Arctic soils. Arct. Antarct. Alp. Res. 36, 528–538.

ESRI - Environmental Systems Research Institute (2014): ArcGIS Desktop 10.3 Data Management Toolbox, Create Random Points tool.

Everitt, B.S. (1980): Cluster Analysis. Wiley, New York.

Fotheringham, A.S., Brunsdon, C., Charlton, M. (2002): Geographically Weighted Regression: The Analysis of Spatially Varying Relationships. Wiley.

Freeman, G.T. (1991): Calculating catchment area with divergent flow based on a regular grid. Comput. Geosci. 17, 413–422.

Friedrich, K. (1996): Digitale Reliefgliederungsverfahren zur Ableitung bodenkundlich relevanter Flächeneinheiten. Frankfurter Geowissenschaftliche Arbeiten 21.

Gries, P., Schmidt, K., Scholten, T., Kühn, P. (2020): Regional and local scale variations in soil organic carbon stocks in West Greenland. J. Plant Nutr. Soil Sci. 183, 292–305.

Grimm, R, Behrens, T., Märker, M., Elsenbeer, A. (2008): Soil organic carbon concentrations and stocks on Barro Colorado Island - Digital soil mapping using Random Forests analysis. Geoderma 146, 102–113.

Guisan, A., Weiss, S. B., Weiss, A. D. (1999): GLM versus CCA spatial modeling of plant species distribution. Plant Ecol. 143, 107–122.

Guijarro, J.A. (2019): climatol: Climate Tools (Series Homogenization and Derived Products). R package.

Hengl, T., de Jesus J.M., Heuvelink, G.B.M., Ruiperez Gonzalez, M., Kilibarda, M., Blagotić, A., Shangguan, W., Wright, M.N., Bauer-Marschallinger, B., Guevara, M.A., Vargas, R., MacMillan, R.A. (2017) SoilGrids250m: Global gridded soil information based on machine learning. PLoS ONE 12: e0169748.

Hengl, T, de Jesus, J.M., MacMillan, R.A., Batjes, N.H., Heuvelink, G.B.M., Ribeiro, E., Samuel-Rosa, A., Kempen, B., Leenaars, J.G.B., Walsh, M.G., Ruiperez Gonzales, M. (2014) SoilGrids1km — Global Soil Information Based on Automated Mapping. PLoS ONE 9: e105992.

Hengl, T., Panagos, P., Jones, A., Toth, G. (2007): Status and prospect of soil information in south-eastern Europe: soil databases, projects and applications. EUR 22646 EN Scientific and Technical Research series, Office for Official Publications of the European Communities, Luxemburg.

Hengl, T., Heuvelink, G.B.M., Stein, A. (2004): A generic framework for spatial prediction of soil variables based on regression-kriging. Geoderma 120, 75–93.

Henkner, J., Scholten, T., Kühn, P. (2016): Soil organic carbon stocks in permafrost-affected soils in West Greenland. Geoderma 282, 147–159.

Henriksen, N. (2008): Geological History of Greenland: Four billion Years of Earth Evolution. Geological Survey of Denmark and Greenland, Copenhagen.

Hobbie, S.E., Schimel, J.P., Trumbore, S.E., Randerson, J.R. (2000): Controls over carbon storage and turnover in high-latitude soils. Glob. Chang. Biol. 6, 196–210.

Horwath Burnham, J.L., Sletten, R.S. (2010): Spatial distribution of soil organic carbon in northwest Greenland and underestimates of High Arctic carbon stores. Global Biogeochem. Cycles 24, 1–14.

Hugelius, G., Strauss, J., Zubryzycki, S., Harden, J., Schuur, E., Ping, C., Schirrmeister, L., Grosse, G., Michaelson, G., Koven, C., O'Donnell, J., Elberling, B., Mishra, U., Camill, P., Yu, Z., Palmtag, J., Kuhry, P. (2014): Estimated stocks of circumpolar permafrost carbon with quantified uncertainty ranges and identified data gaps. Biogeosciences 11, 6573–6593.

Hugelius, G., Tarnocai, C., Broll, G., Candell, J.G., Kuhry, P., Swanson, D.K. (2013): The Northern Circumpolar Soil Carbon Database: spatially distributed datasets of soil coverage and soil carbon storage in the northern permafrost regions. Earth Syst. Sci. Data 5, 3–13.

IPCC, International Panel on Climate Change (2019): IPCC Special Report on the Ocean and Cryosphere in a Changing Climate.

Iversen, C.M., Sloan, V.L., Sullivan, P.F., Euskirchen, E.S., McGuire, A.D., Norby, R.J., Walker, A.P., Warren, J.M., Wullschleger, S.D. (2015): The unseen iceberg: plant roots in arctic tundra. New Phytol. 205, 34–58.

Jenny, H. (1941) Factors of Soil Formation: A System of Quantitative Pedology. McGraw-Hill Book Company Inc., New York.

Jensen, L., Hollesen, J., Elberling, B. (2006): Accumulation of Soil Organic Carbon Linked to Holocene Sea Level Changes in West Greenland. Arct. Antarct. Alp. Res. 38, 378–383.

Joggáby, E.G., Jackson, R.B. (2000): The vertical distribution of soil organic carbon and its relation to climate and vegetation. Ecol. Appl. 10, 423–436.

Jones, A., Stolbovoy, V., Tarnocai, C., Broll, G., Spaargaren, O., Montanarella, L. (2009): Soil Atlas of the Northern Circumpolar Region, Luxembourg.

Karl, J.W., Maurer, B.A. (2010): Spatial dependence of predictions from image segmentation: A variogram-based method to determine appropriate scales for producing land-management information. Ecol. Informatics 5, 194–202.

Kerry, R., Oliver, M.A. (2011): Soil geomorphology: Identifying relations between the scale of spatial variation and soil processes using the variogram. Geomorphology 130, 40–54.

Köchy, M., Hiederer, R., Freibauer, A. (2015): Global distribution of soil organic carbon – Part1: Masses and frequency distributions of SOC stocks for the tropics, permafrost regions, wetlands, and the world. Soil 1, 351–365.

Kuhn, M. (2017): Caret: Classification and Regression Training. R package.

Kühn, P., Henkner, J., (2019). Permafrost-affected Soils, Climate, and Feedbacks in West Greenland. In: Lal, R., Stewart, B. A. (eds.). Soil and Climate. Advances in Soil Science, CRC Press, pp. 92–97.

Lagacherie, P., McBratney, A.B, Voltz, M. (2006): Digital Soil Mapping. Developments in Soil Science 31. Elsevier.

Lal, R. (2004): Soil carbon sequestration impacts on global climate change and food security. Science 304, 1623.

Lal, R. and Stewart, M.A. (2019). Soil and Climate. Advances in Soil Science, CRC Press.

Levy, L. B., Kelly, M. A., Howley, J. A., Virginia, R. A. (2012): Age of the Ørkendalen moraines, Kangerlussuaq, Greenland: constraints on the extent of the southwestern margin of the Greenland Ice Sheet during the Holocene. Quaternary Sci. Rev. 52, 1–5.

Lohr, S.L. (2021): Sampling - Design and Analysis. Chapman and Hall CRC. New York.

Martini, I.P.., French, H.M., Perez Alberti, A. (2011): Ice-Marginal and Periglacial Processes and Sediments. Geological Society of London 354, London.

Matsuoka, N. (2011): Climate and material controls on periglacial soil processes: Toward improving periglacial climate indicators. Quat. Res. 75, 356–365.

Matsuoka, N. (2001): Solifluction rates, processes and landforms: a global review. Earth Sci. Rev. 55, 107–133.

Mackay, J.R. (1995): Ice wedges on hillslopes and landform evolution in the late Quaternary, western Arctic coast, Canada. Can. J. Earth Sci. 32, 1093–1105.

McBratney, A.B., Mendoca Santos, M.L., Minasny, B. (2003): On digital soil mapping. Geoderma 117, 3–52.

McGuire, A.D., Lawrence, D.M., Koven, C., Clein, J.S., Burke, E., Chen, G., Jafarow, E., MacDougall, A.H., Marchenko, S., Nicolsky, D., Peng, S., Rinke, A., Ciais, P., Gouttevin, I., Hayes, D.J., Ji, D., Krinner, G., Moore, J.C., Romanovsky, V., Schädel, C., Schaefer, K., Schuur, E.A.G., Zhuang, Q. (2018): Dependence of the evolution of carbon dynamics in the northern permafrost region on the trajectory of climate change. Biological Sciences 115.

Meltofte, H. (2008): High-Arctic Ecosystem Dynamics in a Changing, Vol. 40. Advances in ecological research, Elsevier, Amsterdam, Heidelberg.

Mishra, U., Riley, W.J. (2012): Alaskan soil carbon stocks: spatial variability and dependence on environmental factors. Biogeosciences 9, 3637–3645.

Moore, I. D., Grayson, R. B., Ladson, A. R. (1991): Digital terrain modelling: a review of hydrological, geomorphological, and biological applications. Hydrol. Process. 5, 3–30.

Moran, C., Bui, E. (2002): Spatial data mining for enhanced soil map modelling. Int. J. Geog. Inf. Sci. 16, 533–549.

Müller, M., Thiel, C., Kühn, P. (2016): Holocene palaeosols and aeolian activities in the Umimmalissuaq valley, West Greenland. The Holocene 26, 1149–1161.

OpenStreetMap contributors (2015): https://planet.osm.org/historical-shapefiles/shoreline_ 300.tar.bz2 (Last access 14.11.2019)

Ozols, U., Broll, G. (2003): Soil ecological processes in vegetation patches of well drained permafrost affected sites (Kangerlussuaq - West Greenland). Polarforschung 73, 5–14.

Padarian, J., Minasny, B., McBratney, A.B. (2020): Machine learning and soil sciences: a review aided by machine learning tools. SOIL, 6, 35–52.

Palmtag, J., Cable, S., Christiansen, H. H., Hugelius, G., Kuhry, P. (2018): Landform partitioning and estimates of deep storage of soil organic matter in Zackenberg, Greenland. The Cryosphere 12, 1735–1744.

Palmtag, J., Hugelius, G., Lashchinskiy, N., Tamstorf, M.P., Richter, A., Elberling, B., Kuhry, P. (2015): Storage, Landscape Distribution, and Burial History of Soil Organic Matter in Contrasting Areas of Continuous Permafrost. Arct. Antarct. Alp. Res. 47, 71–88.

Patzner, M.S., Mueller, C.W., Malusova, M., Baur, M., Nikeleit, V., Scholten, T., Hoeschen, C., Byrne, J.M., Borch, T., Kappler, A., Bryce, C. (2020): Iron mineral dissolution releases iron and associated organic carbon during permafrost thaw. Nat. Commun. 11:6329.

Petrenko, C.L., Bradley-Cook, J.I., Lacroix, E.M., Friedland, A.J., Virginia, R.A. (2016): Comparison of carbon and nitrogen storage in mineral soils of graminoid and shrub tundra sites, western Greenland. Arctic Sci. 2, 165–182.

Ping, C.L., Jastrow, J.D., Jorgenson, M.T., Michaelson, G.J., Shur, Y.L. (2015): Permafrost soils and the carbon cycling. SOIL 1, 147–171.

Ping, C.L., Bockheim, J.G., Kimble, J.M., Michaelson, G.J., Walker, D.A. (1998): Characteristics of cryogenic soils along a latitudinal transect in arctic Alaska. J. Geophys. Res. 103, 917–928.

Poeplau, C., Vos, C., Don, A. (2017): Soil organic carbon stocks are systematically overestimated by misuse of the parameters bulk density and rock fragment content. SOIL, 3, 61–66.

Poggio, L., de Sousa, L.M., Batjes, N.H., Heuvelink, G.B.M., Kempen, B., Ribeiro, E., Rossiter, D. (2021): SoilGrids 2.0: producing soil information for the globe with quantified spatial uncertainty. SOIL, 7, 217–240.

Porter, C., Morin, P., Howat, I., Noh, M.-J., Bates, B., Peterman, K., Keesey, S., Schlenk, M., Gardiner, J., Tomko, K., Willis, M., Kelleher, C., Cloutier, M., Husby, E., Foga, S., Nakamura, H., Platson, M., Wethington, M., Williamson, C., Bauer, G., Enos, J., Arnold, G., Kramer, W., Becker, P., Doshi, A., D'Souza, C., Cummens, P., Laurier, F., Bojesen, M. (2018): ArcticDEM, Harvard Dataverse, V1.

Post, W.M., Emanuel, W.R., Zinke, P.J., Stangenberger, A.G. (1982): Soil carbon pools and world life zones. Nature 298, 156–159.

R Development Core Team (2013): R: A Language and Environment for Statistical Computing.

Ramage, J., Fortier, D.C., Hugelius, G., Lantuit, H., Morgenstern, A. (2019): Distribution of carbon and nitrogen along hillslopes in three valleys on Herschel Island, Yukon Territory, Canada. Catena 178, 132–140.

Rentschler, T., Werban, U., Ahner, M., Behrens, T., Gries, P., Scholten, T., Teuber, S., Schmidt, K. (2020): 3D mapping of soil organic carbon content and soil moisture with multiple geophysical sensors and machine learning. Vadose Zone J. 19.

Rentschler, T., Gries, P., Behrens, T., Bruelheide, H., Kühn, P., Seitz, S., Shi, X., Trogisch, S., Scholten, T., Schmidt, K. (2019): Comparison of catchment scale 3D and 2.5D modelling of soil organic carbon stocks in Jiangxi Province, PR China. PLoS ONE 14:e0220881.

Rothenhöfer, P., Huber, A., Kainzmaier B., Wohnlich, S., Pfeiffer, S. (2000): Ein Vergleich von vier Methoden zur Bestimmung des Karbonatgehaltes. Wasser und Boden 52, 37-42.

Schmidt, K., Behrens, T., Daumann, J., Ramirez-Lopez, L., Werban, U., Dietrich, P., Scholten, T. (2014): A comparison of calibration sampling schemes at the field scale. Geoderma 232-234, 243–256.

Schmidt, K., Behrens, T., Scholten, T. (2010): A method to generate soilscapes from soil maps. J. Plant Nutr. Soil Sc. 173, 163–172.

Schmidt, K., Behrens, T., Scholten, T. (2008): Instance selection and classification tree analysis for large spatial datasets in digital soil mapping. Geoderma 146, 1–2.

Stäblein, G. (1977). Arktische Böden Westgrönlands: Pedovarianz in Abhängigkeit vom geoökologischen Milieu. Polarforschung 47, 11–25.

Scholten, T., Goebes, P., Kühn, P., Seitz, S., Assmann, T., Bauhus, J., Bruelheide, H., Buscot, F., Erfmeier, A., Fischer, M., Härdtle, W., He, J.-S., Ma, K., Niklaus, P. A., Scherer-Lorenzen, M., Schmid, B., Shi, X., Song, Z., von Oheimb, G., Wirth, C., Wubert, T., Schmidt, K. (2017): On the combined effect of soil fertility and topography on tree growth in subtropical forest ecosystems – a study from SE China. Plant Ecol 10, 111–127.

Schuur, E. A., McGuire, D. A., Schädel, C., Grosse, G., Harden, J. W, Hayes, D. J., Hugelius, G., Koven, C. D., Kuhry, P., Lawrence, D. M., Natali, S. M., Olefeldt, D., Romanovsky, E. V., Schaefer, K., Turetsky, M. R., Treat., C. C., Vonk, J. E. (2015): Climate change and the permafrost feedback. Nature 520, 171–179.

Siewert, M. B., Hugelius, G., Heim, B., Faucherre, S. (2016): Landscape controls and vertical variability of soil organic carbon storage in permafrost-affected soils of the Lena River Delta. Catena 147, 725–741.

Stumpf, F., Schmidt, K., Goebes, P., Behrens, T., Schönbrodt-Stitt, S., Wadoux, A., Xiang, W., Scholten, T. (2017): Uncertainty-guided sampling to improve digital soil maps. Catena 153, 30–38.

Taghizadeh-Mehrjardi, R., Khademi, H., Khayamim, F., Zaraatpisheh, M., Heung, B., Scholten, T. (2022): A comparison of model averaging techniques to predict the spatial distribution of soil properties. Remote Sens. 14, 472.

Taghizadeh-Mehrjardi, R., Schmidt, K., Amirian-Chakan, A., Rentschler, T., Zeraatpisheh, M., Sarmadian, F., Valavi, R., Davatgar, N., Behrens, T., Scholten, T. (2020): Improving the Spatial Prediction of Soil Organic Carbon Content in Two Contrasting Climatic Regions by Stacking Machine Learning Models and Rescanning Covariate Space. Remote Sens. 12, 1095.

Tarnocai, C., Canadell, J.G., Schuur, E.A.G., Kuhry, P., Mazhitova, G., Zimov, S.A. (2009): Soil organic carbon pools in the northern circumpolar permafrost region. Glob. Biogeochem. Cy. 23, 1–11.

Van Huissteden, J. and Dolman, A.J. (2012): Soil carbon in the Arctic and the permafrost carbon feedback. Curr. Opp. Environ. Sustainability 4, 545–551.

Van Tatenhove, F. G. M., Olesen, O. B. (1994): Ground Temperature and Related Permafrost Characterictics in West Greenland. Permafrost Periglac. 5, 199–215.

Webster, R., Beckett, P. H. T (1968): Quality and Usefulness of Soil Maps. Nature 219, 680–682.

Viscarra Rossel, R., Lee, J., Behrens, T., Luo, Z., Baldock, J., Richards, A., (2019): Continental-scale soil carbon composition and vulnerability modulated by regional environmental controls. Nat. Geosci. 12, 547–552

Westermann, S., Elberling, B., Højlund Pedersen, S., Stendel, M., Hansen, B.U., Liston, G.E. (2015): Future permafrost conditions along environmental gradients in Zackenberg, Greenland. The Cryosphere, 9, 719–735.

Willemse, N. W., Koster, E. A., Hoogakker, B., Van Tatenhove, F. G. (2003): A continuous record of Holocene eolian activity in West Greenland. Quaternary Res. 59, 322–334.

Wilson, J.P., Gallant, J.C. (2000): Terrain Analysis: Principles and Applications. John Wiley and Sons, New York.

Wojcik, R., Palmtag, J., Hugelius, G., Weiss, N., Kuhry, P. (2019): Land cover and landform-based upscaling of soil organic carbon stocks on the Brøgger Peninsula, Svalbard. Arct. Antarct. Alp. Res. 51, 40–57.

Wood, J. (1996) The Geomorphological Characterisation of Digital Elevation Models. Ph.D. Thesis, University of Leicester, Leicester.

Wu, C. (2011): VisualSFM: a visual structure from motion system. http://ccwu.me/vsfm/

Wu, C., Agarwal, S., Curless, B., Seitz, S.M. (2011): Multicore bundle adjustment. CVPR 2011, 3057–3064.

Zevenbergern, L.W., Thorne, C.R. (1987): Quantitative analysis of land surface topography. Earth Surf. Proc. Land. 12, 47–56.

Zubrzycki, S., Kutzbach, L., Pfeiffer, E. (2014): Permafrost-affected soils and their carbon pools with a focus on the Russian Arctic. Solid Earth 5, 595–609.

Appendix

Manuscript 1:

Gries, P., Schmidt, K., Scholten, T., Kühn, P. (2020): Regional and local scale variations in soil organic carbon stocks in West Greenland. J. Plant Nutr. Soil Sci., 183, 292–305.

Manuscript 2:

Gries, P., Kühn, P., Scholten, T., Schmidt, K., (unpublished): Feature construction and machine learning for the spatial analysis of soil organic carbon stocks in West Greenland.

Manuscript 3:

Behrens, T., Schmidt, K., Viscarra Rossel, R.A., Gries, P., Scholten, T., MacMillan, R.A. (2018): Spatial modelling with Euclidean distance fields and machine learning. Eur. J. Soil. Sci., 69, 757–770.

Manuscript 4:

Rentschler, T., Gries, P., Behrens, T., Bruelheide, H., Kühn, P., Seitz, S., Shi, X., Trogisch, S., Scholten, T., Schmidt, K. (2019): Comparison of catchment scale 3D and 2.5D modelling of soil organic carbon stocks in Jiangxi Province, PR China. PLoS ONE 14(8): e0220881.

Manuscript 5:

Rentschler, T., Werban, U., Ahner, M., Behrens, T., Gries, P., Scholten, T., Teuber, S., Schmidt, K. (2020): 3D mapping of soil organic carbon content and soil moisture with multiple geophysical sensors and machine learning. Vadose zone journal 19, 1.

Acknowledgements

Manuscript 1: Regional and local scale variations in soil organic carbon stocks in West Greenland

Published in: Journal of Plant Nutrition and Soil Science, 183.

Authors: Philipp Gries[1], Karsten Schmidt[1], Thomas Scholten[1], Peter Kühn[1]

[1] Department of Geosciences, Chair of Soil Science and Geomorphology, University of Tübingen, 72070 Tübingen, Germany

Key words:

Arctic, landscape classification, permafrost-affected soils, tundra vegetation

Abstract:

The soil organic carbon (SOC) pool of the Northern Hemisphere contains about half of the global SOC stored in soils. As the Arctic is exceptionally sensitive to global warming, temperature rise and prolonged summer lead to deeper thawing of permafrost-affected soils and might contribute to increasing greenhouse gas emissions progressively. To assess the overall feedback of soil organic carbon stocks (SOCS) to global warming in permafrost-affected regions the spatial variation in SOCS at different environmental scales is of great interest. However, sparse and unequally distributed soil data sets at various scales in such regions result in highly uncertain estimations of SOCS of the Northern Hemisphere and here particularly in Greenland. The objectives of this study are to compare and evaluate three controlling factors for SOCS distribution (vegetation, landscape, aspect) at two different scales (local, regional). The regional scale reflects the different environmental conditions between the two study areas at the coast and the ice margin. On the local scale, characteristics of each controlling

factor in form of defined units (vegetation units, landscape units, aspect units) are used to describe the variation in the SOCS over short distances within each study area, where the variation in SOCS is high. On a regional scale, we investigate the variation in SOCS by comparing the same units between the study areas. The results show for both study areas that SOCS are with 8 kg m^{-2} in the uppermost 25 cm and 16 kg m^{-2} in the first 100 cm of the soil, i.e. 3 to 6 kg m^{-2} (37.5 %) higher than existing large scale estimations of SOCS in West Greenland. Our approach allows to rank the scale-dependent importance of the controlling factors within and between the study areas. However, vegetation and aspect better explain variations in SOCS than landscape units. Therefore, we recommend vegetation and aspect for determining the variation in SOCS in West Greenland on both scales.

1 Introduction

Soils store up to 3000 Pg carbon worldwide, which is twice the amount of the biosphere and the atmosphere together (*Köchy* et al., 2015). The northern circumpolar permafrost region stores about 1300 Pg soil organic carbon (SOC), whereof 217 Pg SOC are stored in the top 30 cm and 472 Pg in the first meter of the soil (*Hugelius* et al., 2013; 2014). The increase in air temperature of the Arctic overrides the global mean significantly over the last decades (*IPCC*, 2019), assuming a much stronger influence on permafrost soils than previously expected (*Chadburn* et al., 2017). This causes environmental alterations accelerating microbial breakdown of organic carbon and enhancing the release of the greenhouse gases to the atmosphere (*Schuur* et al., 2015). To assess the impact of global warming and greenhouse gas emission in permafrost-affected regions the spatial distribution and the amount of SOC stored in the soils have to be estimated as precise as possible.

However, the estimation of soil organic carbon stocks (SOCS) of permafrost-affected soils is highly uncertain as, for one reason, there is an unbalanced distribution of studies across the Arctic focusing on Alaska, Siberia and Canada while Greenland is underrepresented (*Tarnocai* et al., 2009; *Hugelius* et al., 2014; *Köchy* et al., 2015; *Ping* et al., 2015). For West Greenland predominantly Umbrisols and Cambisols are reported (cf. *Jensen* et al., 2006; *Bradley-Cook* and *Virginia*, 2016; *Petrenko* et al., 2016; *Kühn* and *Henkner*, 2019) which could store a significantly higher amount of SOC than thin and less developed soils in East and North Greenland (*Elberling* et al., 2008a; 2008b, *Palmtag* et al., 2015; 2018).

On a regional scale, SOCS are typically related to climate in terms of precipitation and temperature (*Post* et al., 1982). In West Greenland, mean annual air temperature (MAT) and mean annual precipitation (MAP) decrease from the coast at Sisimiut (MAT; MAP: -3.5 °C; 383 mm) to the ice margin at Kangerlussuaq (-5.7 °C; 149 mm) over a distance of 150 km on the regional scale (*Cappelen* et al., 2001; *Carstensen* and *Jørgensen*, 2009). At the ice margin, the air temperature is 3 K higher during the growing season (May-September) and 5 K lower from October until April than at the coast (*Cappelen* et al., 2001). Vegetal activity (*CAVM Team,* 2003) and permafrost thickness (*Van Tatenhove* and *Olesen*, 1994) increase towards the ice margin. Another interpretation of lower amounts of SOCS with increasing distance from the coast to the ice margin in West Greenland is related to the Holocene deglaciation history of the Greenland Ice Sheet, with decreasing age of exposed surfaces from the coast to the ice margin (*Levy* et al., 2012; *Bradley-Cook* and *Virginia*, 2016). However, these findings are in contrast with large scale estimates of SOCS in West Greenland showing no differences between the coast and the ice margin (*Jones* et al., 2009; *Hugelius* et al., 2014; *Köchy* et al., 2015).

On a local scale, vegetation and topography influence SOCS distribution in Greenland (*Ozols* and *Broll*, 2003; *Jensen* et al., 2006; *Elberling* et al., 2008b; *Horwath Burnham* and *Sletten*, 2010; *Henkner* et al., 2016) and also in other Arctic environments (*Palmtag* et al., 2015; 2018; *Siewert* et al., 2015; 2016; *Wojcik* et al., 2019). The topography affects both the local and the regional climate, thaw depth of the active layer, deflation, erosion by water and related accumulation processes (*Van Tatenhoven* and *Olesen*, 1994; *Müller* et al., 2016). Katabatic winds take control in east-west direction, with more arid and colder conditions close to the ice margin over distances of some hundred meters to a few kilometers (*Müller* et al., 2016). In addition, topsoil SOCS are connected to distribution pattern of vegetation and soil moisture (*Henkner* et al., 2016) whereas slope processes, cryoturbation and active layer thickness affect the vertical distribution of SOC in the subsoil (*Bockheim*, 2007; *Palmtag* et al., 2015; 2018; *Siewert* et al., 2015; 2016; *Wojcik* et al., 2019). However, vegetation pattern and the soil water regime are related to topographic positions as well (*Elberling* et al., 2008a), mainly determined by the local Holocene deglaciation history resulting in moraines stretching across valley from north to south (*Henkner* et al., 2016). Given such strong differences in controlling environmental conditions on various scales, a similar fluctuation of SOCS is expected. If that holds true, such scale-dependent variations in SOCS cannot be described by the existing large scale estimations satisfactory.

The objectives of this study are to compare and evaluate three controlling factors for SOCS distribution (vegetation, landscape, aspect) at two different scales (local, regional). The regional scale reflects the different climate conditions and related vegetation patterns on SOCS between two study areas. On the local, characteristics of each controlling factor in form of defined units (vegetation units, landscape units,

aspect units) are used to describe the variation in SOCS over short distances within each study area. On a regional scale we investigate the variation in SOCS by comparing the same units between the study areas. This approach allows to rank the scale-dependent importance of the controlling factors of SOCS within and between the study areas.

2 Material and methods

2.1 Study areas

The study area at the coast (SISI) is 1.5 km² in size and located around 4 km east to the city of Sisimiut (66° 57 N, 53° 33' W). The coastal area is characterized by oceanic climate conditions with frequently occurring fog, coastal westerly winds, MAT of -3.5°C and MAP of 383 mm (*Cappelen* et al., 2001; *Carstensen* and *Jørgensen*, 2009). SISI is located within a deep valley with northeast-southwest orientation and steep north- and south-facing slopes. The northern boundary of the study area consists of steep slopes (> 30°) with sparse vegetation cover and thin soils. A lake defines the eastern boundary and a small river the western boundary. The small river crosses the study area from the northeast to the southwest characterised by adjacent flat areas and depressions in smooth transition with slightly inclined slopes and moraines. A ridge with steep north-facing slopes marks the southern boundary of the study area (Fig. 1).

The study area at the ice margin (RUSS) comprises around 1.8 km² and is located directly at the ice margin, around two kilometres west of the Russell Glacier (67° 6' N, 50° 17' W), which is an outlet glacier of the Greenland Ice Sheet. The ice margin area is characterized by an arctic continental climate with MAT of -5.7 °C and MAP of 149 mm and katabatic winds blowing down from the Greenland Ice Sheet predominantly to

the west (*Cappelen* et al., 2001; *Carstensen* and *Jørgensen*, 2009). RUSS is located in an east-west oriented valley with steep north- and south-facing slopes and lakes in the east and west which define the boundaries of the study area. Sand dunes occur in the northeaster part caused by the katabatic winds taking up sediment from the outwash plains (cf. *Müller* et al., 2016). Different terminal moraines cross the valley in north-south direction (Fig. 1). Mountain vegetation on non-carbonate bedrock, i.e. mostly granite in SISI and gneiss in RUSS defines the vegetation in both study areas (*CAVM Team*, 2003; *Henriksen,* 2008). Sedges cover depressions, flat and bankside areas, whereas mosses, lichens and prostrate dwarf shrubs grow on steep slopes and ridges. Dwarf shrubs < 40 cm in height in SISI and > 40 cm in RUSS occur in wind sheltered areas and slightly inclined slopes. Since the last deglaciation, predominantly periglacial processes reshaped the glacial landscape (*Stäblein*, 1977; *Ozols* and *Broll*, 2003; *Willemse* et al., 2003; *Henriksen,* 2008; *Müller* et al., 2016). The maximal possible time for soil formation since the last deglaciation is around 10,000 years in SISI and 6800 years in RUSS (c.f. *Bradley-Cook* and *Virginia*, 2016). Dominant soils are acid haplic Cambisols and Cryosols in both study areas (*Stäblein* 1977; *Jones* et al., 2009; *Henkner* et al., 2016; *Kühn* and *Henkner*, 2019). The majority of soils at steep slopes, moraine crests, ridges and summits are less developed on coarse substrate with an active layer thickness >200 cm. Wind sheltered locations of dunes and at slightly inclined slopes are characterized by warm and dry soil conditions and sandy substrate. On these locations, soil formation results in organic rich soils of which some are buried by aeolian sediments. Soils in depressions, flat and bankside area have thick organic horizons with silty texture, high soil moisture content and a thin active layer (60.08 ± 35.34 cm). Further impressions of the study areas are given by photographs in the online supplement (S1, S2).

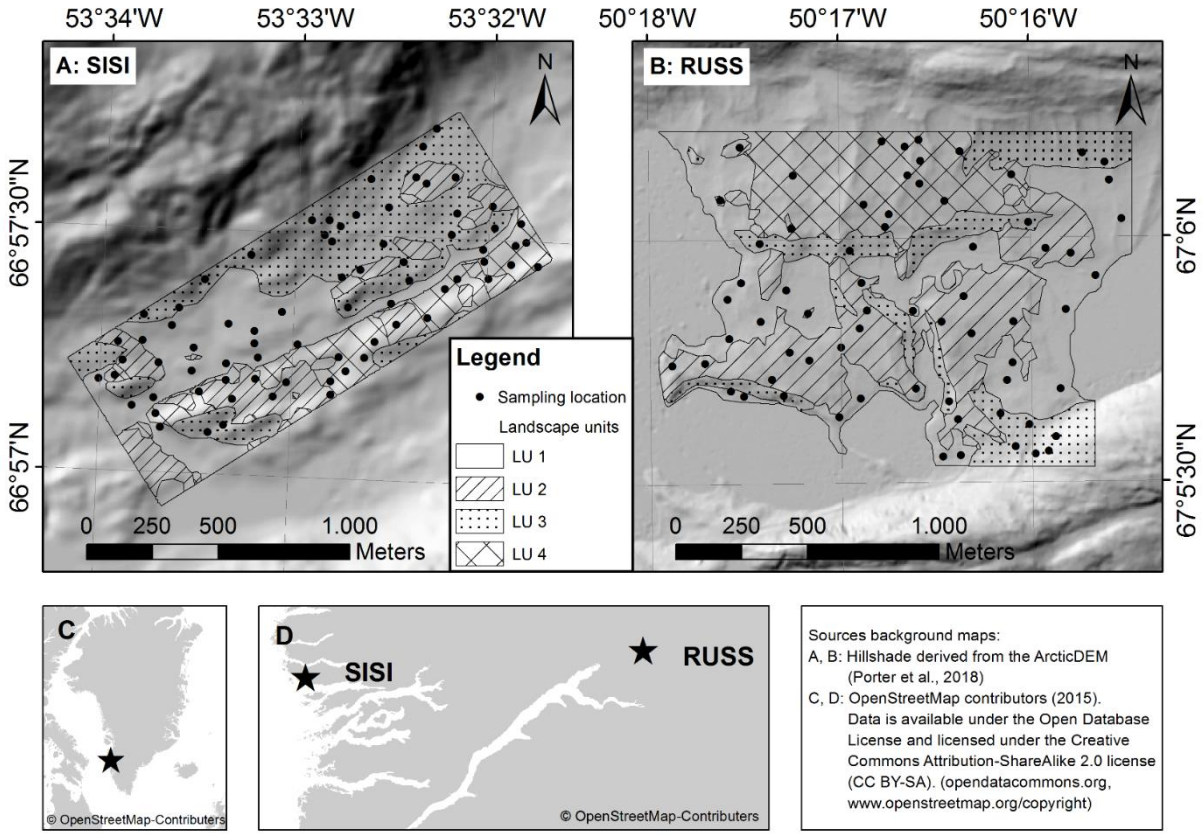

Figure 1: Study areas near Sisimiut (SISI) at the coast and close to the Russell Glacier (RUSS) at the ice margin of the Greenland Ice Sheet with sampling locations and landscape units.

2.2 Delineation of landscape units and sampling design

Landscape units (LU) are delineated as spatial entities that represent the spatial extend of homogenous landforms according to the deglaciation history and geomorphology of the land surface (Tab. 1). To structure the topography of the study areas, we used a set of local, regional and combined terrain covariates which are relevant for the spatial distribution of SOCS (Tab. S3, supplementary material). The terrain covariates are derived from a digital elevation model with a resolution of 5 x 5 m computed from aerial images from the Geodetic Institute of Denmark using

VisualSFM (*Wu*, 2011; *Wu* et al., 2011), where structure from motion is combined with photogrammetry to estimate three dimensional terrain surface objects from satellite image sequences (*Carrivick* et al., 2016).

To delineate the LU, we used k-means cluster analysis for automated and unsupervised classification of terrain covariates (*Burrough* et al., 2000; *Schmidt* et al., 2010). The aim of the cluster analysis is to divide the study area into homogeneous classes with high interclass variance and small intraclass variance (*Webster* and *Beckett*, 1968; *Everitt*, 1980). The selection of the number of clusters aims at a best-structured and less-fragmented representation of the two study areas. According to *Schmidt* et al. (2010) we set k=10 as maximum number of LUs to address feasibility of the subsequent sampling design and determined the optimal number of classes by using the number of fragments and their perimeter per class (Fig. 2). The smaller the number of fragments and the perimeter, the lower the degree of fragmentation of the classes and thus optimally suited for the designation of LU. The intersection represents the optimal size of k which is both 3.68 and 4.34 for SISI and 4.18 for RUSS. Finally, we chose four classes for LUs for both study areas. The paired t-test of the terrain parameters of each LU ensures the pairwise comparability of related LUs between both study areas (Tab. 1).

In total 140 sampling points were proportionally allocated to the LUs according to surface percentage and fragmentation. The sampling points were randomly distributed based on software (*Create Random Points* tool, ArcGIS Desktop 10.3, *ESRI*, 2014) within each LU (Fig. 1).

Table 1: Results of t-test (significance level, α = 0.05) to verify the comparability of each LU between SISI and RUSS and the major landform elements they represent.

Landscape unit	Landform element	p-value (t-test)
LU1	Depression, flat and bankside area	0.037
LU2	Moraine crest, ridge, summit	0.027
LU3	Plateau area	0.019
LU4	Steep slope	0.020

Figure 2: Determination the optimal number of classes (c) in SISI (black) and RUSS (grey) by using the number of fragments (points) and their perimeter (triagles) per class. The intersections represent the optimal number of classes which is both 3.68 and 4.34 for SISI and 4.18 for RUSS.

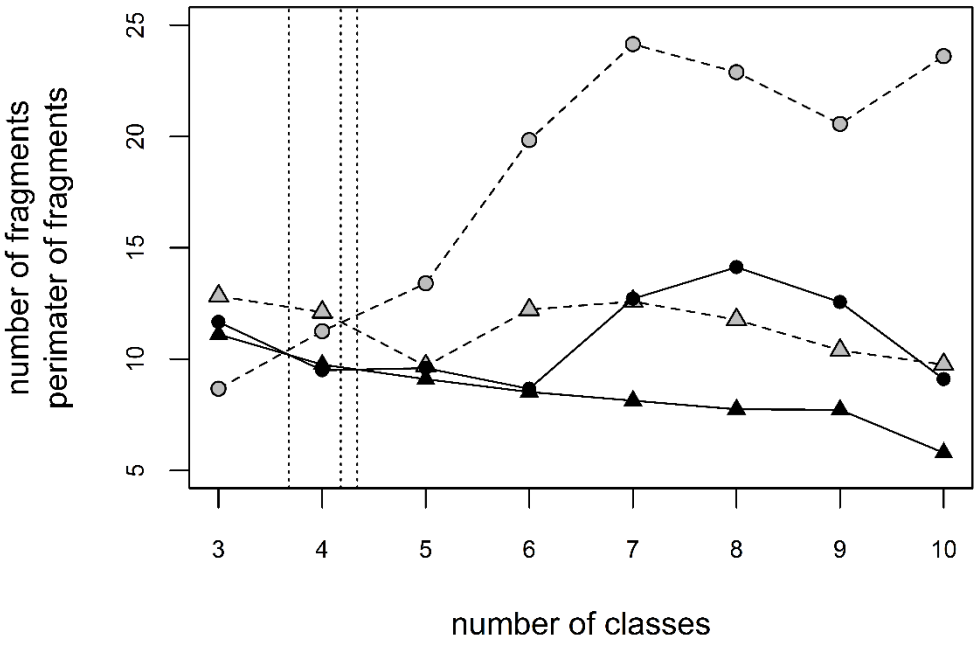

2.3 Field work, laboratory and statistical analysis

During a field campaign in summer 2016, vegetation cover (VEG) was recorded by species and their growth height according to *Bliss* (2000) (Tab. 2) and the aspect (ASP) was determined at all sampling locations. We used a hand-driven, half-open Pürckhauer auger (0-100 cm; slot width 18 mm) with an extension (100-200 cm; slot width 16 mm) for sampling of SOC and bulk density (BD) (e.g. *Don* et al., 2007) at four depth increments (0-25, 25-50, 50-100 and 100-200 cm). Only unfrozen ground was sampled. The first depth increment (D1) was set to 0-25 cm as according to an earlier field survey the maximal thickness of the upper organic horizon was found to be 25 cm in both study areas. Since the minimal thickness of the active layer (AL) is around 50 cm at comparable landscape conditions in West Greenland, the second depth increment (D2) was set to 25-50 cm (cf. *Bradley-Cook* et al., 2016; *Henkner* et al., 2016). The third depth increment (D3) was set to 50-100 cm, because a large amount of SOC can be stored in the subsoil (*Tarnocai* et al., 2009; *Hugelius* et al., 2014). We set the fourth depth increment (D4) to 100-200 cm to include soil heterogeneity caused by cryoturbation (*Ping* et al., 1998).

For SOC analysis, we sampled three soil cores at each sampling location to have three replicates of each depth increment over the complete depth. The replicates of each depth increment were bulked. If a depth increment could not be sampled completely due to frozen subsoil conditions or bedrock the SOCS of the not-sampled part was set to 0. Due to the subsoil conditions 140 samples were taken from D1, 138 samples from D2, 127 samples from D3 and 91 samples from D4. We sampled 16 locations for BD, covering all LUs. BD samples were collected from the middle of each depth increment (10-15, 35-40, 72.5-77.5 and 147.5-152.5 cm) from the soil cores.

Samples for SOC were dried at 40°C, sieved (< 2mm) and analysed using oxidative heat combustion at 1150°C in a helium atmosphere (element analyser Vario EL II, Elementar Analysesysteme GmbH, Germany, in CN mode). Measurements below the detection limit (carbon: 0.2 %) were set to zero. Since the gasvolumetrical determination of carbonate content according to Scheibler (*Rothenhöfer* et al., 2000) was negative for all samples, we assumed that total carbon content equals SOC [%]. The BD samples were dried at 105 °C to determine the mass (*mass*, [g]) gravimetrically to calculate the BD [g cm^{-3}] according to Eq. 1 and Eq. 2 and to determine the mass proportion of the coarse fraction [%] >2 mm (CF [%]) to calculate the SOCS [kg m^{-2}] according to Eq. 3 (Scholten et al., 2017). Eq. 2 is necessary to calculate the volume of a sample taken from a half-open Pürckhauer auger.

$$BD = mass \bullet Vs^{-1} \text{ (Eq. 1)},$$

$$Vs = Vc + 0.5 \bullet Ve = w \bullet h \bullet l + 0.5 (\pi \bullet a \bullet b \bullet l) \text{ (Eq. 2)},$$

where Vs (volume of the sample , [cm^3]) is a combination of the volume of a cuboid Vc [cm^3] and the half of an ellipse Ve [cm^3]; *w* is the slot width of the auger, *h* the height of the cuboid and *l* the depth of the BD samples; *a* is the half of the slot width *w* and *b* the height of the ellipse; *w*, *h*, *l*, *a* and *b* are given in [cm].

$$SOCS = SOC \bullet BD \bullet D \bullet (1 - CF). \text{ (Eq. 3)},$$

where D [cm] is the thickness of the depth increments D1-D4. If the entire depth increment could not be sampled due to bedrock or the permafrost table, the actual depth was used for D. For analysing field and lab data we used the statistical software R and the *stats* package version 3.4.2 (*R Development Core Team*, 2013). We used ANOVA to determine statistical connections.

Table 2. Vegetation units according to *Bliss* (2000).

Vegetation unit		Dominant species	Growth height [cm]	Percentage area [%] (SISI/RUSS)	Position
VEG1	Dwarf shrub heath tundra	*Betula nana, Dryas integrifolia*	5-20 cm	28 / 10	Steep slopes, ridges, moraine crests, summits
VEG2	Low shrub tundra	*Betula nana*	20-40 cm	38 / 39	Slopes
VEG3	Tall shrub tundra	*Salix glauca*	>40 cm	4 /18	Slightly inclined slopes
VEG4	Graminoid-moss tundra	*Carex rariflora Eriophorum angustifolium*	5-20 cm	30 / 33	Depressions, flat areas, bankside areas

3 Results

First, we present the results on the local variation in SOCS related to VEG, LU and ASP within each study area. Regional differences between the study areas are explained in chapter 3.2.

3.1 Local scale variations in SOCS

3.1.1 Vegetation units

Dwarf shrub heath tundra (VEG1) is predominant at steep slopes, moraine crests, ridges and summits characterized by sandy texture at 0-25 cm with increasing silt content down to 100 cm depth, a thick active layer and a wide range of soil moisture content in both study areas. Low shrub tundra (VEG2) and tall shrub tundra (VEG3) mainly cover slightly inclined slopes and wind sheltered areas. Topsoil material (0-25 cm) has higher silt content on locations covered by VEG2 and VEG3 compared to VEG1. Graminoid-moss tundra (VEG4) has highest soil moisture content compared to the other VEG.

In SISI, topsoil SOCS are highest for VEG3 (12.20 ± 4.76 kg m^{-2}) which is 27 % higher than for VEG2 and VEG4 and 7.52 kg m^{-2} higher than for VEG1. Within 25-50 cm and 50-100 cm, SOCS are highest for VEG4 but highest for VEG3 within 100-200 cm. In general, SOCS are lowest for VEG1 at all depth increments in SISI (Fig. 3). The uppermost 25 cm of soil show no significant correlation between VEG and SOCS in SISI (Tab. 3).

In RUSS, the general picture is the same as in SISI. SOCS are highest for VEG3 (10.88 ± 2.20 kg m^{-2}) which is 31 % higher than for VEG2 and VEG4 and 54 % higher than for VEG1 within 0-25 cm (4.98 ± 4.03 kg m^{-2}). Besides, SOCS are highest for VEG3 (25-50 cm, 50-100 cm) as well but 80 % lower than for VEG2 and VEG4 within 100-200 cm (Fig. 3). For the uppermost 25 cm, VEG and SOCS are significantly correlated (Tab. 3).

3.1.2 Landscape units

The landscape units represent specific landform elements similar in both study areas (Tab. 1). Sampling locations in LU1, dominated by graminoid-moss tundra (VEG4), are characterized by sandy texture, wet and cold soil conditions and low active layer thickness in both study areas. In both study areas, in LU2 tall shrub tundra (VEG4) is not existent and LU3 is dominated by low shrub tundra (VEG2).

In SISI, SOCS are highest within 0-25 cm in LU3 (10.82 ± 8.83 kg m^{-2}) which is 37 % higher than in LU1, 42 % in LU2 and 44 % in LU4. But SOCS are lowest in LU2 within Figure 3: Variation in SOCS (mean, SD) by VEG and LU in SISI and RUSS. Missing SD in 100-200 cm relates to n = 1 and SD > mean.

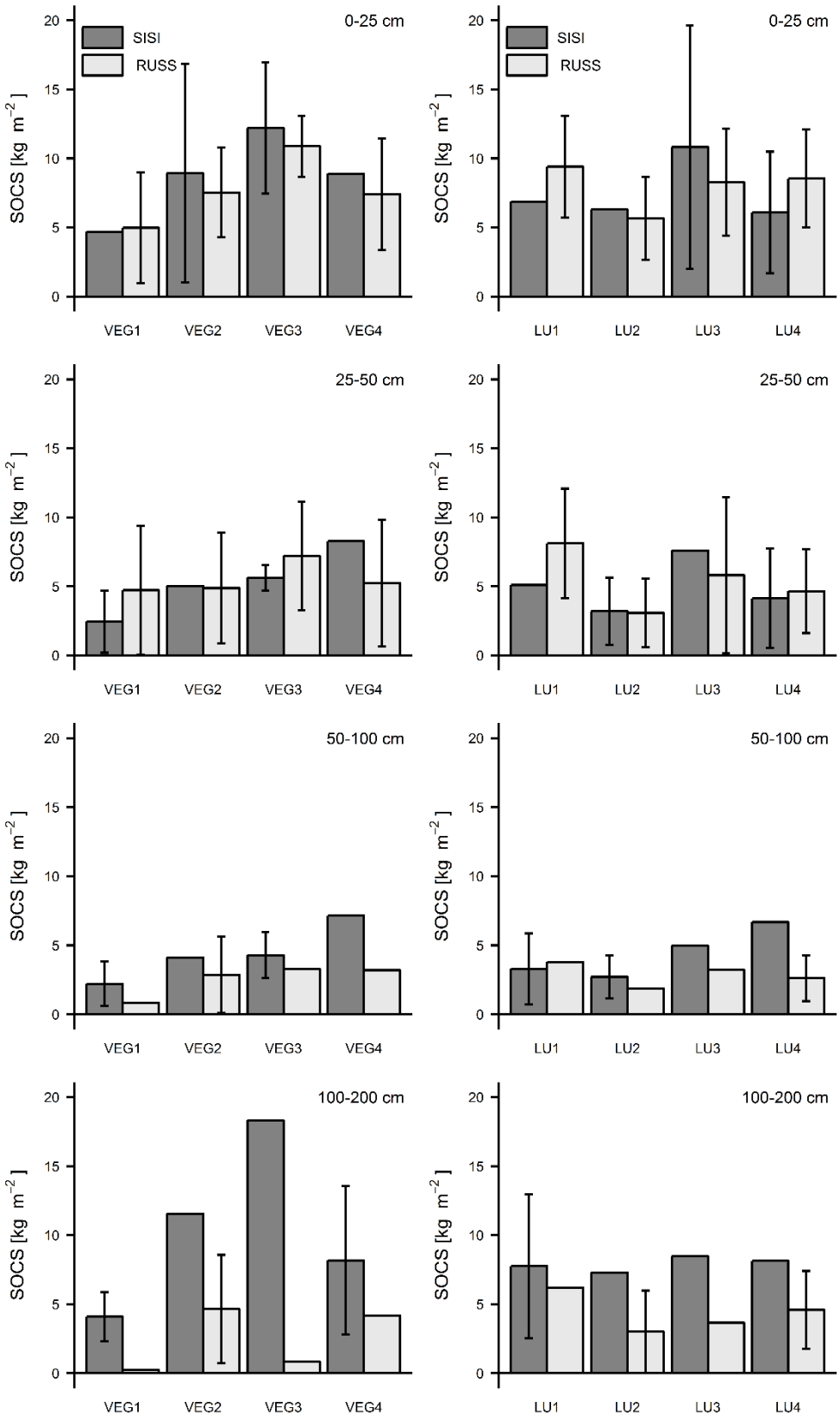

Figure 4: Variation in SOCS (mean: dashed line) related to the aspect in SISI and RUSS.

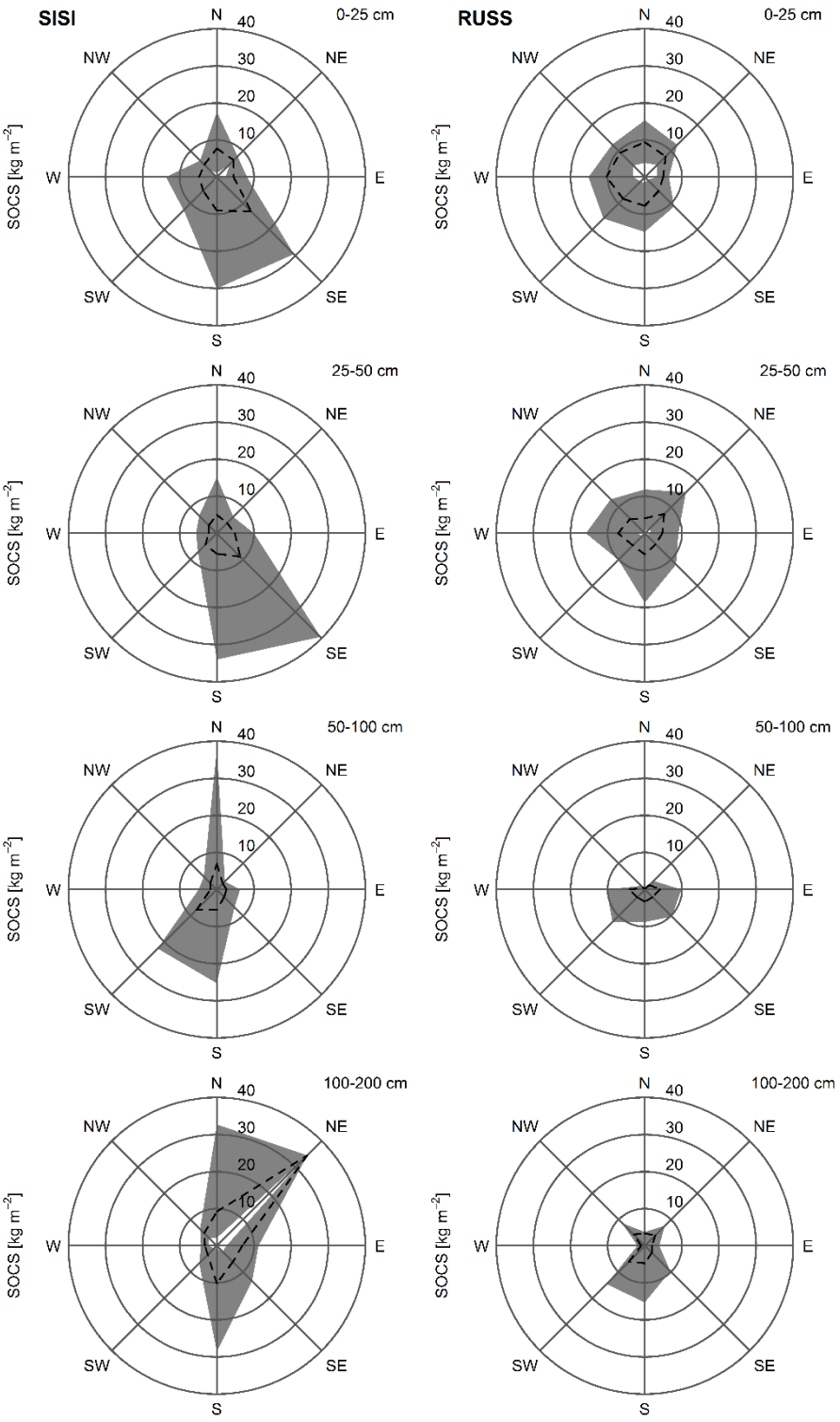

all depth increments below 0-25 cm. Within 100-200 cm, there is no distinct difference in SOCS of the different LUs (Fig. 3).

In RUSS, SOCS are lowest in LU2 within all depth increments decreasing from 5.66 ± 3.00 kg m^{-2} (0-25 cm) to 3.01 ± 2.98 kg m^{-2} (100-200 cm). In LU1, SOCS are highest within all depth increments being 50-60 % higher than within all depth increments in LU2 (Fig. 3). SOCS are with 8.28 ± 3.87 kg m^{-2} and 8.54 ± 3.54 kg m^{-2} similar in LU3 and LU4 within the uppermost 25 cm. There is a significant correlation between LU and SOCS within 0-25 and 20-50 cm in RUSS (Tab. 3).

3.1.3 Aspect

In SISI, SOCS are lowest (mean < 5 kg m^{-2}) on east-, northwest- and west-facing locations and with up to about 30 kg m^{-2} highest on south-facing (S, SE) locations in 0-25 cm (Fig. 4). Average SOCS on north-facing locations are 7.75 ± 5.22 kg m^{-2} in the uppermost 25 cm, which is about 2 kg m^{-2} respectively 1 kg m^{-2} higher than within 25-50 cm and 50-100 cm but about 2 kg m^{-2} lower within 100-200 cm. There is a significant relationship between SOCS and ASP in SISI at 100-200 cm (Tab. 3).

In RUSS, there is a large difference up to 15.17 kg m^{-2} between the lowest on east-facing locations (4.95 ± 1.19 kg m^{-2}) and highest SOCS on west-facing locations within the first depth increment. Generally, soils on north-facing locations show higher SOCS (NE, N, NW: 8.91 ± 3.25 kg m^{-2}) than on south-facing locations (SE, S, SW: 7.16 ± 3.84 kg m^{-2}) (Fig. 4). Tall shrub tundra (VEG3) is only present on south- and southeast-facing locations.

Table 3: Anova (F-Value) of environmental parameters and significance (p-values: *** <0.0001, ** < 0.001, * <0.05) in SISI and RUSS.

Study area		Depth [cm]	LU	VEG	ASP
SISI	SOCS	0-25	1.82	1.85	1.48
(coast)		25-50	1.39	2.40	0.70
		50-100	1.32	2.23	1.03
		100-200	0.04	3.00*	2.72*
	LU			0.02	3.66*
	VEG				1.65
	ASP				
RUSS	SOCS	0-25	4.09*	4.64*	2.14
(ice margin)		25-50	5.85*	0.91	0.66
		50-100	1.16	0.96	0.97
		100-200	0.72	1.86	0.46
	LU			0.33	0.71
	VEG				1.94
	ASP				

3.2 Regional scale variations in SOCS

On average, SOCS are similar in both study areas within 0-25 cm (around 8 kg m^{-2}) and 25-50 cm (around 5 kg m^{-2}) but have distinct differences within 50-100 cm and 100-200 cm with 36 % respectively 53 % higher SOCS in SISI than in RUSS. In addition, maximum SOCS within all depth increments are 47-68 % higher in SISI than in RUSS (Tab. 4).

3.2.1 Vegetation units

In SISI, SOCS (0-25 cm) are 11 to 17 % higher for VEG2, VEG3 and VEG4 but 6 % lower for VEG1 than in RUSS. Over all soil depth increments, SOCS are higher in SISI compared to RUSS. Only for VEG3, RUSS shows with 7.20 ± 3.93 kg m^{-2} higher SOCS within 25-50 cm than in SISI (5.64 ± 0.93 kg m^{-2}) (Fig. 3).

3.2.2 Landscape units

Topsoil SOCS (0-25 cm) in LU2 and LU3 are 10 % respectively 23 % lower in RUSS compared to SISI, where LU1 and LU4 are around 30 % lower than in RUSS. Within 25-50 cm, SOCS are similar with around 3 kg m^{-2} and 4 kg m^{-2} in LU2 respectively LU4 in both study areas. Within 100-200 cm SOCS are 20-59 % higher in all LUs than in RUSS (Fig. 3).

3.2.3 Aspect

In both study areas, SOCS is lowest on east facing locations. SOCS on south-east facing locations is 59 % higher in SISI than in RUSS where SOCS are 54 % higher on west facing locations compared to SISI. Within all depth increments, SOCS is higher on south facing locations in SISI than in RUSS. In RUSS, SOCS are higher on west facing locations within the depth increments of the uppermost 100 cm but lower within 100-200 cm compared to SISI (Fig. 4).

Table 4: Descriptive statistics of SOC content, BD, SOCS, soil moisture and AL thickness in SISI and RUSS (value with "<" indicates the detection limit).

Study area	Soil characteristic	Depth [cm]	n	Min	Mean ± SD	Max
SISI (coast)	SOC content [%]	0-25	74	0.28	6.14 ± 7.00	28.96
		25-50	73	<0.02	2.09 ± 2.69	14.37
		50-100	66	<0.02	0.82 ± 1.00	5.65
		100-200	42	0.20	1.02 ± 0.98	4.30
	BD [g cm^{-3}]	0-25	8	0.43	0.65 ± 0.30	1.23
		25-50	8	1.02	1.17 ± 0.08	1.33
		50-100	8	1.13	1.34 ± 0.09	1.45
		100-200	8	1.38	1.42 ± 0.09	1.68
	SOCS [kg m^{-2}]	0-25	74	0.34	7.85 ± 7.77	30.05
		25-50	73	<0.02	5.25 ± 7.72	39.52
		50-100	66	<0.02	4.42 ± 6.18	38.10
		100-200	42	0.87	7.91 ± 8.10	34.48
	Soil moisture [%]	0-5	74	0.70	26.80 ± 23.48	92.60
	Lower limit of AL [cm]	0-200	17	4.00	70.00 ± 42.70	144.00
		>200	57	-	- -	
RUSS (ice margin)	SOC content [%]	0-25	66	0.46	3.23 ± 1.45	6.27
		25-50	65	0.20	2.41 ± 2.05	9.44
		50-100	56	<0.02	0.97 ± 1.30	7.29
		100-200	33	<0.02	0.54 ± 0.67	3.47
	BD [g cm^{-3}]	0-25	8	0.84	0.97 ± 0.08	1.10
		25-50	8	0.82	1.12 ± 0.18	1.39
		50-100	8	0.83	0.99 ± 0.30	1.40
		100-200	8	1.06	1.24 ± 0.22	1.75
	SOCS [kg m^{-2}]	0-25	66	1.01	7.86 ± 3.74	15.79
		25-50	65	0.58	5.41 ± 4.24	18.75
		50-100	56	<0.02	2.82 ± 3.13	12.32
		100-200	33	<0.02	3.74 ± 3.97	15.33
	Soil moisture [%]	0-5	66	0.70	8.33 ± 7.08	25.50
	Lower limit of AL [cm]	< 200	37	6.00	53.00 ± 28.09	142.00
		> 200	29	-	- -	

4 Discussion

4.1 Local scale variations in SOCS

4.1.1 Vegetation units

Generally, topsoil SOCS are controlled by vegetation cover because most Arctic plants root within the upper 25-30 cm (*Iversen* et al., 2015). Vegetation varies in its spatial distribution and portions affecting the spatial distribution of SOCS in Arctic environments (*Elberling* et al., 2008b; *Horwath Burnham* and *Sletten*, 2010; *Palmtag* et al., 2015; *Siewert* et al., 2015; *Wojcik* et al., 2019). In SISI, VEG1 predominantly covers west- and north-west-facing locations where plant growth might be restricted by constant onshore winds and high direct solar radiation. For VEG1, SOCS are lowest due to low accumulation rates of SOC in coastal regions in West Greenland (*Jensen* et al., 2006). Besides, organic material is relocated from steep slopes covered by VEG1 to depressions and flat areas covered by VEG4. Soils covered by VEG4 have thick and humus rich topsoil horizons because of dense rooting, low decomposition rates and a constant accumulation of SOM under moist soil conditions due to oceanic climate conditions (*Stäblein*, 1977; *Jensen* et al., 2006). Similar SOCS for VEG2 and VEG3 result from similar mechanisms of SOC storage (*Petrenko* et al., 2016). However, SOCS are highest for VEG3, which is sparsely occurring and not characteristic for coastal areas in West Greenland (*CAVM Team*, 2003). In SISI, SOCS with combined shrub tundra vegetation (VEG2 and VEG3: 10.57 ± 6.33 kg m^{-2}) correspond to findings by *Bradley-Cook* and *Virginia* (2016) of 10.20 kg m^{-2} with comparable vegetation in coastal West Greenland.

In RUSS, accumulation of SOM in the topsoil is mainly caused by the incorporation of leaf remains of *Salix glauca* (*Ozols* and *Broll*, 2003), the dominant species of VEG3.

Under dry soil conditions decomposition of SOM is lower and so SOCS are higher for VEG3 than VEG2. In contrast, decomposition of SOM is also limited by high soil moisture conditions in depressions, flat and bankside areas predominantly covered by VEG4. Similar SOCS for VEG2 and VEG4 correspond to findings of *Petrenko* et al. (2016) detecting no significant differences in SOCS in 0-50 cm between graminoid and shrub vegetation at the ice margin in West Greenland. Dry katabatic winds and low precipitation rates during the growing season influence the growth of VEG1 and reduce biomass productivity on wind-exposed areas as well as the incorporation of organic matter into the soil (*Ozols* and *Broll*, 2003).

4.1. 2 Landscape units

In SISI, topsoil SOCS vary spatially with different LUs. LU3 includes the foot slope of a large catchment area in the north of SISI into which SOC is transported by overland and subsurface flow (*Stäblein*, 1977). At coastal area of West Greenland cryoturbation processes were found as a characteristic phenomenon (*Stäblein*, 1977, *Jensen* et al., 2006). Deep thawing of soils during summer fosters vertical relocation of SOC via cryoturbation processes and results in high SOCS at 50-100 and 100-200 cm at all landscape units in SISI. In LU4, SOCS are highest at 50-100 cm which might be connected a thick active layer since the isolating effect of sites with low-growing vegetation is less than on sites with shrub vegetation leading to deep thawing and relocation of SOC in LU4. Besides cryoturbation, SOCS can also be high in the subsoil caused by buried organic material which was deposited or covered by slope processes related to various topographic positions within different landscape patterns (*Palmtag* et al., 2015; 2018; *Wojcik* et al., 2019).

In RUSS, a spatial variation in SOCS can be related to the varying impact of local climate conditions. Climate conditions at the ice margin in West Greenland commonly have dry and cold katabatic winds blowing from the Greenland Ice Sheet to the west. These dry winds increase evapotranspiration and prevent growth of vegetation (*Cappelen* et al., 2001), especially at wind-exposed areas like moraine crests with east-facing upper slopes (LU2). Since tall shrub tundra has highest SOCS (Fig. 3), but does not occur in LU2, SOCS are the lowest in all depth increments in LU2. Lowest SOCS within 0-25 cm in LU2 in RUSS (5.66 ± 3.00 kg m^{-2}) correspond to findings in the Umimmalissuaq valley, located at the ice margin 20 km to the south of RUSS, where SOCS from 0-30 cm are also lowest with 6.01 ± 2.49 kg m^{-2} at crest positions with similar environmental conditions as in LU2 in RUSS (*Henkner* et al., 2016).

A common geomorphological feature are terminal moraines oriented perpendicular to the dominant wind direction in RUSS. These moraines reduce the negative effects of katabatic winds on the vegetation cover on leeside locations leading to higher SOCS within 0-25 cm in LU1, LU3 and LU4. Hence, landscape conditions affect the variation in SOCS in RUSS in 0-25 cm by negative effects of katabatic winds to plant growth, which result in higher SOCS on leeside positions than in wind-exposed areas in RUSS.

Including all depressions and lake-surrounding areas, LU1 includes generally very moist and wet soil conditions, which explain highest SOCS within 0-25 cm (9.40 ± 3.70 kg m^{-2}) and 25-50 cm (8.11 ± 3.97 kg m^{-2}). In LU1, highest SOCS also occur in 50-100 cm and 100-200 cm, which can be linked to organic matter buried by lake sediments from alternating lake water levels during the Holocene (*Willemse* et al., 2003) or by relocated sediments (*Palmtag* et al, 2018). Lower SOCS in LU4 than in LU1 can be explained by generally dry hillslope areas in LU4 and the availability of oxygen and the microbial activity is higher causing higher decomposition of SOC (*Elberling* et al., 2004).

4.1.3 Aspect

In SISI, SOCS are lowest on west-facing (SW, W, NW) locations. Due to high solar energy input on north-west-facing and west-facing locations, high decomposition rates benefit from warm soil conditions resulting in low SOCS (*Elberling* et al., 2004). On east-facing locations direct solar radiation is low caused by frequently occurring fog until noon (*Cappelen* et al., 2001). After the fog has lifted, the sun stands in the southern sky causing lower direct solar radiation on east-facing locations than on west- and north-west-facing locations. In SISI, SOCS are highest on south-facing locations because of better growing conditions than on north-facing locations. Generally, south-facing locations have a high solar energy input and higher water availability caused by the water discharge from a large catchment area in the north of SISI. These particular natural conditions result in better plant growth and reduced decomposition processes of SOCS on south-facing locations with moist soil conditions.

In RUSS, SOCS on east-facing and west-facing locations are related to katabatic winds constantly blowing from the Greenland Ice Sheet. Therefore, lowest SOCS at 0-25 cm were found on east- and south east-facing locations as biomass production and input of organic matter into the soil is restricted by these winds (*Henkner* et al., 2016). In contrast, west- and northwest facing locations have highest SOCS within 0-25 cm because these leeside locations are favoured by shrub vegetation responsible for high SOCS (*Ozols* and *Broll*, 2003; *Petrenko* et al., 2016). The same reason applies for south and south-west-facing locations with higher SOCS compared to east-facing and north east-facing locations. According to the findings of *Henkner* et al. (2016) in the Umimmalissuaq valley, higher SOCS on north-facing than on south-facing locations result from higher mineralization rates due to higher soil temperatures and lower soil moisture content on south-facing locations. Wind exposed crest positions in the

Umimmalissuaq valley also show lowest topsoil SOCS (6.01 ± 2.49 kg m^{-2}, 0-30 cm) comparable to east- and south-east-facing locations in RUSS (5.17 ± 2.16 kg m^{-2}, 0-25 cm). Also, SOCS on south- and southwest-facing locations, which are less influenced by katabatic winds, are similar between RUSS (8.04 ± 4.20 kg m^{-2}, 0-25 cm) and the Umimmalissuaq valley (8.35 ± 4.16 kg m^{-2}, 0-30 cm; *Henkner* et al. 2016).

North-facing slopes in RUSS have highest SOCS. Differences in SOCS between RUSS and the Umimmalissuaq valley might result from different calculation approaches for SOCS as *Henkner* et al. (2016) did not account for the volume and density of the coarse fraction being important for determining SOCS (*Tarnocai* et al., 2009). The Umimmalissuaq valley and RUSS are both located in valleys with comparable environmental conditions including elevation (about 200 m a.s.l), orientation (south-east to north-west), vegetation (dominant species), distance to the ice margin (< 10 km) and climate conditions (*Cappelen* et al., 2001; *Henkner* et al., 2016). Thus, comparable environmental conditions on a local scale are reflected by similar SOCS at comparable topographic positions in ice marginal areas in West Greenland. In several locations close to the ice margin in RUSS, higher SOCS were found in 25-50 cm because of buried dark and organic-rich horizons potentially representing Holocene palaeosols (cf. *Müller* et al., 2016).

4.2 Regional scale variations in SOCS

On average, SOCS in 0-25 cm and 25-50 cm are similar in both study areas which correspond generally to large scale estimations showing no differences in SOCS between the coastal and the ice margin area. However, SOCS are lower on average and have larger ranges in areas at the coast and at the ice margin than we found

between SISI and RUSS (*Jones* et al., 2009; *Hugelius* et al., 2014; *Köchy* et al., 2015). *Hugelius* et al. (2014) found SOCS with 0.1-5 kg m^{-2} within 0-30 cm, which is lower than the average SOCS in both study areas (SISI: 7.85 ± 7.77 kg m^{-2}; RUSS: 7.86 ± 3.74 kg m^{-2}). The ranges of the SOCS within 0-25 cm in SISI and RUSS are sixfold respectively threefold the range of estimated SOCS within 0-30 cm (*Hugelius* et al., 2014).

On average, SOCS in 50-100 cm and 100-200 cm are 1.60 kg m^{-2} and 4.17 kg m^{-2} higher in SISI than in RUSS (Tab. 4). These differences can be explained by cryoturbation processes which are characteristic at the coast in SISI (*Stäblein*, 1977) but are not present at the ice margin in RUSS in West Greenland (see *Petrenko* et al., 2016). Additionally, higher maximum values of SOCS in all depth increments in SISI compared to RUSS might result from the different landscape ages. Soil formation lasted 3000 years longer and could accumulate more SOM at the coast at Sisimiut compared to the ice marginal areas in West Greenland around Kangerlussuaq (*Bradley-Cook* and *Virginia*, 2016), which was deglaciated around 6.8 ka ago (e.g. *Levy* et al., 2012).

However, differences in SOCS within 0-100 cm and 100-200 cm between SISI and RUSS are in contrast to large scale estimations mentioned above. *Hugelius* et al. (2014) found similar SOCS with 5-15 kg m^{-2} in 0-100 cm and 100-200 cm, whereas *Jones* et al. (2009) suggest SOCS from 0-100 cm with 9-15.9 kg m^{-2} and *Köchy* et al. (2015) with 10 kg m^{-2}. In both study areas, SOCS within 0-100 cm (SISI: 16.87 ± 14.79 kg m^{-2}; RUSS: 15.49 ± 8.75 kg m^{-2}) are slightly higher than estimated by *Jones* et al. (2009) and *Hugelius* et al. (2014) within the first 100 cm and around 30% higher than the results by *Köchy* et al. (2015). In 100-200 cm, the wide range of SOCS in SISI represents the high variation of SOCS in the study area and is with 33.61 kg m^{-2} twice

the estimated range of 5-15 kg m^{-2} (*Hugelius* et al., 2014), which corresponds to the range of SOCS in RUSS (15.33 kg m^{-2}).

Such general estimations of SOCS have a tendency to be uncertain, caused by the underlying datasets containing data gaps, which have to be filled mathematically. Additionally specific soil characteristics may have a high uncertainty, e.g. the bulk density, which is a crucial parameter for the calculation of SOCS (*Tarnocai* et al., 2009; *Hugelius* et al., 2014; *Köchy* et al., 2015; *Ping* et al., 2015). Furthermore, the available data may have been not representative for regions, which counts particularly for Greenland (*Hugelius* et al., 2014; *Köchy* et al. 2015).

The SOCS in SISI and RUSS are higher compared to northern coastal regions in Greenland. At Zackenberg in Northeast Greenland, SOCS from 0 to 50 cm are with 11.00 ± 1.5 kg m^{-2} (*Elberling* et al., 2004) lower than in SISI with 13.18 ± 12.82 kg m^{-2} (0-50 cm). On Thule peninsula in Northwest Greenland, SOCS are 6.10 kg m^{-2} from 0 to 100 cm (*Horwath Burnham* and *Sletten*, 2010) and 6.7 kg m^{-2} from 0 to 60 cm on Disko Island (*Jensen* et al., 2006). Differences in SOCS may be caused by colder climate conditions in the north. Further, it has to be noted other study areas as mentioned above cover also vegetation and landscape patterns with lower SOCS, which do not occur in our study areas. For a better understanding of differences in SOCS between SISI and RUSS on the regional scale, differences in the controlling factors between the coast and the ice margin are pointed out in the following.

4.2.1 Vegetation units

Differences in vegetation between SISI and RUSS correspond to the bioclimatic zonation of the Circumpolar Arctic Vegetation Map indicating a higher net annual

production at the ice margin compared to the coast (*CAVM Team*, 2003). This suggests the possibility of higher SOCS in RUSS than in SISI. However, SOCS are generally around 1.40 kg m^{-2} (0-25 cm) higher within the same vegetation unit (VEG2, VEG3, VEG4) in SISI than in RUSS, except for VEG1 where SOCS are 0.30 kg m^{-2} (0-25 cm) lower in SISI. Oceanic climate suggests better growing conditions in SISI than in RUSS where plant growth is limited by dry climate at the end of the growing season. With increasing mean summer temperatures and decreasing mean annual precipitation from the coast towards the ice margin (*Cappelen* et al., 2001), the decomposition of SOM in Greenland is higher under drier and warmer conditions (*Elberling* et al., 2004; *Jensen* et al., 2006). Higher SOCS in the uppermost 20 cm in coastal areas compared to lower SOCS in inland areas with same vegetation cover are related to the deglaciation history (*Bradley-Cook* and *Virginia*, 2016). In summary, this results in higher SOCS in SISI than in RUSS within the same vegetation unit.

Besides effecting the amount of SOCS in SISI and RUSS in different ways, regional climate conditions also influence the spatial distribution of SOCS within both study areas. There is a significant relation between vegetation and SOCS at 0-25 cm in RUSS but not in SISI. Due to higher mean annual precipitation at the coast, SOC is relocated by overland and interflow processes (*Stäblein*, 1977), whereas only little effect of them is noticeable on the spatial distribution of SOC at the ice margin. Therefore, SOCS are result of the in situ-production and incorporation of organic material into the soil in RUSS.

4.2.2 Landscape units

Corresponding landscape units between both study areas are characterized by the same landscape conditions, but have different SOCS caused by different climate conditions between the coastal and the ice margin area. In general, SOCS at 0-25 cm

are higher in RUSS than in SISI as shrub growth is favoured at wind-sheltered areas leading to high SOCS (LU1, LU3 and LU4) in RUSS. Katabatic winds negatively affect SOCS in LU2 only in RUSS, which results in higher SOCS within 0-25 cm in LU2 in SISI. Induced by higher mean annual precipitation at the coast, SOC is relocated by overland flow resulting in higher SOCS in LU3 in SISI than in RUSS, where overland flow is limited due to the dry climate at the ice margin.

4.2.3 Aspect

In both study areas, SOCS are lowest on east-facing locations as plant growth is negatively affected by the following climate conditions: increased evapotranspiration by katabatic winds in RUSS and reduced direct solar radiation by morning fog in SISI. The leeside areas of terminal or lateral moraines favour the growth of VEG2 and VEG3 in RUSS, west-facing locations in SISI represent locations with restricted plant growth by coastal west winds. Thus, SOCS on west-facing locations are higher in RUSS than in SISI.

4.3 The role of controlling factors to describe the spatial distribution of SOCS in West Greenland

SOCS have a high spatial variation in West Greenland on both the local and the regional scale. The chosen controlling factors differ in their ability to describe the variation in SOCS on both scales in different ways. We ranked the controlling factors by their potential (+++ high; ++ medium; + low) to account for the variation in SOCS (Tab. 5). The ranking is expert-based on comparing the potential of each unit to be unique according to the used classification scheme. A high potential means each unit

represents a specific range of the SOCS distribution within the study areas (local scale) and the ranking is also stable over both study areas (regional scale) (cf. Fig. 3, Fig. 4).

Vegetation units have a great potential to describe both local and regional scale variation in SOCS, because vegetation incorporates to a certain extent local distribution patterns of wind, geomorphology and insolation as well as their differences between the coast and the ice margin on the regional scale. However, topsoil SOCS are similar for VEG2 and VEG4 which results from water driven relocation of SOC in SISI. The negative effect of katabatic winds on SOCS is best described by ASP, which can be explained by the continental climate conditions in RUSS. In addition, vegetation units have distinct differences in SOCS for all depth increments below 25 cm. Therefore, VEG is highly suitable to describe the variation in SOCS (+++) on the local scale. On the regional scale, SOCS have similar distribution patterns for different VEG but differences in the amount of SOCS between SISI and RUSS. This accounts for VEG a high potential to describe the variation in SOCS (+++) on the regional scale as well. In general, landscape and landform classifications are common approaches to address the horizontal and vertical distribution of SOCS (*Palmtag* et al., 2018; *Siewert* et al., 2016; *Wojcik* et al., 2019). Further, such classifications are suitable to represent local patterns like accumulation areas with additional input of SOC (as in SISI) or lower SOCS on convex shaped moraines (as in RUSS). In addition, LUs comprise the influence of local climate conditions in RUSS. However, in this study, LUs have low potential (+) to describe the variation in SOCS on the local scale. Representing comparable geomorphological features between SISI and RUSS, LUs account for the effect of different climate conditions and the variations in SOCS on the regional scale (++) by different amounts of SOCS of the related LU.

ASP performs high with both scales (+++). It represents locally strong differences in solar radiation between north- and south facing and east- and west facing topographic positions. Regionally, ASP describes climate conditions between the coast and the ice margin, i.e. mainly different wind systems. Our results correspond to the findings of other studies using landform classification approaches in Arctic environments (*Elberling* et al., 2008b; *Henkner* et al., 2016; *Siewert* et al., 2016; *Palmtag* et al., 2018; *Wojcik* et al., 2019) and show that both LU and ASP yield additional relevant information to analyse and understand the spatial distribution of SOCS in West Greenland. Both, LU and ASP reflect specific environmental conditions on the local scale within the study areas and on a regional scale differences between the study areas. Most importantly, ASP has a high potential to describe the variations in SOCS on both scales, which is not the case for LUs. Thus, to have the best description of the variations in SOCS, we recommend to use vegetation units and the aspect. Vegetation extracted from remote sensing data provides the advantage to describe the variations in SOCS with a high resolution across large areas. In addition, the aspect can be taken from digital elevation models (DEM) by using various GIS software.

Table 5: Potential of controlling factors to describe the variation in SOCS on the local and the regional scale. (VEG: vegetation, LU: landscape unit, ASP: aspect, +++ high potential, ++ medium potential, + low potential)

	Local scale	Regional scale
VEG	+++	+++
LU	+	++
ASP	+++	+++

5 Conclusions

This study presents new data of SOCS from two different regions of West Greenland, a coastal (SISI, oceanic climate) and an ice marginal (RUSS, continental climate) area. We focused on three controlling factors (VEG, LU, ASP) to describe the variation in SOCS on two different scales (local, regional). The local scale reflects the spatial variation in the controlling factors over short distances within each study area and the regional scale the different climate conditions between both study areas.

On a local scale, VEG and ASP have the highest potential to describe the distribution of SOCS in both study areas. SOCS vary spatially and vertically with different vegetation pattern, landscape units and aspect. In both study areas, SOCS within 0-25 cm are highest with tall shrub tundra (VEG4) and lowest with dwarf shrub heath tundra (VEG1) covering predominantly areas exposed to local wind patterns or areas with a high solar radiation input. Both are limiting plant growth and the accumulation of SOC. Except for VEG1, SOCS are around 1.40 kg m^{-2} higher in SISI than in RUSS due to effect of different climate conditions.

On the regional scale, also VEG and ASP have the highest potential to describe the distribution of SOCS. In both study areas, the mean SOCS are similar from 0-25 cm and 25-50 cm. Due to oceanic climate conditions, cold and moist soil conditions support accumulation of soil organic matter in SISI. In contrast, we assume production and decomposition of soil organic matter to increase due to warmer and drier conditions in RUSS. Mean SOCS within 50-200 cm are up to 53 % higher in SISI than in RUSS. Coastal climate conditions in SISI foster vertical relocation of soil organic carbon by cryoturbation processes, which plays in contrast a minor role to the vertical distribution of SOCS in RUSS. Additionally, a longer period of soil formation at the coast – related to earlier deglaciation of the landscape - results in a wider range of

SOCS being two times higher in all depth increments (0-25, 25-50, 50-100, 100-200 cm) in SISI than in RUSS.

Generally, SOCS are up to six times higher at 0-25 cm, up to 30% higher at 0-100 cm and two times higher in 100-200 cm in both study areas in comparison to existing large scale estimations. This may be caused by sparse and unequal distributed soil data available for large scale estimations resulting in a high uncertainty. However, it should be considered that our study was carried out in two small study areas (around 2 km^2 each) and therefore we propose to add further representative areas for a comprehensive comparison on a larger scale, e.g. West Greenland.

The applied controlling factors VEG, LU, and ASP are suitable to examine horizontal and vertical distribution of SOCS on both the local and the regional scale. Our results show that vegetation in combination with additional environmental factors such as landscape units and aspect better explain the variation in SOCS on both scales. However, we recommend to use at least the aspect together with vegetation, because this yielded excellent results to determine the variation in SOCS in alpine zones as e.g. in West Greenland on both scales.

Supplement material

Figure S1: Section of the study area at the coast in West Greenland (SISI) with view to the north (Photo by L. Kandolf).

Figure S2: Overview of the study area at the ice margin in West Greenland (RUSS) with view to the southeast (Photo by L. Kandolf).

Table S3: Terrain covariates, related influence on SOCS and descriptive statistics (mean ± SD) for each LU for each study area (SISI, RUSS).

Acknowledgements

This study has been realised with financial support by a graduation fellowship from the state of Baden-Wuerttemberg, Germany. The authors would like thank all co-workers for their help with the field campaign and the laboratory analyses. We would like to thank Kangerlussuaq International Science Support (KISS) for assistance during our field campaign.

References

Beven, K. J., Kirkby, M. J. (1979): A physically based, variable contributing area model of basin hydrology. *Hydrol. Sci. B.* 24, 43-69.

Bliss, L. C. (2000): Arctic tundra and polar desert biome, in *Barbour, M. G.* (ed.): North American terrestrial vegetation. Cambridge University Press, Cambridge, pp. 1–40.

Bock, M., Böhner, J., Conrad, O., Köthe, R., Ringeler, A. (2007): XV. Methods for creating Functional Soil Database and applying Digital Soil Mapping to SAGA GIS, in *Hengl*, T. et al. (eds.): Status and prospect of soil information in south-eastern Europe: soil databases, projects and applications. EUR 22646 EN Scientific and Technical Research series, Office for Official Publications of the European Communities, Luxemburg, p.149-162.

Bockheim, J. G. (2007): Importance of Cryoturbation in Redistributing Organic Carbon in Permafrost-Affected Soils. *Soil. Sci. Soc. Am. J*. 71, 1335-1342.

Bradley-Cook, J. I., Virginia, R. A. (2016): Soil carbon storage, 548 respiration potential, and organic matter quality across an age and climate gradient in southwestern Greenland. *Polar. Biol.* 39, 1283-1295.

Bradley-Cook, J. I., Petrenko, C. L., Friedland, A. J., Virginia, R. A. (2016): Temperature sensitivity of mineral soil carbon decomposition in shrub and graminoid tundra, west Greenland. Clim. Chang. Responses 3, 1-15.

Burrough, P. A., van Gaans, P. F. M., MacMillan, R.A. (2000): High-resolution landform classification using fuzzy k-means. Fuzzy Set. Syst. 113, 37-52.

Cappelen, J., Jørgensen, B. V., Laursen, E. V., Stannius, L. S., Thomsen, R. S. (2001): The observed climate of Greenland, 1958–99 - with climatological standard normals, 1961–90. Technical Report 00–18. Danish Meteorological Institute Ministry of Transport and Energy, Copenhagen.

Carrivick, J. L., Smith, M. W., Quincey, D. J. (2016). *Structure from Motion in the Geosciences*. Wiley-Blackwell.

Carstensen, L. S., Jørgensen, B. V. (2009): Weather and climate data from Greenland 1958–2008: dataset available for research and educational purposes. Descriptions and documentation of observations of temperature, precipitation, wind, could cover, air pressure, humidity and depth of snow. Technical Report 09–11. Danish Meteorological Institute Ministry of Transport and Energy, Copenhagen.

Chadburn, S. E, Burke, E. J., Cox, P. M., Friedlingstein, P., Hugelius, G. and Westermann, S. (2017): An observation-based constraint on permafrost loss as a function of global warming. *Nat. Clim. Change* 7, 340–344.

CAVM Team (2003): Circum Arctic Vegetation Map. (1:7,500,000 scale), Conservation of Arctic Flora and Fauna (CAFF) Map No. 1. U.S. Fish and Wildlife Service, Anchorage, Alaska.

Elberling, B., Nordstroem, C., Groendahl, L., Soegaard, H., Friborg, T., Christensen, T. R., Stroem, L., Marchand, F., Nijs, I. (2008a): High-arctic soil CO2 and CH4

production controlled by temperature, water, freezing and snow, in: Meltofte, H. (ed.), High-Arctic Ecosystem Dynamics in a Changing, Vol. 40. *Advances in ecological research*, Elsevier, Amsterdam, Heidelberg, pp. 441–472.

Elberling, B., Tamstorf, M. P., Michelsen, A., Arndal, M. F., Sigsgaard, C., Illeris, L., Bay, C., Hansen, B. U., Christensen, T. R., Hansen, E. S., Jakobsen, B. H., Beyens, L. (2008b): Soil and plant community-characteristics and dynamics at Zackenberg, in: *Meltofte, H.* (ed.), High-Arctic Ecosystem Dynamics in a Changing, Vol. 40. *Advances in ecological research*, Elsevier, Amsterdam, Heidelberg, pp. 223–248.

Elberling, B., Jakobsen, B. H., Berg, P., Sondergaar, J., Sigsgaard, C. (2004): Influence of vegetation, temperature, and water content on soil carbon distribution and mineralization in four high Arctic soils. *Arct. Antarct. Alp. Res*. 36, 528–538.

Environmental Systems Research Institute (ESRI), (2014): ArcGIS Desktop 10.3 Data Management Toolbox, Create Random Points tool.

Everitt, B. S. (1980): Cluster Analysis. Wiley, New York.

Freeman, G. T. (1991): Calculating catchment area with divergent flow based on a regular grid. *Comput. Geosci*. 17, 413-422.

Friedrich, K. (1996): Digitale Reliefgliederungsverfahren zur Ableitung bodenkundlich relevanter Flächeneinheiten. *Frankfurter Geowissenschaftliche Arbeiten*, 21.

Guisan, A., Weiss, S. B., Weiss, A. D. (1999): GLM versus CCA spatial modeling of plant species distribution. *Plant Ecol.* 143, 107-122.

Henkner, J., Scholten, T., Kühn, P. (2016): Soil organic carbon stocks in permafrost-affected soils in West Greenland. *Geoderma* 282, 147-159.

Henriksen, N. (2008): Geological History of Greenland: Four billion Years of Earth Evolution. Geological Survey of Denmark and Greenland, Copenhagen.

Horwath Burnham, J.L., Sletten, R.S. (2010): Spatial distribution of soil organic carbon in northwest Greenland and underestimates of High Arctic carbon stores. *Global Biochemical Cycles* 24.

Hugelius, G., Strauss, J., Zubryzycki, S., Harden, J., Schuur, E., Ping, C., Schirrmeister, L., Grosse, G., Michaelson, G., Koven, C., O'Donnell, J., Elberling, B., Mishra, U., Camill, P., Yu, Z., Palmtag, J., Kuhry, P. (2014): Estimated stocks of circumpolar permafrost carbon with quantified uncertainty ranges and identified data gaps. *Biogeosciences* 11, 6573-6593.

Hugelius, G., Tarnocai, C., Broll, G., Candell, J.G., Kuhry, P., Swanson, D.K. (2013): The Northern Circumpolar Soil Carbon Database: spatially distributed datasets of soil coverage and soil carbon storage in the northern permafrost regions. Earth Syst. Sci. Data 5, 3-13.

IPCC, International Panel on Climate Change (2019): IPCC Special Report on the Ocean and Cryosphere in a Changing Climate. In press.

Iversen, C. M., Sloan, V. L., Sullivan, P. F., Euskirchen, E. S., McGuire, A. D., Norby, R. J., Walker, A. P., Warren, J. M. & Wullschleger, S. D. (2015): The unseen iceberg: plant roots in arctic tundra. New Phytol. 205, 34–58.

Jensen, L., Hollesen, J., Elberling, B. (2006): Accumulation of Soil Organic Carbon Linked to Holocene Sea Level Changes in West Greenland. *Arct. Antarct. Alp. Res.* 38, 378-383.

Jones, A., Stolbovoy, V., Tarnocai, C., Broll, G., Spaargaren, 599 O., Montanarella, L. (2009): Soil Atlas of the Northern Circumpolar Region, Luxembourg.

Köchy, M., Hiederer, R., Freibauer, A. (2015): Global distribution of soil organic carbon – Part1: Masses and frequency distributions of SOC stocks for the tropics, permafrost regions, wetlands, and the world. *Soil* 1, 351-365.

Kühn, P., Henkner, J., (2019). Permafrost-affected Soils, Climate, and Feedbacks in West Greenland, in: *Lal, R., Stewart, B. A. (eds.).* Soil and Climate. *Advances in Soil Science*, CRC Press, pp. 92-97.

Levy, L. B., Kelly, M. A., Howley, J. A., Virginia, R. A. (2012): Age of the Ørkendalen moraines, Kangerlussuaq, Greenland: constraints on the extent of the southwestern margin of the Greenland Ice Sheet during the Holocene. *Quaternary Sci. Rev.* 52, 1-5.

Moore, I. D., Grayson, R. B., Ladson, A. R. (1991): Digital terrain modelling: a review of hydrological, geomorphological, and biological applications. *Hydrol. Process.* 5, 3-30.

Müller, M., Thiel, C., Kühn, P. (2016): Holocene palaeosols and aeolian activities in the Umimmalissuaq valley, West Greenland. *The Holocene* 26, 1149–1161.

OpenStreetMap contributors (2015): https://planet.osm.org/historical-shapefiles/shoreline_300.tar.bz2 (Last access 14.11.2019)

Ozols, U., Broll, G. (2003): Soil ecological processes in vegetation patches of well drained permafrost affected sites (Kangerlussuaq - West Greenland). *Polarforschung* 73, 5–14.

Palmtag, J., Cable, S., Christiansen, H. H., Hugelius, G., Kuhry, P. (2018): Landform partitioning and estimates of deep storage of soil organic matter in Zackenberg, Greenland. *The Cryosphere* 12, 1735-1744.

Palmtag, J., Hugelius, G., Lashchinskiy, N., Tamstorf, M. P., Richter, A., Elberling, B., Kuhry, P. (2015): Storage, Landscape Distribution, and Burial History of Soil Organic Matter in Contrasting Areas of Continuous Permafrost. *Arct. Antarct. Alp. Res.* 47:1, 71-88.

Petrenko, C. L., Bradley-Cook, J. I., Lacroix, E. M., Friedland, A. J., Virginia, R.A. (2016): Comparison of carbon and nitrogen storage in mineral soils of graminoid and shrub tundra sites, western Greenland. *Arctic Sci.* 2, 165-182.

Ping, C. L., Jastrow, J. D., Jorgenson, M. T., Michaelson, G. J., Shur, Y. L. (2015): Permafrost soils and the carbon cycling. *SOIL* 1, 147-171.

Ping, C. L., Bockheim, J. G., Kimble, J. M., Michaelson, G. J., Walker, D. A. (1998): Characteristics of cryogenic soils along a latitudinal transect in arctic Alaska. *J. Geophys. Res.* 103, 917-928.

Porter, C., Morin, P., Howat, I., Noh, M.-J., Bates, B., Peterman, K., Keesey, S., Schlenk, M., Gardiner, J., Tomko, K., Willis, M., Kelleher, C., Cloutier, M., Husby, E., Foga, S., Nakamura, H., Platson, M., Wethington, M., Williamson, C., Bauer, G., Enos, J., Arnold, G., Kramer, W., Becker, P., Doshi, A., D'Souza, C., Cummens, P., Laurier, F., Bojesen, M. (2018): ArcticDEM, https://doi.org/10.7910/DVN/OHHUKH, Harvard Dataverse, V1.

Post, W. M., Emanuel, W. R., Zinke, P. J., Stangenberger, A. G. (1982): Soil carbon pools and world life zones. *Nature* 298, 156-159.

R Development Core Team (2013): R: A Language and Environment for Statistical Computing.

Rothenhöfer, P., Huber, A., Kainzmaier B., Wohnlich, S., Pfeiffer, S. (2000): Ein Vergleich von vier Methoden zur Bestimmung des Karbonatgehaltes. *Wasser und Boden* 52, 37-42.

*Schmidt, K., Behrens, T., Scholten, T. (*2009): A method to generate soilscapes from soil maps. *J. Plant Nutr. Soil Sc.* 173, 163-172.

Stäblein, G. (1977). Arktische Böden Westgrönlands: Pedovarianz in Abhängigkeit vom geoökologischen Milieu. *Polarforschung* 47, 11-25.

Scholten, T., Goebes, P., Kühn, P., Seitz, S., Assmann, T., Bauhus, J., Bruelheide, H., Buscot, F., Erfmeier, A., Fischer, M., Härdtle, W., He, J.-S., Ma, K., Niklaus, P. A., Scherer-Lorenzen, M., Schmid, B., Shi, X., Song, Z., von Oheimb, G., Wirth, C., Wubert, T., Schmidt, K. (2017): On the combined effect of soil fertility and topography on tree growth in subtropical forest ecosystems – a study from SE China. *Plant Ecol 10*, 111-127.

Schuur, E. A., McGuire, D. A., Schädel, C., Grosse, G., Harden, J. W, Hayes, D. J., Hugelius, G., Koven, C. D., Kuhry, P., Lawrence, D. M., Natali, S. M., Olefeldt, D., Romanovsky, E. V., Schaefer, K., Turetsky, M. R., Treat., C. C., Vonk, J. E. (2015): Climate change and the permafrost feedback. *Nature* 520, 171-179.

Siewert, M. B., Hugelius, G., Heim, B., Faucherre, S. (2016): Landscape controls and vertical variability of soil organic carbon storage in permafrost-affected soils of the Lena River Delta. *Catena* 147, 725-741.

Siewert, M. B., Hanisch, J., Weiss, N., Kuhry, P., Maximov, T. C., Hugelius, G. (2015): Comparing carbon storage of Siberian tundra and taiga permafrost ecosystems at very high spatial resolution. *J. Geophys. Res. Biogeosci.* 120, 1973-1994.

Tarnocai, C., Canadell, J. G., Schuur, E. A. G., Kuhry, P., Mazhitova, G., Zimov, S. A. (2009): Soil organic carbon pools in the northern circumpolar permafrost region. *Glob. Biogeochem. Cy.* 23, 1-11.

Van Tatenhove, F. G. M., Olesen, O. B. (1994): Ground Temperature and Related Permafrost Characterictics in West Greenland. *Permafrost Periglac.* 5, 199-215.

Webster, R., Beckett, P. H. T (1968): Quality and Usefulness of Soil Maps. *Nature* 219, 680-682.

Willemse, N. W., Koster, E. A., Hoogakker, B., Van Tatenhove, F. G. (2003): A continuous record of Holocene eolian activity in West Greenland. *Quaternary Res.* 59, 322–334.

Wojcik, R., Palmtag, J., Hugelius, G., Weiss, N., Kuhry, P. (2019): Land cover and landform-based upscaling of soil organic carbon stocks on the Brøgger Peninsula, Svalbard. *Arct. Antarct. Alp. Res.* 51:1, 40-57.

Wu, C. (2011): VisualSFM: a visual structure from motion system. http://ccwu.me/vsfm/

Wu, C., Agarwal, S., Curless, B., Seitz, S. M. (2011): Multicore bundle adjustment. CVPR.

Zevenbergern, L. W., Thorne, C. R. (1987): Quantitative analysis of land surface topography. *Earth Surf. Proc. Land.* 12, 47-56.

Manuscript 2: Feature construction and machine learning for the spatial analysis of soil organic carbon stocks in West Greenland

Authors: Philipp Gries[1,2], Peter Kühn[1,2], Thomas Scholten[1,2], Karsten Schmidt[1,2,3]

[1] Department of Geosciences, Chair of Soil Science and Geomorphology, University of Tübingen, 72070 Tübingen, Germany

[2] SFB 1070 ResourceCultures, University of Tübingen, 72070 Tübingen, Germany

[3] eScience Center, University of Tübingen, 72070 Tübingen, Germany

Key words: contextual spatial modelling, Euclidean distance fields, multi-scale terrain features

Abstract

Soils of the northern circumpolar region are a key organic carbon storage strained by global warming. Thawing of permafrost-affected soils increases greenhouse-gas emissions whose quantification is limited by sparse, uncertain and spatially diverse soil organic carbon stocks (SOCS) data across this region. The spatial distribution of SOCS results from interactions and feedbacks of environmental factors and processes varying across scales. Recent developments in machine learning allow to entangle effects of multiple scales in soil data using contextual feature construction techniques.

The objective of this study is to identify dominant spatial scales and process interactions relevant to the spatial interpretation of SOCS in periglacial landscapes of Arctic low mountains using contextual spatial modelling. This study includes SOCS data from 140 sampling locations from two study areas (coast and ice margin) in West

Greenland and a set of multi-scale terrain features reflecting soil forming factors and relocation processes. Random forest models were applied to account for scale-dependent effects within the data set.

Variation in model accuracy across different scales shows that the distribution of SOCS in both study areas is scale-dependent. Aspect and curvature are key terrain features to interpret the distribution of SOCS. On a the hill scale, both represent the heterogeneous periglacial landscape with different site conditions (microclimate) and relocation processes (solifluction), both of which influence SOCS. On the catchment scale, the aspect reflects the effects of different climatic conditions on SOCS, such as dry katabatic winds at the ice margin and moist onshore winds at the coast. Such processes act over long distances and have a generalised effect on the SOCS distribution. Such spatial trends in SOCS are additionally respected by spatial features showing higher feature importance at the coast than at the ice margin. Differences in the importance of spatial and terrain features as well as different relevant scales between the coast and the ice margin confirms the regional variation in soil-landscape interrelations which has to be considered for large scale estimations of the SOCS.

1 Introduction

Globally, the pedosphere contains up to 3000 Pg carbon (Köchy et al., 2015) which corresponds to twice the amount of carbon stored in the atmosphere and the biosphere together (Lal 2004). In the northern circumpolar region, organic soils (peatlands) and permafrost-affected mineral soils store about 1300 Pg soil organic carbon (SOC) (Tarnocai et al., 2009) of which 217 Pg SOC is within 0-30 cm and 472 Pg within 0-100 cm (Hugelius et al., 2013; 2014). This huge amount of organic carbon stored in

permafrost and permafrost-affected soils has been of growing concern in the recent decade because permafrost is expected to considerably degrade under almost all global warming scenarios (IPCC, 2019; Chadburn et al. 2017). Yet, the ability to quantify potential greenhouse-gas release from thawing permafrost is limited, among other, by the uncertainty in distribution and vulnerability of the permafrost SOC stocks (SOCS) in undersampled areas of the northern circumpolar region (Mishra et al. 2013; Hugelius et al. 2014).

Along with undersampling, SOCS in permafrost-affected soils in Arctic environments have a very high spatial diversity. Interactions and feedbacks between environmental factors on SOCS are highly scale-dependent in periglacial landscapes of Arctic low mountain ranges (Ping et al., 2015; Gries et al. 2020), which contain a great variety of sediments, soils, paleosols and complex forms such as sand dunes and terminal moraines (e.g. Ping et al. 1998, Palmtag et al. 2015, Siewert et al. 2015, Müller et al. 2016), and have strong local and regional climate gradients related to topography and distance from the ice margin (Bradley-Cook and Virginia, 2016). Typical and important processes that control SOCS in Arctic environments like freezing and thawing, reduction and oxidation, aeolian transport, and drainage depend on the spatial scale (Wojcik et al., 2019, Gries et al., 2020). Geomorphological units such as slopes and valleys are often decisive for certain processes. Ramage et al. (2019) reported strong variations in SOCS along hillslopes on Herschel Island with high SOCS on summits and toeslope positions due to cryoturbation or impeded drainage and low SOCS on backslopes and footslopes. Henkner et al. (2016) showed that SOCS vary with the aspect that indirectly affects the microclimate resulting in higher amount of SOC on north-facing slopes than on south-facing slopes in a valley in West Greenland. In consequence, the spatial pattern of SOC distribution is related to different

environmental scales. Examples from West Greenland show that the controlling processes interact different on small, i.e. along a catena, towards larger scales, i.e. between regions (e.g. Stäblein, 1977; Ozols and Broll, 2003; Henkner et al., 2016 Petrenko et al., 2016). Nevertheless, there is still a deficiency of reliable scale-dependent information on the distribution of SOCSs and on how different scales are interlinked.

Recent developments in machine learning (ML) allow to entangle effects of multiple scales in soil data (e.g. Behrens ret al. 2014). Scale-related contextual feature construction and pattern recognition techniques can detect multiscale sources and interactions of spatial variation in soil (Burrough 1983), for example the ConMap approach (Behrens et al. 2010), the analysis of teleconnections (Behrens et al. 2019), modelling with an effective scale space calculated from the variogram of soil properties (Karl and Maurer 2010, Behrens et al. 2019), Euclidian distance fields (Behrens et al. 2018) and wavelet transformation (Biswas et al. 2013). To additionally address spatial scale-related processes of soil formation that vary over scale, feature selection and construction techniques are able to distinguish between scales of soil information and can provide a set of multi-scale environmental features, for example hyper-scale digital soil mapping (Behrens et al. 2009, 2014), Gaussian scale space (Behrens et al. 2018) or generating soilscapes (Schmidt et al. 2010). Regarding SOC, ML techniques have been successfully used to provide reliable estimates of SOC in different environments (Grimm et al., 2008; Mishra and Riley, 2012; Schmidt et al., 2014; Stumpf et al., 2018; Rentschler et al., 2019; Viscarra Rossel et al., 2019; Taghizadeh-Mehrjardi et al., 2020). Additionally, Behrens et al. (2019) illustrated a positive effect on the modelling accuracy by deriving the relevant range of scales which improved the understanding of the spatial distribution of loess deposits in a periglacially shaped landscape. A robust

ML technique that has been used frequently in soil science is random forest (RF, Breiman 2001). An important advantage of RF is the measurement of the importance of environmental features which allows an expert-based interpretation of the model in a pedological context. Thus, ML techniques can contribute to a better understanding of spatial scale-related processes of soil formation and the environmental factors controlling them in general, but also at local and regional level in Arctic low mountain ranges with limited soil information, as in Greenland.

In this study, we aim (1) to analyse environmental scale effects and interactions on the variation and estimation of SOCS in permafrost-affected soils for two study areas in West Greenland using contextual spatial ML. We further aim (2) to identify dominant spatial scales and process interactions relevant for the interpretation of the spatial variation of SOCS. This can help to better understand how relevant soil formation processes changed over spatial scales and respond to environmental factors. To analyse the effect of different scale interactions, we combined multi-scale terrain analysis with spatial feature construction using contextual spatial modelling (CSM) method and Euclidean distance fields (EDF).

2 Data and methods

2.1 Study areas

The study is located in West Greenland (Fig. 1) and comprises two study areas with different climate conditions at the coast (SISI) and the ice margin (RUSS). SISI (4 km east of Sisimiut, 66° 57 N, 53° 33’ W, 1.5 km²) has oceanic climate conditions with a mean annual temperature (MAT) of -3.5 °C and a mean annual precipitation (MAP) of 383 mm (Cappelen et al., 2001; Carstensen and Jørgensen, 2009). RUSS (2 km west of the Russell Glacier at the margin of the Greenland Ice Sheet, 67° 6’ N, 50° 17’ W,

1.8 km²) is characterized by Arctic continental climatic conditions with MAT of -5.7 °C and MAP of 149 mm) and katabatic winds mainly blowing from the east (*Cappelen* et al., 2001; *Carstensen* and *Jørgensen*, 2009). Both study areas are part of east-west oriented valleys bordered by steep valley slopes. SISI is bordered to the west by a lake and to the east by a small river that crosses the study area from northeast to southwest. The landscape consists of flat areas and depressions in gentle transition to moraines and slightly inclined slopes. In RUSS, terminal moraines cross the valley from north to south and lakes define the boundaries to the east and west (Gries et al., 2020). The vegetation in both study areas is defined as mountain vegetation on non-carbonate bedrock which consists mostly of granite in SISI and gneiss in RUSS (*CAVM Team*, 2003; *Henriksen,* 2008). Since the last deglaciation, the land surface of West Greenland has been reshaped by periglacial processes (*Stäblein*, 1977; *Willemse* et al., 2003; *Müller* et al., 2016). Soil formation began after deglaciation about 10,000 years ago in SISI and 6,800 years ago in RUSS (c.f. *Bradley-Cook* and *Virginia*, 2016). Acid haplic Cambisols and Cryosols are the dominant Reference Soil Groups after WRB (*Jones* et al., 2009; *Kühn* and *Henkner*, 2019).

2.2 Soil data

The soil data consist of SOCS for 0-25 cm from 74 sampling locations in SISI and 66 in RUSS (Fig. 1), which were sampled in 2016 (Gries et al., 2020). The sampling locations were selected by k-means cluster analysis of an environmental dataset consisting of local, regional and combined terrain features relevant for SOC distribution (for details see Gries et al., 2020). Samples for SOC [%] were dried (40 °C), sieved (< 2 mm) and analysed using an element analyser (Vario EL II, Elementar Analysesysteme GmbH, Germany, in CN mode). Samples for bulk density BD [kg cm^{-3}]

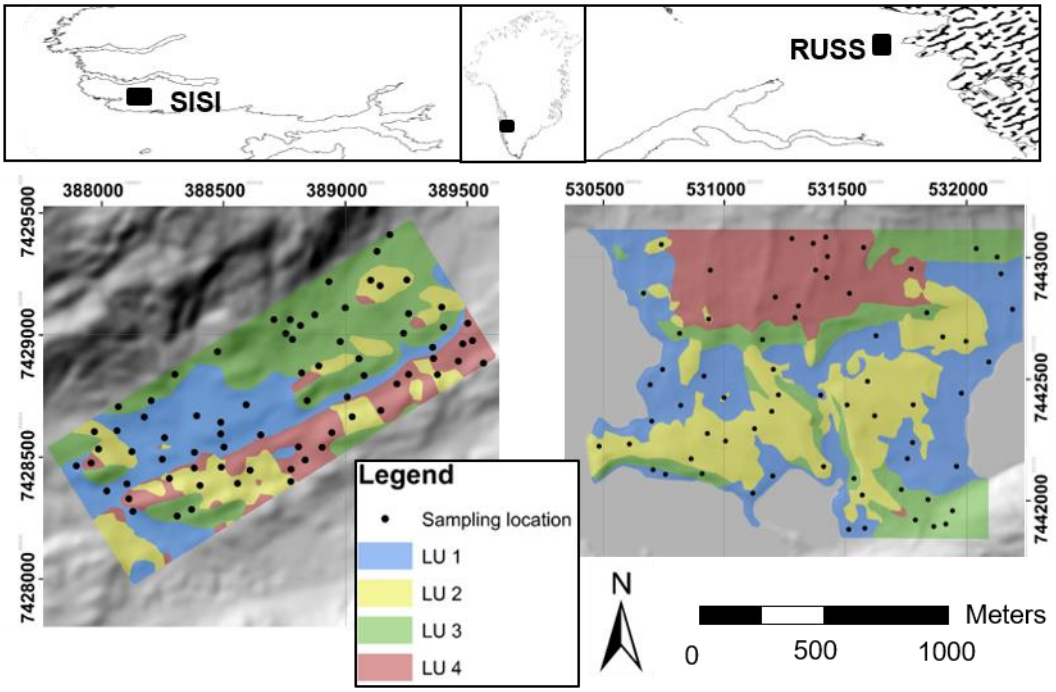

Figure 1: Stratified random sampling design based on four landscape units with comparable environmental conditions between the coastal study area SISI and RUSS located at the margin of the Greenland Ice Sheet in West Greenland. (Overview map: © openstreetmap contributers; Hillshade: ArcticDEM, Porter et al., 2018).

were dried at 105 °C and corrected for the coarse fraction (CF, > 2mm, [%]). SOCS were calculated according to Eq. 1, where D is the thickness of the sampled depth increment (0-25 cm).

$$SOCS = SOC \bullet BD \bullet D \bullet (1 - CF). \text{ (Eq. 1)} \quad [1]$$

2.3 Multi-scale terrain and spatial feature construction

We applied contextual spatial modelling as a multi-scale hierarchical mapping approach which enables a multi-scale analysis of soil formation processes (Behrens et

al., 2018a). It combines two domains, multi-scale terrain feature construction and spatial feature construction. Terrain features were constructed with a Gaussian pyramid as hierarchical multiscale representation of a digital elevation model (DEM). Smoothing and scaling steps (Burt and Adelson, 1983) have been used to stepwise reduce the resolution of the original DEM by half until no further scales are possible. The resulting sequence cover all possible scales based on the original resolution of the DEM. To avoid any artefacts by combining gridded datasets of different cell sizes we upsampled any gridded dataset within the sequence to the original resolution based on the Gaussian filter approach as described in Behrens et al (2018a). We calculated elevation (Elev), steepest slope downslope (Slope), sine and cosine transformation of the aspect (sinAsp, cosAsp), average curvature (AvCurv), cross-sectional curvature (CrCurv) and longitudinal curvature (LoCurv) based on the algorithms by Zevenbergen and Thorne (1987).

Euclidean distance fields (EDF, Behrens et al., 2018b) are representing the distance to the edges (X1, Y1), corners (C1, C2, C3, C4) and the center (CC) of an artificial grid bordering the study areas and were applied to detect spatial non-linear relationships within the modelling framework. As such, EDFs are a set of auto-correlated indicators of the relative spatial position within the study area. These spatial features are grids with the same resolution as the terrain features where each pixel contains its Euclidean distance to the respective position. Based on distance measurements to different reference points, these features allowed to include spatially varying trends within the soil sample set into a spatial modelling approach and to consider spatial non-stationarity (Behrens et al. 2018b). They are only valid for a specific study area and can increase the local understanding of soil formation by incorporating distance measurement into contextual models.

Environmental scales

Multi-scale spatial features were constructed for 22 scales from the upsampled sequence of DEM representations computed for the Gaussian pyramid. The scales were class-divided into three environmental scales calculated with the maximum horizontal distance between key geomorphological elements of the periglacial landscape and the pixel size of the DEMs of the Gaussian pyramid. All DEMs whose pixel size is smaller or similar to the maximum horizontal distance of each scale are grouped into the three following environmental scales (Fig. 2):

- The moraine scale represents surface heterogeneity of the study area given by small-sized geomorphic elements like moraines and small hills. It includes the scales 1-10 with pixel sizes ranging from 2 x 2 m to 48 x 48 m corresponding to the maximum horizontal difference of 54 m between ridge and footslope of moraines and small hills. This scale addresses freeze-thaw processes like solifluction affecting the relocation of soil material along small-size geomorphologic elements.
- The valley scale represents the shape of the valleys and covers the potential of downslope processes relocating soil components from the valley slopes into the study areas, for example hillwash or interflow. It comprises scales 11-14 with pixel sizes between 64 x 64 m and 192x192 m which corresponds to the maximum horizontal distance of 145 m representing sections of the valley slopes in both study areas where relocations processes take place.
- The catchment scale addresses teleconnected processes over long distances, for example aeolian transport of silt particles or dominant weather direction influencing the water amount. This class contains the scales 15-22 with pixel sizes between 256 x 256 m and 3072 x 3072 m.

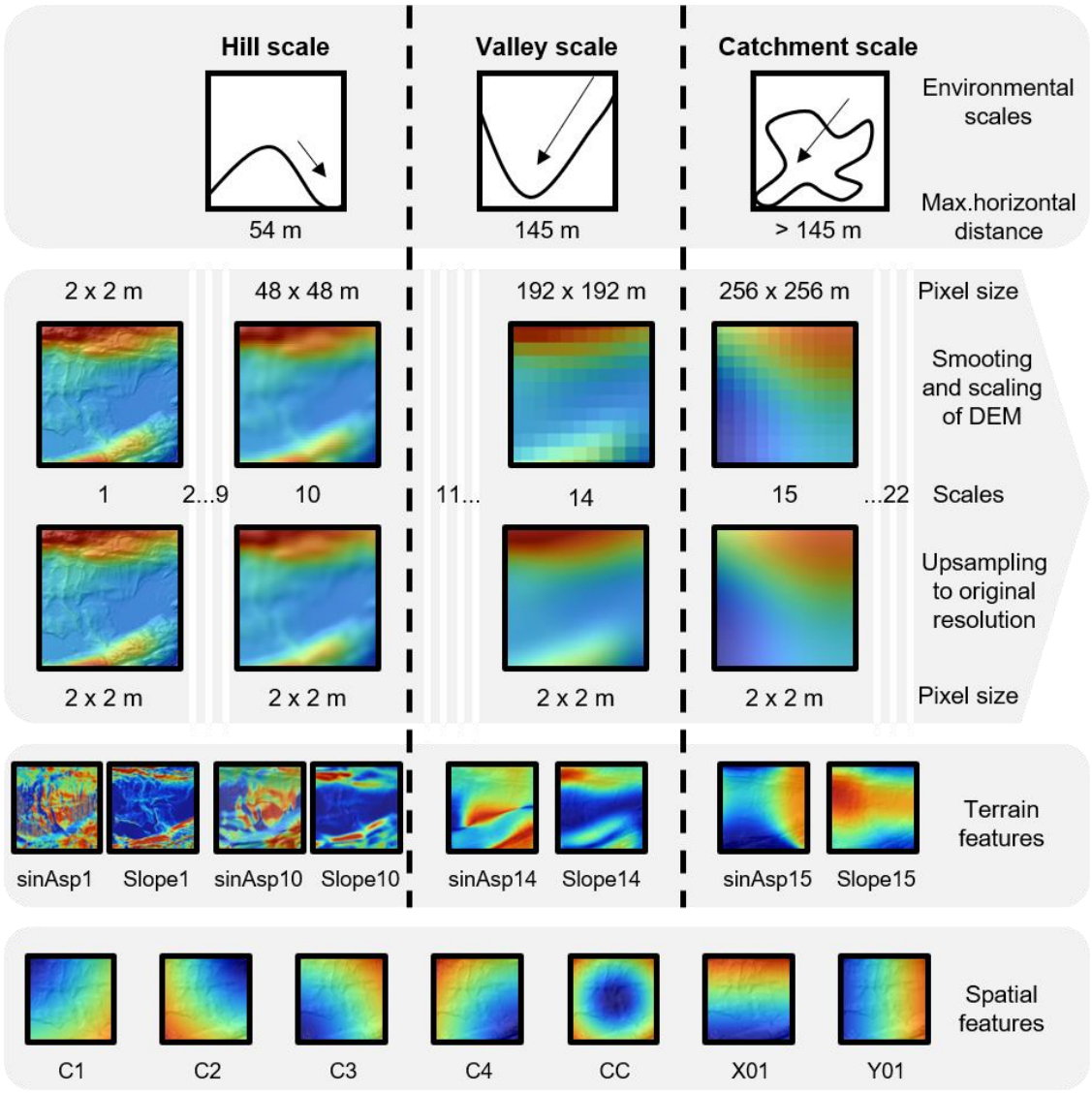

Figure 2: Environmental scales and feature construction. Definition of the moraine, valley and catchment scale according to the maximum horizontal distance of key geomorphological elements and corresponding pixel sizes of DEMs which result from sequenced smoothing and scaling steps. After resampling all DEMs to the original resolution (2 x 2 m), terrain features are delineated at overall 22 scales. Due to the smoothing and scaling and resampling steps, the representation of the landscape by the terrain features has changed which is exemplified by the sine of the aspect (sinAsp) and steepest slope downslope (Slope) at first and last scale of the moraine scale (1, 10), the last of the valley scale (14) and the first of the catchment scale (15) to demonstrate the trend in the delineation of the landscape at the respective environmental scale. The spatial features include the Euclidean distance fields (EDF) representing the distance to the upper left (C1), upper right (C2), lower left (C3) and lower right corner (C4), the centre (CC), the lower (X01) and left edge (Y01) of an artificial grid around the study area.

2.4 Analysis of feature importance and scales

Random forests (RF, Breiman, 2001) is a widely used ML technique in pedometrics for the spatial estimation of soil characteristics by extracting their relationships to given environmental features. RF is a combination of numerous Classification and Regression Trees (CART; Breiman, 1984). Each CART is built on a randomly chosen samples of the training data. The samples were drawn with replacement, known as bootstrapping, which means that some samples were used multiple times in a single tree and some were left out. The part of the training data left out is used to validate the particular CART model. In addition, for each split a random set of features is used. The consideration of these random effects made this approach robust against outliers and improved model accuracy. We used the "caret" package (Kuhn, 2017) in R (R Development Core Team, 2017) for grid learning (cf. Schmidt et al., 2008) to determine the optimal number of features at each split (*mtry*). Ten times 10-fold cross-validation was applied to calculate the accuracy of the RF models expressed by the coefficient of determination (R^2, equation [2]) and the normalized root mean square error (nRMSE, equation [3]):

$$R^2 = \left(\frac{\sum_{i=1}^{n}(y-\mu_y)(\hat{y}-\mu_{\hat{y}})}{\sqrt{\sum_{i=1}^{n}(y-\mu_y)^2}\sqrt{\sum_{i=1}^{n}(\hat{y}-\mu_{\hat{y}})^2}}\right)^2 \quad [2]$$

$$nRMSE = \sqrt{\frac{1}{n}\sum_{i=1}^{n}(y_i-\hat{y}_i)^2}\,/\,(y_{max}-y_{min}) \quad [3]$$

with y and $\hat{y}$ as the observed and predicted values and μ_y and $\mu_{\hat{y}}$ as the means of the observed and predicted values. An advantage of RF is a build-in measure of feature or feature importance by calculating the mean decrease in accuracy. The general simple and attractive idea behind the feature importance measure is to permute the values of each feature and measure how much the permutation decreases the

accuracy of the model. Clearly, for unimportant features, the permutation should have little to no effect on model accuracy, while permuting important variables should significantly decrease it. We applied RF and the feature importance measurement in different setups to address and identify important scales and spatial dependencies on the distribution of SOCS within each study area separately as well as for regional spatial dependencies in West Greenland independently from the specific study area.

To achieve this, we sequenced RF modelling to account for scale-dependent effects on the spatial distribution of SOCS in the study areas and the corresponding feature importance. The first RF model used the terrain features from the first out of 22 scales only. The next RF model was extended by the terrain features of the subsequent scale, and so on. This ascending approach was applied to determine the effect of small scales first and omit superimposition. The procedure was repeated in reverse order, where the first model used the largest scale only. This descending approach was used to analyse the importance of large scales. Both approaches are applied for both SISI and RUSS separately. The area-specific approach is a RF model based on all multi-scale terrain features to predict the area-specific SOCS distribution in SISI ($SISI_{area\text{-}specific}$) and RUSS ($RUSS_{area\text{-}specific}$) respectively.

To account for spatial dependencies within each study area, we applied the spatial approach: a RF model based on all multi-scale terrain features and the spatial features for SISI and RUSS ($SISI_{spatial}$/$RUSS_{spatial}$). The comparison of the importance of terrain and spatial features indicates for potential spatial trends within the soil data sets not being covered by the terrain features. Both models were used to estimate SOCS for SISI and RUSS separately.

To account for regional dependencies and transferability the combined approach and crosswise approach are applied. With the crosswise approach, we trained RF models

crosswise for SISI and RUSS using all multi-scale terrain features ($SISI_{crosswise}$/$RUSS_{crosswise}$) and model the SOCS for SISI with the RF model build for RUSS and vice-versa to examine the role of different environmental conditions. In addition, one RF model was trained to a unified data set including soil data sets from both SISI and RUSS and all multi-scale terrain features and to the above described ascending and descending approach. This combined approach was designed to determine the effect of small and large scales on the SOCS distribution in West Greenland from the ice margin to the coast.

3 Results

3.1 Scale dependencies

The multi-scale spatial feature analyses show distinct variation in the accuracy of the ascending and descending RF models for SISI and RUSS (Fig. 3). In SISI, the model accuracy quantified by the proportion of the variation in the data that is explained by the RF model as R^2 is more or less constant over all scales with a mean of 0.20. In RUSS, R^2 decreases over scale with high values at the moraine scale and distinctly lower values at the valley and catchment scale for the descending RF modelling chain. For the moraine, valley and catchment scale of the ascending RF model chain, R^2 values are much higher for RUSS than for SISI. Representing the accuracy by the difference between the measured and predicted values in dependence to the range of the measured values, the nRSME shows the same overall picture independent from the modelling direction, with an almost constant magnitude of average error of the RF models ranging from 0.25 to 0.27 in SISI and from 0.19 to 0.26 in RUSS. The mean nRMSE of the ascending and descending approach is with 0.26 (SISI) and 0.21 (RUSS) the lowest in the moraine scale. The highest variation of the model accuracy

between single scales can be observed in the moraine scale for SISI and in the valley and catchment scale for RUSS. This is also shown by the confidence interval. Interestingly, although differences occur for single scales, this general trend holds true for the ascending and descending modelling approach. Differences between the two approaches are clearly visible for RUSS with much lower model accuracy and higher average error for the descending model chain at the valley and catchment scale.

The results of the feature importance measurement of both study sites are plotted cumulative over scale as decrease in accuracy for the ascending and descending approaches (Fig. 4). The higher the decrease in model accuracy and the steeper the ascent of the curves between two adjacent environmental scales the greater is the feature importance within a scale. In SISI, the ascending model has a very constant cumulative decrease function. All three curvature measures behave more or less equal. The cosine of the aspect is the most important feature at moraine scale. The sine of aspect and slope are less important compared to all other terrain attributes. Regarding the descending model, the sequence of feature importance is the same as for the ascending model. However, the rise of the curve for the cosine of aspect is comparably steeper and the feature bundle is expanded over a larger range of feature importance. The sine of the slope becomes more important at the catchment scale for pixel sizes between 256 and 3072 m, which represent processes over long distances like aeolian transport or weather phenomena. At the valley scale, longitudinal curvature is most important and sine of the aspect and slope at the catchment scale.

In RUSS, both bundles of cumulative feature importance are very similar in shape and sequence of features for the ascending and descending models (Fig. 4). In general, a steep increase in the cumulative importance of all features is the highest at the moraine scale. The highest increase of importance shows the cross-sectional curvature over all

scales for the ascending model and for the moraine and valley scale for the descending model. At the valley scale, cosine of the aspect and slope show the highest increase in the cumulative feature importance. In addition, cosine of the aspect is also important at the catchment for the ascending approach. At the catchment scale, the curve of slope has the steepest ascent.

3.2 Spatial dependencies

Here, we compare the importance of the seven terrain attributes with spatial attributes derived from EDFs in SISI (Tab. 1) and RUSS (Tab. 2), that representing the distance to the edges, corners and the center of SISI and RUSS to describe spatial non-linear relationships. Similar to Fig. 4, the feature importance represents the percentage mean decrease in accuracy of the model when using the permuted feature. In SISI, the importance of the terrain features ranges between 3.6 and 6.1 % with mean decrease of the accuracy of 1.36 ± 1.61 %. The most important terrain features are sine of the aspect, elevation, slope and cosine of the aspect at the catchment scale also with higher importance than the spatial features. The importance of the spatial features is with an average of 2.02 ± 0.54 % higher but with a maximal importance of 2.61 % (C1) lower than for the terrain features (6.05 %, sinAsp of scale 18 at the catchment scale; Tab.1). In RUSS, the mean importance of the terrain features is with 2.22 ± 3.46 % twice the mean importance of the spatial features with 1.10 ± 2.14 %. Cross-sectional curvature at the moraine scale is the most important terrain feature with up 15.57 %, which is three times higher than for the spatial features with 4.48 % (C1; Tab. 2).

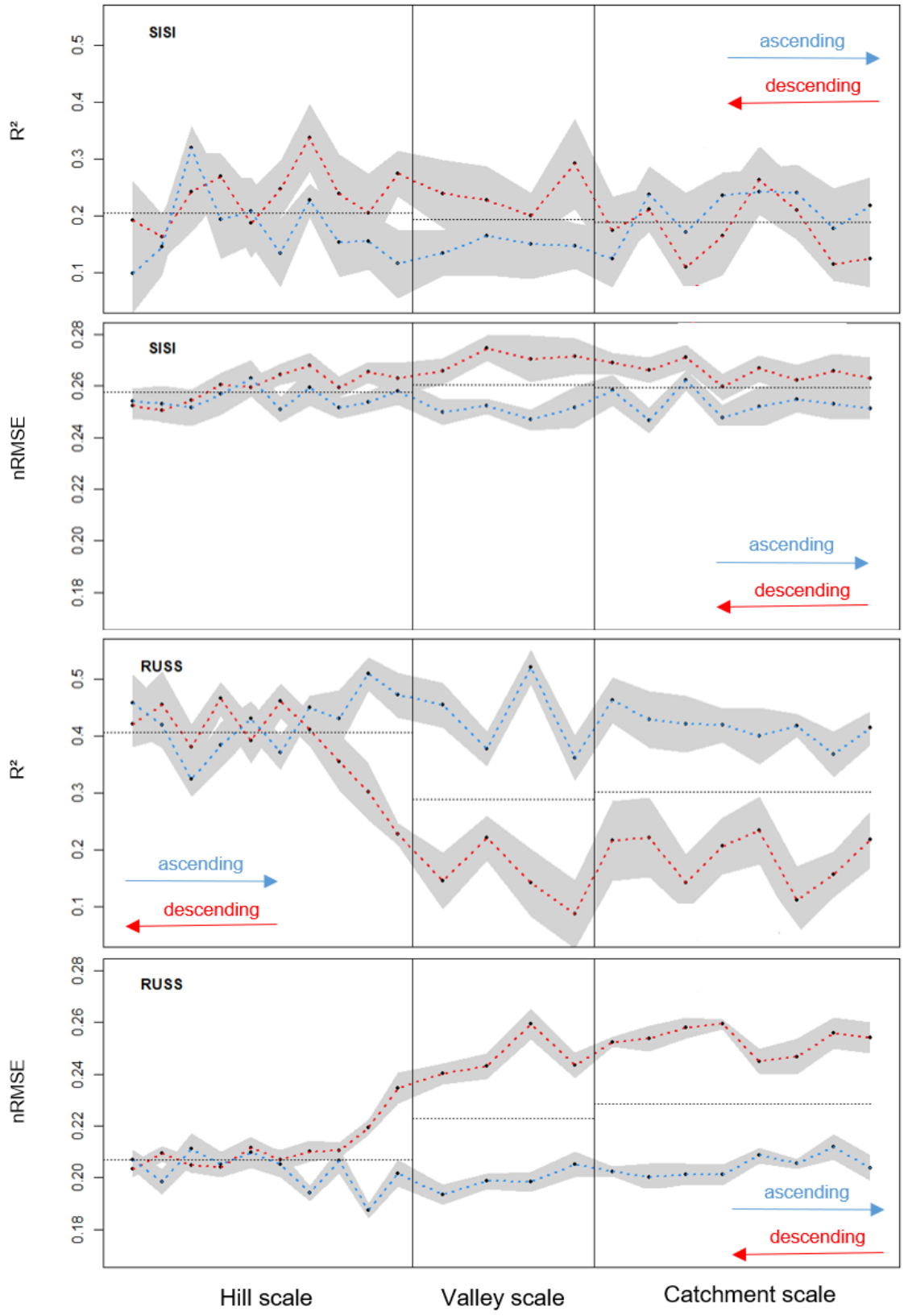

Figure 3: Variation in model accuracy (R^2, nRMSE) of the ascending and descending models for different scales in SISI and RUSS. The black dots represent single scales, the blue line represents the ascending, the red line the descending approach, and vertical lines are limits of the environmental scales.

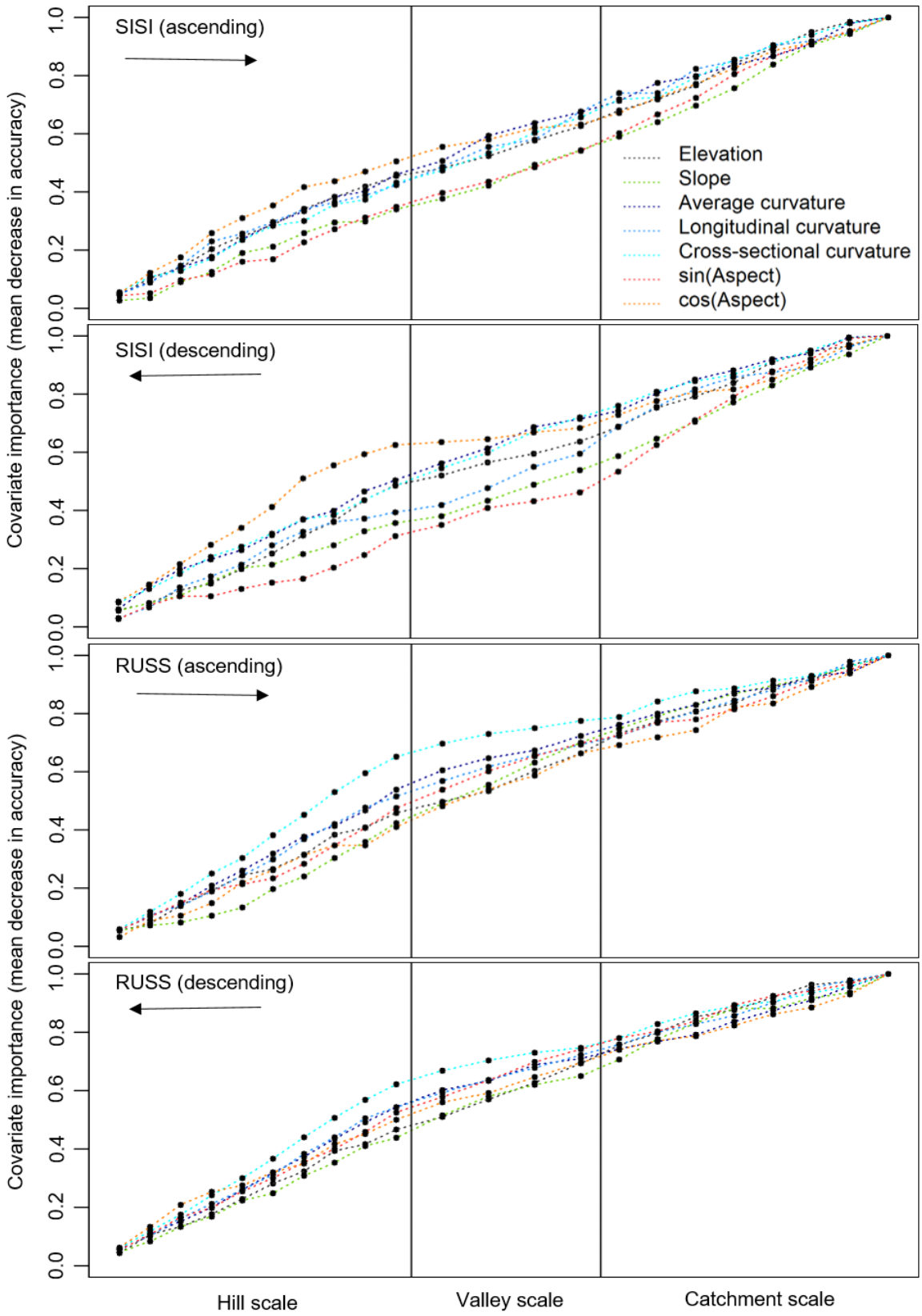

Figure 4: Cumulative importance of terrain features over different scales for the ascending and descending approaches for SISI and RUSS. The black dots represent single scales and the vertical lines are limits of the environmental scales.

Table 1: Importance of terrain and spatial features of the spatial approach for SISI ($SISI_{spatial}$).

Terrain features	Single scales																						Spatial features	
	1	2	3	4	5	6	7	8	9	10	11	12	13	14	15	16	17	18	19	20	21	22		
Elevation	1.88	2.19	3.16	-0.04	-0.44	1.05	0.32	0.78	1.35	1.39	2.15	0.6	0.5	2.58	3.2	4.14	3.19	4.23	-1.17	3.01	0.7	1.79	1.23	**X01**
Average curvature	1.53	0.91	2.37	1.16	2.18	3.05	2.29	2.55	1.62	1.59	0.33	3.55	2.79	2.03	0.38	-0.51	3.86	1.44	2.98	3.76	-0.23	-0.58	2.61	**Y01**
Slope	3.34	1.88	-0.68	-0.17	-0.8	-1.3	-1.47	-0.47	-0.77	0.38	0.98	3.01	3.48	1.17	1.14	0.98	-0.08	2.09	4.19	-0.91	1.7	2.83	2.43	**C1**
Cross-sectional curvature	0.51	1.57	2.64	1.56	1.59	1.86	0.3	1.45	0.48	-1.1	0.6	0.81	-0.39	1.98	2.7	1.4	2.76	3.66	3.06	0.7	1.54	0.41	1.65	**C2**
Longitudinal curvature	1.63	2.52	0.17	0.71	1.87	2.96	2.33	-1.8	-1.06	-2.2	0.81	-0.01	1.38	1.56	2.01	1.34	0.27	0.6	2.48	-3.55	2.17	-0.64	2.24	**C3**
cos(Aspect)	1.6	1.22	1.46	1.22	2.87	1.33	3.57	1.06	-1.28	-0.5	-1.6	-0.14	-0.29	0.47	1.84	3.04	0.19	1.87	2.72	3.78	3.18	1.3	2.46	**C4**
sin(Aspect)	-1.7	-0.72	0.61	0.84	-1.28	-1.06	-0.49	1.9	1.92	0.88	1.7	1.54	1.59	1.18	4.06	5.73	3.94	6.05	3.5	2.49	3.16	3.14	1.53	**CC**
	Hill scale										Valley scale				Catchment scale									

Table 2: Importance of terrain and spatial features of the spatial approach for RUSS ($RUSS_{spatial}$).

Terrain features	Single scales																						Spatial features	
	1	2	3	4	5	6	7	8	9	10	11	12	13	14	15	16	17	18	19	20	21	22		
Elevation	1.71	2.75	-0.06	2.34	2.76	2.29	1.36	1.16	2.25	0.98	0.55	3.14	3.48	4.85	3.44	-0.23	1.81	-0.14	-0.39	0.06	0.75	0.36	1.07	**X01**
Average curvature	1.77	-2.08	-1.58	-1.56	5.89	-1.67	-1.49	4.06	0.9	7.01	1.25	2.65	2.61	-1.59	-0.65	0.16	0.56	-2	-3.83	-3.16	-1.15	2.36	-0.58	**Y01**
Slope	-0.37	3.39	3.74	4.03	-1.56	6.24	4.95	-2.31	4.09	0.92	6.64	1.42	2.17	0.57	2.1	0.62	-1.72	-1.66	0.83	0.14	-2.12	3.96	4.48	**C1**
Cross-sectional curvature	7.33	8.46	7.39	9.38	10.14	12.67	15.57	12.48	9.65	2.11	3.35	2.84	1.63	-1.85	0.09	1.28	-0.11	-1.66	-0.97	-1.04	-0.9	2.82	-0.54	**C2**
Longitudinal curvature	2.68	3.5	4.72	3.3	4.89	6.87	8.96	8.57	4.93	1.85	3.56	1.44	1.9	1.3	-0.72	0.8	-1.49	0.1	2.2	3.53	-3.33	-0.34	1.08	**C3**
cos(Aspect)	0.74	-0.4	0.25	1.05	-1.2	2.1	1.58	0.28	-0.01	0.09	0.07	-0.88	-0.22	-0.83	-0.79	-2.27	-1.34	-1.8	-1.26	1.72	2.04	1.11	3.38	**C4**
sin(Aspect)	7.84	7.34	8.55	7.08	4.87	0.95	5.57	6.17	6.28	7.55	9.15	7.47	5.18	4.04	2.22	-0.2	0.24	1.69	1.97	3.8	2.92	1.54	-1.21	**CC**
	Hill scale										Valley scale				Catchment scale									

3.3 Regional dependencies

Different model approaches were used to estimate the spatial distribution of SOCS in SISI (Fig.5) and RUSS (Fig. 6). The validation results of the estimations are expressed by the R^2 and nRMSE on the basis of the difference between the measured and estimated values and are given in Table 2. In SISI, there is a distinct difference between the area-specific and the combined approach showing lower SOCS in the northeast. The SOCS estimation of the cross-transferred approach results in low SOCS in general. In RUSS, the SOCS are higher and vary less than with the combined and area-specific approach (Fig. 6). The R^2 is the highest for the area-specific (0.76) and the lowest for the cross-transferred approach (0.00) in SISI. In RUSS the combined (0.88) and area-specific approach (0.85) shows similar results. The nRMSE is the highest with the cross-transferred models for SISI (0.26) and RUSS (0.58). In SISI, the area-specific model provides the best SOCS estimation result with the lowest nRMSE (0.16). In RUSS, the combined approach shows the lowest nRMSE with 0.12. Except for the cross-transferred approach, the models generate smaller errors for RUSS than SISI (Tab. 3).

Table 3: Validation of the spatial SOCS predictions in SISI and RUSS.

Approach	**SISI**		**RUSS**	
	R^2	nRMSE	R^2	nRMSE
Area-specific	0.76	0.16	0.85	0.13
Spatial	0.84	0.15	0.87	0.11
Combined	0.64	0.21	0.88	0.12
Cross-transferred	0.00	0.26	0.02	0.58

4 Discussion

4.1 Scale dependencies

In SISI, the SOCS distribution is connected to small scale environmental and coastal climate conditions and related processes (Stäblein, 1977; Gries et al., 2020) acting at the moraine and catchment scale. The importance of both scales can be concluded from the variation of the model accuracy decreasing at the valley scale and subsequent increasing at the catchment scale for the ascending approach in SISI (Fig.2). The increase in the model accuracy at the moraine scale with the descending approach additionally points out the importance of the environmental conditions and related processes within the study area controlling the SOCS distribution. Low model accuracy for both approaches result from a weak connection of SOCS to the present terrain as landscape age and coastal climate fostered relocation of soil material in the past. But, considering the landscape across multiple scales reflects additional soil forming factors not being used as predictors (Behrens et al., 2014; Behrens et al., 2018a). However, further processes and factors controlling the SOCS distribution cannot be represented by the included terrain features. The model accuracy is higher in RUSS than in SISI as SOCS at 0-25 cm is stronger connected to landscape conditions at the ice margin than at the coast (Gries et al., 2020). In RUSS, the ascending and the descending approach demonstrate clearly the importance of the moraine scale suggesting small scale processes control the SOCS distribution at the ice margin. The ascending and descending approaches show that it is important to consider multiple scales for the interpretation of SOCS distribution as this allows to address the effect of scale-dependant interactions between landscape and environmental conditions towards the distribution of soil properties (Pike, 1988; Gerrard, 1981; Hole, 1978; Behrens et al., 2010a; Kerry and Oliver, 2011; Viscarra Rossel, 2011). Differences in the model

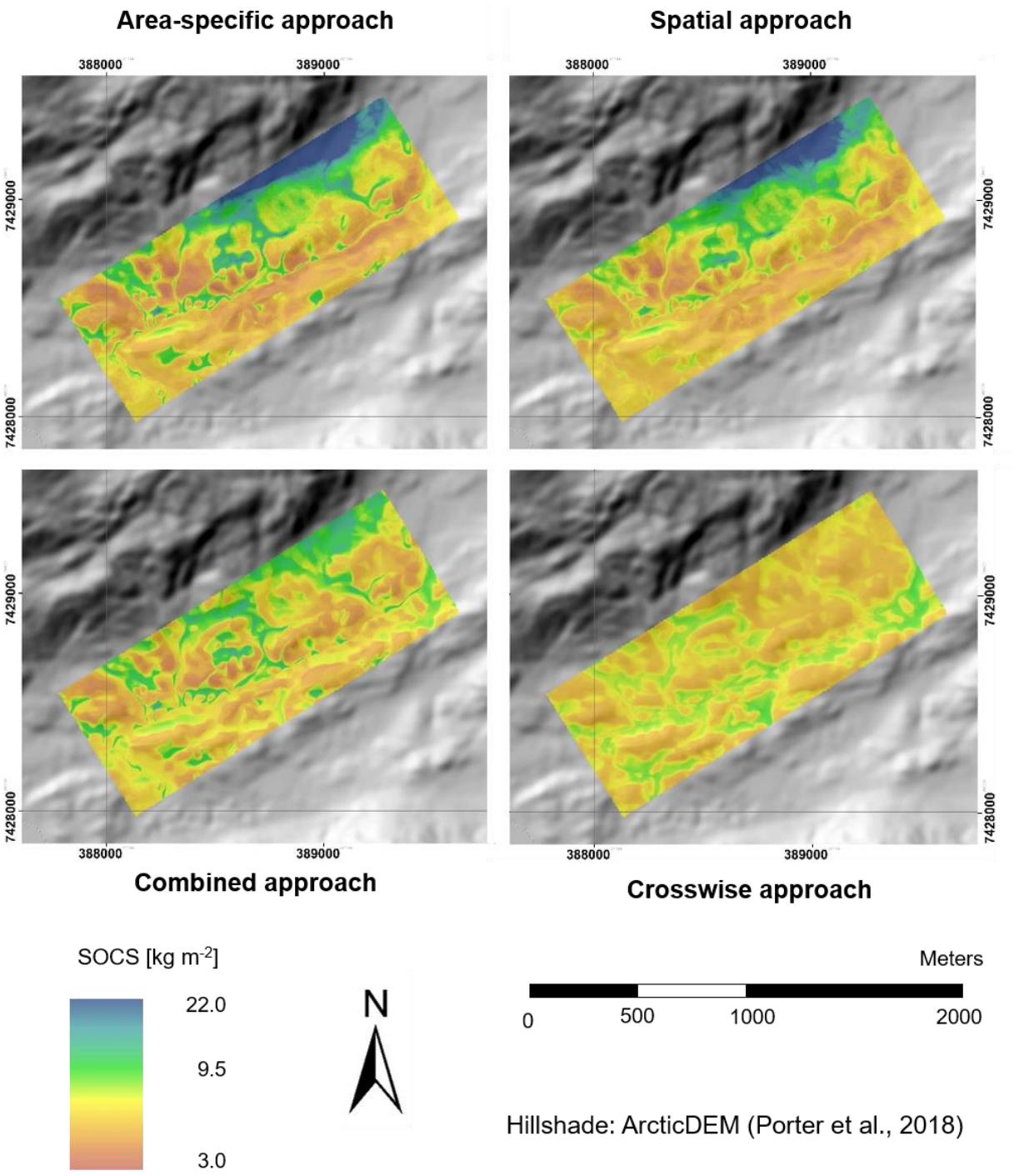

Figure 5: Prediction of the spatial SOCS distribution with different approaches in SISI. The area-specific approaches uses multi-scale terrain features only. The spatial approach includes multi-scale and spatial features. The combined approach is based on a combined data set from SISI and RUSS and uses multi-scale terrain features to predict SOCS in SISI. The crosswise approach comprises a RF model trained with a data set from RUSS to predict SOCS in SISI.

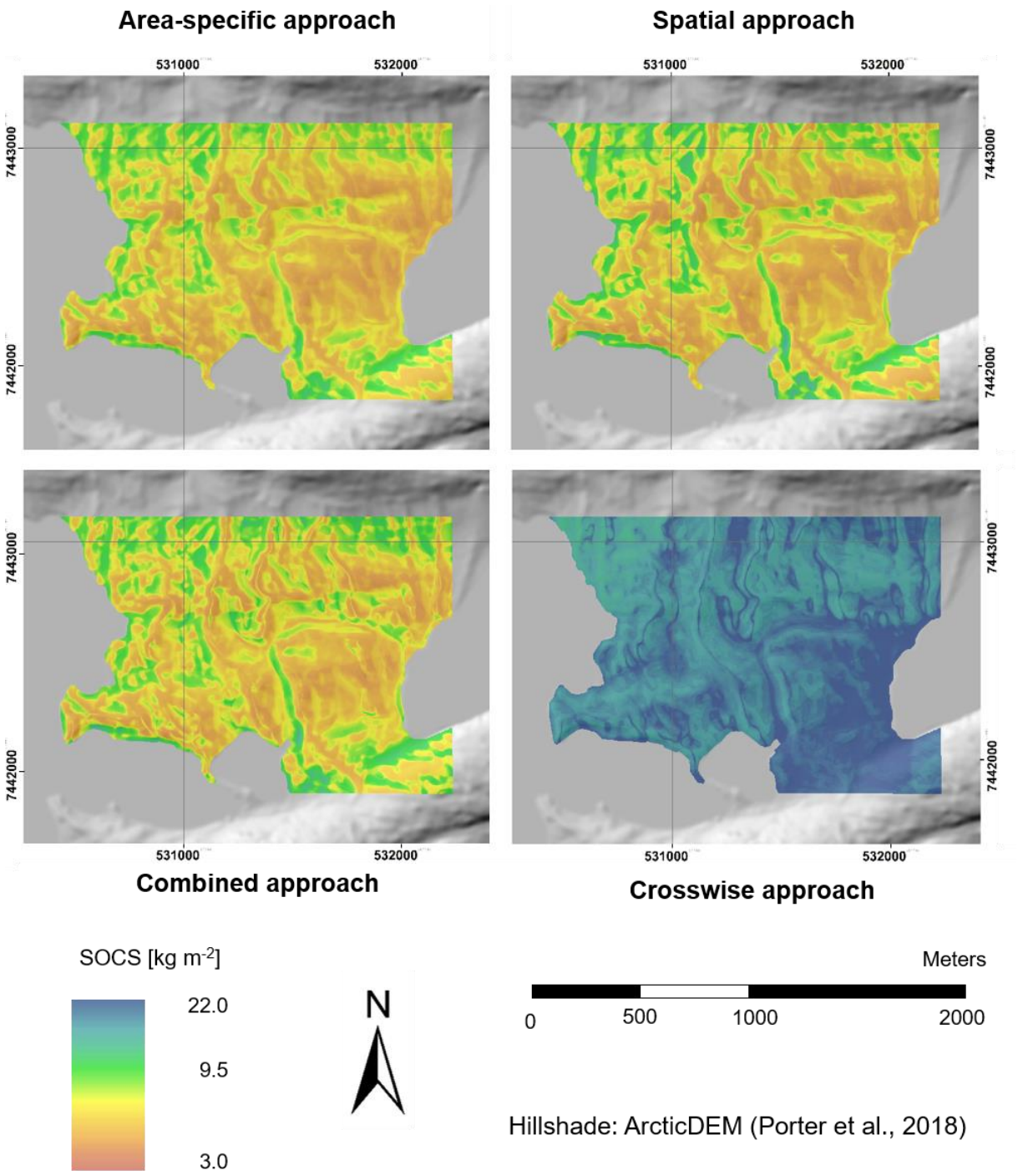

Figure 6: Prediction of spatial SOCS distribution with different approaches in RUSS. The area-specific approaches uses multi-scale terrain features only. The spatial approach includes multi-scale and spatial features. The combined approach is based on a combined data set from SISI and RUSS and uses multi-scale terrain features to predict SOCS in RUSS. The crosswise approach comprises a RF model trained with a data set from SISI to predict SOCS in RUSS.

accuracy and dominant scales between SISI in RUSS also indicate the variation in processes affecting the SOCS distribution in West Greenland. Viscarra Rossel et al. (2019) also showed that environmental factors and related processes influencing SOC vary over different scales in Australia.

The variation of the model accuracy over different scales results from the scale-dependant importance of specific terrain features (Fig. 3). With different scales, terrain features represent different landscape conditions (Fig. 2) and thus different related environmental processes. Behrens et al. (2010) identified four scale levels to differentiate between processes affecting the spatial variation of soil texture. Also at coastal area in West Greenland, soil texture distribution is linked to small-sized landscape elements and valley slopes (Stäblein, 1977). For SOCS, the aspect is a suitable abiotic factor to determine SOCS on different scales in West Greenland (Gries et al., 2020). This is confirmed by the aspect being the most important terrain feature at the moraine and catchment scale in SISI and at the valley scale at RUSS. (Fig. 4).

At small-sized landscape elements at the moraine scale at SISI, the aspect indirectly affects microclimate and growing conditions (Auslander et al., 2003) and thus is strongly connected to vegetation cover and the spatial distribution of SOCS in West Greenland (Jensen et al., 2006; Horwarth Burnham et al., 2010; Henkner et al., 2016; Gries et al., 2020). In addition, Behrens et al. (2010; 2018a) consider the aspect as a proxy for wind controlling the variation of loess within a periglacial shaped landscape. In SISI, the sine of the aspect at the catchment scale reflects characteristics of coastal climate conditions. Plant growth is negatively affected by westerly onshore winds and by reduced solar energy input due to coastal fog which results in lower SOCS at east-facing locations (Gries et al., 2020). In addition, slope at the catchment scale point out the effect of the surrounding landscape on the predominant wind system. As a result,

there are wind-protected areas in the northeast of the study area favouring the growth of tall shrub tundra and high SOCS (Gries et al., 2020). In general, curvature describes geomorphological patterns which can be calculated at any scale. Thereby, the geomorphology is more generalised or specific landforms become more apparent with an increased scale (Wood 1996). In SISI, the curvature displays the variation of the shape and related processes and thus the distribution of SOCS along different slopes. Curvature at the moraine scale represents the slope of moraines and small hills within the study area characterised by a downslope increase in SOCS (Gries et al., 2020). The curvature at the valley scale represents the shape of the valley. On valley slopes, solifluction and erosion result in colluvial deposits and SOC accumulation at the footslope (Stäblein, 1977; Palmtag et al., 2015; Henkner et al., 2016; Ramage et al., 2019). In SISI, the area along the northern border of the study area covers the footslope of the valley slope and thus shows high SOCS (Gries et al., 2020).

In RUSS, cross-sectional curvature at the moraine scale is the most important terrain feature addressing the relocation of soil components along moraine slopes which results in SOCS increasing downslope and being the highest at moraine footslopes and in depressions (Gries et al., 2020). In addition, cross-sectional curvature at the moraine scale displays moraine ridges being exposed to katabatic winds negatively affecting plant growth which results in lowest SOCS in RUSS (Gries et al., 2020). Besides, katabatic winds initiate aeolian processes affecting soil formation as well as the spatial distribution of SOC stocks within the study area (Ozol and Broll, 2003; Willemse et al., 2003; Henkner et al., 2016; Müller et al., 2016; Gries et al., 2020). The cosine of the aspect at the moraine scale is also an important terrain feature. It represents the variation in solar energy input causing frequent occurrence of freeze-thaw cycles and low SOCS on south-facing locations and high SOCS on north-facing

locations by accumulating organic material under cold and moist soil conditions (Henkner et al., 2016).

At the valley scale, cross-sectional curvature represents the shape of the valley and points out the highest moraine ridge which divides the valley bottom into a wind exposed and wind protected area. In RUSS, SOCS are higher in the western than the eastern part as wind protected areas benefits growth of tall shrub tundra connected to high SOCS at the ice margin area (Ozols and Broll, 2003; Henkner et al., 2016; Petrenko et al., 2016; Gries et al., 2020). At the catchment scale, the cosine of the aspect represents katabatic winds blowing from the Greenland Ice Sheet negatively affecting plant growth, increasing SOC decomposition and relocate soil particles. Additionally, slope at the valley and catchment scale is important to explain the spatial distribution of SOCS in RUSS (Fig.3). Slope at the valley scale show the variation in steepness of the valley slope and thus the variation in SOCS being higher at footslopes than at main slopes due to downslope processes (Ramage et al., 2019). On the catchment scale, slope represents the effect of the landscape on environmental processes acting over large distances, e.g. aeolian distribution of loess (Behrens et al., 2018a).

4.2 Spatial dependencies

The spatial feature Y representing the Euclidean distance from the southern boundary and reflects the increase in SOCS towards the northern boundary in SISI. This specific area covers the footslope of the valley being characteristic for high SOCS due to downslope transport processes (Palmtag et al., 2015; Ramage et al., 2019) which is also reflected by slope at the catchment scale. In general, terrain features at the

catchment scale are the most important features representing climate conditions, major landscape elements, valley orientation and related processes controlling the spatial distribution of SOCS increasing from the southwest to the northeast in SISI. This spatial trend is also expressed by the corner distances (C1, C2, C3 and C4) which are the most important spatial features also representing the orientation of the valley. However, terrain features are more suitable to represent spatial trends as they combine both spatial and terrain information in SISI.

In RUSS, the highest moraine ridge crosses the study area from the northwest to the southeast and thus influences the effectiveness of katabatic winds across the study area. The spatial features C1 and C4 show above average importance as they describe the orientation of this moraine ridge and thus cover the spatial trend with higher SOCS in the western than in the eastern part in RUSS. However, cross-sectional curvature at the moraine scale shows distinct higher feature importance than the spatial features which suggests that the SOCS distribution mainly depends on small scaled environmental conditions and processes acting on small-sized landscape elements.

4.3 Regional dependencies

There is a non-linear gradient in environmental conditions and related processes controlling SOC accumulation between the coast and the ice margin area in West Greenland (Bradley-Cook and Virginia, 2016; Gries et al., 2020). This gradient is reflected in the scales and feature importance being different in SISI and RUSS. Considering such scale-dependant and spatially varying environmental interrelations results in reliable large scale estimations and enables the interpretation in a pedological context (Behrens et al., 2010, 2014, 2018a, 2018b, 2019; Viscarra Rossel

et al., 2019). However, large scale estimations of SOCS of the northern circumpolar area are limited to account for such varying interrelations due to sparse soil data (Jones et al., 2009; Tarnocai et al., 2009; Hugelius et al., 2013; 2014; Köchy et al., 2015; Hengl et al., 2017). Spatial predictions require similar environmental conditions between the training and the validation area both being represented by a balanced training data considering relevant environmental factors (Behrens et al., 2009; Taghizadeh-Mehrjardi et al., 2020). This is reflected in the validation of the predicted SOCS with the cross-transferred approach being the lowest in SISI and RUSS (Tab. 3). Also, the application of an inadequate model causes high uncertainty of the target variable leading to an underestimation and overestimation of SOCS in SISI and RUSS respectively (Fig. 5; Fig. 6). This holds true for local studies in West Greenland showing higher SOCS than existing large scale estimations (Kühn and Henkner, 2019). Due to the represented scale, largescale estimations show low variation in SOCS between the coast and the ice margin area in West Greenland (Jones et al., 2009; Hugelius et al., 2013; 2014; Köchy et al., 2015) but which is confirmed by similar mean SOCS in SISI and RUSS (Gries et al., 2020). With a finer scale, differences in landscape and climate pattern can be taken into account for the estimation of SOCS spatially varying in West Greenland (Hengl et al., 2014; 2017). However, SoilGrids (Hengl et al., 2017) account only for soil landscape interactions at the valley and catchment scale due to the resolution and thus cannot consider differences in environmental conditions and related relocation processes at the moraine scale. Furthermore, sparse soil data additionally complemented by pseudo-observations results in uncertain SOCS estimations in West Greenland (Hengl et al., 2014; 2017).

The combined approach emphasizes the importance of representative soil data for high resolution SOCS estimations as additional data enables the model to distinguish

between spatially varying and site-related soil landscape interrelations and produce more reliable results compared to the cross-transferred approach (Tab. 3). However, with the combined approach SOCS are still underestimated at the coast especially in the northeastern area in SISI (Fig. 5). Due to the strong link between soil and terrain in RUSS, scale-dependent soil landscape interrelation might be mistakenly transferred from the ice margin area to the coastal area. In contrast, for RUSS, the combined approach achieves slightly better validation results compared to the area-specific approach (Tab. 3) which might be related to characteristics of statistical models like RF. Having several advantages, RF is widely used in pedometrics but is also limited in the reproduction of the range of the observed values in the predictions. So, additional soil information from SISI artificially extends the range of the SOCS in RUSS which leads to a better coverage of the range of the observed values and a higher consistency by the predicted values (Fig. 6).

Conclusion

There is a high spatial variation in SOCS in both study areas which can be described by the application of several RF models comprising different sets of multi-scale terrain and spatial features in SISI and RUSS. The advantage of using sequenced RF models allows to measure the feature importance of single terrain features to identify relevant scales and explain the spatial SOCS distribution by accompanied environmental processes. In SISI, the aspect indicates the importance of downslope processes on the moraine scale and the role of wind related processes on the catchment scale being relevant for the spatial SOCS distribution at the coast as well. Further, the curvature highlights the effect of water-driven relocation processes on the valley scale which results in high SOCS along the northern boundary of the study area in SISI. In RUSS,

katabatic winds are characteristic for the ice margin area and influence the SOCS distribution in different ways which is illustrated in detail by single terrain features of different scales. The aspect points out the negative effect of katabatic winds on the moraine scale which results in SOCS being lower on east-facing than on wind-sheltered west-facing locations in RUSS. This can be transferred to the valley scale, where in the west to the highest moraine ridge, illustrated by the curvature, the SOCS is higher than in the eastern and wind-exposed part of the study area. Further, the aspect reflects increasing SOCS with distance from the ice margin which results from decreasing strength of the katabatic winds on the catchment scale. These scale-dependent soil-landscape interrelations confirm the hypothesis that small-scale processes primarily affect the SOCS distribution on the one hand but on the other hand accentuate the importance to consider secondary large-scale processes in spatial analysis of SOCS.

Different soil-landscape interrelations between both study areas were inferred from differences in the importance and relevant scales of the terrain features and differences in related environmental processes. A climatic gradient is expressed in opposing wind systems and decreasing amount of water over a long distance from the coast to the ice margin of West Greenland. Feature importance and relevant scales in SISI demonstrate the importance of relocation processes by water for SOCS at the coast. In contrast, a strong connection to the terrain and a subordinate role of respective scales and features indicate minor redistribution due to surface runoff at the ice margin. However, the aspect also captures the differential effect of the role of solar energy input and wind direction on the SOCS between both study areas. Additionally, differences in relevant scales of the aspect between SISI and RUSS point out the multi-

scale SOCS dependency on katabatic winds at the ice margin. There, we recommend multi-scale approaches for the spatial analysis of SOCS in permafrost-affected soils.

References

Auslander, M., Nevo, E., Inbar, M. (2003): The effects of slope orientation on plant growth, development instability and susceptibility to herbivores. J. Arid Environ. 55, 405–416.

Behrens, T., MacMillan, R.A., Viscarra Rossel, R.A., Schmidt, K., Lee, J. (2019a): Teleconnections in spatial modelling. Geoderma, Volume 354, 113854.

Behrens, T., Viscarra Rossel, R. A., Kerry, R., MacMillan, R., Schmidt, K., Lee, J., Scholten, T., Zhu, A-X. (2019b): The relevant range of scales for multi-scale contextual spatial modelling. Sci. Rep. 9, 14800.

Behrens, T., Schmidt, K., MacMillan, R.A., Viscarra Rossel, R. (2018a): Multi-scale Digital Soil Mapping with deep learning. Sci Rep. 8, 15244.

Behrens, T., Schmidt, K., Viscarra Rossel, R.A., Gries, P., Scholten, T., MacMillan, R.A. (2018b): Spatial modelling with Euclidean distance fields and machine learning. Eur. J. Soil. Sci., 69, 757–770.

Behrens, T., Schmidt, K., MacMillan, R.A., Viscarra Rossel, R.A. (2017): Multiscale contextual spatial modelling with the Gaussian scale space. Geoderma 310, 128–137.

Behrens, T., Schmidt, K., Ramirez-Lopez, L., Gallant, J., Zhu, A-X., Scholten, T. (2014): Hyper-scale digital soil mapping and soil formation analysis. Geoderma 213, 578–588.

Behrens, T., Schmidt, K., Zhu, A.X. und Scholten, T. (2010): The ConMap approach for terrain-based digital soil mapping. Eur. J. Soil Sci. 61, 133–143.

Behrens, T., Scholten, T. (2006): A Comparison of Data Mining Approaches in Predictive Soil Mapping. In: Lagacherie, P., McBratney, A.B, Voltz, M. (eds.): Digital Soil Mapping. Developments in Soil Science 31, 353–617.

Biswas, A., Cresswell, H., Viscarra Rossel, R., Si, B.C. (2013): Characterizing scale- and location-specific variation in non-linear soil systems using the wavelet transform. Eur. J. Soil Sci. 64, 706–715.

Breiman, L. (2001): Random Forests. Machine Learning, 45, 5–32.

Breiman, L., Friedman, J.H., Olshen, R.A., Stone, C.J. (1984): CART: Classification and Regression Trees. Wadsworth, Belmont, CA.

Bradley-Cook, J.I., Virginia, R.A. (2016): Soil carbon storage, respiration potential, and organic matter quality across an age and climate gradient in southwestern Greenland. Polar. Biol. 39, 1283–1295.

Burrough, P.A., van Gaans, P.F. M., MacMillan, R.A. (2000): High-resolution landform classification using fuzzy k-means. Fuzzy Set. Syst. 113, 37–52.

Burrough, P.A. (1983): Multiscale sources of spatial variation in soil the application of fractal concepts to nested levels of soil variation. J. Soil Sci. 34, 577–597.

Burt, P., Adelson, E. (1983): The laplacian pyramid as a compact image code. IEEE Trans. Commun. 31, 532–540.

Cappelen, J., Jørgensen, B.V., Laursen, E.V., Stannius, L.S., Thomsen, R.S. (2001): The observed climate of Greenland, 1958–99 - with climatological standard normals, 1961–90. Technical Report 00–18. Danish Meteorological Institute Ministry of Transport and Energy, Copenhagen.

Carstensen, L.S., Jørgensen, B.V. (2009): Weather and climate data from Greenland 1958–2008: dataset available for research and educational purposes. Descriptions and documentation of observations of temperature, precipitation, wind, could cover, air pressure, humidity and depth of snow. Technical Report 09–11. Danish Meteorological Institute Ministry of Transport and Energy, Copenhagen.

CAVM Team (2003): Circum Arctic Vegetation Map. (1:7,500,000 scale), Conservation of Arctic Flora and Fauna (CAFF) Map No. 1. U.S. Fish and Wildlife Service, Anchorage, Alaska.

Chadburn, S.E, Burke, E.J., Cox, P.M., Friedlingstein, P., Hugelius, G., Westermann, S. (2017): An observation-based constraint on permafrost loss as a function of global warming. Nat. Clim. Change 7, 340–344.

Gries, P., Schmidt, K., Scholten, T., Kühn, P. (2020): Regional and local scale variations in soil organic carbon stocks in West Greenland. J. Plant Nutr. Soil Sci. 183, 292–305.

Grimm, R, Behrens, T., Märker, M., Elsenbeer, A. (2008): Soil organic carbon concentrations and stocks on Barro Colorado Island - Digital soil mapping using Random Forests analysis. Geoderma 146, 102–113.

Hengl, T., de Jesus J.M., Heuvelink, G.B.M., Ruiperez Gonzalez, M., Kilibarda, M., Blagotić, A., Shangguan, W., Wright, M.N., Bauer-Marschallinger, B., Guevara, M.A., Vargas, R., MacMillan, R.A. (2017) SoilGrids250m: Global gridded soil information based on machine learning. PLoS ONE 12: e0169748.

Hengl, T, de Jesus, J.M., MacMillan, R.A., Batjes, N.H., Heuvelink, G.B.M., Ribeiro, E., Samuel-Rosa, A., Kempen, B., Leenaars, J.G.B., Walsh, M.G., Ruiperez Gonzales,

M. (2014) SoilGrids1km — Global Soil Information Based on Automated Mapping. PLoS ONE 9: e105992.

Henkner, J., Scholten, T., Kühn, P. (2016): Soil organic carbon stocks in permafrost-affected soils in West Greenland. Geoderma 282, 147–159.

Henriksen, N. (2008): Geological History of Greenland: Four billion Years of Earth Evolution. Geological Survey of Denmark and Greenland, Copenhagen.

Horwath Burnham, J.L., Sletten, R.S. (2010): Spatial distribution of soil organic carbon in northwest Greenland and underestimates of High Arctic carbon stores. Global Biogeochem. Cycles 24, 1–14.

Hugelius, G., Strauss, J., Zubryzycki, S., Harden, J., Schuur, E., Ping, C., Schirrmeister, L., Grosse, G., Michaelson, G., Koven, C., O'Donnell, J., Elberling, B., Mishra, U., Camill, P., Yu, Z., Palmtag, J., Kuhry, P. (2014): Estimated stocks of circumpolar permafrost carbon with quantified uncertainty ranges and identified data gaps. Biogeosciences 11, 6573–6593.

Hugelius, G., Tarnocai, C., Broll, G., Candell, J.G., Kuhry, P., Swanson, D.K. (2013): The Northern Circumpolar Soil Carbon Database: spatially distributed datasets of soil coverage and soil carbon storage in the northern permafrost regions. Earth Syst. Sci. Data 5, 3–13.

IPCC, International Panel on Climate Change (2019): IPCC Special Report on the Ocean and Cryosphere in a Changing Climate.

Jensen, L., Hollesen, J., Elberling, B. (2006): Accumulation of Soil Organic Carbon Linked to Holocene Sea Level Changes in West Greenland. Arct. Antarct. Alp. Res. 38, 378–383.

Jones, A., Stolbovoy, V., Tarnocai, C., Broll, G., Spaargaren, O., Montanarella, L. (2009): Soil Atlas of the Northern Circumpolar Region, Luxembourg.

Karl, J.W., Maurer, B.A. (2010): Spatial dependence of predictions from image segmentation: A variogram-based method to determine appropriate scales for producing land-management information. Ecol. Informatics 5, 194–202.

Kerry, R., Oliver, M.A. (2011): Soil geomorphology: Identifying relations between the scale of spatial variation and soil processes using the variogram. Geomorphology 130, 40–54.

Köchy, M., Hiederer, R., Freibauer, A. (2015): Global distribution of soil organic carbon – Part1: Masses and frequency distributions of SOC stocks for the tropics, permafrost regions, wetlands, and the world. Soil 1, 351–365.

Kuhn, M. (2017): Caret: Classification and Regression Training. R package.

Kühn, P., Henkner, J., (2019). Permafrost-affected Soils, Climate, and Feedbacks in West Greenland. In: Lal, R., Stewart, B. A. (eds.). Soil and Climate. Advances in Soil Science, CRC Press, pp. 92–97.

Lal, R. (2004): Soil carbon sequestration impacts on global climate change and food security. Science 304, 1623.

Levy, L. B., Kelly, M. A., Howley, J. A., Virginia, R. A. (2012): Age of the Ørkendalen moraines, Kangerlussuaq, Greenland: constraints on the extent of the southwestern margin of the Greenland Ice Sheet during the Holocene. Quaternary Sci. Rev. 52,1–5.

Mishra, U., Riley, W.J. (2012): Alaskan soil carbon stocks: spatial variability and dependence on environmental factors. Biogeosciences 9, 3637–3645.

Müller, M., Thiel, C., Kühn, P. (2016): Holocene palaeosols and aeolian activities in the Umimmalissuaq valley, West Greenland. The Holocene 26, 1149–1161.

OpenStreetMap contributors (2015): https://planet.osm.org/historical-shapefiles/shoreline_ 300.tar.bz2 (Last access 14.11.2019)

Ozols, U., Broll, G. (2003): Soil ecological processes in vegetation patches of well drained permafrost affected sites (Kangerlussuaq - West Greenland). Polarforschung 73, 5–14.

Palmtag, J., Cable, S., Christiansen, H. H., Hugelius, G., Kuhry, P. (2018): Landform partitioning and estimates of deep storage of soil organic matter in Zackenberg, Greenland. The Cryosphere 12, 1735–1744.

Palmtag, J., Hugelius, G., Lashchinskiy, N., Tamstorf, M.P., Richter, A., Elberling, B., Kuhry, P. (2015): Storage, Landscape Distribution, and Burial History of Soil Organic Matter in Contrasting Areas of Continuous Permafrost. Arct. Antarct. Alp. Res. 47, 71–88.

Petrenko, C.L., Bradley-Cook, J.I., Lacroix, E.M., Friedland, A.J., Virginia, R.A. (2016): Comparison of carbon and nitrogen storage in mineral soils of graminoid and shrub tundra sites, western Greenland. Arctic Sci. 2, 165–182.

Ping, C.L., Jastrow, J.D., Jorgenson, M.T., Michaelson, G.J., Shur, Y.L. (2015): Permafrost soils and the carbon cycling. SOIL 1, 147–171.

Ping, C.L., Bockheim, J.G., Kimble, J.M., Michaelson, G.J., Walker, D.A. (1998): Characteristics of cryogenic soils along a latitudinal transect in arctic Alaska. J. Geophys. Res. 103, 917–928.

Porter, C., Morin, P., Howat, I., Noh, M.-J., Bates, B., Peterman, K., Keesey, S., Schlenk, M., Gardiner, J., Tomko, K., Willis, M., Kelleher, C., Cloutier, M., Husby, E.,

Foga, S., Nakamura, H., Platson, M., Wethington, M., Williamson, C., Bauer, G., Enos, J., Arnold, G., Kramer, W., Becker, P., Doshi, A., D'Souza, C., Cummens, P., Laurier, F., Bojesen, M. (2018): ArcticDEM, Harvard Dataverse, V1.

R Development Core Team (2013): R: A Language and Environment for Statistical Computing.

Ramage, J., Fortier, D.C., Hugelius, G., Lantuit, H., Morgenstern, A. (2019): Distribution of carbon and nitrogen along hillslopes in three valleys on Herschel Island, Yukon Territory, Canada. Catena 178, 132–140.

Schmidt, K., Behrens, T., Daumann, J., Ramirez-Lopez, L., Werban, U., Dietrich, P., Scholten, T. (2014): A comparison of calibration sampling schemes at the field scale. Geoderma 232-234, 243–256.

Schmidt, K., Behrens, T., Scholten, T. (2010): A method to generate soilscapes from soil maps. J. Plant Nutr. Soil Sc. 173, 163–172.

Schmidt, K., Behrens, T., Scholten, T. (2008): Instance selection and classification tree analysis for large spatial datasets in digital soil mapping. Geoderma 146, 1–2.

Stäblein, G. (1977). Arktische Böden Westgrönlands: Pedovarianz in Abhängigkeit vom geoökologischen Milieu. Polarforschung 47, 11–25.

Siewert, M. B., Hugelius, G., Heim, B., Faucherre, S. (2015): Landscape controls and vertical variability of soil organic carbon storage in permafrost-affected soils of the Lena River Delta. Catena 147, 725–741.

Tarnocai, C., Canadell, J.G., Schuur, E.A.G., Kuhry, P., Mazhitova, G., Zimov, S.A. (2009): Soil organic carbon pools in the northern circumpolar permafrost region. Glob. Biogeochem. Cy. 23, 1–11.

Viscarra Rossel, R., Lee, J., Behrens, T., Luo, Z., Baldock, J., Richards, A., (2019): Continental-scale soil carbon composition and vulnerability modulated by regional environmental controls. Nat. Geosci. 12, 547–552.

Willemse, N. W., Koster, E. A., Hoogakker, B., Van Tatenhove, F. G. (2003): A continuous record of Holocene eolian activity in West Greenland. Quaternary Res. 59, 322–334.

Wojcik, R., Palmtag, J., Hugelius, G., Weiss, N., Kuhry, P. (2019): Land cover and landform-based upscaling of soil organic carbon stocks on the Brøgger Peninsula, Svalbard. Arct. Antarct. Alp. Res. 51, 40–57.

Wood, J. (1996) The Geomorphological Characterisation of Digital Elevation Models. Ph.D. Thesis, University of Leicester, Leicester.

Zevenbergern, L.W., Thorne, C.R. (1987): Quantitative analysis of land surface topography. Earth Surf. Proc. Land. 12, 47–56.

Manuscript 3: Spatial modelling with Euclidean distance fields and machine learning

Published in: European Journal of Soil Science, September 2018, 69, 757–770

Authors: Thorsten Behrens[1], Karsten Schmidt[1], Raffael A. Viscarra Rossel[2], Philipp Gries[1], Thomas Scholten[1], Robert A. MacMillan[3]

[1] Department of Geosciences, Chair of Soil Science and Geomorphology, University of Tübingen, 72070 Tübingen, Germany

[2] CSIRO Land and Water, GPO Box 1700, Canberra ACT 2601, Australia

[3] LandMapper Environmental Solutions Inc., 7415 118 A Street NW, Edmonton, Alberta Canada

Summary

This study introduces a hybrid spatial modelling framework, which accounts for spatial non-stationarity, spatial autocorrelation and environmental correlation. A set of geographic spatially autocorrelated Euclidean distance fields (EDF) was used to provide additional spatially relevant predictors to the environmental covariates commonly used for mapping. The approach was used in combination with machine-learning methods, so we called the method Euclidean distance fields in machine-learning (EDM). This method provides advantages over other prediction methods that integrate spatial dependence and state factor models, for example, regression kriging (RK) and geographically weighted regression (GWR). We used seven generic (EDFs) and several commonly used predictors with different regression algorithms in two digital soil mapping (DSM) case studies and compared the results to those achieved with ordinary kriging (OK), RK and GWR as well as the multiscale methods ConMap,

ConStat and contextual spatial modelling (CSM). The algorithms tested in EDM were a linear model, bagged multivariate adaptive regression splines (MARS), radial basis function support vector machines (SVM), Cubist, random forest (RF) and a neural network (NN) ensemble. The study demonstrated that DSM with EDM provided results comparable to RK and to the contextual multiscale methods. Best results were obtained with Cubist, RF and bagged MARS. Because the tree-based approaches produce discontinuous response surfaces, the resulting maps can show visible artefacts when only the EDFs are used as predictors (i.e. no additional environmental covariates). Artefacts were not obvious for SVM and NN and to a lesser extent bagged MARS. An advantage of EDM is that it accounts for spatial non-stationarity and spatial autocorrelation when using a small set of additional predictors. The EDM is a new method that provides a practical alternative to more conventional spatial modelling and thus it enhances the DSM toolbox.

Highlights

- We present a hybrid mapping approach that accounts for spatial dependence and environmental correlation.
- The approach is based on a set of generic Euclidean distance fields (EDF).
- Our Euclidean distance fields in machine learning (EDM) can model non-stationarity and spatial autocorrelation.
- The EDM approach eliminates the need for kriging of residuals and produces accurate digital soil maps.

Introduction

The spatial variation and distribution of soil properties can be represented by random fields (i.e. random functions in the geographical space that are spatially correlated) (Matérn, 1960). Soil variation and its spatial distribution are also often strongly related to the parametric distribution of the 'clorpt' soil forming factors (i.e. climate, organisms, relief, parent material and time) described by Jenny (1941). Here, we introduce Euclidean distance fields (EDFs) (Rosenfeld & Pfaltz, 1968) as new, spatially relevant, covariates for modelling soil spatial variation. The EDFs can be used alone as predictors in regression approaches for mapping, or in combination with other more commonly used predictors, such as climate and terrain attributes, when there is a need to account for both spatial dependence and environmental correlation. We propose the use of EDFs with machine learning methods; therefore, we call the method Euclidean distance fields in machine learning (EDM). Spatial dependence refers to the covariation of variables within geographic space and includes descriptions of spatial autocorrelation and non-stationarity. Spatial autocorrelation is a quality of the data whereby observations are interrelated in space. It is used by methods for spatial interpolation to estimate values at unobserved locations using values at observed locations in a neighbourhood (Oliver & Webster, 1990; Páez, 2004). Spatial non-stationarity is a condition in which a global regression model cannot explain the relations between some sets of variables (i.e. where variation in relations occurs over space and where models that allow local variation are required) (Brunsdson et al., 1996). Models that account explicitly and simultaneously for both spatial dependence and environmental correlation are called 'hybrid' models. In this respect the 'scorpan' approach introduced by McBratney et al. (2003) is an extension of Jenny's clorpt state factor equation to account more explicitly for spatial effects. In addition to Jenny's

clorpt factors, the scorpan model adds ‘s’ for other soil properties and ‘n’, which is important for hybrid models because it refers to space or location, and thus any spatial dependence in the data. Two well-known hybrid approaches are regression kriging (RK) (Neuman & Jacobson, 1984; Odeh et al., 1994) and geographically weighted regression (GWR) (Brunsdon et al., 1996). In the case of RK, a regression model is first generated using a set of environmental covariates followed by kriging (spatial prediction) of the regression residuals. Both models are summed to generate the final prediction map. In contrast, GWR is based on localized calibrations, where different regression models are applied in different regions using local sets of sample points. Kriging is commonly used to predict spatially autocorrelated variables under assumptions of stationarity, whereas GWR was developed to predict spatially non-stationary variables. Local RK approaches (Sun et al., 2012) adapt the GWR idea to the RK framework and derive local models within a given geographic neighbourhood. Another approach to account for spatial dependence is trend surface mapping (TSM) (Unwin, 1975), which is often used for detrending (i.e. separating relatively large-scale systematic spatial trends from non-systematic small-scale variation arising from local effects) (Krumbein, 1959). It is based on fitting linear or polynomial regression equations to the geographic (x, y) coordinates. Applying the concept of TSM with non-linear modelling approaches, such as artificial neural networks or decision trees, should produce local rather than global trend models that can characterize local variation. Including additional EDFs as predictors (i.e. not only x, y) should help to map complex processes that are characterized by both global and local spatial variation. We suggest here a set of five generic geographic EDFs that can be used as additional spatial predictors in ‘scorpan’ models. Because EDFs partition geographic space into sub-regions, the regression model can deal with the interactions between

environmental covariates and soil that vary non-linearly over space. This is a common advantage of EDM, GWR and local RK. In contrast, RK cannot account for spatial non-stationarity because of its two-step approach in setting up a global regression model with fixed geographical relations and subsequent interpolation by kriging to account for spatial autocorrelation in the residuals. Compared to EDM, the regression models in GWR are explicitly local and thus based only on a local subset of sample data. Therefore, the local regression models in GWR might not reveal important global spatial dependencies. There are additional hybrid methods described in the DSM literature. These are mostly variations of RK (i.e. RK with regression approaches other than the linear model) or combinations of GWR and kriging, such as GWR-kriging or local RK (e.g. Kumar et al., 2012; Viscarra Rossel et al., 2015; Sun et al., 2012). Although local kriging models can handle non-stationarity better than the usual RK, all local models have the same theoretical drawbacks. Regression kriging with non-linear regression models can, in some cases, improve the accuracy of prediction (Viscarra Rossel et al., 2014). Another category of hybrid DSM methods comprises those that use multiscale contextual derivatives or indicators of environmental covariates, such as terrain; that is ConMap (Behrens et al., 2010), ConStat (Behrens et al., 2014) and contextual spatial modelling (CSM, Behrens et al., 2018), referred to as contextual mapping in the following. They do not rely on spatial predictors, such as in EDM, and are not based on local regression models as in GWR. Rather, they make use of spatial contextual environmental covariate information. This contextual information is extracted at local to supra-regional scales in terms of circular spatial neighbourhoods or decomposed scales, and considers much larger neighbourhoods than common multiscale approaches (e.g. Wood, 1996; Moran & Bui, 2002; Behrens et al., 2018). These contextual mapping approaches account for the source of spatial dependence

(i.e. small to large-scale interactions between environmental covariates across the landscape), instead of using spatial autocorrelation or factoring in non-stationarity for mapping directly, as with GWR or RK. In this respect, contextual mapping represents a contrasting approach to EDM. Although EDM makes use of spatial autocorrelation, the contextual mapping approaches try to remove the spatially autocorrelated part of the residuals. Our aims here are to describe the EDM concept, to demonstrate its application with two datasets and to compare the efficacy of EDM against ordinary kriging (OK), RK, GWR and contextual mapping methods.

Materials and methods

Study sites

The aim of this study was to introduce and evaluate a new hybrid spatial mapping approach using Euclidean distance fields embedded in a ‘scorpan’ framework with additional environmental covariates; therefore, we needed datasets with both spatial dependence and some correlation with environmental factors. Consequently, we used the same two datasets analysed previously by Behrens et al. (2010, 2014, 2018) because they met the required criteria.

The study site in Rhine-Hesse, Germany, is a large wine-growing and loess-covered region of approximately 1150 km2. The mean annual precipitation ranges from 500 to 850 mm. Luvisols, Cambisols and Podzols characterize this region. The major process that influenced topsoil silt content, which is analysed in this study, was local translocation of loess during the Wuerm glaciation. The loess was blown out of the surrounding riverbeds and deposited on the plateaus and in lee areas. This process is not well reflected by the underlying parent material (map) or by current climate

conditions or land cover. Historical land use might be relevant to explain subsequent erosion processes better. However, data on historical land use are not available. Therefore, the only relevant data available for prediction of this property in this area are those on terrain. Terrain shape modulated climate conditions, leading to translocation of loess. Gravity, and thus terrain, is also the major controlling factor of soil erosion. Other relevant processes in this region, such as the formation of periglacial slope deposits, are controlled by solar insolation (i.e. slope and aspect) and contributing area. In total we used 342 samples to predict topsoil silt content (0–10 cm) with a digital elevation model (DEM) with a resolution of 20 m (Figure 1). The topsoil silt content ranges from 2 to 83%. The Piracicaba study area covers an area of approximately 300 km2 and is in the state of São Paulo (Brazil); the area comprises mainly sugarcane fields. The mean annual precipitation is 1328 mm. The geology of the area is characterized by sandstone, siltstone and shale, and to a lesser extent limestone, basalt and colluvial deposits (Mezzalira, 1965). Arenosols, Ferralsols, Acrisols, Alisols, Nitisols, Cambisols and Lixisols are the major soil types. Because of the predominantly sedimentary substrates, ranging from sandstone to limestone, clay content, which is modelled in this study, has a wide range of values from 6 to 72%. Therefore, parent material plays a major role, but there is no appropriate map of parent material available. Nevertheless, the effect of parent material can be inferred from the geomorphic signature (Behrens et al., 2014, 2018). Land use does not play a role because all the data come from sugarcane fields. Hence, terrain was again used as the only relevant covariate. In total 321 soil samples were available to predict topsoil clay content (0–10 cm) with a shuttle radar topography mission (SRTM) DEM with a resolution of 90 m (Figure 1).

Environmental covariates

The hypothesis behind this study is that spatial dependence, and more specifically spatial autocorrelation and spatial non-stationarity, can be modelled by the EDM approach. To interpret the effect of spatial dependence in relation to environmental correlation, we compare EDM with OK, RK using a linear regression model, GWR and the three contextual mapping approaches. The idea was to compare the proposed EDM approach with several of the most commonly used spatial prediction approaches. Because we are introducing a new methodology, to be able to focus on the EDF predictors and make comparisons with previous studies (Behrens et al., 2010, 2014, 2018), we use only terrain attributes as the environmental covariates.

We derived the following seven, moderately correlated (maximum r =0.66), terrain attributes from the DEMs as environmental covariates for both study sites with the common terrain analysis tools provided in SAGA GIS 6.0 (Conrad et al., 2017): valley depth, topographic wetness index (TWI), slope, longitudinal curvature, elevation, cross-sectional curvature and aspect. Sine and cosine transforms (sinAspect and cosAspect) were applied to linearize the circular measurements of aspect. Thus, including elevation, eight terrain attributes were computed and used. All terrain attributes were subsequently log10 transformed and rescaled to a range of 0 to1.

Euclidean distance fields and terrain attribute subsets

The X and Y coordinates used alone as spatial predictors in soil mapping might not be sufficient to produce accurate models. Thus, additional spatial Euclidean distance fields (Krumbein, 1959) can be used as explicitly autocorrelated indicators of spatial position and context for ‘scorpan’ models in common regression approaches. We integrated the following generic Euclidean distance fields in the EDM:

• X and Y coordinates, which are distance fields to the edges of a rectangle around the sample set.

• the distances to the corners of a rectangle around the sample set (C1, C2, C3, C4).

• and the distances to the centre location of the sample set (CC).

Figure 2 shows an example of these spatial predictors for a quadratic region. The idea behind the selection of the corners and centre distance was that these provide additional (non-linear) information about position without introducing too many additional predictors, to maintain parsimony in the models. Moreover, this set of EDFs is independent from the sample locations and can easily be calculated in any geographic information system (GIS). Other metrics related to position might also be possible. However, some measures would be required to determine the positions of the location of the origin of the EDFs. Using the corners (and the same applies for XY) ensures that a specific distance is directionally unique across the study area (i.e. the minimum and maximum are located at different corners or boundaries). The converse is the centre distance, which does not provide directionally unique distances. Yet, in combination with the X and Y coordinates and the corner EDFs it might help to account for non-linear effects. Another approach, instead of using the seven generic EDFs applied in this study, would be to use a distance transform for each sample location (i.e. sample EDFs). This might enable less complex regression algorithms to reveal local effects better, but it would also increase markedly the number of predictors and computation by a factor of 45 in this study. We used the minimum and maximum values of the X and Y coordinates of the sample set to determine the origin of the distance transforms. An additional buffer is not required and, because EDM might be considered an interpolation method, spatial extrapolation is not recommended.

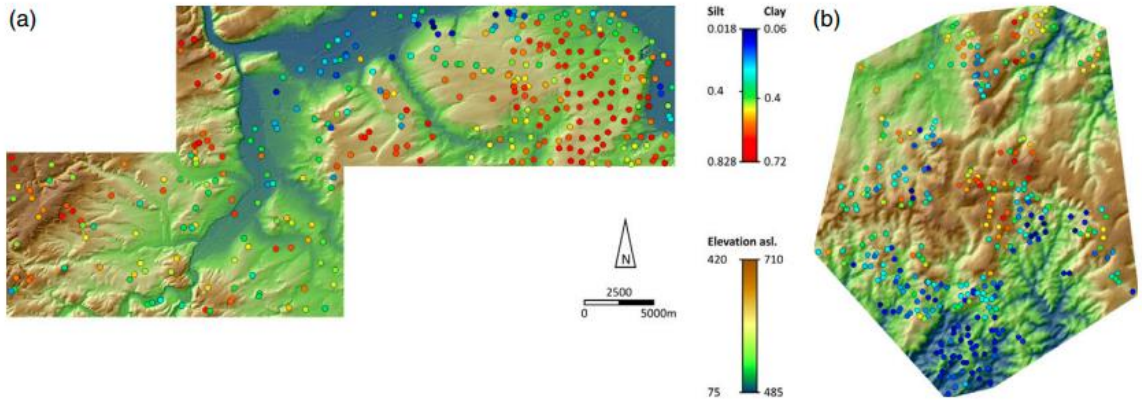

Figure 1 Sample locations showing the silt and clay content and elevation a.s.l. (m) for (a) Piracicaba and (b) Rhine-Hesse.

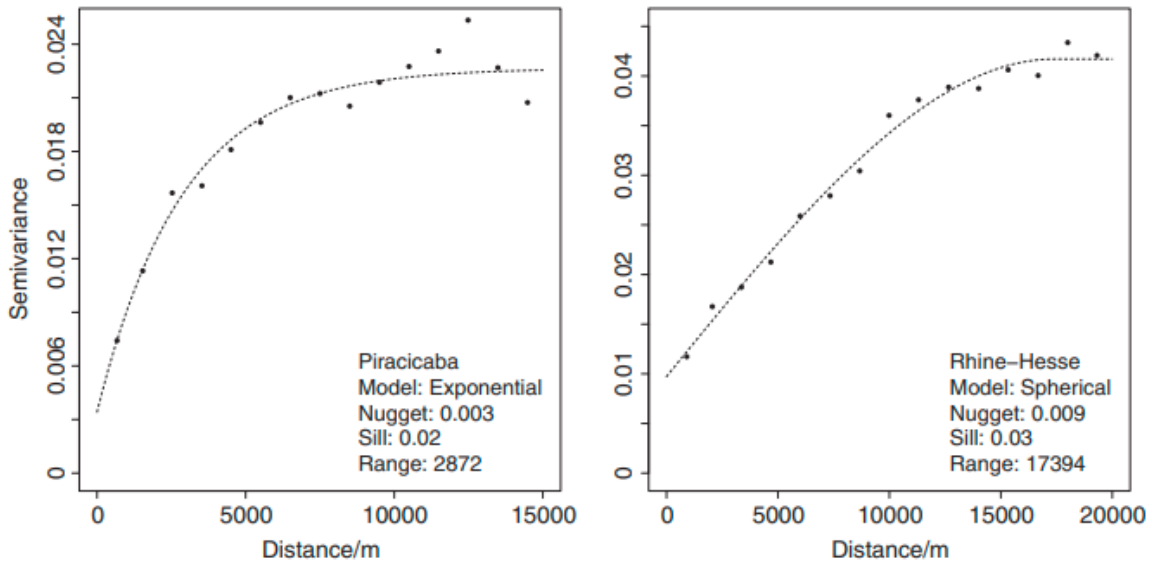

Figure 2 Experimental variograms (dots) and fitted models (dashed lines) for the clay dataset of Piracicaba and the silt dataset of Rhine-Hesse.

To evaluate the effects of combining EDFs with relevant, and partially irrelevant, terrain attributes on the performance of different models, we produced two terrain attribute subsets (T1, T2) from a feature-importance analysis. We derived the average

feature importance with the model-specific feature-importance analysis functions implemented in random forests (RF) and Cubist, together with a model-independent filter approach that uses the R2 value from a locally weighted scatterplot smoothing (LOESS) regression for each feature. All calculations were carried out using the R package caret (Kuhn, 2017). The first terrain subset (T1) contains only the most important terrain attribute and the second subset (T2) contains the three most important terrain attributes. The T3 subset contains all eight terrain attributes. To determine the effect of the EDF predictors, their combinations and the influence of the terrain attributes, we evaluated the following combinations of EDM predictors with the environmental covariates:

• X and Y coordinates (XY)

• Corner distances+centre distance (CD)

• X and Y coordinates+corner distances + centre distance (XY +CD)

• All terrain attributes (T3)

• X and Y coordinates+terrain attribute subset 1 (XY +CD +T1)

• X and Y coordinates+terrain attribute subset 2 (XY +CD +T2)

• X and Y coordinates+all terrain attributes (XY +CD +T3)

• X and Y coordinates+corner distances+centre distance+ terrain attribute subset 1 (XY +CD +T1)

• X and Y coordinates+corner distances+centre distance+ terrain attribute subset 2 (XY +CD +T2)

• X and Y coordinates+corner distances+centre distance+all terrain attributes (XY +CD +T3)

The range of the feature space of all spatial predictors was standardized to values between 0 and 1, which is required for some algorithms such as neural networks (NN) (cf. Behrens et al., 2005). All models used the same data without any further model-specific preprocessing in terms of variable selection or scaling.

Regression approaches tested with the EDF predictors

The choice of the regression can be important for EDM because of the effect it has on the map of predictions. Most transitions in nature are relatively smooth, over longer or shorter distances. The use of a decision tree on continuous X and Y spatial coordinates to interpolate a spatially correlated field can produce discontinuous response surfaces (sharp boundaries), which are unnatural and not visually appealing (Figures 10 and 11). Yet, these discontinuous surfaces might produce a model that is well validated. Therefore, implementing EDM requires careful choice of the appropriate regression for the specific aim. Consequently, we compared several algorithms. Table 1 lists the models tested using the caret package in R (Kuhn, 2017). The following sections provide a short overview of the methods. Most of these methods have already been applied successfully in the context of digital soil analysis and mapping (e.g. Grimm et al., 2008; Bui et al., 2009; Viscarra Rossel & Behrens, 2010; Schmidt et al., 2014).

Linear regression

Multiple linear regression examines linear correlations between multiple independent variables and a dependent variable. We applied the least square criterion for calibrating the model (Rao & Toutenburg, 1999). It is the most general and widely used model and served as a reference in this study. It was also used as part of regression kriging and GWR in this study.

Table 1 Regression models and the corresponding R libraries compared for Euclidean distance fields in machine learning (EDM) in this study.

Regression model	Method	R library	Library reference
Linear regression			
Linear model	lm	base	R Core Team, 2017
Support vector regression			
Radial basis function kernel	svmRadial	kernlab	Karatzoglou *et al.*, 2004
Regression trees			
Random forest (RF)	RF	randomForest	Liaw & Wiener, 2002
Cubist	Cubist	cubist	Quinlan, 1992; Kuhn, 2017
MARS			
Bagged multivariate adaptive regression splines	bagEarth	earth	Milborrow, 2017; Kuhn, 2017
Neural networks			
Model averaged neural network	avNNet	nnet	Venables & Ripley, 2002; Kuhn, 2017

Support vector machines

Support vector machines are a kernel-based learning method from statistical learning theory. They make use of an implicit mapping of the input data into a high-dimensional feature space defined by a kernel function (Karatzoglou et al., 2004). It is possible to derive a linear hyperplane as a decision function for non-linear problems and then apply a back-transformation in the non-linear space. We used the typical general-purpose radial basis function kernel in this study (Karatzoglou et al., 2004).

Decision tree ensembles

One of the most recent improvements in ensemble learning, which has become widely adopted, is RF (Breiman, 2001; Grimm et al., 2008). It aggregates multiple classification or regression tree predictions based on changes in the training dataset through sampling in the instance and feature space. Cubist uses if–then rules that partition the data. When the conditions in each rule are satisfied, a linear least squares model is used to predict the response (Quinlan, 1992). There are various examples of the use of Cubist for digital soil mapping (e.g. Bui et al., 2009).

Multivariate adaptive regression splines

Multivariate adaptive regression splines (MARS) introduced by Friedman (1991) are a generalization of recursive partitioning regression approaches such as classification and regression trees (CART, Breiman et al., 1984). By applying linear basis functions between the splits of the partitioned space, MARS generates piecewise linear models instead of piecewise constant models like CART. Therefore, when the underlying function is continuous, the accuracy of prediction is expected to be higher with MARS (Friedman, 1991). The piecewise functions are aggregated in terms of an additive model.

Single hidden layer artificial neural networks

Neural networks are frequently used in DSM studies (e.g. Behrens et al., 2005). In this study we used single hidden layer feed-forward NN as described in Venables & Ripley (2002). Kuhn (2017) extended the model in terms of an ensemble approach, which aggregates the same NN model based on a different random number seeds.

Reference algorithms currently used for DSM

Kriging. Kriging is applied in several fields of environmental science; it was one of the first and most important, spatial interpolation techniques. Kriging is based on the theory of regionalized variables (Matheron, 1963) and is a spatial distance-weighted interpolation method that assumes stationarity or intrinsic stationarity of the mean (Webster & Oliver, 2007). The weighting is based on the spatial autocorrelation function, which can be visualized and analysed using a variogram. Regression kriging (RK) is a hybrid extension of the above that combines a linear regression model with kriging of the residuals (Neuman & Jacobson, 1984; Odeh et al., 1994). The advantage of RK is the inclusion of an external trend. Regression kriging is equivalent to universal kriging or kriging with external drift (e.g. Hengl et al., 2003). We used the gstat package (Pebesma, 2004) in R for variography and kriging.

Geographically weighted regression. Geographically weighted regression (GWR) is a local distance-weighted linear regression technique that accounts for local spatial variation (Brunsdon et al., 1996). It enables regional prediction of properties based on a linear regression with spatially varying regression coefficients. The spatial kernel used to weight observations in the regression is based on their distance to the centre and can be constant or adaptive. We used an adaptive Gaussian spatial kernel as implemented in the GWmodel package in R (Gollini et al., 2015), which ensured that the kernel size was adapted to the sample density.

Contextual mapping. In contrast to common DSM approaches based on derivatives computed from digital terrain analysis, ConMap (Behrens et al., 2010) and ConStat (Behrens et al., 2014) do not derive standard terrain attributes. Both ConMap and ConStat are designed to analyse simultaneously a wide range of spatial scales, from

the local or point scale to supra-regional scales, which is not typically accomplished with conventional terrain analysis. In the Rhine-Hesse case study the largest scale or neighbourhood size was 1000 times larger than the cell size of the DEM.

ConMap and ConStat differ in the way that terrain features are generated and described. ConMap uses elevation differences from the centre pixel to each pixel in a sparse circular neighbourhood. ConStat uses statistical measures within growing, sparse circular neighbourhoods. In both cases, the terrain indices extracted for each location are used as predictors. The advantage of ConStat is that the resulting model can be interpreted in terms of soil genesis using feature importance analysis and partial dependence models (Behrens et al., 2014). Both methods depend on terrain indices only; therefore, they have no explicit geographic component as in RK, GWR or EDM. However, they can account for spatial dependence (Behrens et al., 2010, 2014). A related approach to the above methods is CSM (Behrens et al., 2018). In contrast to ConMap and ConStat, CSM uses a small set of common terrain attributes derived from scaled versions of the DEM generated by a Gaussian pyramid approach. The advantages compared to ConMap and ConStat are that the models are easier to interpret, the entire range of scales can be covered, and the approach is computationally less demanding. The maximum spatial context analysed with ConMap and ConStat in this study was set to a neighbourhood radius of 20 km for Rhine-Hesse and 25 km for Piracicaba. The variograms of the clay and silt distribution are shown in Figure 3.

Validation. Several aspects have to be considered regarding validation accuracy:

• the effect of different EDF and terrain predictor combinations on modelling accuracy,

• the differences between regression approaches tested with the EDF predictors, and

• the comparison of EDM predictions against the reference approaches (OK, RK, GWR and contextual mapping).

Ten times 10-fold cross-validation was used to determine modelling accuracy for all models. Begleiter & El-Yaniv (2008) proposed that estimation of parameters by the regression approaches and accuracy of estimates from modelling should be embedded within one cross-validation procedure. Therefore, we tested different parameter settings in a grid learning approach (e.g. Schmidt et al., 2008) implemented in the R package caret (Kuhn, 2017). Therefore, we used a single ten-fold cross-validation approach. Ten times ten-fold cross-validation was used to derive the final modelling accuracy and the 95% confidence intervals of the accuracies from ten-fold cross-validation. We used the coefficient of determination (R2) as the criterion to interpret the differences between the models and the study sites.

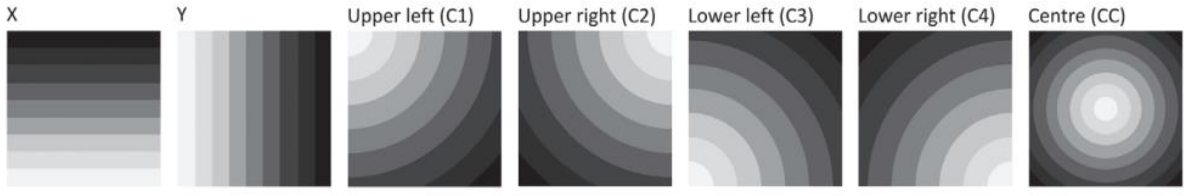

Figure 3 Visualization of the Euclidean distance fields in machine learning (EDM) predictors.

Results

Correlation and feature importance

The correlation between the soil properties and the EDFs, as well as the terrain attributes, was comparable at both study sites, indicating a similar effect of terrain and spatial dependence on the distribution of the soil property (Table 2). In Piracicaba, the maximum value of the correlation coefficient was 0.56 for the EDFs and for the terrain attributes. In Rhine-Hesse, the maximum was 0.27 for the EDFs and 0.29 for terrain, indicating a more complex landscape and thus pedogenesis.

Table 2 Pearson correlation coefficients between clay (Piracicaba) and silt (Rhine-Hesse), and the EDFs and terrain attributes.

Predictor	Clay	Silt
Y	0.56	−0.11
X	0.10	0.19
CC	−0.20	0.27
C4	0.45	−0.25
C3	−0.51	−0.13
C2	0.49	0.15
C1	−0.48	0.25
Valley depth	−0.46	−0.13
TWI	0.03	−0.03
Slope	0.05	0.14
Longitudinal curvature	0.19	−0.01
Elevation	0.56	0.29
Cross-sectional curvature	0.09	−0.08
sin(Aspect)	0.08	0.17
cos(Aspect)	0.03	0.05

CC, distances to the centre location of the sample set; C1, C2, C3, C4, distances to the corners of a rectangle around the sample set; EDF, Euclidean distance fields; TWI, topographic wetness index.

Figures 4 and 5 show that the general trend of the three feature-importance measures is relatively consistent. The trend appears to be more important for the EDFs than the terrain attributes for both study sites. Elevation was the most important terrain attribute in both cases and was the only one with the same range of importance as the EDF predictors. All other terrain attributes had average importance values below the weakest EDF. For Rhine-Hesse, the most useful remaining terrain attributes selected for subset T2 were slope and sin(Aspect) (Figure 5). For Piracicaba, the additional terrain attributes for T2 were valley depth and TWI (Figure 4).

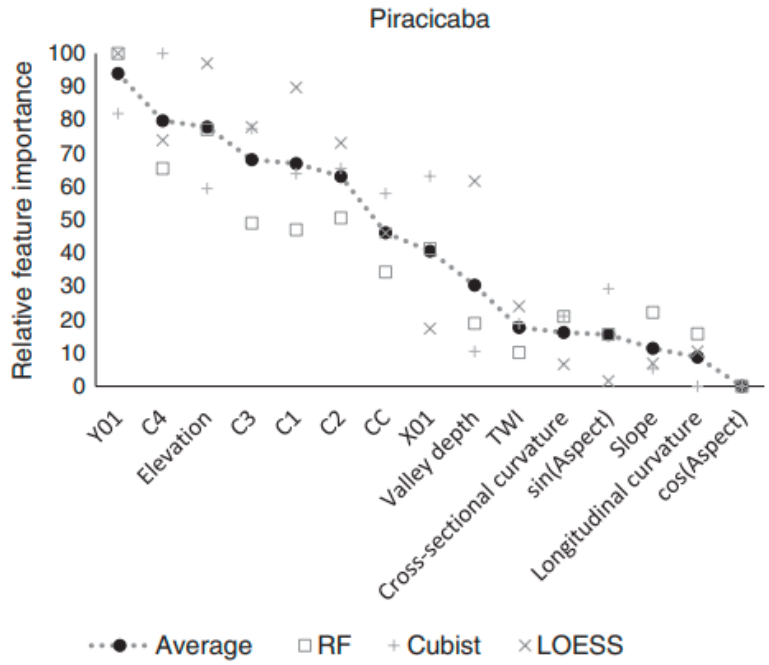

Figure 4 Feature-importance values for Piracicaba. Feature-importance values calculated by random forests (RF), Cubist and locally weighted scatterplot smoothing (LOESS) regression using the R package caret.

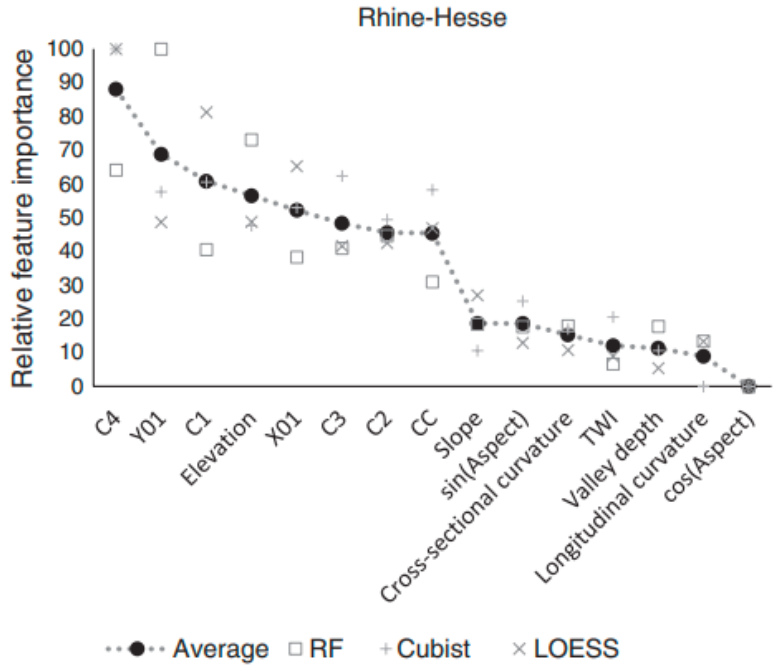

Figure 5 Feature-importance values for Rhine-Hesse. Feature-importance values calculated by random forests (RF), Cubist and locally weighted scatterplot smoothing (LOESS) regression using the R package caret.

Validation

Because the results of both study sites show similar general patterns, in most cases, the results are described together. Figure 6 shows the R2 cross-validation values and the corresponding 95% confidence intervals of the EDM approaches averaged across all regression algorithms. Figures 7 and 8 give the R2 values and corresponding 95% confidence intervals for the regression approaches for Piracicaba and Rhine-Hesse, respectively. Figure 9 shows the R2 cross-validation results of the reference mapping approaches. The R2 values of the CSM approach are taken from Behrens et al. (2018). The largest validation accuracies within each group of predictor combinations indicate that the two tree-based modelling approaches, Cubist and RF, generally performed

best (Figures 7 and 8). For the predictor combinations including terrain attributes, bagEarth also had large validation accuracies. The svmRadial and avNNet methods were in some cases similar to bagEarth but were less accurate overall. The linear model did not perform well in any of the scenarios tested. The main results of the comparison of combinations of the X and Y coordinates (XY), the corner and centre distance transforms (CD) and the terrain attributes, are:

• prediction accuracy of the CD data was generally significantly greater than for the XY data,

• prediction accuracy of the XY +CD data was generally significantly higher than the CD data alone,

• the increase in prediction accuracy when adding CD to XY was comparable for both study sites,

• although correlation analysis suggested a comparable effect of terrain and EDF predictors, the prediction accuracy was least when only terrain attributes were used,

• the largest prediction accuracies were obtained when EDF and terrain attributes were combined,

• in general, the XY +CD +T models attained significantly greater accuracies than the corresponding XY +T models,

• in some cases for Cubist and RF there was no significant difference when the CD were added to XY,

• adding non-relevant predictors, such as in T3, often had a significant negative effect on prediction accuracy, which was an effect of fitting noise,

• analysis of single regression approaches showed that the strength of the negative effect of non-relevant predictors was related to the regression approaches,

• radialSVM was the most adversely affected by noisy predictors, whereas the linear regression model (lm) was not affected at all,

• bagEarth, RF and Cubist analysed the EDF+T datasets best,

• the negative effect of noise was less pronounced with XY +CD +T data than XY +T data, and

• the greatest increase in R2 with XY and CD combined was for lm and avNNet, showing that less complex models benefit from the additional information.

Importantly, the additional CD spatial location predictors with XY or XY +T significantly increased prediction accuracy in most cases.

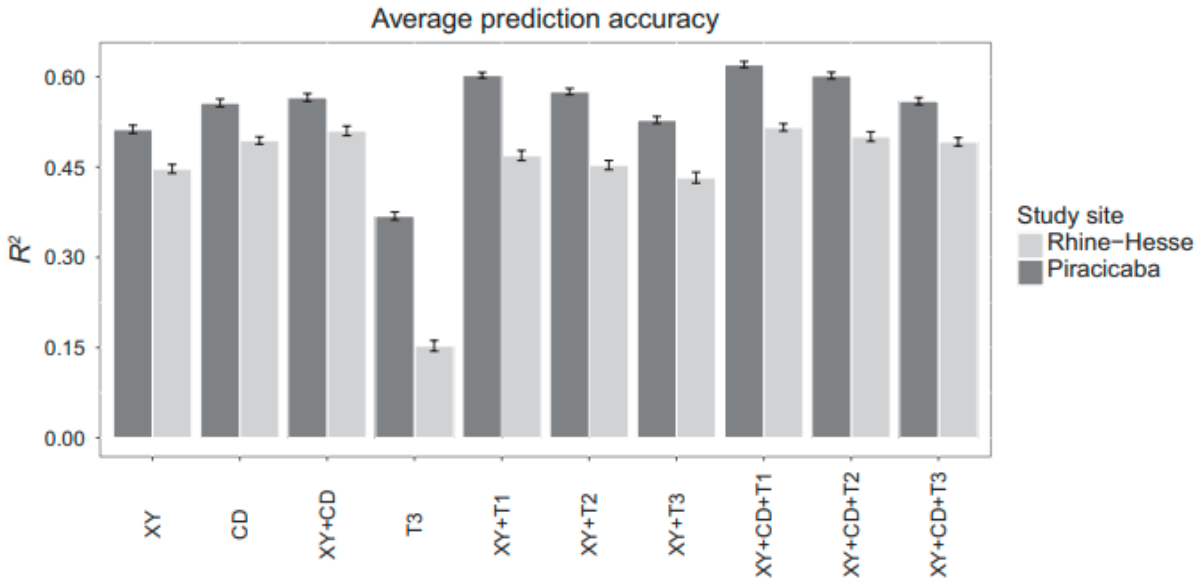

Figure 6 Average R^2 values of the Euclidean distance fields in machine learning models for Piracicaba and Rhine-Hesse. The lines indicate the 95% confidence interval

Mapping

Visualization of the model results is part of interpreting the behaviour of the machine learning approaches when using different combinations of EDFs and environmental covariates. We illustrate the most relevant models based on the XY, XY +CD, T3 and XY +CD +T3 predictors. The EDM predictions and the maps of the reference DSM approaches for Piracicaba are shown in Figure 10, and for Rhine-Hesse in Figure 11. In each case, the legends are restricted to the range of the soil property values in the sample data. The following sections pertain to the mapping.

The EDM XY and XY+CD models

The most interesting comparisons concern the EDM modelling approaches that use only EDFs as predictors. In general, the local patterns were stronger when XY +CD were used as predictors instead of XY only. In this case, even the linear regression model showed the general spatial trend of the silt and clay distributions. However, only Cubist, RF and svmRadial showed details comparable to OK. Cubist and RF, and to a lesser extent bagEarth, produced visible artefacts, which stemmed from the methods.

The EDM XY+CD +T3 models

Visually, the EDM XY +CD +T3 RF, Cubist and bagEarth predictions resembled the ConMap predictions most closely. SvmRadial and avNNet showed a similar pattern, but with more spatial variation, which might be a function of fitting non-relevant predictors, resulting in spurious spatial detail. Like ConMap, the EDM predictions with RF, Cubist and bagEarth showed less local variation than for svmRadial, but they achieved greater prediction accuracies. Thus, they were less affected by noisy or irrelevant predictors.

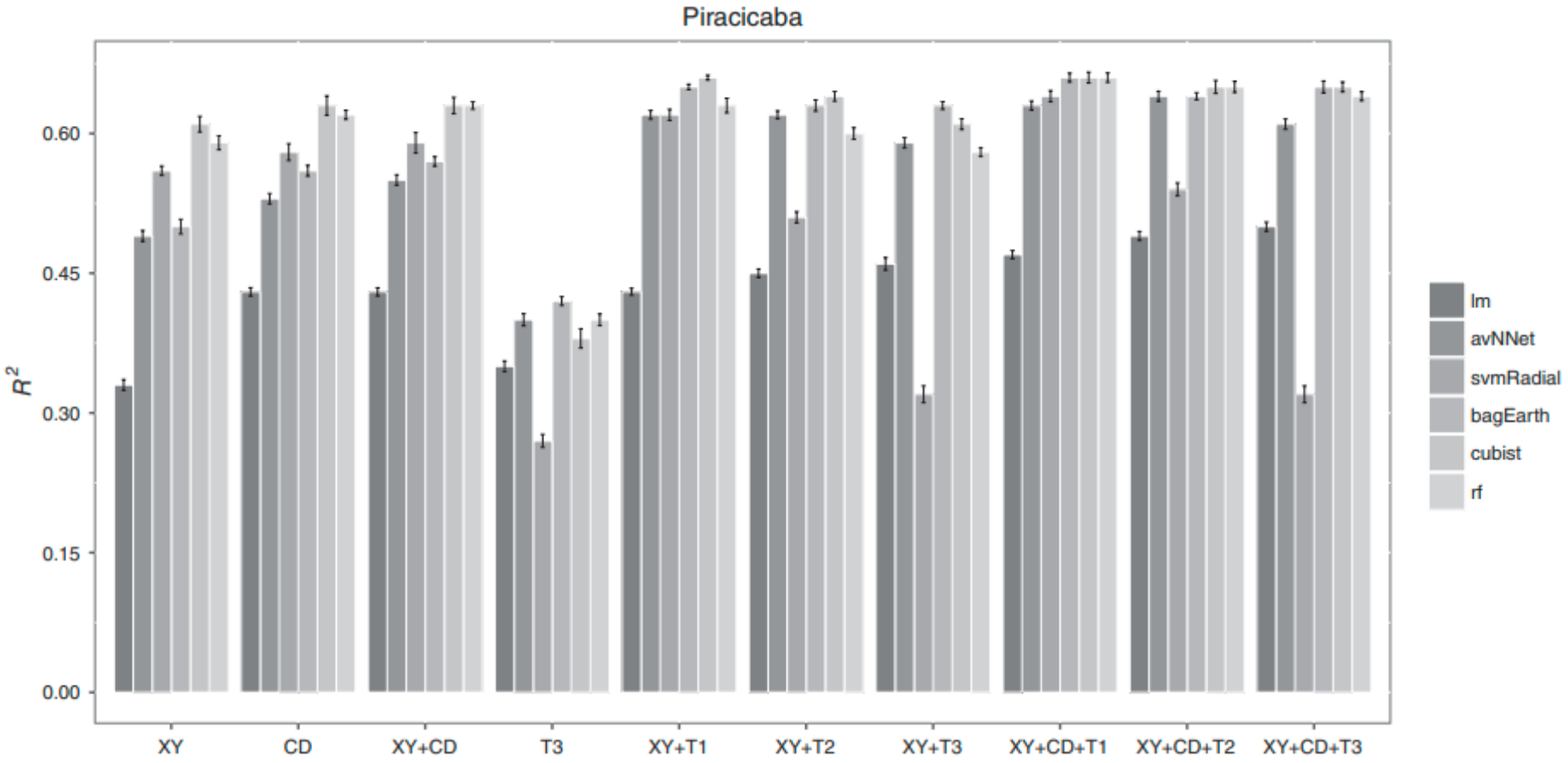

Figure 7 The R^2 values of the Euclidean distance fields in machine learning (EDM) models for Piracicaba. The lines indicate the 95% confidence interval.

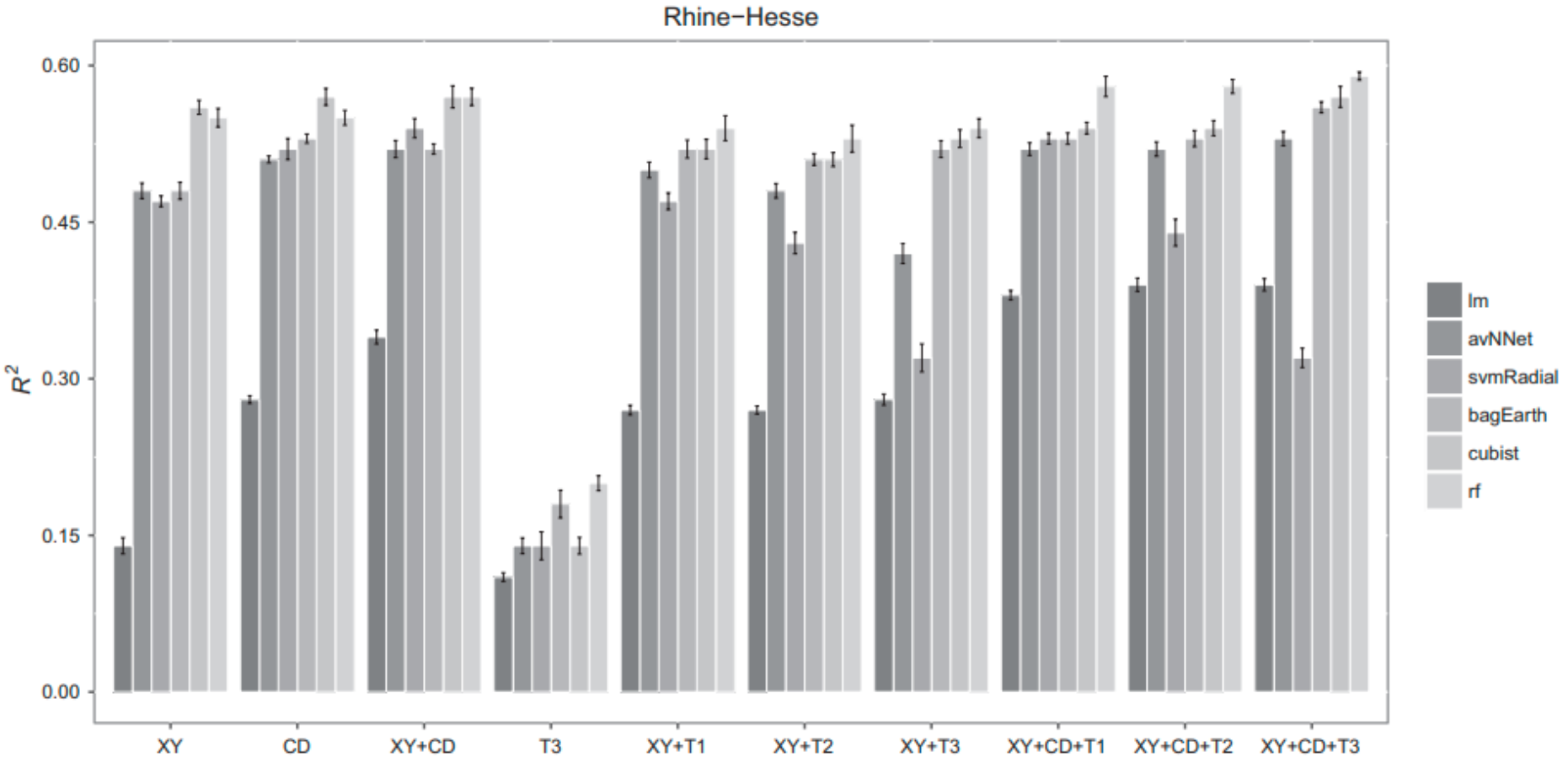

Figure 8 The R^2 values of the Euclidean distance fields in machine learning (EDM) models for Rhine-Hesse. The lines indicate the 95% confidence interval.

The EDM predictors and piece-wise models

The XY models clearly showed artefacts related to the piece-wise modelling approaches of the tree-based ensembles and to a lesser extent the bagEarth model. Although this resulted in unnatural looking response surfaces, they were the best performing interpolation approaches based on the EDF+T datasets tested so far. One advantage of this behaviour might be that we are immediately reminded that we are looking at a model and not at ground truth. The addition of CD to the XY +T predictors also produced similar artefacts (e.g. abrupt boundaries), but they were less obvious. When we included terrain data as additional covariates in hybrid 'scorpan' modelling, only a very few such artefacts remained visible.

Comparison of EDM to the reference mapping approaches

Both EDM (XY +CD +T3) and RK produced similar accuracies. The contextual mapping approaches gave results that were slightly better than all other models in Rhine-Hesse. In Piracicaba they were similar to RK and the XY +CD +T models. In both study areas, GWR was only slightly better than lm. The local GWR regressions seemed to lack the global information required to derive a good general model. The relations are also non-linear in general so that local linear models do not account well for spatially varying geographical relationships. Another reason is the generally small effect of terrain at the scale of the DEM resolution, which might be a case where GWR should not be considered. The generally smaller contribution of common terrain attributes to model accuracy in Rhine-Hesse also seemed to account for the poorer validation accuracy of RK compared to OK. Therefore, the residuals used in the kriging part of RK seemed to provide less information than the original data, which must also be attributed to the adverse effect of non-relevant predictors.

In Piracicaba RK was equivalent to the contextual mapping approaches. However, it performed less well in Rhine-Hesse. The best EDM approaches in Rhine-Hesse were based on RF and Cubist, which were similar to OK, but their R2 values were approximately 5% smaller than for contextual mapping (Figures 7–9).

It is unlikely that a different set of conventional terrain attributes at the scale of resolution of the DEM would help to increase the prediction accuracy of the EDM approach, RK or GWR in both regions significantly. For Rhine-Hesse the set of reference terrain attributes in Behrens et al. (2010) for ConMap was different and contained many more attributes. Nevertheless, the R2 value obtained with RF in that study was also smaller than 0.2. It seems for both datasets that the better the terrain-based predictions performed, the more comparable were the validation accuracies between all models.

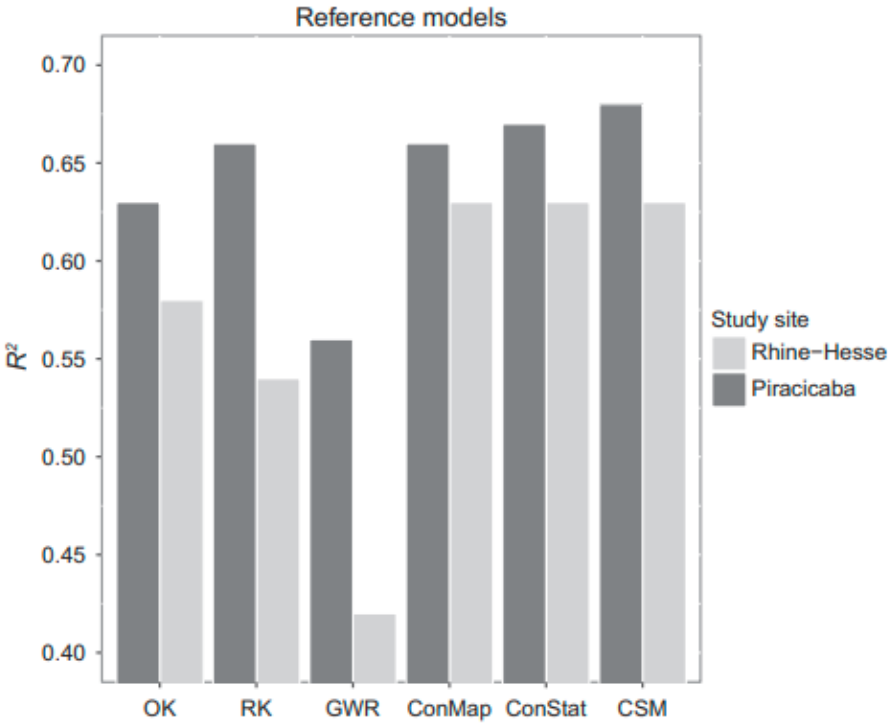

Figure 9 The R2 values of the reference modelling approaches for Piracicaba and Rhine-Hesse.

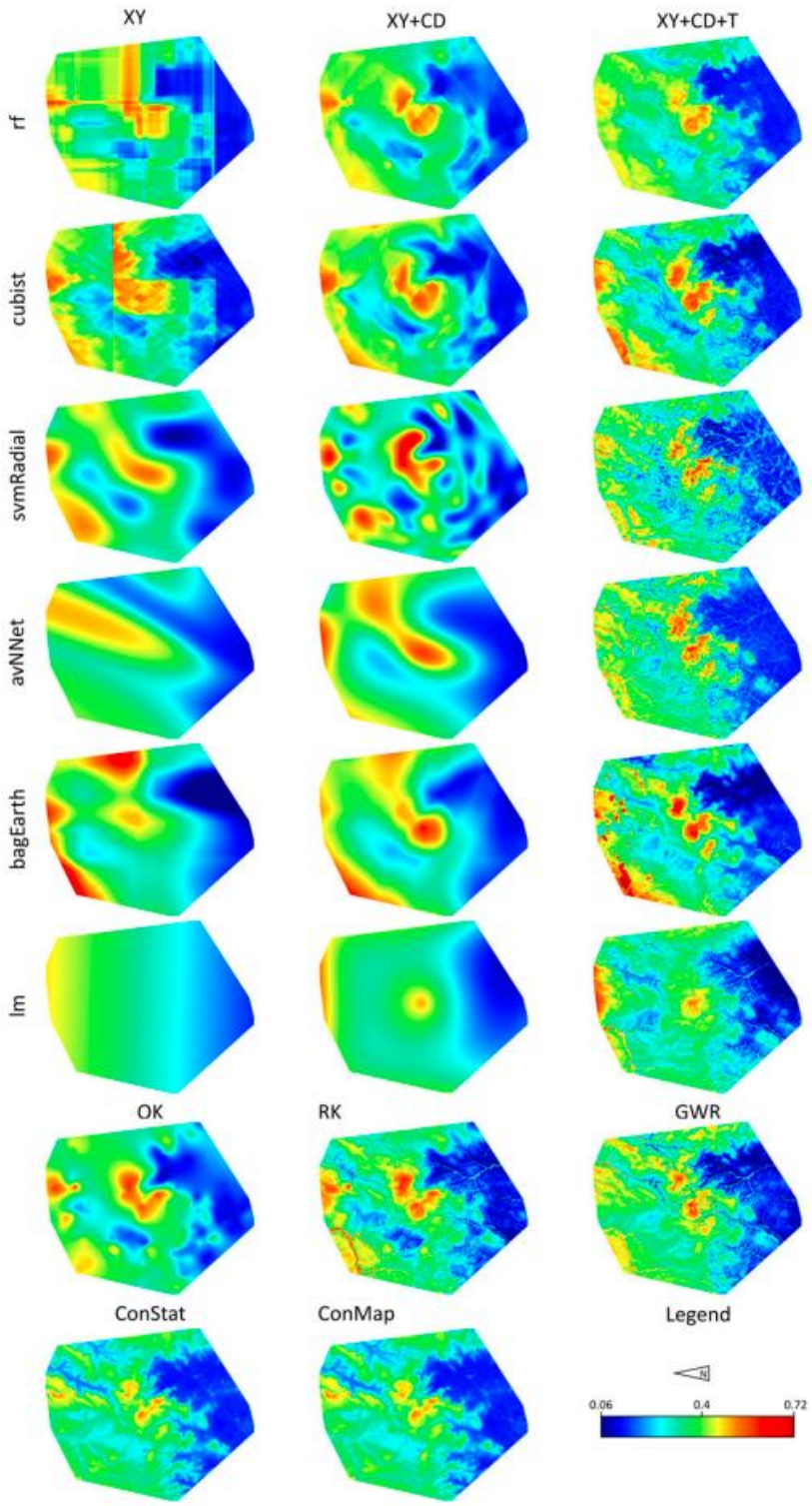

Figure 10 Spatial modelling results for Piracicaba. The upper section shows the spatial models arranged as a matrix where the rows reference the machine learning algorithms and the columns the different Euclidean distance fields in machine learning (EDF) combinations used for modelling (XY, XY +CD and XY +CD +T). The lower section shows the spatial models of the reference algorithms OK, RK, GWR, ConMap and ConStat.

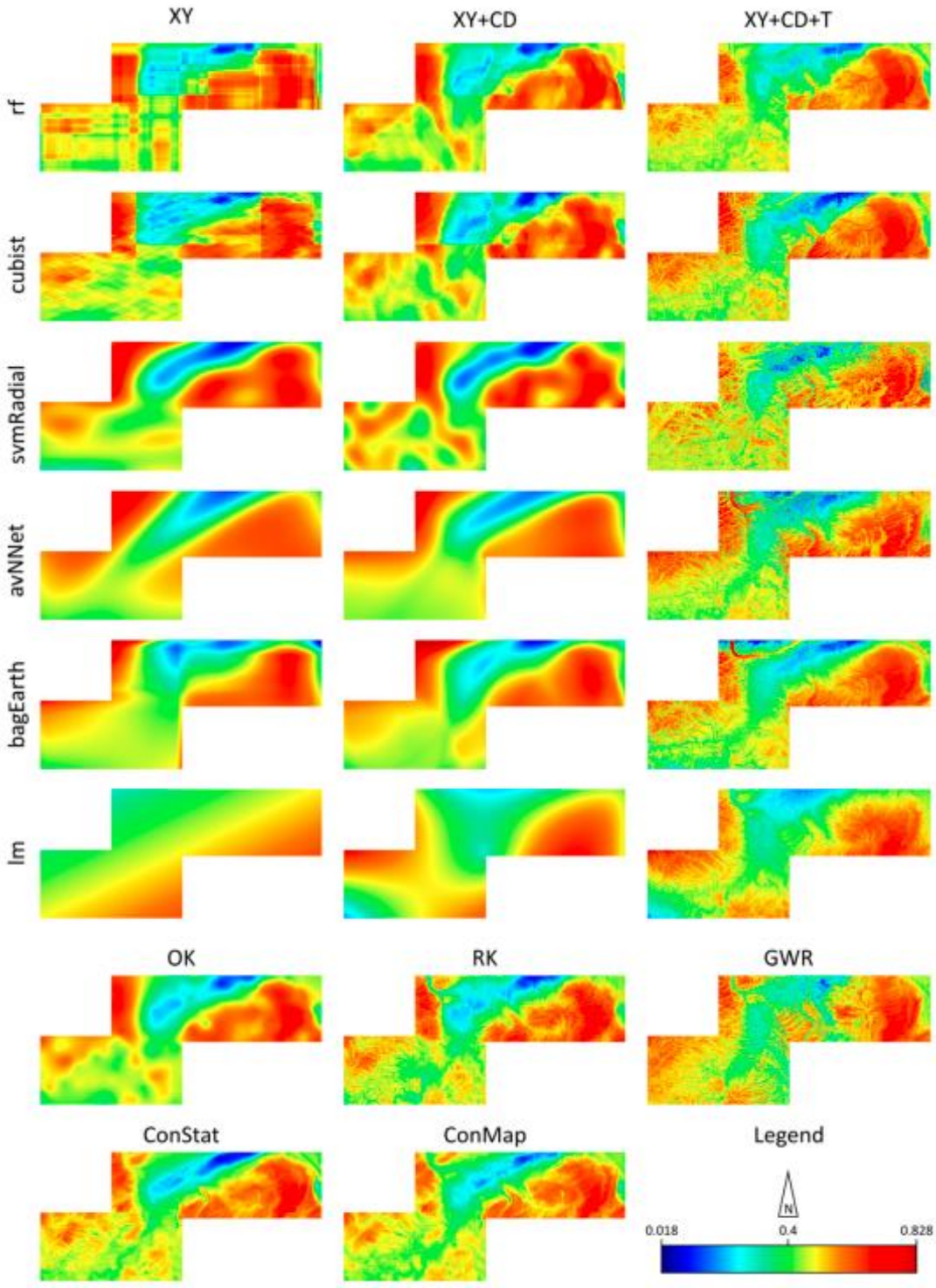

Figure 11 Spatial modelling results for Rhine-Hesse. The upper section shows the spatial models arranged as a matrix where the rows reference the machine learning algorithms and the columns the different Euclidean distance fields in machine learning (EDF) combinations used for modelling (XY, XY +CD and XY +CD +T). The lower section shows the spatial models of the reference algorithms OK, RK, GWR, ConMap and ConStat.

Discussion

Contextual spatial modelling, EDM and GWR differ from RK in their ability to consider non-stationary relations between a soil property and environmental covariates directly. The contextual mapping approaches and EDM account for spatial autocorrelation by using covariates that identify and describe some of the spatial structure in a target variable (e.g. de Knegt et al., 2010). In the case of contextual mapping, these covariates represent substitutes for environmental factors, whereas for EDM they are explicit spatially autocorrelated Euclidean distance fields that are not specific regarding the location and values of the sample set and environmental covariates. These EDFs enable the regression model to infer the relevant spatial dependence when predicting unknown values at new locations based on known values at nearby sampled locations. This is the opposite of GWR, for which local models are used, which also aim to extract the spatial structure that is not described by environmental covariates. Contextual mapping, EDM and RK differ from GWR because GWR does not use the entire sample set for creating the regression model at specific locations, but only local subsets. Thus, it might fail to reveal relevant parts of the soil–environmental relations, which might only be extractable from the entire dataset.

The theoretical advantages of EDM have not resulted here in clear increases in prediction accuracy compared to the other (reference) methods, although the accuracy attained by EDM was similar to that of RK, which cannot account for changing geographical relations. However, the theoretical advantage of EDM should result in greater prediction accuracies when there is strong spatial autocorrelation, when the relation of the dependent variable to the environmental covariates is strong and when the extent of changes in the geographic relations in space are large.

The GWR, and similar local models, often cannot develop relations from the entire dataset because it might not be useful for DSM. As shown in the Rhine-Hesse dataset, RK can be less accurate than OK if the regression model is developed on ‘noisy’ and potentially artificial relations. In the presence of non-stationarity, EDM might perform better than RK because regional variation can be dealt with directly. If the spatial structure shows a large-scale trend ConMap and ConStat might not be able to resolve it fully. In such cases, EDM, RK and GWR might outperform ConMap and ConStat.

Linear models should also be able to produce results strongly correlated with those of OK when the distances to each sample location are used as additional predictors for interpolation. However, from a comparison with the reference methods, a further increase in prediction accuracy with additional distance fields is not expected in hybrid ‘scorpan’ models for non-linear regressions. Nevertheless, it might help to improve the performance of some algorithms, such as artificial neural networks.

For the regression methods tested with EDM, the application of machine learning algorithms depends on the dataset and they can perform differently (cf. Viscarra Rossel & Behrens, 2010). Random forests, Cubist and bagged MARS seem to be good options for EDM. In many cases, SVM and NN should provide good predictions. An outstanding question is what to do about the visible artefacts in the response surfaces of the tree-based approaches.

Most of the methods tested, including EDM, are not suited for interpreting the models entirely in terms of the processes that result in soil formation. Such interpretations are achieved best with machine learning methods (e.g. RF or Cubist), together with the contextual mapping. Conversely, EDM is fast because it requires only a small set of additional predictors.

Conclusions

The generic EDFs that we described and evaluated represent a new option for improving representation of the spatial factor (n) in the ‘scorpan’ model. We showed that the accuracy of predictions made with several commonly used machine-learning approaches generally improved when the new location covariates, or EDFs, were included in the analysis. These additional measures of spatial context and position can, and do, undoubtedly contribute to improvements in spatial prediction of soil properties and spatial data mining, in general. They enable machine-learning models to vary predictions locally to model non-stationary conditions and to make locally varying predictions that use information that quantifies local spatial autocorrelation.

The results of this paper add to the growing body of evidence which suggests that machine learning models that use covariates describing spatial position or spatial context might eliminate the need for a second, separate step to correct residuals, as done in the kriging step of RK. They do this in a single-stage spatially varying prediction model. The remaining residuals ought not to exhibit any remaining spatial dependence.

Acknowledgements

This research was funded by the German Research Foundation (DFG) under the PedoScale project (BE 4023/3-1). We are very grateful to José A.M. Demattê for providing the Brazilian dataset and to the Federal Geological Survey of Rhineland Palatinate for providing the Rhine-Hesse dataset.

References

Begleiter, R. & El-Yaniv, R. 2008. A Generic Tool for Performance Evaluation of Supervised Learning Algorithms. Technical Report No CS-2008-01. Computer Science Department, Technion, Israel [WWW document]. URL http://www.cs.technion.ac.il/users/wwwb/cgi-bin/trget.cgi/2008/CS/CS-2008-01.pdf [accessed on 27 April 2018].

Behrens, T., Förster, H., Scholten, T., Steinrücken, U., Spies, E.-D. & Goldschmitt, M. 2005. Digital soil mapping using artificial neural networks. Journal of Plant Nutrition and Soil Science, 168, 21–33.

Behrens, T., Schmidt, K., Zhu, A.-X. & Scholten, T. 2010. The ConMap approach for terrain based digital soil mapping. European Journal of Soil Science, 61, 133–143.

Behrens, T., Schmidt, K., Ramirez-Lopez, L., Gallant, J., Zhu, A.-X. & Scholten, T. 2014. Hyper-scale digital soil mapping and soil formation analysis. Geoderma, 213, 578–588.

Behrens, T., Schmidt, K., MacMillan, R.A. & Viscarra Rossel, R.A. 2018. Multiscale contextual spatial modelling with the Gaussian scale space. Geoderma, 310, 128–137.

Breiman, L. 2001. Random forests. Machine Learning, 45, 5–32.

Breiman, L., Friedman, J.H., Olshen, R.A. & Stone, C.J. 1984. Classification and Regression Trees. Wadsworth, Belmont, CA.

Brunsdon, C., Fotheringham, A.S. & Charlton, M.E. 1996. Geographically weighted regression: a method for exploring spatial nonstationarity. Geographical Analysis, 28, 281–298.

Bui, E., Hendersen, B. & Viergever, K. 2009. Using knowledge discovery with data mining from the Australian soil resource information system database to inform soil carbon mapping in Australia. Global Biogeochemical Cycles, 23, 1–15.

Conrad, O., Bechtel, B., Bock, M., Dietrich, H., Fischer, E., Gerlitz, L. et al. 2017. System for Automated Geoscientific Analyses (SAGA). Version 3.0 [WWW document]. URL http://www.saga-gis.org/en/index.html [accessed on 31 May 2017].

Friedman, J.H. 1991. Multivariate adaptive regression splines. Annals of Statistics, 19, 1–67.

Gollini, I., Lu, B., Charlton, M., Brunsdon, C. & Harris, P. 2015. GWmodel: an R package for exploring spatial heterogeneity using geographically weighted models. Journal of Statistical Software, 63, 1–50.

Grimm, R., Behrens, T., Märker, M. & Elsenbeer, A. 2008. Soil organic carbon concentrations and stocks on Barro Colorado Island–digital soil mapping using random forests analysis. Geoderma, 146, 102–113.

Hengl, T., Heuvelink, G. & Stein, A. 2003. Comparison of Kriging with External Drift and Regression Kriging. International Institute for Geo-information Science and Earth, Enschede [WWW document]. URL https://webapps.itc.utwente.nl/librarywww/papers_2003/misca/hengl_comparison.pdf [accessed on 26 April 2018].

Jenny, H. 1941. Factors of Soil Formation. McGraw-Hill, New York.

Karatzoglou, A., Smola, A., Hornik, K. & Zeileis, A. 2004. kernlab–An S4 package for kernel methods in R. Journal of Statistical Software, 11, 1–20.

de Knegt, H.J., van Langevelde, F., Coughenour, M.B., Skidmore, A.K., de Boer, W.F., Heitkönig, I.M.A. et al. 2010. Spatial autocorrelation and the scaling of species–environment relationships. Ecology, 91, 2455–2465.

Krumbein, W.C. 1959. Trend surface analysis of contour type maps with irregular control-point spacing. Journal of Geophysical Research, 64, 823–834.

Kuhn, M. 2017. Caret: Classification and Regression Training. R Package Version 6.0–76 [WWW document]. URL https://CRAN.R-project.org/package=caret [accessed on 31 May 2017].

Kumar, S., Lal, R. & Liu, D. 2012. A geographically weighted regression kriging approach for mapping soil organic carbon stock. Geoderma, 189–190, 627–634.

Liaw, A. & Wiener, M. 2002. Classification and regression by random Forest. R News, 2, 18–22.

Matérn, B. 1960. Spatial variation. Meddelanden från Statens Skogsforskningsinstitut, 2nd edn (1986), Lecture Notes in Statistics, No 36 edn, Volume 49. Springer, New York.

Matheron, G. 1963. Principles of geostatistics. Economic Geology, 58, 1246–1266.

McBratney, A.B., Mendonca Santos, M.L. & Minasny, B. 2003. On digital soil mapping. Geoderma, 117, 3–52.

Mezzalira, S. 1965. Descrição Geográfica e Geológica das folhas de Piracicaba e São Carlos (SP). In: Boletim do Instituto Geográfico e Geológico No 43. Instituto Geográfico e Geológico, Sao Paulo.

Milborrow, S. 2017. Earth: Multivariate Adaptive Regression Splines. R Package Version 4.5.0 [WWW document]. URL https://CRAN.R-project.org/package=earth [accessed on 31 May 2017].

Moran, C. & Bui, E. 2002. Spatial data mining for enhanced soil map modelling. International Journal of Geographical Information Science, 16, 533–549.

Neuman, S.P. & Jacobson, E.A. 1984. Analysis of nonintrinsic spatial variability by residual kriging with application to regional groundwater level. Mathematical Geology, 16, 499–521.

Odeh, I., McBratney, A. & Chittleborough, D. 1994. Spatial prediction of soil properties from landform attributes derived from a digital elevation model. Geoderma, 63, 197–214.

Oliver, M.A. & Webster, R. 1990. Kriging: a method of interpolation for geographical information systems. International Journal of Geographical Information Systems, 4, 313–332.

Páez, A. 2004. Anisotropic variance functions in geographically weighted regression models. Geographical Analysis, 36, 299–314.

Pebesma, E.J. 2004. Multivariable geostatistics in S: the gstat package. Computers & Geosciences, 30, 683–691.

Quinlan, R. 1992. Learning with continuous classes. In: Proceedings of the 5th Australian Joint Conference on Artificial Intelligence (A. Adams & L. Sterling), 343–348, World Scientific, Singapore.

R Core Team 2017. R: A Language and Environment for Statistical Computing. R Foundation for Statistical Computing, Vienna [WWW document]. URL https://www.R-project.org/ [accessed on 31 May 2017].

Rao, C. & Toutenburg, H. 1999. Linear Models: Least Squares and Alternatives. Springer, New York.

Rosenfeld, A. & Pfaltz, J.L. 1968. Distance functions and digital pictures. Pattern Recognition, 1, 33–61.

Schmidt, K., Behrens, T. & Scholten, T. 2008. Instance selection and classification tree analysis for large spatial datasets in digital soil mapping. Geoderma, 146, 138–146.

Schmidt, K., Behrens, T., Daumann, J., Ramirez-Lopez, L., Werban, U., Dietrich, P. et al. 2014. A comparison of calibration sampling schemes at the field scale. Geoderma, 232–234, 243–256.

Sun, W., Minasny, B. & McBratney, A. 2012. Analysis and prediction of soil properties using local regression-kriging. Geoderma, 171–172, 16–23.

Unwin, D. 1975. An Introduction to Trend Surface Analysis (Concepts and Techniques in Modern Geography; No5). Geo Abstracts, Norwich.

Venables, W.N. & Ripley, B.D. 2002. Modern Applied Statistics with S, 4th edn. Springer, New York.

Viscarra Rossel, R.A. & Behrens, T. 2010. Data mining and knowledge discovery techniques to model and interpret soil diffuse reflectance spectra. Geoderma, 158, 46–54.

Viscarra Rossel, R.A., Webster, R., Bui, E.N. & Baldock, J.A. 2014. Baseline map of organic carbon in Australian soil to support national carbon accounting and monitoring under climate change. Global Change Biology, 20, 2953–2970.

Viscarra Rossel, R.A., Chen, C., Grundy, M.J., Searle, R., Clifford, D. & Campbell, H. 2015. The Australian three-dimensional soil grid: Australia's contribution to the Global Soil Map project. Soil Research, 53, 845–864.

Webster, R. & Oliver, M.A. 2007. Geostatistics for Environmental Scientists. Second Edition. John Wiley & Sons Ltd., Chichester. Wood, J., 1996. The geomorphological characterization of digital elevation models. Doctoral thesis, University of Leicester, Leicester, UK.

Manuscript 4: Comparison of catchment scale 3D and 2.5D modelling of soil organic carbon stocks in Jiangxi Province, PR China

Published in: PloS one 14 (8), e0220881.

Authors: Tobias Rentschler[1,2], Philipp Gries[1,2] , Torsten Behrens[1] , Helge Bruelheide[3,4], Peter Kühn[1,2] , Stefen Seitz[1] , Xuezheng Shi[5] , Stefan Trogisch[3,4], Tomas Scholten[1] and Karsten Schmidt[1,2]

[1] Chair of Soil Science and Geomorphology, Department of Geosciences, University of Tübingen, Tübingen, Germany

[2] SFB 1070 ResourceCultures, University of Tübingen, Tübingen, Germany

[3] Department of Geobotany and Botanical Garden, Institute of Biology, Martin Luther University Halle-Wittenberg, Halle, Germany.

[4] German Centre for Integrative Biodiversity Research (iDiv) Halle-Jena-Leipzig, Leipzig, Germany

[5] Institute of Soil Science, State Key Laboratory of Soil and Sustainable Agriculture, Chinese Academy of Sciences, Nanjing, China

Abstract

As limited resources, soils are the largest terrestrial sinks of organic carbon. In this respect, 3D modelling of soil organic carbon (SOC) offers substantial improvements in the understanding and assessment of the spatial distribution of SOC stocks. Previous three-dimensional SOC modelling approaches usually averaged each depth increment for multi-layer two-dimensional predictions. Therefore, these models are limited in their vertical resolution and thus in the interpretability of the soil as a volume as well as in the accuracy of the SOC stock predictions. So far, only few approaches used spatially modelled depth

functions for SOC predictions. This study implemented and evaluated an approach that compared polynomial, logarithmic and exponential depth functions using non-linear machine learning techniques, i.e. multivariate adaptive regression splines, random forests and support vector machines to quantify SOC stocks spatially and depth-related in the context of biodiversity and ecosystem functioning research. The legacy datasets used for modelling include profile data for SOC and bulk density (BD), sampled at five depth increments (0-5, 5-10, 10-20, 20-30, 30-50 cm). The samples were taken in an experimental forest in the Chinese subtropics as part of the biodiversity and ecosystem functioning (BEF) China experiment. Here we compared the depth functions by means of the results of the different machine learning approaches obtained based on multi-layer 2D models as well as 3D models. The main findings were (i) that 3rd degree polynomials provided the best results for SOC and BD (R^2 = 0.99 and R^2 = 0.98; RMSE = 0.36% and 0.07 g cm^{-3}). However, they did not adequately describe the general asymptotic trend of SOC and BD. In this respect the exponential (SOC: R^2 = 0.94; RMSE = 0.56%) and logarithmic (BD: R^2 = 84; RMSE = 0.21 g cm^{-3}) functions provided more reliable estimates. (ii) random forests with the exponential function for SOC correlated better with the corresponding 2.5D predictions (R^2: 0.96 to 0.75), compared to the 3rd degree polynomials (R^2: 0.89 to 0.15) which support vector machines fitted best. We recommend not to use polynomial functions with sparsely sampled profiles, as they have many turning points and tend to overfit the data on a given profile. This may limit the spatial prediction capacities. Instead, less adaptive functions with a higher degree of generalisation such as exponential and logarithmic functions should be used to spatially map sparse vertical soil profile datasets. We conclude that spatial prediction of SOC using exponential depth functions, in conjunction with random forests is well suited for 3D SOC stock modelling, and provides much finer vertical resolutions compared to 2.5D approaches.

Introduction

Soils are a fundamental part of ecosystem functioning and services [1]. As finite resources, soils contribute to food production, nutrient cycling, biodiversity and freshwater quality [2]. Furthermore, they are interconnected with other ecosystem functions and services, such as local and global climate alteration; and therefore, contribute indirectly to human well-being [3]. Among soil properties, soil organic carbon (SOC) plays an important role in this context. SOC increases the water-holding capacity (e.g. important for agriculture, forest and flood management), improves the physical properties of soils, such as nutrient availability for plants in agriculture and forestry, and accounts for carbon sequestration to mitigate climate change [4–6]. In forestry, there is strong interest in the effects of tree species and tree diversity on soil carbon input and mineralization as well as the net effects of these processes [7]. Knowledge about the interconnection between SOC, forests and the diversity of tree species as well as SOC stock degradation by soil erosion [8,9] and land cover change [10,11] can also help to implement countermeasures to reduce global warming [7]. Consequently, the implementation of a credible soil carbon auditing and monitoring to verify changes in SOC is crucial regarding soil security and carbon sequestration [7,12].

To preserve the functions and services provided by soils, a good quantitative understanding of the SOC stocks is required–both in the vertical domain of a soil profile as well as in the spatial domain over landscapes [13,14]. However, conventional soil maps use soil classes in horizontal dimension and soil horizons in vertical dimension. This categorical setup is often not precise enough and not well suited for interpreting soil functions and processes as well as for decision-making, since soil properties mostly vary continuous in space and time [15,16].

For the spatial prediction of continuous soil properties, such as SOC, methods of digital soil mapping (DSM) are suitable [17–19]. DSM is based on the soil forming factor concept [20] and the *scorpan* model introduced by McBratney et al. [21]. Both approaches illustrate soil information as a function of environmental covariates, influencing the process of soil formation. Terrain parameters, describing the shape of the land surface, are used widely as an environmental covariate in DSM. Terrain is an essential factor of soil formation and controls the effects of gravity, climate, lithology, water and biota [22–24]. Hence, models that are based on terrain parameters reproduce displacement and reallocation of soil (i.e. mass movements and soil erosion) and are of particular interest when modelling SOC at catchment scale [25]. Furthermore, terrain can not only be used to estimate or model soil displacement and reallocation, but also as a proxy for environmental covariates, which are not used as predictors, or inaccessible *scorpan*-factors. For instance, slope and aspect can serve as proxy for microclimate through its influence on local solar insulation [24]. The catchment area can serve as a proxy for soil fertility because of terrain driven water and SOC accumulation [19] and elevation, slope and aspect can act as proxy for parent material, tectonics and periglacial climate through strike and dip of the geological sediments and down-cutting processes [22,23,26].

For spatially modelling soil properties, different approaches have been established to derive relationships between soil properties and environmental covariates. However, for a reliable estimation of SOC stocks, the vertical dimension is crucial [13]. A common way of three-dimensional mapping is to consider the vertical dimension as multiple two-dimensional predictions, which can be interpreted in a three-dimensional way [17,27–29]. Because, multi-layered predictions do not provide full 3D soil information, since they are limited to the mapped depth increments. Information of the space

between the mapped depth increments has to be derived on an interpretative and subjective basis. One approach is to vertically interpolate the single layers to construct a volumetric model, which is computationally intensive [30,31].

Therefore, multi-layered models are referred to as pseudo-3D mapping or 2.5D mapping [32]. To overcome these drawbacks, it is favourable to map soil properties as continuous depth function in the spatial domain [13,18], where the vertical distribution of soil properties is represented by depth functions, that are predicted spatially. These predictions allow the calculation of SOC stocks over the integral of the functions [33] as well as the calculation of fully three-dimensional maps at any vertical resolution [32,34–37].

Besides geostatistical frameworks [38,39], different depth functions have been applied for 3D modelling: power, logarithmic [32,40], exponential decay [32,33], polynomial [34,36] and equal-area spline functions [31,41].

While with 2.5D mapping soil properties are directly predicted at specific depth levels using the environmental covariates [17,29], 3D approaches use environmental covariates to predict parameters of the depth functions [34], which are abstract soil properties. According to the *scorpan* model, soil properties can be spatially mapped with neighbourhood relations solely [21], which also have been used for 3D modelling [36,40,42,43]. Over the past years, machine learning techniques have become a standard technique in DSM due to several advantages like dealing with non-linearity or the handling of large datasets. Aldana Jague et al. [33] used multiple linear regression (MLR) to model SOC incorporating terrain covariates, while Gasch et al. [43] compared spatial and terrain covariates using random forests (RF) and regression kriging for mapping SOC at different depth layers. Piikki et al. [27] used multivariate

adaptive regression splines (MARS) to model clay and sand fractions as well as organic matter based on proximal soil sensing data. Several other studies also suggest that machine learning techniques, such as artificial neural networks (ANN; [41,44]), random forests (RF; [17]) and support vector machines (SVM; [45]), can be applied successfully in DSM.

The objectives of this study were to test the spatial prediction of four soil profile depth functions for modelling SOC content and bulk density with different machine learning methods based on multi-scale terrain covariates. The tested soil profile depth functions are polynomials of 2nd and 3rd degree, natural logarithmic and exponential functions. The machine learning methods used to model the depth functions spatially were multivariate adaptive regression splines (MARS), random forests (RF) and support vector machines (SVM) with radial basis functions. We validated the machine learning models with 10-fold cross-validation and evaluated the results of the 3D mapping approach by comparing it with the predictions of the more common multi-layered 2.5D modelling approach based on five layers.

Material and methods

Study area and sampling design

The BEF-China study sites are artificial biodiversity experiments on property leased and managed by the project partner Institute of Botany, Chinese Academy of Sciences, 20 Nanxincun, Xiangshan, Bejing, 100093, PR China. Field studies did not involve endangered or protected species and no specific permissions for field research were required.

The biodiversity and ecosystem functioning (BEF) China project [46] is located near Xingangshan, Jiangxi Province, PR China (UTM/WGS84: 50R 588000 3222000), about 400 km south-west of Shanghai (Fig 1). The study site is a topographically heterogeneous environment in a small catchment of 26.7 ha leased by the Institute of Botany of the Chinese Academy of Sciences (CAS). It features an elevation ranging from 105 to 275 m a.s.l., slopes inclined 29° in average and a maximum slope inclination of 45°, which are typically convex [19]. Non-calcareous slates with varying sand and silt content and grey-green sandstone constitute the bedrock. Predominant soil types are Endoleptic Cambisols with Anthrosols at the hillsides and Gleysols at the valley bottom. The mean soil depth is 0.6 m with underlaying isomorphic weathered slate (saprolite; [19]). Soil texture ranges from silt loam to silty clay loam [47]. The climate is typically subtropical with monsoons in summer, a mean annual temperature of about 17 °C and long-term average annual rainfall of about 1800 mm [48] but with a drier period from 2009 to 2012 [49].

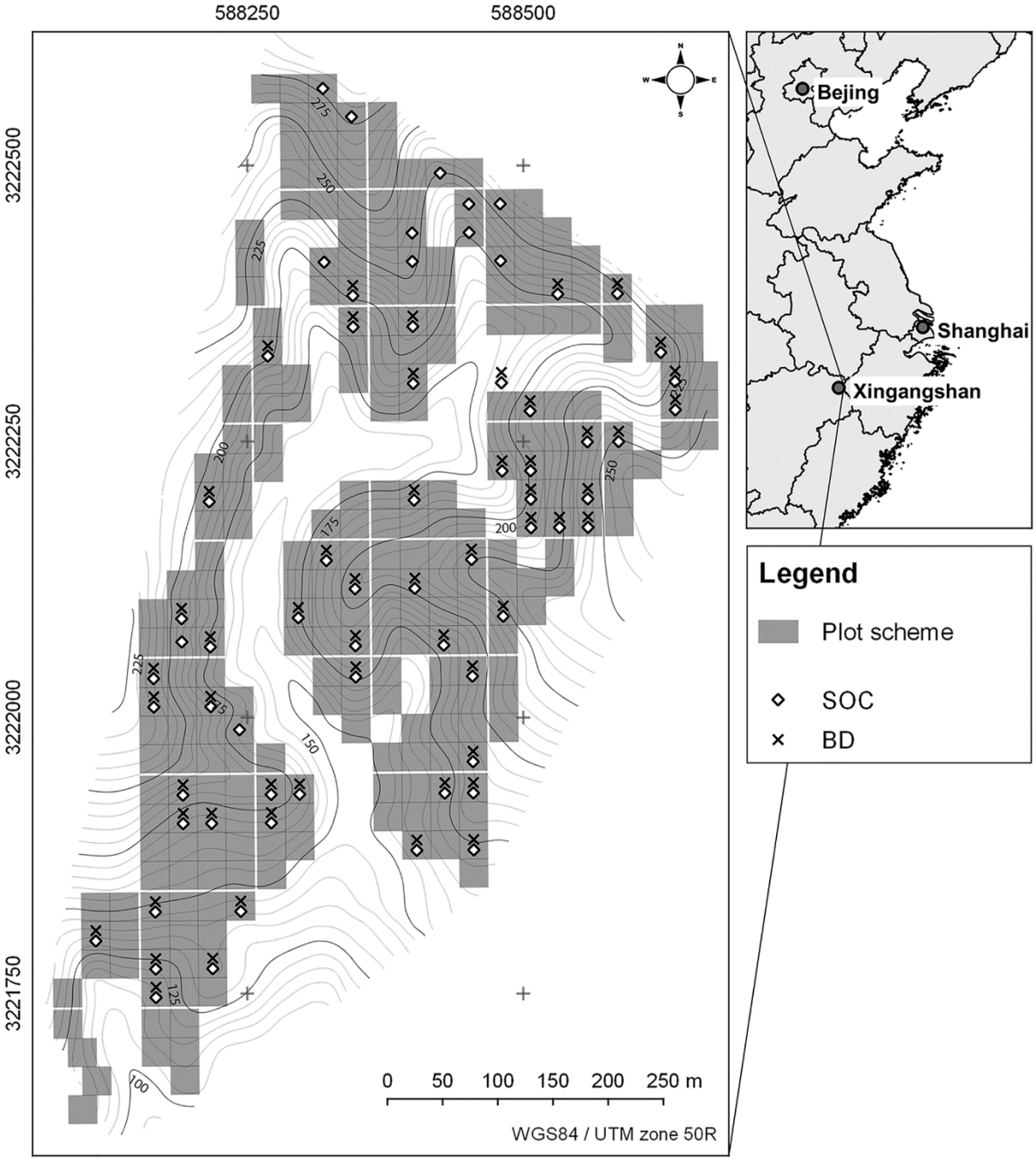

Fig 1. Study area in mainland China with BEF-China plot scheme and indication of sampled plots.

Upper right panel with permission by R. Hijmans; https://gadm.org/.

About 18 ha were covered with 271 experimental plots. In total 8.7 ha at the valley bottom were not part of the experimental design due to paths and rivulets. Plots had a size of 25.8 m × 25.8 m (traditional Chinese unit of 1 mu, 1/15 ha) and were replanted

in 2008 after clear-cut of a commercial Chinese fir plantation. One plot comprised 400 (20 × 20) trees in monocultures and mixtures of 2, 4, 8, 16 and 24 species. Species composition of the plots was based on random as well as non-random (plant trait-oriented) extinction scenarios, where all species were represented equally (broken-stick design). The datasets used in this study comprised soil samples from random subsets of all species and species richness levels referred to as VIPs (Very Intensively Studied Plots). For details on the experimental design, see Bruelheide et al. [46] and Trogisch et al. [50].

Datasets

All described datasets are part of the legacy database of BEF-China. Soil sampling was conducted in 2014. Nine cores on a regular grid basis (3 cm in diameter) were taken at each of the 67 VIPs according to the BEF-China experimental design (Fig 1; [46]). The samples were bulked for each depth increment (0–5 cm, 5–10 cm, 10–20 cm, 20–30 cm and 30–50 cm) and were referred to as dataset SOC (n = 67; Fig 2). Fine roots and charcoal were sorted out manually. For dry combustion CNS-analysis, a Vario EL III (Elementar, Hanau, Germany) was used. Due to acidic soil conditions there was no detectable carbonate fraction, and thus total carbon represented SOC [19]. SOC content ranged from 5.06 to 0.35% decreasing with depth.

Bulk density samples (n = 55) were taken in April 2015 with soil sample rings (100 cm^3) and five replicates for each depth increment at the VIPs. Bulk density was determined gravimetrically and was referred to as dataset BD (Fig 2). Bulk density ranged from 0.75 to 1.84 g cm^{-3} increasing with depth. Since some plots with SOC samples did not have BD data (Fig 1), both soil properties were modelled individually instead of calculating and modelling the SOC stocks directly. This ‘model-then-calculate’

approach is a useful alternative to the ‘calculate-then-model’ approach. Both were compared by Orton et al. [51]. The digital elevation model (DEM) had a resolution of 5 m and was generated by ordinary kriging [52] based on differential global positioning system data (DGPS) with 1956 points (73 points per ha; [19]). The distribution of datasets SOC and BD over the DEM is shown in Fig 3. Dataset SOC covered the elevation data more comprehensively compared to the dataset BD.

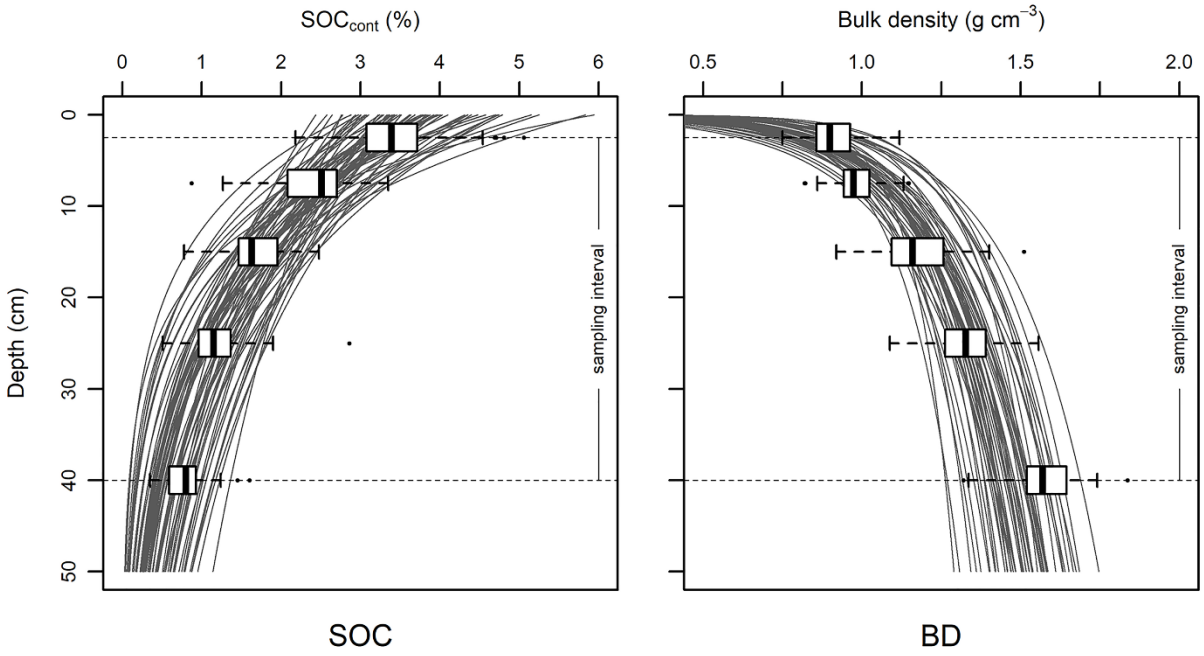

Fig 2. Datasets for SOC and BD used in this study summarized in boxplots.

The boxplots show the variation of the SOC and BD values for each depth increment. SOC and BD samples were taken in five depth increments and 9 cores per plot were bulked (Note that depth increments do not increase linearly). The grey lines show model depth functions (3rd degree polynomial for SOC and natural logarithmic function for BD; see subsection “3D mapping with soil depth functions”).

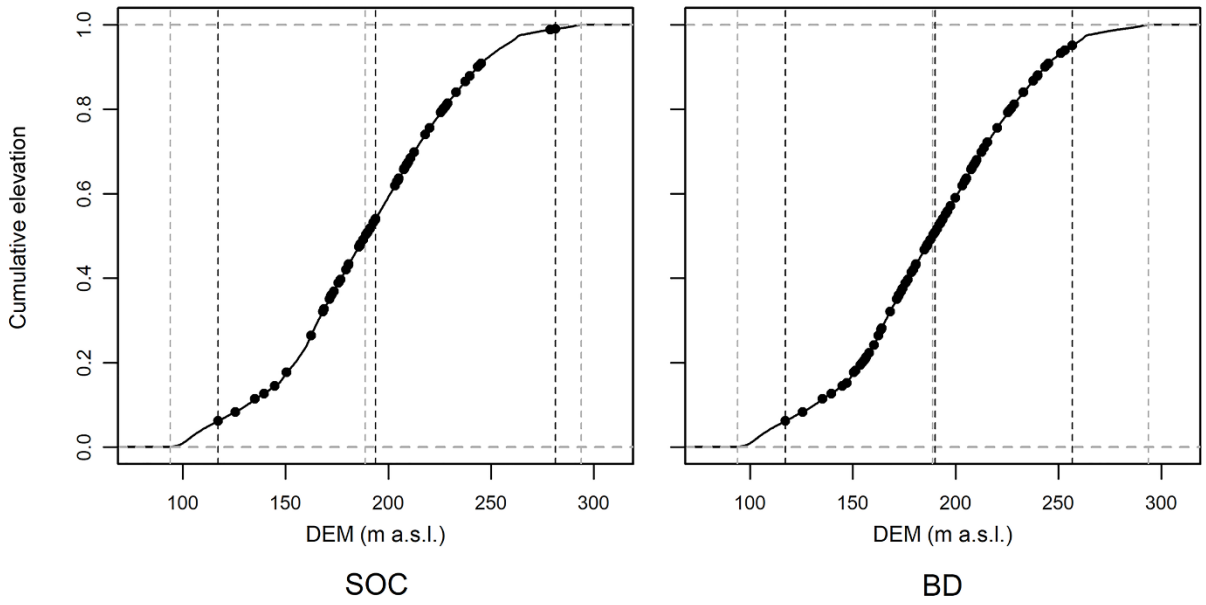

Fig 3. Empirical cumulative distribution functions (ECDF) for SOC and BD datasets.

The ECDFs show the locations of the sampling sites in the state space of the elevation (DEM) in metres above sea level (m a.s.l.). The aim is to show the coverage of the DEM feature space by the samples. It can be seen that most samples are located in the mid-range of the elevation values. Therefore, predictions at grid locations which are only sparsely covered by the samples (i.e. locations close to the minimum and maximum values of the DEM) may be less accurate. The minimum, median and maximum values of both datasets (DEM and sampling locations) are shown with vertical lines (dashed grey: DEM, dashed black: sampling locations) to compare the full range of the respective feature spaces.

Digital terrain analysis

Environmental covariates that describe the morphometry of a landscape are grouped in four major classes of terrain attributes: local, regional, combined (i.e. combinations of local and regional) and solar morphometric variables. Given that many terrain attributes can be calculated based on different equations or modelling approaches and because it is unknown which version would be most suitable for modelling SOC and BD within the study area, we used multiple established methods to derive single terrain attributes, if available. Given the circular nature of aspect, we used sine and cosine

transformations to derive eastness and northness. Overall, we calculated 58 terrain attributes (Table 1) with SAGA GIS 2.3.1 [53].

Table 1. Terrain attributes used for SOC and bulk density modelling.

	Covariates	Method	Author(s)
Local	Slope and aspect	Fitted 2nd degree polynomial	[54]
		Fitted 3rd degree polynomial	[55]
		Least squares fitted plane	[56]
		Maximum triangle slope	[57]
		Fitted 2nd degree polynomial	[58]
	Plan, profile, longitudinal, tangential and flowline curvature	Fitted 2nd degree polynomial	[54]
		Fitted 3rd degree polynomial	[55]
		Fitted 2nd degree polynomial	[58]
	Vertical distance to channel network		[53]
	Sky visibility, sky view factor, direct and diffusive insolation		[59]
Regional	Catchment area	Top-down	[60]
		Recursive	
Combined	Topographic Wetness Index (TWI)	Any combination of slope and catchment area	[61]
	Slope length and steepness factor (LS-Factor)	Any combination of slope and catchment area	[61,62]

https://doi.org/10.1371/journal.pone.0220881.t001

Terrain attributes derived from a DEM with a given resolution may not be suitable for landscape characterization and for digital soil mapping due to a non-representative DEM resolution [63], since the terrain attributes are not derived on the most relevant scale [64,65]. To examine the influence of scale, [65] applied simple smoothing (mean) filters with different neighbourhood sizes. This approach was applied on every terrain attribute used in this study with five circular neighbourhoods (radii of 1, 2, 4, 6 and 8 pixels), resulting in 290 terrain attributes in total. The maximum radius was set to 8 pixels to represent the local catena scale of 90 m.

Machine learning techniques

We compared three data mining methods to test the 3D prediction of soil profile depth functions for SOC and BD based on terrain covariates. Given the large number of 290

covariates (instances) and sample sizes of n = 67 and n = 55, not all available techniques could be applied. For example, the interpretable multiple linear regression (MLR) analysis used for spatial modelling of polynomial depth functions by Aldana Jague [34] requires more samples (n) than instances (p; [66]). Furthermore, we have to account for multi-collinearity. Many terrain covariates in this study are calculated by different algorithms for the same terrain attribute and on different spatial scales with the same algorithm, which is often seen as a constraint in machine learning [66]. To reduce the covariate space to either enable MLR or handle the 'curse of dimensionality', principal component analysis (PCA) is often applied. However, feature reduction with PCA can have negative effects on model accuracy with multi-scale terrain data and models with the full set of covariates have higher accuracies [65]. Other feature reduction methods increase accuracy only marginally [65]. In this study, we applied multivariate adaptive regression splines (MARS), random forests (RF) and support vector machine (SVM). These machine learning methods are robust against multi-collinearity, can handle n<p [66] and select the most informative covariates without expert knowledge. Further, we omitted feature reduction.

For modelling, R version 3.3.1 was used [67]. For accessing the machine learning packages, the uniform interface *caret* [68] was used, which also offers data handling and model validation methods.

Multivariate adaptive regression splines (MARS).

MARS was introduced by Friedman [69] and is a generalisation of recursive partitioning regression approaches using piecewise linear models. With its linear basis functions, it overcomes the discontinuous response of other recursive partitioning models like Classification and Regression Trees (CART; [70]) and can generate continuous

surfaces. Therefore, prediction accuracy of MARS is expected to be higher [69]. MARS is a partial linear function, where each new part is added with an exhaustive search for best fit and models a finite quantity of the regression. Thus, the model measures variable importance by its nature and is insensitive to non-informative instances. MARS require very little pre-processing and are non-affected by collinearity, since the predictor selection is random during iteration and redundant features are used equally [66]. This may affect measurement of variable importance and interpretation, which, however, is out of scope in this study. For modelling using MARS, the *earth* package version 4.4.6 [71] was used.

Random forests (RF).

RF is a widely used machine learning technique in digital soil mapping [17,22,64,72]. It was introduced by Breiman [73] and is an ensemble technique with CART [70] as a base learner. The single decision tree uses binary splits to create more homogenous groups in respect to the response. To grow an ensemble of trees, different random subsets of covariates (bootstrap sampling) and features (random set of features for every split) are used to build a single tree. The final prediction is created by averaging all individual tree outputs. Breiman [73] has proven that random forests with a large number of trees is robust against overfitting. Moreover, it is robust against noise, non-informative and correlated features. RF also returns feature importance measures (affected by correlation as MARS; [66]) and there is little need for fine-tuning [74]. The *randomForest* package version 4.6–12 [75] was used for modelling with RF.

Support vector machine (SVM).

Originally, SVM has been developed for classification problems [76]. It is a kernel method and uses hyperplanes to linearly separate classes of objects. For regression

problems, Drucker et al. [77] developed support vector regression machines (SVR), which are an extension of SVM. Therefore, the term SVM is often used in both cases. The kernel function defines a transformation of the input data into a high dimensional feature space. In this feature space, it is possible to derive a linear regression hyperplane for non-linear relationships. Afterwards, it is back-transformed to non-linear space. Smola and Schölköpf [78] provide a comprehensive and detailed insight into SVR. The kernel used in this study is a radial basis function, where the scaling parameter σ is estimated by *caret* after a method by Caputo et al. [79]. In contrast to MARS, Drucker et al. [77] suggest that SVM should be used when the number of features is larger than the number of instances, since its optimisation does not depend on the dimensionality of feature space. Furthermore, SVM is partially insensitive to outliers (depending on cost factor) and does not require feature reduction to reduce multi-collinearity [66]. The *kernlab* package version 0.9–25 [80] was used for radial support vector regression modelling.

Data pre-processing.

Some algorithms are sensitive to the scale and the range of the covariate space (e.g. SVM). To reduce effects of small values and little variance, SVM needs centred and scaled covariates [66], which was computed using the scale and centre-option in *caret*. To make all models comparable, this was also done for MARS and RF.

Spatial 2.5D and 3D models

Differences between 2.5D models and spatial prediction of depth functions.

The environmental covariates were used to train regression models (MARS, RF and SVM) to predict SOC and BD. For 2.5D predictions this was done for each sampled depth increment individually, were we assigned the mid-depth of the sampled

increments as depth of the respective layer. This method to obtain volumetric soil information has several advantages. For modelling of each standard depth individually, there are no further requirements to abstract soil information in terms of vertical variability, i.e. a soil profile function. Furthermore, there is no error propagation through secondary models that describe depth functions. On the other hand, in contrast to 3D modelling, 2.5D modelling has the disadvantage that the individual model outcomes are purely two-dimensional. Soil properties of the depth increments between the standard depths are not used in the model and have to be derived on an interpretative basis [15] or through further processing [30] after spatial prediction. However, this is a well-established and well-documented approach. Therefore, we compare the results of the 3D approach described below directly with the 2.5D results.

3D mapping with soil depth functions.

For the spatial modelling of depth functions, which we handled similar to the soil properties in terms of modelling, we applied 3rd degree polynomial functions proposed by Aldana Jague [34] and less flexible 2nd degree polynomials as well as logarithmic and exponential functions [32]. The workflow of the 3D mapping (Fig 4) of this study involved five main steps:

i). Mathematical approximation of depth functions to the five depth increments with a linear least squares approach. These were

$$f_1(x) = c_0 + c_1 x + c_2 x^2 + c_3 x^3 \text{ (1) [34]}$$

$$f_2(x) = c_0 + c_1 x + c_2 x^2 \text{ (2)}$$

$$f_3(x) = c_1 * \ln(c_2 x) \text{ (3) [32]}$$

$$f_4(x) = exp^{c_1 + c_2 x} \text{ cf. [32]}$$

where $f_{1,2,3,4}(x)$ is SOC and BD at a specific depth x (depth of the lower corner of a voxel in cm), c_0 is the intercept that equals SOC and BD at depth 0 (cm) and the function coefficients c_1, c_2 and c_3 are dimensionless. This altogether described the vertical distribution of SOC in respect to depth x at a certain location.

ii). Evaluation of model error for all equations in (i).

iii). Spatial modelling of the function coefficients c_1, c_2, c_3 and c_0 (analogous to two-dimensional modelling of SOC and BD) of the depth function with the lowest error (ii) with MARS, RF and SVM. The depth function parameters were treated and evaluated similar to a soil property.

iv). Evaluation of the cross-validation results for MARS, RF and SVM models of the depth function coefficients.

v). Solving the depth functions with spatially modelled coefficients (iii) at each grid location to generate a three-dimensional model.

The depth functions were solved for depths from 0 cm to 50 cm in 5 cm increments. The resulting 11 depth layers (matrices) were stacked to two three-dimensional models (one for SOC and BD each), where individual values are represented by voxels, which are the volumetric 3D analogue of 2D pixels. Due to the nature of the polynomial depth functions, negative SOC predictions in the profiles are possible. Consequently, the values of these voxels had to be set to zero. This is not required for logarithmic and exponential functions.

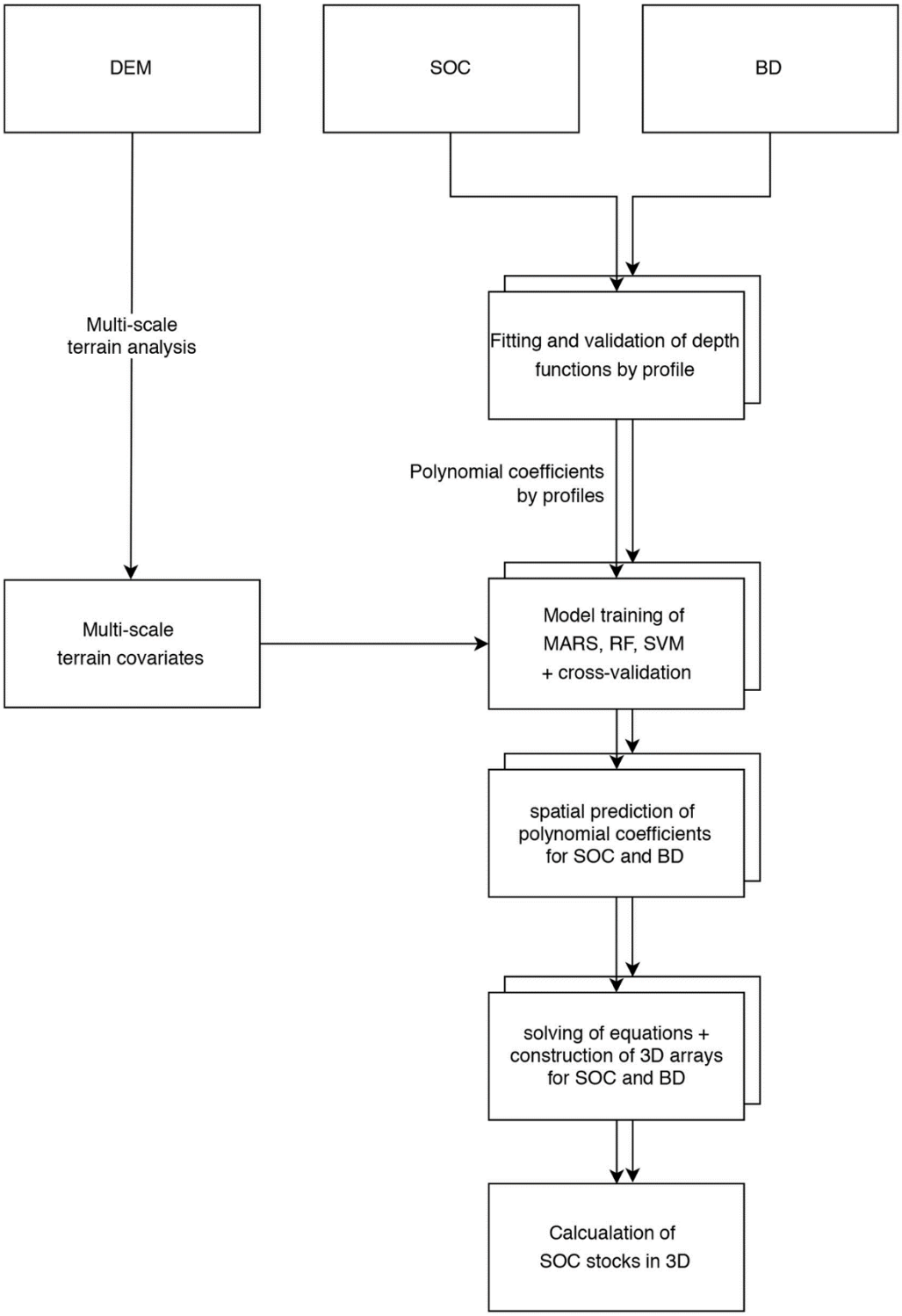

Fig 4. Flow chart summarizing the methodology steps of the 3D mapping and the used datasets at each step.

Compared to the standard depth method, the main advantages of spatially modelled depth functions are a higher vertical resolution and the fact that the result can be interpreted as volumetric structure. Instead of pixels with SOC and BD information in multiple layers, volumetric elements–so called voxels–in a three-dimensionally georeferenced stack of matrices with user-defined vertical resolution are obtained. Since the depth functions are secondary models, the error which is propagated by the depth function model to the spatial model depends on the chosen function. Due to the limited number of samples per profile, cross-validation of the depth functions was omitted.

The final models for SOC and BD were validated internally against the measured values of the input datasets.

Validation and evaluation

The evaluation consists of two independent steps for the 2.5D multi-layered model predictions and the volumetric 3D model predictions of SOC and BD, where we treat the depth function parameters as soil properties.

In a first step, we evaluated each model of the soil properties SOC and BD as well as the spatial models of the depth function parameters, by using a 10-fold cross-validation with the coefficient of determination (R2) and the root mean square error (RMSE) as quality criterion. In this step, the models were tuned over the default grid- or hyper-learning sequence of parameters [81] using the tune grid function of caret to identify the most suitable combination of tuning parameters with the lowest RMSE and to reduce the model error, while preserving the models ability to generalise. The tuning parameters are degree and nprune for MARS, mtry for RF and cost for SVM. For RF

ntree was set to the default value and σ for SVM was calculated by a method after Caputo et al. [79]. All models used the same set of folds to make cross-validation results comparable. The final models were selected from this sequence by the lowest RMSE.

To estimate the effect of overfitting of the depth function models based on grid learning, we evaluated the 3D model results with the datasets SOC and BD by R2 and RMSE (observed-predicted-evaluation). Overfitting is indicated by large differences in the prediction error between the training and the validation sets [81].

Further, we compared the 3D models against the 2.5D predictions of the same datasets to evaluate the performance of the 3D models. We chose this approach, because the legacy datasets are too small to hold out a larger subset for independent validation. The model results should be similar, if the spatial prediction of depth function parameters is reproducing the spatial distribution of the soil properties. This means that independently from the modelling framework (modelling of SOC and BD or modelling depth function as soil property) the results of the 3D model are reasonable, if both models are similar.

We see this comparison as a valid method for the evaluation of the 3D models, since Brus et al. [38] report strong correspondence between 2.5D and 3D geostatistical models and MARS, RF and SVM are well established for 2D and 2.5D soil mapping and in data science [17,27,66]. Therefore, we use the 2.5D layered predictions at the specific mid-depth of the increments as reference predictions. For the comparison between the 2.5D models and the corresponding depths of the 3D models, we used the coefficient of determination R2, Lin's concordance correlation coefficient (ρc; [82]), which validates the models against the 1:1 line, and the RMSE.

Estimation of SOC stocks

The three-dimensional array of SOC stocks was calculated by

$$SOC_{stock} = \frac{SOC}{100} * BD * 500^2 * 5$$

where SOC_{stocks} (g voxel^{-1}) is the soil organic carbon storage, SOC is SOC content (%), BD is bulk density (g cm^{-3}), 500^2 is the base area of a voxel (cm^2) related to the DEM resolution of 500 cm and 5 is the vertical resolution in cm. Consequently, 1 voxel represented 1.25 m^3 of soil. Adjustment with the fraction of coarse material (> 2 mm) was omitted, since the coarse fraction was negligible low (< 5 vol.-%) at the VIPs and cannot be determined precisely by coring. According to Orton et al. [51] calculating the SOC stocks from two models of SOC and BD is an useful alternative when the samples are not taken at the same locations.

Results

2.5D predictions of standard depths as reference

For the models of SOC, the mean cross-validation R^2 of MARS was 0.33 with a root mean square error of 0.39%, compared to RF with an R^2 of 0.41 (RMSE 0.34%) and SVM with an R^2 of 0.39 (RMSE 0.35%; cf. Table 2). Models for BD showed a mean R^2 of 0.43 (MARS), 0.39 (RF) and 0.39 (SVM) and mean RMSE values of 0.09 g cm^{-3} (MARS), 0.08 g cm^{-3} (RF) and 0.08 g cm^{-3} (SVM). In addition to the mean values, Table 2 shows the prediction accuracies and the RMSE's for each depth increment and all three machine learning techniques of both SOC and BD.

Table 2. Performance of 10-fold cross-validation for MARS, RF and SVM applied on the sampled standard depths of SOC and BD.

		R^2			RMSE		
	depth (cm)	MARS	RF	SVM	MARS	RF	SVM
SOC (%)	0–5	0.28	0.41	0.37	0.59	0.48	0.51
	0–10	0.25	0.41	0.42	0.46	0.4	0.4
	10–20	0.31	0.31	0.26	0.37	0.32	0.34
	20–30	0.46	0.47	0.46	0.3	0.28	0.29
	30–50	0.38	0.45	0.43	0.24	0.2	0.21
	$\bar{X}$	0.34	0.41	0.39	0.39	0.34	0.35
BD (g cm^{-3})	0–5	0.51	0.53	0.61	0.07	0.06	0.06
	0–10	0.5	0.52	0.49	0.07	0.06	0.06
	10–20	0.31	0.26	0.24	0.11	0.11	0.11
	20–30	0.41	0.35	0.33	0.1	0.1	0.1
	30–50	0.42	0.31	0.3	0.09	0.09	0.09
	$\bar{X}$	0.43	0.39	0.39	0.09	0.08	0.08

https://doi.org/10.1371/journal.pone.0220881.t002

Table 3. Performance of a 10-fold cross-validation for MARS, RF and SVM applied on function coefficients of a 3rd degree polynomial (f1 for SOC and BD with four coefficients) and natural logarithmic function (f3 for BD with two coefficients).

		R^2			RMSE			nRMSE		
		MARS	RF	SVM	MARS	RF	SVM	MARS	RF	SVM
SOC (f_1)	c_0	0.29	0.28	0.26	0.83	0.75	0.79	0.20	0.18	0.19
	c_1	0.36	0.43	0.46	0.15	0.13	0.14	0.22	0.19	0.20
	c_2	0.29	0.28	0.24	0.008	0.007	0.007	0.2	0.18	0.18
	c_3	0.3	0.21	0.31	0.0001	0.0001	0.0001	0.14	0.14	0.14
	$\bar{X}$	0.31	0.3	0.32	-	-	-	0.19	0.17	0.18
BD (f_1)	c_0	0.56	0.45	0.38	0.09	0.09	0.09	0.23	0.2	0.20
	c_1	0.38	0.34	0.218	0.02	0.02	0.02	0.14	0.14	0.14
	c_2	0.38	0.17	0.26	0.001	0.001	0.001	0.2	0.2	0.2
	c_3	0.25	0.27	0.31	0.00002	0.00002	0.00002	1.3×10^5	1.2×10^5	1.2×10^5
	$\bar{X}$	0.39	0.31	0.28	-	-	-	3.2×10^4	3×10^4	3×10^4
BD (f_3)	c_1	0.56	0.48	0.53	0.09	0.09	0.09	0.2	0.18	0.18
	c_2	0.34	0.24	0.2	0.03	0.04	0.04	0.14	0.19	0.14
	$\bar{X}$	0.45	0.36	0.36	-	-	-	0.17	0.19	0.16

Note that coefficients dimensions are different and specifying a mean of the RMSE is not reasonable.

https://doi.org/10.1371/journal.pone.0220881.t003

Soil depth functions

For SOC, all equations showed R^2 values higher than 0.9 (0.99 for f_1, 0.96 for f_2, 0.96 for f_3 and 0.94 for f_4) with a RMSE ranging from 0.36 (f_1) to 0.7% (f_2). For BD, the performance in terms of R^2 was similar (RMSE = 0.07 g cm^{-3}), except for f_3 with R^2 = 0.84 (RMSE = 0.22 g cm^{-3}), which is the natural logarithmic function. The 3rd degree polynomial (f_1) resulted in the best fits for SOC and BD. However, the general trend of SOC in the profiles was exponential (Fig 2). Hence, both the 3rd degree polynomial and the exponential functions were chosen for further spatial modelling and comparison in this study. With higher errors and without being able to reproduce the general trend in the profiles profile the 2nd order polynomial (f_2) was omitted in the following steps.

Spatial modelling of soil depth functions

The cross-validation results for the machine learning methods applied on the depth functions (c.f. Table 3) showed, that the polynomial depth functions for MARS, RF and SVM for SOC were comparable in their goodness of fit with marginal differences (mean R^2 from 0.3 to 0.32). R^2 of the exponential depth functions ranged from 0.3 for MARS to 0.44 for RF.

The models of the function coefficients could not be compared directly because c_0 represented the SOC in % and BD in g cm^{-3}, whereas c_1, c_2 and c_3 were dimensionless. Hence, we compared these models by the normalised RMSE (nRMSE), which is the RMSE divided by the coefficients range (Table 3). The nRMSE showed little variation of around 0.18 for all coefficient predictions of the 3rd polynomial depth function of SOC. RF had the lowest mean of nRMSE over all coefficients (0.17).

The lowest nRMSE (0.09) for SOC was achieved by the exponential depth functions (RF and SVM).

The models based on the 3rd degree polynomial depth functions of BD had a mean R^2 of about 0.23–0.4, while the mean nRMSE was about 3×10^4, due to the low performance of models with c_3. Given such high errors, none of the models could reasonably predict the 3rd degree polynomial depth function for bulk density. The exponential function was not able to reproduce the vertical trend of BD. Thus, we used the logarithmic depth function, although it fitted the five depth increments least. However, these spatial depth function models performed better (mean R^2 from 0.36 to 0.45; nRMSE of about 0.16 for SVM).

Evaluation of 3D predictions

For the comparison of 3D models against the 2.5D reference predictions, we used the coefficient of determination R^2, Lin's concordance correlation coefficient ρ_c and the RMSE in corresponding depths (Table 4).

The three-dimensional MARS prediction for SOC with the 3rd degree polynomial depth function showed the largest difference to its counterpart. The prediction at 2.5 cm ranged from close to zero to 15% SOC compared to 1.5 to 4% SOC in the two-dimensional prediction (Fig 5). The other depth increments showed a similar pattern with values down to -15% SOC. For the 2.5 cm increment the performance of RF was slightly better than that of SVM, but subsequently dropped with increasing depth. Especially at 40 cm, but also at 25 cm and 15 cm, the three-dimensional prediction of RF differed more from the two-dimensional predictions than the three-dimensional predictions of SVM differed from their counterparts. There was no distinct over- or

Table 4. Coefficient of correlation (R2), Lin's concordance correlation coefficient (ρc) and RMSE of 2.5D reference predictions and correspondent depths of 3D predictions with polynomial (f1), logarithmic (f3) and exponential (f4) depth function.

		R^2			ρ_c			RMSE		
		MARS	RF	SVM	MARS	RF	SVM	MARS	RF	SVM
SOC (%; f_1)	2.5 cm	0.02	0.92	0.89	-0.03	0.95	0.79	4.13	0.09	0.12
	7.5 cm	0	0.69	0.89	-0.01	0.81	0.85	3.84	0.16	0.1
	15 cm	0.02	0.41	0.72	-0.03	0.43	0.47	2.42	0.37	0.22
	25 cm	0	0.17	0.45	0	0.17	0.66	9.09	0.68	0.15
	40 cm	0	0.07	0.15	0	0.04	0.31	46.96	1.73	0.33
	$\bar{X}$	0.01	0.45	0.62	-0.01	0.48	0.62	13.29	0.61	0.18
SOC (%; f_4)	2.5 cm	0	0.96	0.93	0	0.93	0.79	19.22	0.11	0.14
	7.5 cm	0.1	0.84	0.67	0	0.39	0.29	26.25	0.38	0.35
	15 cm	0	0.89	0.88	0	0.94	0.93	29.42	0.06	0.05
	25 cm	0.06	0.85	0.93	0	0.55	0.79	31.28	0.21	0.1
	40 cm	0.02	0.88	0.75	0	0.31	0.26	32.71	0.31	0.3
	$\bar{X}$	0.04	0.88	0.83	0	0.62	0.61	27.78	0.21	0.19
BD (g cm^{-3}; f_3)	2.5 cm	0.02	0.94	0.87	-0.05	0.39	0.53	0.48	0.09	0.07
	7.5 cm	0	0.8	0.71	0	0.29	0.24	0.44	0.09	0.1
	15 cm	0.01	0.66	0.5	-0.05	0.48	0.31	0.46	0.05	0.07
	25 cm	0.01	0.44	0.57	0.02	0.59	0.53	0.43	0.04	0.04
	40 cm	0.02	0.76	0.43	-0.12	0.17	0.08	0.64	0.1	0.11
	$\bar{X}$	0.01	0.72	0.62	-0.04	0.38	0.34	0.49	0.07	0.08

https://doi.org/10.1371/journal.pone.0220881.t004

Table 5. Internal validation results of the final 3D models with the exponential function for SOC and the logarithmic function for BD.

	SOC (%)		BD (g cm^{-3})	
	R^2	RMSE	R^2	RMSE
2.5 cm	0.88	0.32	0.87	0.29
7.5 cm	0.74	0.47	0.85	0.07
15 cm	0.77	0.24	0.72	0.12
25 cm	0.76	0.29	0.74	0.08
40 cm	0.8	0.31	0.66	0.12
$\bar{X}$	0.79	0.33	0.77	0.14

https://doi.org/10.1371/journal.pone.0220881.t005

underestimation of RF, but random scattering between -4 and 4% SOC for 40 cm (Fig 5). SVM showed lower deviation at 15 cm, 25 cm and even 40 cm. There were less predictions with negative values and less scattering. The predicted depth intersections of spatially modelled depth functions corresponded to the two-dimensional predictions by SVM largely by R^2 and ρ_c, while RMSE is low (Table 4).

In contrast, the 3D predictions of RF and SVM based on the exponential function showed good correspondence for all five depth increments (Table 4). The 3D predictions overestimated SOC for the 0–5 and 5–10 cm increments and underestimated it for 20–30 and 30–50 cm slightly due to the exponential nature of the equation, but there was no wide scattering as it was the case with the polynomial prediction for RF.

The results of the internal validation showed high correspondence between the chosen models (RF with exponential function for SOC and RF with logarithmic function for BD) and respective input data at all five sampled depth increments (Table 5). The R^2 and RMSE values of the internal validation were similar to the validation results of the model comparison, indicating that model overfitting of both models is similar (Table 4). This partly accounts to the propagation error of the profile depth function. The spatial prediction of the exponential function for SOC had an average R^2 of 0.79 with an average RMSE of 0.33% and the prediction of the logarithmic function used for BD had a R^2 of 0.77 with an average RMSE of 0.14 g cm^{-3}.

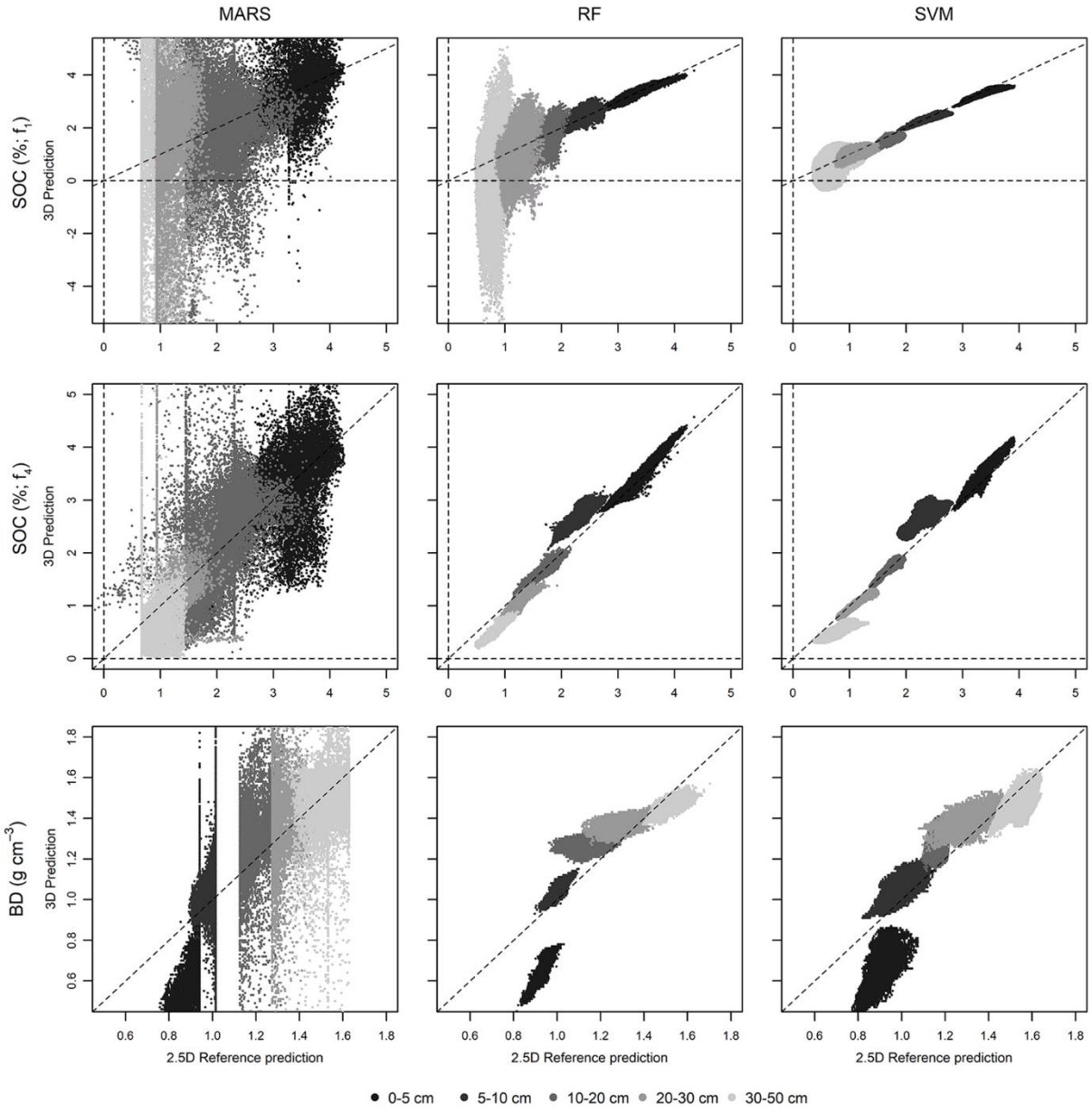

Fig 5. 3D predictions of sampled depth increments plotted against corresponding 2.5D predictions.

3D prediction of SOC was calculated with 3rd degree polynomials (upper row) and exponential function (middle row). The 3D prediction for BD with logarithmic function (lower row).

SOC stocks

The 2.5D models showed SOC stocks of 61.9 Mg ha^{-1} from 0 to 40 cm, with 19, 14.7, 12, 8.9 and 7.3 Mg ha^{-1} in the individual depth increments (from surface downwards).

The 3D model predicted 78.3 Mg ha^{-1} over the whole interval. The upper 20 cm of soil contained about 46.4 Mg ha^{-1}. This depth is often designated as topsoil [83,84] and is also a critical soil depth for modelling plant productivity and community assembly [85]. 31.9 Mg ha^{-1} SOC are stored in the subsoil from 20 to 40 cm. Considering that the rooting depth varies, depending on the species and individual age, a static discrimination between topsoil and subsoil may be not appropriate. The model showed that plants with shallow roots down to 5 cm mainly interacted with a carbon pool of 10.9 Mg ha^{-1}, whereas plants with roots in 25 cm depth interacted with a pool of 54.5 Mg ha^{-1}. Fig 6 shows the 3D prediction of SOC stocks as vertical intersections of the solum. The highest stocks in the upper 5 cm were predicted in the central upper slopes and at the western slopes. Predictions for this depth at the valley bottom were around 20% lower. However, at the valley bottom the predictions for intermediate depth increments (around 30 cm) were higher than predictions at the upslope positions. The depth function for SOC stocks was much steeper and the SOC stock decline with depth was more pronounced at upslope positions compared to downslope and valley positions.

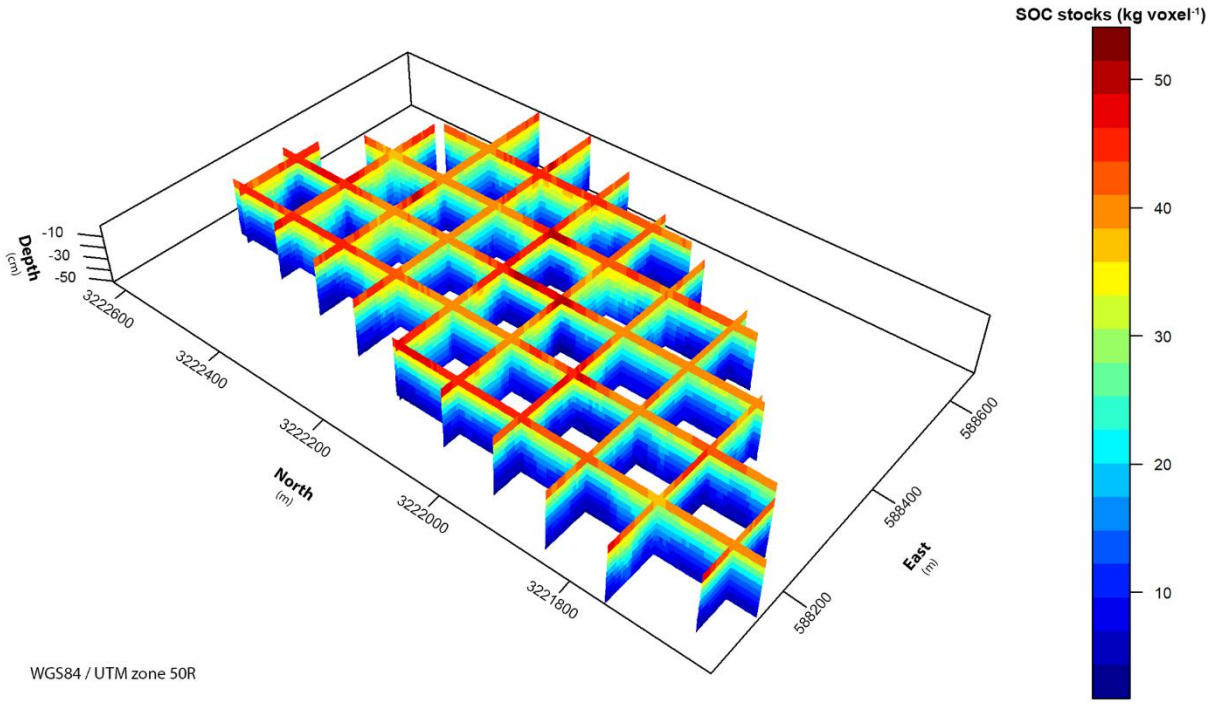

Fig 6. Three-dimensional prediction of SOC stocks for the whole catchment.

The final 3D SOC stock model is shown in vertical slices 150 m apart to display the vertical variability, which is larger than the spatial variability.

Discussion

2.5D predictions of standard depths as reference

As RF returned the lowest error for the 2.5D models, this was the best choice for modelling SOC. SVM ranked slightly below. Compared to the results presented by Lacoste et al. [30], who used Cubist for 2.5D SOC stock mapping, the accuracy of our results was similar and reasonable.

However, the sampled VIPs do not represent the terrain of the study site adequately, since they were chosen based on species richness levels, which were distributed

randomly, and not representative for the study site. For example, a representative sampling design could be achieved with Conditioned Latin Hypercube Sampling (cLHS) [72,86].

For bulk density SVM and RF performed equal by means of R^2 and RMSE and showed a similar pattern, especially at 15 cm and 40 cm. MARS performed least for BD. In general, RF resulted in the most stable predictions and is therefore recommended over SVM.

Evaluation of 3D predictions

The negative values in the prediction results and the pronounced difference between the 3D models, with predictions up to 15% SOC, and the 2.5D models indicated that MARS is not capable of adequately predicting the depth functions in space, although the cross-validation showed similar results as for RF and SVM models. The latter showed better correspondence between the 3D and the 2.5D models (Fig 5, Table 4). According to the results of the direct comparison between the multi-layered prediction and the corresponding depths in the 3D model, RF with exponential functions was most suitable for SOC modelling. RF and SVM with polynomials performed well at upper depth increments and less in lower increments. MARS models were not suitable of reproducing the 2.5D predictions. Lower performance of all techniques with polynomials in the lower depth increments may be referred to lower influence of the terrain as a driving factor to explain SOC accumulation and redistribution (e.g. by erosion). Other factors accounting for SOC redistribution in deeper soil horizons may be bioturbation or vertical transport in the liquid soil phase. Additionally, it is possible, that accumulation layers in the solum, that would reflect the lateral distribution, were not fully covered by the legacy dataset and, therefore, the interpretation remains

difficult. All these processes and others relevant for SOC concentration as well as SOC stocks cannot be fully covered by a distinct set of terrain parameter and lead to a dilution effect by predicting the deeper horizons. Lower accordance of the models also may be referred to uncertain models of function coefficients (c_3) and (c_2), which have significant influence at greater depths (cubic and squared) and exponentiate up this error. Based on the results, we chose RF with exponential depth functions for three-dimensional mapping of SOC and the logarithmic depth function for BD.

SOC stocks

Compared to other studies in this area, the estimated SOC stocks were well in line. Scholten et al. [19] calculated mean SOC stocks of 70 Mg ha^{-1} for the upper 50 cm with the same data but a different approach. Chen et al. [83] compared five plantations with different species in five age groups and calculated SOC stocks for the upper 20 cm. Especially the age of the trees and shrubs and their biomass have a strong impact on SOC stocks. Very young forest communities showed SOC stocks ranging from 20 to 25 Mg ha^{-1} and plantations with older trees of 7 to 10 years 30–40 Mg ha^{-1}. The latter were slightly older than the trees of BEF-China, where 42 Mg ha^{-1} were predicted. Diverse species pools in these studies may explain differences. Tang et al. [87] found SOC stocks in the top 60 cm in bamboo forests ranging from 60 to 200 Mg ha^{-1}.

The introduced approach is capable of summing SOC stocks at any depth interval. Since topsoil depth varies spatially, conventional static assumptions of topsoil thickness can result in inaccurate SOC stock calculations for individual horizons. Incorporating spatial models of topsoil depth into 3D SOC stock mapping can overcome this drawback and help to improve ecological and biodiversity models as conducted in the BEF-China experiment. In particular, consideration of biotic predictors

like forest biomass, tree species richness and functional plant diversity might further improve model fit and accuracy of estimated SOC stocks [14]. This would allow one to quantify terrain-specific effects of changes in forest cover and composition on SOC stocks. The developed models could also help to identify areas that are especially prone to loss of SOC stocks (e.g. by soil erosion or land cover change).

Furthermore, continuous three-dimensional SOC mapping can support models of a national SOC inventory. Yang et al. [37] applied depth functions to categorical soil types and estimated SOC stocks for mainland China. Combining models with high vertical resolution by Yang et al. [37] and continuous spatial modelling like in this study can improve accuracy of SOC mapping compared to the categorical mapping approach. This combination can also help to estimate and understand carbon fluxes between topsoil and subsoil [88] as well as between soil and the atmosphere [5]. Both objectives play major roles in inventory estimation, SOC auditing and decision making in respect to ecosystem services and carbon sequestration [1,5,7,12,89].

Conclusion

This study comprises the spatial prediction of soil depth functions for three-dimensional modelling of SOC and bulk density. The spatial prediction of the function coefficients enabled the calculation of two three-dimensional arrays by solving the depth functions for depths from 0 to 50 cm by 5 cm increments. This was used to estimate the SOC stocks in high spatial (5 m) and vertical (5 cm) resolution. The main conclusions of this study are:

- The general trend of SOC as visualised by the boxplots (Fig 2) was exponential. However, polynomial depth functions described the soil profiles for SOC with higher accuracy and the logarithmic functions for BD showed better results in spatial modelling. Therefore, we conclude that functions resulting in high accuracies based on the soil profile data may not be the most suitable for spatial modelling, as they may overfit the vertical trend of SOC content.
- The 3D RF models correspond best with the 2.5D counterparts (R^2 up to 0.96). Thus, RF is recommended to predict SOC based on exponential depth functions and bulk density with logarithmic depth functions in high vertical resolution. The 2.5D and 3D predictions of SOC with RF correlated much better, especially when using exponential functions, and lacked accuracy in deeper layers for SOC when modelled based on polynomial functions.
- Comparisons between conventional 2D and 2.5D predictions at the sampled depth and the corresponding depth of the three-dimensional predictions showed that MARS is not suitable for modelling corresponding 2.5D and 3D models, although cross-validation of the individual models showed similar performance in R^2.

Minor conclusions are: polynomial functions may be an option, when the problem of propagated errors and the ability to generalise in the horizontal domain is investigated further, however, polynomials of any degree have to be used carefully. To overcome these shortcomings, a higher sampling density in the vertical and horizontal domain and in combination with other depth functions, such as equal-area splines [90], should be considered, since exponential functions are not suitable for soil properties that do not increase or decrease continuously.

The 3D approach presented in this study is promising for SOC auditing in various disciplines and especially for decision making regarding climate and land use policies. Future work should focus on sampling design to cover valley positions outside the established plots at site A of BEF-China project. Given the dynamics of SOC stocks, we recommend the analyses of time series data and the expansion of the current database for four-dimensional models.

Acknowledgments

We are indebted to the BEF-China members from China, Switzerland and Germany. In particular, we thank Lars Arne Meier, Philipp Goebes, Dominik Leimgruber, Chen Lin, Yang Bo and Zhengshan Song for their assistance with field and lab work.

References

1.Adhikari K, Hartemink AE. Linking soils to ecosystem services—A global review. Geoderma. 2016; 262: 101–111.

2.Montanarella L, Pennock DJ, McKenzie N, Badraoui M, Chude V, Baptista I, et al. World's soils are under threat. SOIL. 2016; 2: 79–82.

3.Costanza R, d'Arge R, de Groot R, Farber S, Grasso M, Hannon B, et al. The value of the world´s ecosystem services and natural capital. Nature. 1997; 387: 253–360.

4.Dexter AR, Richard G, Arrouays D, Czyż EA, Jolivet C, Duval O. Complexed organic matter controls soil physical properties. Geoderma. 2008; 144: 620–627.

5.Lal R. Soil carbon sequestration to mitigate climate change. Geoderma. 2004; 123: 1–22.

6.Rawls WJ, Pachepsky YA, Ritchie JC, Sobecki TM, Bloodworth H. Effect of soil organic carbon on soil water retention. Geoderma. 2003; 116: 61–76.

7.Liu X, Trogisch S, Schmid B, He J-S, Bruelheide H, Tang Z, et al. Diversity and stand age increase carbon storage and fluxes in subtropical forests. 2019: submitted.

8.Lal R. Soil erosion and the global carbon budget. Environment International. 2003; 29: 437–450. pmid:12705941

9.Song Z, Seitz S, Li J, Goebes P, Schmidt K, Kühn P, et al. Tree diversity reduced soil erosion by affecting tree canopy and biological soil crust development in a subtropical forest experiment. Forest Ecology and Management. 2019; 444: 69–77.

10. Brevik EC, Cerdà A, Mataix-Solera J, Pereg L, Quinton JN, Six J, et al. The interdisciplinary nature of SOIL. SOIL. 2015; 1: 117–129.

11. Foley JA, Defries R, Asner GP, Barford C, Bonan G, Carpenter SR, et al. Global consequences of land use. Science. 2005; 309: 570–574. pmid:16040698

12. Minasny B, Malone BP, McBratney AB, Angers DA, Arrouays D, Chambers A, et al. Soil carbon 4 per mille. Geoderma. 2017; 292: 59–86.

13. Jobbagy EG, Jackson RB. The Vertical Distribution of Soil Organic Carbon and Its Relation to Climate and Vegetation. Ecological Applications. 2000; 10: 423.

14. Jackson RB, Lajtha K, Crow SE, Hugelius G, Kramer MG, Piñeiro G. The Ecology of Soil Carbon: Pools, Vulnerabilities, and Biotic and Abiotic Controls. Annual Review of Ecology, Evolution, and Systematics. 2017; 48: 419–445.

15. Hengl T, de Jesus JM, MacMillan RA, Batjes NH, Heuvelink GBM, Ribeiro E, et al. SoilGrids1km—global soil information based on automated mapping. PLoS ONE. 2014; 9: e105992. pmid:25171179

16. Ibáñez JJ, Ruiz Ramos M, Zinck JA, Brú A. Classical Pedology Questioned and Defended. Eurasian Soil Science. 2005; 38: 75–80.

17. Grimm R, Behrens T, Märker M, Elsenbeer H. Soil organic carbon concentrations and stocks on Barro Colorado Island—Digital soil mapping using Random Forests analysis. Geoderma. 2008; 146: 102–113.

18. Minasny B, McBratney AB, Malone BP, Wheeler I. Chapter One—Digital Mapping of Soil Carbon. In: Sparks DL, editor. Advances in Agronomy: Academic Press; 2013. pp. 1–47.

19. Scholten T, Goebes P, Kühn P, Seitz S, Assmann T, Bauhus J, et al. On the combined effect of soil fertility and topography on tree growth in subtropical forest ecosystems—a study from SE China. Journal of Plant Ecology. 2017; 10: 111–127.

20. Jenny H. Factors of soil formation: A system of quantitative pedology. New York: Dover Publications, Inc.; 1941.

21. McBratney AB, Mendonça Santos ML, Minasny B. On digital soil mapping. Geoderma. 2003; 117: 3–52.

22. Behrens T, Schmidt K, MacMillan RA, Viscarra Rossel RA. Multiscale contextual spatial modelling with the Gaussian scale space. Geoderma. 2018; 310: 128–137.

23. Behrens T, Schmidt K, Ramirez-Lopez L, Gallant J, Zhu AX, Scholten T. Hyper-scale digital soil mapping and soil formation analysis. Geoderma. 2014; 213: 578–588.

24. Eichenberg D, Pietsch KA, Meister C, Ding W, Yu M, Wirth C. The effect of microclimate on wood decay is indirectly altered by tree species diversity in a litterbag study. Journal of Plant Ecology. 2017; 10: 170–178.

25. Doetterl S, Berhe AA, Nadeu E, Wang Z, Sommer M, Fiener P. Erosion, deposition and soil carbon: A review of process-level controls, experimental tools and models to address C cycling in dynamic landscapes. Earth-Science Reviews. 2016; 154: 102–122.

26. Pike RJ. The geometric signature: Quantifying landslide-terrain types from digital elevation models. Mathematical Geology. 1988; 20: 491–511.

27. Piikki K, Wetterlind J, Söderström M, Stenberg B. Three-dimensional digital soil mapping of agricultural fields by integration of multiple proximal sensor data obtained from different sensing methods. Precision Agric. 2015; 16: 29–45.

28. Taghizadeh-Mehrjardi R, Neupane R, Sood K, Kumar S. Artificial bee colony feature selection algorithm combined with machine learning algorithms to predict vertical and lateral distribution of soil organic matter in South Dakota, USA. Carbon Management. 2017; 8: 277–291.

29. Viscarra Rossel RA, Chen C, Grundy MJ, Searle R, Clifford D, Campbell PH. The Australian three-dimensional soil grid: Australia's contribution to the GlobalSoilMap project. Soil Res. 2015; 53: 845.

30. Lacoste M, Minasny B, McBratney AB, Michot D, Viaud V, Walter C. High resolution 3D mapping of soil organic carbon in a heterogeneous agricultural landscape. Geoderma. 2014; 213: 296–311.

31. Malone BP, McBratney AB, Minasny B, Laslett GM. Mapping continuous depth functions of soil carbon storage and available water capacity. Geoderma. 2009; 154: 138–152.

32. Liu F, Rossiter DG, Song X-D, Zhang G-L, Yang R-M, Zhao Y-G, et al. A similarity-based method for three-dimensional prediction of soil organic matter concentration. Geoderma. 2016; 263: 254–263.

33. Minasny B, McBratney AB, Mendonça Santos ML, Odeh IOA, Guyon B. Prediction and digital mapping of soil carbon storage in the Lower Namoi Valley. Soil Res. 2006; 44: 233.

34. Aldana Jague E, Sommer M, Saby NPA, Cornelis J-T, van Wesemael B, van Oost K. High resolution characterization of the soil organic carbon depth profile in a soil landscape affected by erosion. Soil and Tillage Research. 2016; 156: 185–193.

35. Kempen B, Brus DJ, Stoorvogel JJ. Three-dimensional mapping of soil organic matter content using soil type–specific depth functions. Geoderma. 2011; 162: 107–123.

36. Veronesi F, Corstanje R, Mayr T. Mapping soil compaction in 3D with depth functions. Soil and Tillage Research. 2012; 124: 111–118.

37. Yang Y, Mohammat A, Feng J, Zhou R, Fang J. Storage, patterns and environmental controls of soil organic carbon in China. Biogeochemistry. 2007; 84: 131–141.

38. Brus DJ, Yang R-M, Zhang G-L. Three-dimensional geostatistical modeling of soil organic carbon: A case study in the Qilian Mountains, China. CATENA. 2016; 141: 46–55.

39. Orton TG, Pringle MJ, Bishop TFA. A one-step approach for modelling and mapping soil properties based on profile data sampled over varying depth intervals. Geoderma. 2016; 262: 174–186.

40. Veronesi F, Corstanje R, Mayr T. Landscape scale estimation of soil carbon stock using 3D modelling. Sci Total Environ. 2014; 487: 578–586. pmid:24636454

41. Liu F, Zhang G-L, Sun Y-J, Zhao Y-G, Li D-C. Mapping the Three-Dimensional Distribution of Soil Organic Matter across a Subtropical Hilly Landscape. Soil Science Society of America Journal. 2013; 77: 1241.

42. Chen C, Hu K, Li H, Yun A, Li B. Three-Dimensional Mapping of Soil Organic Carbon by Combining Kriging Method with Profile Depth Function. PLoS ONE. 2015; 0: e0129038. pmid:26047012

43. Gasch CK, Hengl T, Gräler B, Meyer H, Magney TS, Brown DJ. Spatio-temporal interpolation of soil water, temperature, and electrical conductivity in 3D + T: The Cook Agronomy Farm data set. Spatial Statistics. 2015; 14: 70–90.

44. Behrens T, Förster H, Scholten T, Steinrücken U, Spies E-D, Goldschmitt M. Digital soil mapping using artificial neural networks. Journal of Plant Nutrition and Soil Science. 2005; 168: 21–33.

45. Behrens T, Scholten T. A comparison of data-mining techniques in predictive soil mapping. In: Lagacherie P, McBratney AB, Voltz M, editors. Digital soil mapping. An introductory perspective. 1st ed. Amsterdam, Boston: Elsevier; 2007. pp. 353–365.

46. Bruelheide H, Nadrowski K, Assmann T, Bauhus J, Both S, Buscot F, et al. Designing forest biodiversity experiments: general considerations illustrated by a new large experiment in subtropical China. Methods Ecol Evol. 2014; 5: 74–89.

47. Seitz S, Goebes P, Song Z, Bruelheide H, Härdtle W, Kühn P, et al. Tree species and functional traits but not species richness affect interrill erosion processes in young subtropical forests. SOIL. 2016; 2: 49–61.

48. Yang X, Bauhus J, Both S, Fang T, Härdtle W, Kröber W, et al. Establishment success in a forest biodiversity and ecosystem functioning experiment in subtropical China (BEF-China). Eur J Forest Res. 2013; 132: 593–606.

49. Goebes P, Seitz S, Kühn P, Li Y, Niklaus PA, von Oheimb G, et al. Throughfall kinetic energy in young subtropical forests: Investigation on tree species richness effects and spatial variability. Agricultural and Forest Meteorology. 2015; 213: 148–159.

50. Trogisch S, Schuldt A, Bauhus J, Blum JA, Both S, Buscot F, et al. Toward a methodical framework for comprehensively assessing forest multifunctionality. Ecol Evol. 2017; 7: 10652–10674. pmid:29299246

51. Orton TG, Pringle MJ, Page KL, Dalal RC, Bishop TFA. Spatial prediction of soil organic carbon stock using a linear model of coregionalisation. Geoderma. 2014; 230–231: 119–130.

52. Krige DG. A statistical approach to some basic mine valuation problems on the Witwatersrand. Journal of the Chemical Metallurgical & Mining Society of South Africa. 1951; 52: 119–139.

53. Conrad O, Bechtel B, Bock M, Dietrich H, Fischer E, Gerlitz L, et al. System for Automated Geoscientific Analyses (SAGA) v. 2.3.1. Geoscientific Model Development; 2015: 1991–2007.

54. Evans IS. An Integrated System of Terrain Analysis and Slope Mapping. Final Report (Report 6) on Grant DA-ERO-591-73-G0040. Durham: Department of Geography, University of Durham; 1979.

55. Haralick RM. Ridge and valley detection on digital images. Computer Vision, Graphics and Image Processing. 1983; 22: 29–38.

56. Horn BKP. Hill shading and the reflectance map. Proc. IEEE. 1981; 69: 14–47.

57. Tarboton DG. A new method for the determination of flow directions and upslope areas in grid digital elevation models. Water Resources Management. 1997; 33: 309–319.

58. Zevenbergen LW, Thorne CR. Quantitative Analysis of Land Surface Topography. Earth Surface Processes and Landforms. 1987; 12: 47–56.

59.Böhner J, Antonic O. Land-Surface Parameters Specific to Topo-Climatology. In: Hengl T, Reuter HI, editors. Geomorphometry. Concepts, software, applications. 1st ed. Amsterdam Netherlands, Oxford UK, Boston Mass.: Elsevier; 2009. pp. 195–226.

60. Freeman GT. Calculating catchment area with divergent flow based on a regular grid. Computers & Geosciences. 1991; 17: 413–422.

61. Moore ID, Grayson RB, Ladson AR. Digital terrain modelling: A review of hydrological, geomorphological, and biological applications. Hydrological Processes. 1991; 5: 3–30.

62. Wischmeier WH, Smith DD. Predicting rainfall erosion losses. A guide to conservation planning. In: United States Department of Agriculture, editor. Agriculture Handbook. Washington D. C.; 1978.

63. Wood J. The geomorphological characterization of digital elevation models. Dissertation, University of Leicester. 1996. https://lra.le.ac.uk/handle/2381/34503.

64. Behrens T, Schmidt K, Zhu AX, Scholten T. The ConMap approach for terrain-based digital soil mapping. European Journal of Soil Science. 2010; 61: 133–143.

65. Behrens T, Zhu AX, Schmidt K, Scholten T. Multi-scale digital terrain analysis and feature selection for digital soil mapping. Geoderma. 2010; 155: 175–185.

66. Kuhn M, Johnson K. Applied Predictive Modeling. New York, NY: Springer New York; 2013.

67.R Development Core Team. R: A language and environment for statistical coputing. Wien, Austria: R Foundation for Statistical Computing; 2016.

68. Kuhn M. Building Predictive Models in R Using the caret Package. Journal of Statistical Software, Articles. 2008; 28: 1–26.

69. Friedman JH. Multivariate adaptive regression splines. The Annals of Statistics. 1991; 19: 1–141.

70. Breiman L, Friedman JH, Stone CJ, Olshen RA. Classification and Regression Trees. New York, NY: Chapman and Hall; 1984.

71. Milborrow S. earth: Multivariate Adaptive Regression Splines. Derived from mda:mars by T. Hastie; R. Tibshirani; 2011.

72. Schmidt K, Behrens T, Daumann J, Ramirez-Lopez L, Werban U, Dietrich P, et al. A comparison of calibration sampling schemes at the field scale. Geoderma. 2014; 232–234: 243–256.

73Breiman L. Random Forests. Machine Learning. 2001: 5–32.

74.Díaz-Uriarte R, Alvarez de Andrés S. Gene selection and classification of microarray data using random forest. BMC Bioinformatics. 2006; 7: 3. pmid:16398926

75. Liaw A, Wiener M. Classification and Regression by randomForest. R News. 2002; 2: 19–22.

76. Vapnik VN. The Nature of Statistical Learning Theory. New York, NY: Springer; 1995.

77. Drucker H, Burges CJC, Kaufman L, Smola AJ, Vapnik VN. Support Vector Regression Machines. Advances in Neural Information Processing. 1997; 9: 155–161.

78. Smola AJ, Schölkopf B. A tutorial on support vector regression. Statistics and Computing. 2004; 14: 199–222.

79. Caputo B, Sim K, Furesjo F, Smola AJ. Appearance–Based Object Recognition Using SVMs: Which Kernel Should I Use. Proceedings of NIPS Workshop on Statistical Methods for Computational Experiments in Visual Processing and Computer Vision. 2002.

80. Karatzoglou A, Smola AJ, Hornik K, Zeileis A. kernlab—An S4 Package for Kernel Methods in R. Journal of Statistical Software. 2004; 11: 1–20.

81. Schmidt K, Behrens T, Scholten T. Instance selection and classification tree analysis for large spatial datasets in digital soil mapping. Geoderma. 2008; 146: 138–146.

82. Lin LI-K. A Concordance Correlation Coefficient to Evaluate Reproducibility. Biometrics. 1989; 45: 255. pmid:2720055

83. Chen Y, Yu S, Liu S, Wang X, Zhang Y, Liu T, et al. Reforestation makes a minor contribution to soil carbon accumulation in the short term: Evidence from four subtropical plantations. Forest Ecology and Management. 2017; 384: 400–405.

84. Wang H, Liu S, Wang J, Shi Z, Lu L, Zeng J, et al. Effects of tree species mixture on soil organic carbon stocks and greenhouse gas fluxes in subtropical plantations in China. Forest Ecology and Management. 2013; 300: 4–13.

85. Goebes P, Schmidt K, Seitz S, Both S, Bruelheide H, Erfmeier A, et al. The strength of soil-plant interactions under forest is related to a Critical Soil Depth. Sci Rep. 2019; 98635. pmid:31201351

86. Minasny B, McBratney AB. A conditioned Latin hypercube method for sampling in the presence of ancillary information. Computers & Geosciences. 2006; 32: 1378–1388.

87. Tang X, Xia M, Pérez-Cruzado C, Guan F, Fan S. Spatial distribution of soil organic carbon stock in Moso bamboo forests in subtropical China. Sci Rep. 2017; 7: 42640. pmid:28195207

88. Rumpel C, Chabbi A, Marschner B. Carbon Storage and Sequestration in Subsoil Horizons: Knowledge, Gaps and Potentials. In: Lal R, Lorenz K, Hüttl RF, Schneider BU, von Braun J, editors. Recarbonization of the Biosphere. Ecosystems and the Global Carbon Cycle. Dordrecht: Springer; 2012. pp. 444–464.

89. McBratney AB, Field DJ, Koch A. The dimensions of soil security. Geoderma. 2014; 213: 203–213.

90. Bishop TFA, McBratney AB, Laslett GM. Modelling soil attribute depth functions with equal-area quadratic smoothing splines. Geoderma. 1999; 91: 27–45.

Manuscript 5: 3D mapping of soil organic carbon content and soil moisture with multiple geophysical sensors and machine learning

Published in: Vadose Zone Journal 19, 1.

Tobias Rentschler[1,2], Ulrike Werban[3],*, Mario Ahner[1] , Thorsten Behrens[1,4], Philipp Gries[1,2], Tomas Scholten[1,2,4], Sandra Teuber[1,2], Karsten Schmidt[1,2,4,5]

[1] Dep. of Geosciences, Chair of Soil Science and Geomorphology, Univ. of Tübingen, Rümelinstr. 19-23, Tübingen 72070, Germany

[2] SFB 1070 ResourceCultures, Univ. of Tübingen, Gartenstr. 29, Tübingen 72074, Germany

[3] Dep. of Monitoring and Exploration Technologies, Helmholtz Centre for Environmental Research–UFZ, Permoserstr. 15, Leipzig 04318, Germany

[4] Cluster of Excellence Machine Learning: New Perspectives for Science, Univ. of Tübingen, Maria von Linden Str. 6, Tübingen 72076, Germany

[5] eScience-Center, Univ. of Tübingen, Keplerstr. 2, Tübingen 72074, Germany

Abstract

Soil organic C (SOC) and soil moisture (SM) affect the agricultural productivity of soils. For sustainable food production, knowledge of the horizontal as well as vertical variability of SOC and SM at field scale is crucial. Machine learning models using depth-related data from multiple electromagnetic induction (EMI) sensors and a gamma-ray spectrometer can provide insights into this variability of SOC and SM. In this work, we applied weighted conditioned Latin hypercube sampling to calculate 25 representative soil profile locations based on geophysical measurements on the surveyed agricultural field, for sampling and modeling. Ten additional random profiles were used for independent model validation. Soil samples were taken from four equal depth increments of 15 cm each. These were used to approximate polynomial and

exponential functions to reproduce the vertical trends of SOC and SM as soil depth functions. We modeled the function coefficients of the soil depth functions spatially with Cubist and random forests with the geophysical measurements as environmental covariates. The spatial prediction of the depth functions provides three-dimensional (3D) maps of the field scale. The main findings are (a) the 3D models of SOC and SM had low errors; (b) the polynomial function provided better results than the exponential function, as the vertical trends of SOC and SM did not decrease uniformly; and (c) the spatial prediction of SOC and SM with Cubist provided slightly lower error than with random forests. Hence, we recommend modeling the second-degree polynomial with Cubist for 3D prediction of SOC and SM at field scale.

Abbreviations

CCC	concordance correlation coefficient
cLHS	conditioned Latin hypercube sampling
DSM	digital soil mapping
ECa	apparent electrical conductivity
EMI	electromagnetic induction
HDP	horizontally oriented magnetic dipole
nRMSE	normalized root mean squared error
SM	soil moisture
SOC	soil organic carbon
3D	three-dimensional
VDP	vertically oriented magnetic dipole
wecLHS	weighted conditioned Latin hypercube sampling with extremes.

1 INTRODUCTION

The lack of knowledge about the resource soil is a major gap in agriculture (Godfray et al., 2010). Soils play a key role in sustainable agriculture (Bouma, 2014; Bouma & McBratney, 2013) and thus food production. Soil management practices are directly linked to the spatial knowledge about soil properties and conditions that are relevant indicators for more efficient and effective agriculture. As one of the key soil properties, soil organic C content (SOC) is relevant for soil quality and fertility, as it influences the soil's nutrient availability and structural stability (Dexter et al., 2008). In combination with soil texture, SOC affects the soil water-holding capacity, plant available water, and soil moisture (SM; Rawls, Pachepsky, Ritchie, Sobecki, & Bloodworth, 2003). Understanding the spatial as well as vertical variability of SOC and SM is essential for plant cultivation, which requires fertile soils and sufficient water. Digital soil mapping (DSM) can provide high-resolution information for sustainable agricultural management to facilitate food production on the field and farm scale through the spatial prediction of physical and chemical soil properties (Govers, Merckx, van Wesemael, & van Oost, 2017), such as SOC and SM. This facilitates an improvement in the decision-making processes for fertilization, irrigation, and liming, among others, and subsequently higher productivity of food and biofuels (McBratney, Whelan, Ancev, & Bouma, 2005).

However, soil properties vary in the horizontal as well as in the vertical domain. Hengl et al. (2014) and Viscarra Rossel et al. (2015) mapped soil properties in multiple depths, which can be interpreted three-dimensionally, but do not actually provide continuous three-dimensional (3D) information (Liu et al., 2016). To fully grasp the continuous character of soil, the third dimension should be included in the analysis as continuous entity (e.g., by incorporating mathematical functions that represent the

vertical distribution of soil properties, so-called soil depth functions; Aldana Jague et al., 2016; Minasny, McBratney, Mendonça-Santos, Odeh, & Guyon, 2006; Rentschler et al., 2019; Veronesi, Corstanje, & Mayr, 2014). The spatial distribution of soil depth functions is related to the spatial distribution of environmental covariates given by the soil forming equation (Jenny, 1941; McBratney, Mendonça Santos, & Minasny, 2003):

$$S = f(s, c, o, r, p, a, n)$$

where *S* is the soil or any soil information we would like to explain, *s* stands for other available soil properties at a location, *c* is climate, *o* is organisms, the factor *r* is the terrain, *p* is the parent material, *a* is age, and *n* is the spatial position. The function coefficients of the soil depth functions can be treated as an abstract soil property and therefore modeled and predicted spatially based on comprehensive sets of environmental covariates delineated from digital elevation models representing terrain (Aldana Jague et al., 2016; Minasny et al., 2006; Rentschler et al., 2019; Veronesi et al., 2014), provided by land cover maps representing organisms (Minasny et al., 2006; Veronesi et al., 2014) and gamma-ray sensing data as indicators for soil-forming minerals (Aldana Jague et al., 2016; Cook, Corner, Groves, & Grealish, 1996; Minasny et al., 2006). Besides gamma-ray spectrometry, hydrogeophysical methods, such as electromagnetic induction (EMI) sensors, provide a widely used base in DSM in general (Binley et al., 2015; Cassiani et al., 2012; Martini et al., 2017), as well as in 3D soil mapping specifically (Moghadas, Taghizadeh-Mehrjardi, & Triantafilis, 2016), complementing field sampling by generating high-resolution spatial geophysical covariates. In particular, geophysical sensing technologies and measurements are urgently needed at the field scale, as the distribution of soil properties (*S*) in the vertical domain are decreasingly linked to terrain (*r*) and climate (*c*) variability but more prone to variations in weathering, mineralogy (as parts of *s* and *p*), biological activities, as

well as past anthropogenic influences (*o* and *a*; Jobbágy & Jackson, 2000; Rentschler et al., 2019).

Core Ideas

- Multi-depth ECa and gamma-ray spectrometry describe vertical trends of SOC and soil moisture.
- Machine learning models can predict vertical trends of SOC and soil moisture spatially.
- Cubist models of polynomial depth functions provide accurate 3D maps at field scale.

Apparent electrical conductivity (ECa) from EMI sensors and dose rate, 40K, 238U, and 232Th contents from gamma-ray spectrometers are covariates that are closely linked to numerous soil properties, such as texture, horizonation, bulk density, SOC, and SM in the case of EMI (Cho, Sudduth, & Chung, 2016; Doolittle & Brevik, 2014; Martini et al., 2017), and in the case of gamma-ray spectrometry texture and SOC. Thus, gamma-ray spectrometry and EMI are used either individually or combined (Castrignanò, Wong, Stelluti, Benedetto, & Sollitto, 2012) as a proxy to the mineralogy of the parent material and other soil properties developed or inherited from the parent material (Cook et al., 1996; Jenny, 1941; McBratney et al., 2003). The geophysical measurements are interpolated with geostatistical methods like kriging (Krige, 1951) to obtain spatial information of ECa, 40K, 238U, and 232Th covering the whole field with high spatial resolution (Abdu, Robinson, Seyfried, & Jones, 2008; Schmidt et al., 2014). The interpolations of the geophysical measurements constitute the covariate space of the agricultural field, which is utilized in crucial modules of DSM:

1. The spatial data of 40K, 238U, and 232Th and multi-depth ECa are used to calculate the locations of a representative sampling scheme for soil sampling. The aim is to fully cover potential soil variability that influences the modeled soil property, and that is found on the field at the time of measurement. For that, many approaches use conditioned Latin hypercube sampling (cLHS) or extensions like weighted extreme cLHS (Minasny & McBratney, 2006; Schmidt et al., 2014). The cLHS is a stratified random sampling design that provides an optimal stratification of a covariate space with a reduced number of spatially distinct sample sites (Minasny & McBratney, 2006).
2. The sampled point-wise soil data (i.e., SOC and SM in this work) is linked to the geophysical measurements at the soil profile locations with linear or nonlinear machine learning models (Aldana Jague et al., 2016; Rentschler et al., 2019; Schmidt et al., 2014). The dependent variable of the models are the samples measured at the locations introduced above, and the independent variables are the interpolated geophysical measurements at these locations.
3. The model trained with sampled soil data and geophysical measurements is used to make predictions to the locations of the covariate space where no soil samples were taken.
4. The model predictions are validated with additional soil samples. Ideally, the sampling scheme used for validation is independent from the scheme used for model training, which can be achieved with randomly distributed samples (Brus, Kempen, & Heuvelink, 2011; Steyerberg & Harrell, 2016).

Based on the modules of DSM described above and the potential to measure 3D soil properties provided by geophysical measurements (other available soil properties s in

the soil forming equation), we assume that EMI and gamma-ray spectroscopy are highly suitable for the spatial prediction of soil depth functions, as the combination of multi-coil EMI and gamma-ray spectrometry provides multiple penetration depths and a different sensitivity to soil parameters (Dierke & Werban, 2013; McNeill, 1980a, 1980b). To our knowledge, there are no studies on spatial prediction of soil depth functions with EMI and gamma-ray sensing data as environmental covariates.

The major objective of this study was the prediction of SOC and SM in 3D using soil depth functions based on EMI data from sensors with 12 different penetration depths and gamma-ray spectrometry by capturing the response of the parent material and overlaying soil. For model training, we used Cubist and random forests, two machine learning methods often used in DSM. The hypothesis is that for 3D modeling of SOC and SM, data from EMI and gamma-ray spectrometry will achieve low errors throughout the sampled depth increments, due to the different depth penetration of the sensors.

2 MATERIALS AND METHODS

2.1 Study site

The study site is an agricultural field of 58 ha ≈70 km north of Leipzig, Saxony, Germany (Figure 1). The field is located on the Elbe flood plain and bordered by the creeks Altes Flieth and Fließgraben. There is no visible terrain variation in the field. Present soil types are Gleysols and Gleyic Cambisols consisting of alluvial loam (loam and clay) over Holocene sediments of fluvial sand (LAGB, 2014). At the time of sampling in August 2017, the cultivated wheat (*Triticum aestivum* L.) had been harvested, and the field was bare.

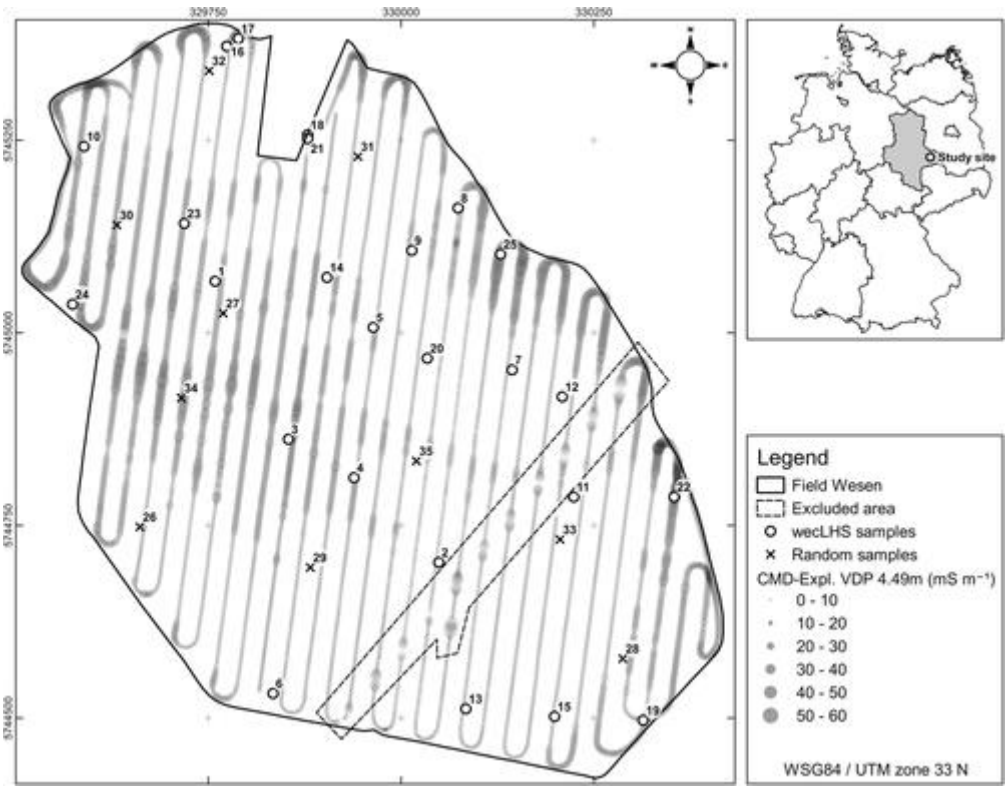

FIGURE 1

Location of the field Wesen near Selbitz, Saxony-Anhalt, Germany, sampling scheme of the geophysical measurements with electromagnetic induction (EMI) and gamma-ray spectrometry, and sampled soil profiles (circle, weighted conditioned Latin hypercube sampling with extremes [wecLHS] samples for calibration, cross, random samples for validation). The signal of the CMD-Explorer with 4.49-m intercoil spacing and vertical dipole orientation (VDP) was noisy due to a grid gas pipe, and therefore measurements of all sensors were omitted in the marked area

2.2 Methodological overview

The workflow consisted of seven individual steps (Figure 2). First, the geophysical measurements were taken with EMI and gamma-ray spectrometry and, subsequently, interpolated geostatistically with ordinary kriging (Krige, 1951) to receive spatial predictions of the environmental covariates. These covariates were used to calculate representative sampling locations with an extension of cLHS (Minasny & McBratney, 2006) and served as independent variables for the soil depth function modeling. In the next step, these models were applied for spatial prediction of the soil depth functions with the independent variables and validated independently in the final step. The subsections below describe this workflow in detail.

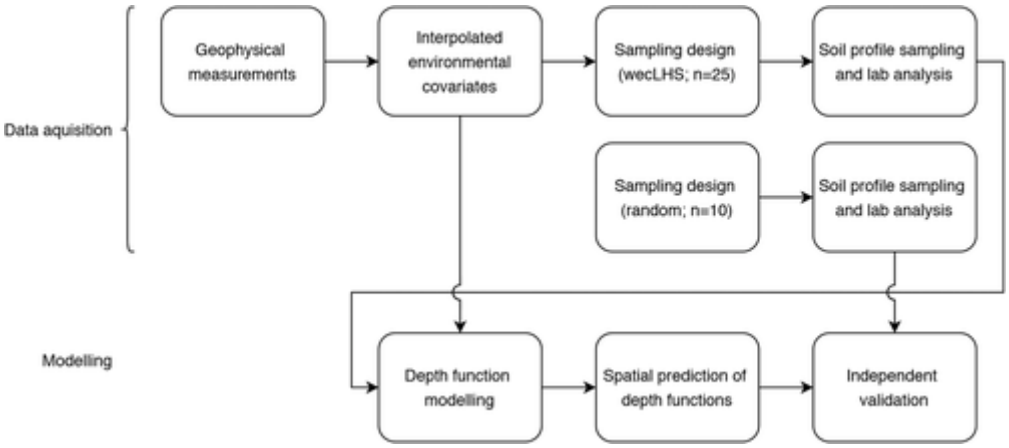

FIGURE 2

Workflow diagram illustrating the individual working steps of this study

The geophysical measurements were recorded with two EMI sensors (CMD-Explorer and CMD-Mini-Explorer, both GF Instruments) and a gamma-ray spectrometer (GS CAR, GF Instruments) in August 2016. The EMI sensors measure the apparent electric conductivity (EC_a in mS m^{-1}). The penetration depth of the magnetic field is mainly controlled by the intercoil spacing and the orientation of the dipoles, as well as the applied frequency. The penetration depth and footprint of the sensor data increase with increasing intercoil spacing. Vertically oriented magnetic dipoles (VDP/coil axis horizontal coplanar [HCP]) provide a higher depth penetration than horizontally oriented magnetic dipoles (HDP/coil axis vertical coplanar [VCP]) while taking into account the different cumulative sensitivity functions of both orientations (Callegary, Ferre, & Groom, 2012; Martini et al., 2017; McNeill, 1980b; von Hebel et al., 2019). The CMD-Explorer and the CMD-Mini-Explorer enable simultaneous multi-depth exploration of EC_a with either VDP or HDP. The instruments have one transmitter and three receiver coils with different intercoil spacings covering six effective penetration depths, which is defined by the manufacturer (GF Instruments) as the depth above which 70% of the signal comes from (Table 1). This multi-sensor setup measuring EC_a and penetration depths of up to 6.7 m enables the detection of textural patterns of the spatially variable subsurface sediments of the Elbe floodplain indirectly (Doolittle & Brevik, 2014). This is important for SM modeling to account for subsurface sediment structures, as gravel lenses with high permeability can drain and clay lenses can retain percolate water or facilitate capillary water rise (Abdu et al., 2008).

The sledge-mounted devices (height of CMD-Explorer 80 cm, height of CMD-Mini-Explorer 10 cm) were towed by a four-wheel vehicle at <10 km h^{-1}, crossing the field in multiple parallel (track distance 27 m) and a few crossed transects. By using overlapping measurements collected at different time from crossing the field in the end,

drifts in the data were assessed and a linear drift function was applied to correct the data (Martini et al., 2017). Before interpolation these quality control lines, as well as outliers related to a gas pipe line, were removed (Figure 1). Within the dataset, negative values of EC_a occurred due to the custom calibration of the instrument (von Hebel et al., 2019). We corrected the measurements with an offset of 3.44 mS m^{-1} (CMD-Mini-Explorer VDP 0.32 m), 4.86 mS m^{-1} (CMD-Mini-Explorer HDP 0.32 m), and 0.21 mS m^{-1} (CMD-Mini-Explorer HDP 0.71 cm) to avoid confusion with these values and to make use of the containing information on spatial variability. Smoothing of the data was not necessary due to low noise conditions. All EMI sensors captured five records per second in any dipole orientation. We refrained from inverting EMI data, since the reliability of the required calibration procedure is limited due to a number of fundamental issues that are not solved yet (Martini et al., 2017).

TABLE 1. Intercoil spacings and effective penetration depth for vertical and horizontal coil orientation for the used electromagnetic induction (EMI) sensors CMD-Mini-Explorer and CMD-Explorer

EMI sensor	Intercoil spacing	Effective penetration depth	
		VDP [a]	HDP [a]
	m		
	0.32	0.50	0.25
CMD-Mini-Explorer	0.71	1.00	0.50
	1.18	1.80	0.90
	1.48	2.20	1.10
CMD-Explorer	2.82	4.20	2.10
	4.49	6.70	3.30

[a] VDP, vertically oriented dipole; HDP, horizontally oriented dipole.

The bulk (≈90%) of aboveground measured gamma radiation is emitted in the top 30–50 cm of soil (Cook et al., 1996). We used a gamma-ray spectrometer with a 4 l NaI(Tl)-crystal and automatic peak-stabilization to measure the concentration of ^{40}K, ^{238}U, and ^{232}Th. The device has 512 channels with an energy range from 100 keV to 3 MeV. Measurements were captured every 5 s. The ^{40}K, ^{238}U, and ^{232}Th were measured as counts per second. The concentration of ^{40}K (in %) and ^{238}U and ^{232}Th (both in μg g^{-1}, where μg g^{-1} = 1 ppm) was calculated corresponding to the decay rate at specific energy levels. The concentration of ^{40}K, ^{238}U, and ^{232}Th was used to calculate the dose rate (Gy h^{-1}; IAEA, 2003).

The geophysical measurements served as a basis for the sampling design (Figure 1) and were interpolated to a grid cell size of 5 m with ordinary kriging (Krige, 1951) using individual exponential semivariogram functions for each dataset in the *gstat* package version 1.1-5 (Pebesma, 2004) in R version 3.4.3 (R Development Core Team, 2017). Beforehand, measurements within 1-m range were averaged. Noisy measurements along a straight line were detected for the CMD-Explorer with the higher depth penetrations, caused by an underground grid gas pipe (Figure 1). For reasons of continuity, all measurements from the EMI sensors and the gamma-ray spectrometer in this area were excluded from further processing. This crucial step is to be evaluated carefully, since all consecutive steps strongly depend on accurate environmental covariates. Therefore, error of the kriging predictions was assessed with a 10-fold cross-validation, which is an out-of-sample testing method to assess the ability of the model to generalize to independent data subsets. For that, the dataset is partitioned in 10 folds of nearly equal size, where nine folds are used to train a model and tested with the 10th fold. This is done 10 times to test all folds, and the quality measure is the average of all models. For the final model, all folds are used.

2.4 Soil sampling

For the estimation of the number of soil profiles to sample, the areas under curve for the empirical cumulative distribution functions were calculated for the proposed sampling set sizes of n = 10, 20, 25, 30, 35, and 40 and the geophysical measurements with the MESS package version 0.5.0 (Ekstrøm, 2018) in R. The mean of the differences between the areas under curve indicated the error for each sample set size and the sample set size with the lowest error is chosen (Ramirez-Lopez et al., 2014; Schmidt et al., 2014). In this case, the optimal sample set size with the lowest error was 35. However, due to costs and feasibility constraints, we agreed on a sample set size of 25 for the representative sampling design as tradeoff between feasibility and a slight increase in model error.

Spatial soil modeling requires specific sampling schemes or designs for sampling and validation (Brus et al., 2011; Schmidt et al., 2014). The aim of a sampling design is to cover the full range of potential driving factors that influence the modeled soil property and that are found on the field at the time of measurement while reducing soil sampling effort and analytical costs. Therefore, we calculated the locations of the soil profiles to sample for model training with a weighted cLHS with extreme values (wecLHS; Schmidt et al., 2014) based on the geophysical covariates with the lowest error in cross-validation of each sensor, to obtain representative sampling locations. The wecLHS extends the cLHS (Minasny & McBratney, 2006) by including samples from the extrema of the used covariate space to cover the full range of data. Further, a weighting scheme according to the explained variation (R2) of the kriging predictions is implemented to account for noise in the interpolation (Schmidt et al., 2014). The wecLHS design was calculated with 150,000 iterations. The settings were a

temperature decrease of 0.95, an initial temperature of 1, optimization every 10 steps, and an initial Metropolis value of 1.

Additionally, we sampled 10 fully randomly distributed profile locations for independent model validation. We chose a fully random sampling design for validation, since wecLHS is a stratified random sampling design and for independent validation a nonstratified sampling strategy is recommended. Further, no assumptions regarding the standard error of the estimated quality measures are required (Brus et al., 2011; Steyerberg & Harrell, 2016). The locations of the sampled profiles are displayed in Figure 1.

The soil profiles were sampled from four equal depth increments to 60-cm depth (0–15, 15–30, 30–45, 45–60 cm) with a hand auger on 2 d with the same weather conditions in August 2017 again after harvest under similar field conditions as during sensing. Sixty centimeters is the depth above which ≈80% of the roots of many agricultural crops are found (Fan, McConkey, Wang, & Janzen, 2016). Samples were taken for each depth increment as mixed subsamples from two corners and the center of 1 m2 (Schmidt et al., 2014), resulting in 100 samples for the training set and 40 samples for the validation set. The positions of the profiles were located with a differential GPS (Leica TPS1200+, Leica Geosystems).

2.5 Laboratory analysis

For SOC determination, the samples were dried at 40 °C for 24 h, sieved (<2 mm), and ground and root fragments were removed. Total C was determined with dry combustion using an ELTRA CHS-580A Helios analyzer (ELTRA). Although LAGB (2014) states that soils in the flood plains of the Elbe river are mostly free of carbonates, pH of the samples ranged from 5.2 to 7.2. Consequently, inorganic C was determined

gravimetrically with 10 % HCl solution. Then, SOC was determined as the difference between total C and inorganic C.

Soil moisture was measured gravimetrically with drying at 90 °C for 24 h. A summary of the training and validation sets for SOC and SM is shown in Figure 3. Training and validation sets were similar. The rather small differences are due to the small sampling set size of the validation set and its sensitivity to extreme values because of its random and nonstratifying nature.

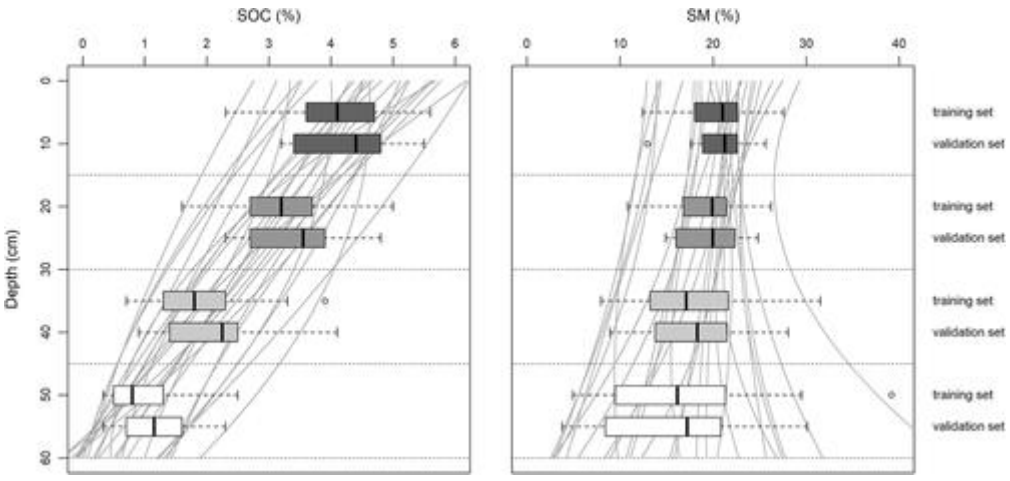

FIGURE 3

Summary of the training and validation sets for soil organic C (SOC) and soil moisture (SM) as boxplots and the respective polynomial soil depth functions. The boxplots show the variation of the samples within the sampled depth increments. Training and validation sets have a similar range at each sampled depth increment and the validation set is suitable for model evaluation. The polynomial soil depth functions show the vertical distribution at the 25 profiles of the training set

2.6 Model training, prediction, and validation

2.6.1 Soil depth functions and 3D predictions

For the 3D modeling of SOC and SM, we tested a second-degree polynomial (Equation 1; Aldana Jague et al., 2016) and an exponential function (Equation 2; Rentschler et al., 2019):

$$f(x)=c0+c1x+c2x2\text{fx=c0+c1x+c2x2} \quad (1)$$

$$f(x)=\exp c1+c2x\text{fx=expc1+c2x} \quad (2)$$

where c_0 is the intercept with the *y* axis, thus the SOC and SM at the surface, and c_1 and c_2 are dimensionless coefficients.

The functions coefficients c_0, c_1, and c_2 were modeled and predicted for the whole study site based on the geophysical data of the EMI sensor and gamma-ray spectrometer with Cubist and random forests. After modeling and spatial prediction of the coefficients of the soil depth functions, the respective function can be solved at every grid location of the study site, and SOC and SM can be calculated with any vertical resolution (Aldana Jague et al., 2016; Liu et al., 2016; Veronesi et al., 2014). However, vertical resolution is limited by the vertical sampling of each profile that reflects the vertical variation within each profile. In this work, the soil depth functions were solved from 0 to 60 cm with a vertical resolution of 5 cm. The main advantage of this approach is that solving the soil depth functions provides data points that represent a three-dimensional entity (voxels) of the response variables instead of two-dimensional pixels. The voxels were stored in an array with the dimensions of the study area in the horizontal domain (Rentschler et al., 2019). A workflow diagram is given in Figure 2.

2.6.2 Supervised machine learning

In many applications in DSM, supervised machine learning is used to train regression models with numeric values, such as the coefficients of soil depth functions. In such models, the function coefficients at each sampling location are the dependent variable (soil property *S* in the soil forming equation) and the geophysical measurements compose the covariate space of independent variables (i.e., EC_a in the measured depth intervals, ^{40}K, ^{238}U, and ^{232}Th) at the location of each sample for regression:

$$S = f(ECa, 40K, 238U, 232Th) \quad (3)$$

Subsequently, the model can predict the dependent variable for each grid location at the field, since the independent variables were measured and interpolated onto the whole study area. Common supervised machine learning methods in DSM are Cubist and random forests.

Cubist uses a robust system called M5 model tree, which was established by Quinlan (1992). It applies a recursive partitioning of data to build a piecewise linear model as a decision tree, where the terminal nodes are linear models. When growing the tree, intra-subset variation is minimized at each split. A leaf of such a tree applied on continuous data contains a linear model connecting the values of the training cases to their attribute values. The procedure is based on building and applying rules. The rules generate subsets of the data according to similar characteristics of predictor and response variables. The rules are structured as if (condition is true), then (regress), else (apply next rule), comprising single or multiple predictor variables. With the rules that fulfil the conditions, soil properties are predicted by ordinary least-squares regression. If the rule does not apply, a new rule is processed for the next node of the tree within an iterative process. These rule sets are appropriate for model interpretation (Quinlan, 1992, 1993).

Random forests were developed by Breiman (2001) as an ensemble of classification and regression trees (Breiman, Friedman, Stone, & Olshen, 1984). Binary splits are used for a single decision tree to homogenize the predictor variables according to the dependent variable, thus minimizing the node impurity. Random forests use a bootstrap approach, where random predictor variables are chosen at each split of a tree. The final regression model results from averaging all decision tree outputs (Breiman, 2001). Random forests are robust against overfitting and interpretable with the feature importance calculated from its randomly permutated trees (Breiman, 2001). However, this is beyond the scope of this study as it requires more detailed analysis of the depth functions as dependent variables.

The tuning parameters for the machine learning methods used were the number of subsequently adjusted trees committing to the final decision tree (committees) and the number of neighboring samples from the training set to adjust the model prediction (neighbors) for Cubist. The number of randomly selected covariates at each split (mtry) was used for tuning of random forests. The number of trees (ntree) and the node size of random forests were set to default as this is not necessary when a large number of trees is computational manageable (Probst & Boulesteix, 2018). To find the best tuning parameters for the models, a grid search (Schmidt, Behrens, & Scholten, 2008) with a 10 times repeated 10-fold cross-validation was applied. The final models were calibrated with the tuning parameters of the models with the lowest RMSE.

2.6.3 Model validation

The 3D predictions are validated independently with the coefficient of determination (R^2, Equation 3) as measure of correlation between the observed and predicted values, Lin's concordance correlation coefficient (CCC, Equation 4), the RMSE (Equation 5),

and the normalized RMSE (nRMSE, Equation 6) as measures of error with the 10 random profiles of four samples each taken at 0–15, 15–30, 30–45, and 45–60 cm. The CCC is a measure of concordance of the model predictions and the measured values on the 1:1 line from the origin. The RMSE is a measure of error, which allows to compare models with observed values of the same magnitude. Since the response of SOC and SM has observed values of different range, the nRMSE is required to compare the models for each depth increment.

The equations for R^2, the CCC, the RMSE, and nRMSE are

$$R^2 = \left[\frac{\sum_{i=1}^{n} (y-\mu y)(\hat{y}-\mu\hat{y})}{\sqrt{\sum_{i=1}^{n} (y-\mu y)2}\sqrt{\sum_{i=1}^{n} (\hat{y}-\mu\hat{y})2}}\right]^2 \quad (1)$$

$$CCC = \frac{2\rho\sigma_y\sigma_{\hat{y}}}{\sigma_{y2}+\sigma_{\hat{y}2}+(\mu_y-\mu_{\hat{y}})^2} \quad (2)$$

$$RMSE = \sqrt{\frac{1}{n}\sum_{i=1}^{n}(y_i - \hat{y}_i)^2} \quad (3)$$

$$nRMSE = \frac{RMSE}{y_{max}-y_{min}} \quad (4)$$

where y and $\hat{y}$ are the observed and predicted values, μ_y and $\mu_{\hat{y}}$ denote the means for the observed and predicted values, respectively, ρ is the correlation coefficient (Pearson's r), σ_y and $\sigma_{\hat{y}}$ are the corresponding variances, y_{max} is the maximum of the observed values, and y_{min} is the minimum of the observed values.

3 RESULTS AND DISCUSSION

3.1 Geophysical measurements and interpolation

The results of the 10-fold cross-validation for the geostatistical interpolation showed a high coefficient of determination (R^2) between the observed and the predicted values for all EMI sensors ($R^2 > .96$) and low errors (nRMSE ≤ 0.08). The predictions for the

CMD-Mini-Explorer with intercoil spacings of 0.71 and 1.18 m and VDPs had the highest coefficient of determination (R^2 = .99 and nRMSE = 0.01), and the predictions for the CMD-Explorer with an intercoil spacing of 4.49 m and horizontally oriented dipole had the lowest coefficient of determination (R^2 = .96 and nRMSE = 0.04).

The cross-validation results of the gamma-ray spectrometer showed coefficients of determination ranging from .75 (^{238}U) up to .92 (dose rate). The lower R^2 compared with EMI sensor interpolation is to be expected due to the noise prone passive nature of statistical counting gamma decays. The errors of the interpolation range from 0.05 (dose rate) to 0.07 (^{238}U). All results of the 10-fold cross-validation are shown in Table 2.

The spatial variation of the measured EC_a varies between the sensors and sensor orientation. The highest values were measured with the CMD-Mini-Explorer VDP (0.71 m; Table 2, Figure 4b), and the lowest values were measured with the CMD-Mini-Explorer HDP (0.32 m; Figure 4d). The measures with the CMD-Mini-Explorer in the same orientation (VDP and HDP) showed considerable changes in EC_a (Figure 4a–4c, 4d–4f) with increasing intercoil spacing, whereas the measurements with CMD-Explorer were more alike (Figure 4g–4l). However, we used all EMI measures as independent variables, since the similar depths of investigation may contain varying information while using different coil orientation resulting in

TABLE 2. Results of the 10-fold cross-validation of the interpolation with ordinary kriging. The sensors and sensor setups we used for the weighted conditioned Latin hypercube sampling with extremes (wecLHS) sampling design are highlighted in bold

Sensor setting (coil distance)[a]	Effective depth range	Min.	Max.	R^2	RMSE[b]	nRMSE[c]
	m					
CMD-Mini-Explorer VDP (0.32 m)	0.5	0.00	45.63	.98	1.07	0.02
CMD-Mini-Explorer VDP (0.71 m)	1.0	13.47	68.83	.99	0.69	0.01
CMD-Mini-Explorer VDP (1.18 m)	1.8	5.92	62.75	.99	0.82	0.01
CMD-Mini-Explorer HDP (0.32 m)	0.25	0.00	27.65	.98	1.05	0.03
CMD-Mini-Explorer HDP (0.71 m)	0.5	0.00	40.25	.98	1.03	0.02
CMD-Mini-Explorer HDP (1.18 m)	0.9	3.69	50.69	.98	0.79	0.02
CMD-Explorer VDP (1.48 m)	2.2	5.89	41.95	.97	1.65	0.04
CMD-Explorer VDP (2.82 m)	4.2	7.26	47.33	.98	2.00	0.05
CMD-Explorer VDP (4.49 m)	6.7	8.50	48.13	.98	1.79	0.04
CMD-Explorer HDP (1.48 m)	1.1	5.31	26.10	.97	1.91	0.08
CMD-Explorer HDP (2.82 m)	2.1	4.94	34.91	.97	1.72	0.05
CMD-Explorer HDP (4.49 m)	3.3	6.61	39.80	.96	1.29	0.04
^{40}K	–	0.60	1.20	.75	0.05	0.08
^{232}Th	–	2.36	9.66	.80	0.48	0.06
^{238}U	–	0.91	3.52	.75	0.24	0.07
Dose rate	–	19.24	51.87	.92	1.50	0.05

[a] VDP, vertically oriented dipole; HDP, horizontally oriented dipole.

[b] RMSE units are mS m^{-1} for electromagnetic induction (EMI) sensors, % for ^{40}K, µg g^{-1} for ^{232}Th and ^{238}U concentrations, and Gy h^{-1} for dose rate.

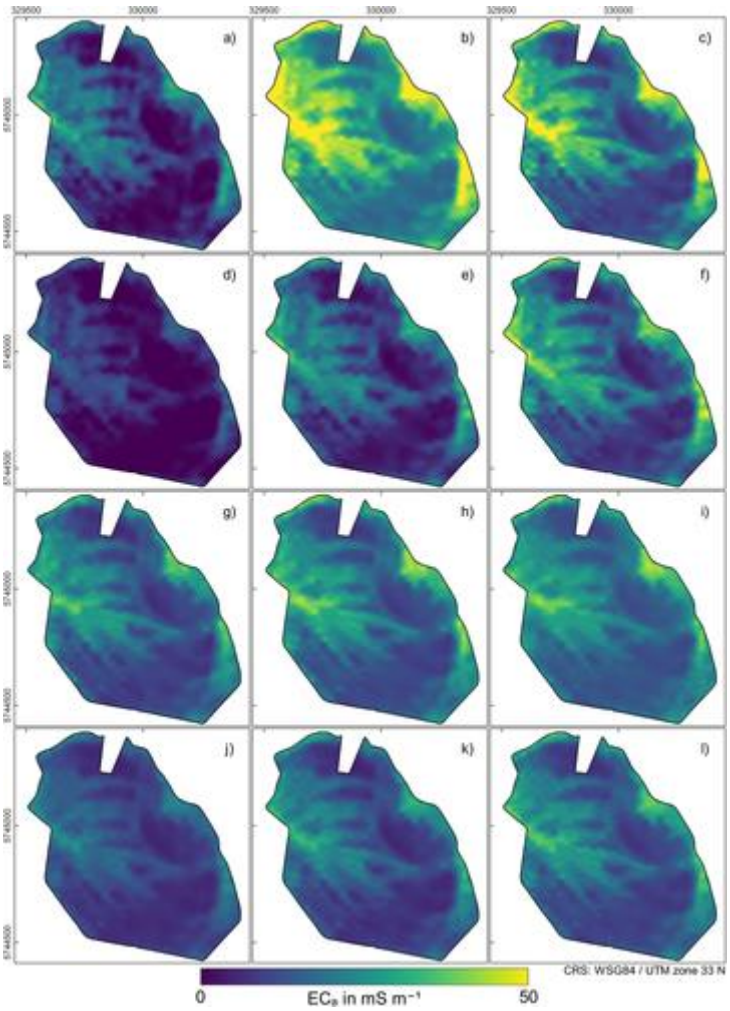

FIGURE 4

Results of the interpolation with ordinary kriging for apparent electrical conductivity (EC_a) measured with an (a–c) CMD-Mini-Explorer vertically oriented magnetic dipole (VDP), (d–f) CMD-Mini-Explorer horizontally oriented magnetic dipole (HDP), (g–i) CMD-Explorer VDP, and (j–l) CMD-Explorer HDP in order of increasing effective depth range. CRS, coordinate reference system; UTM, Universal Transverse Mercator (coordinate system)

different shapes of their sensitivity functions. The interpolations of ^{40}K, ^{232}Th, ^{238}U, and dose rate (Figure 5) showed different spatial trends with some shared local minima in the center and the southeast and a shared local maximum in the west of the field. All results of the interpolations are visualized in Figures 4 and 5.

Given the low error (nRMSE ≤ 8%) of the interpolation for the EMI data and for gamma-ray measurements, the environmental covariates interpolated with ordinary kriging represented the spatial distribution of EC_a at multiple depths, ^{232}Th, ^{238}U, and dose rate adequately. Thus, they were suitable to calculate a wecLHS sampling design, as well as for modeling and mapping of SOC and SM in the horizontal and vertical domain. The covariates with low cross-validation error and high coverage of the covariate space used for wecLHS were dose rate for the gamma-ray spectrometer and CMD-Mini-Explorer with VDP (0.32 m intercoil spacing), CMD-Mini-Explorer with HDP (0.32 m) and CMD-Explorer with VDP (4.49 m) for the EMI sensors.

3.2 Soil depth functions

The fitted soil depth functions showed the vertical trend of SOC and SM at the profile locations (Figure 3). For both polynomial and exponential functions at each profile, the R^2 and RMSE values of the soil depth functions were calculated. The soil depth function with the highest R^2 for SOC and SM was the polynomial function (Equation 1) with a mean R^2 of .98 for SOC and 0.92 for SM (RMSE = 0.14 and 0.00). The exponential soil depth function had lower mean R^2 and a higher error for both SOC and SM. A summary of the evaluation of the soil depth functions is shown in Table 3.

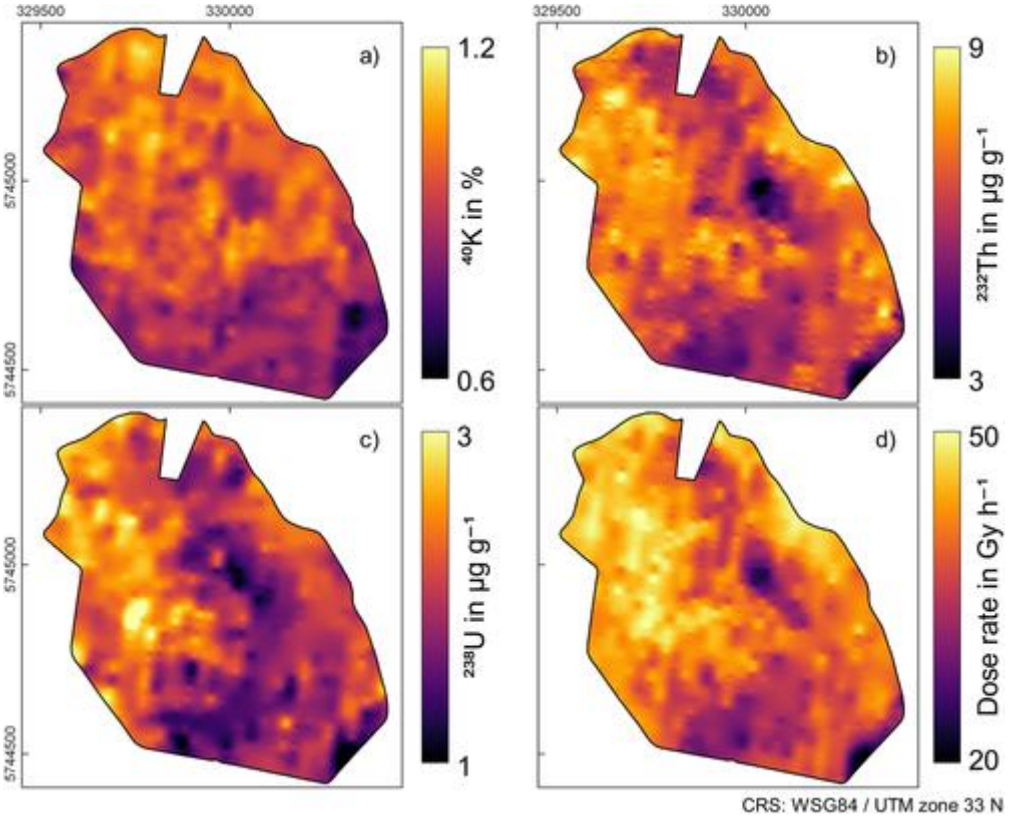

FIGURE 5

Results of the interpolation with ordinary kriging for (a) ^{40}K, (b) ^{232}Th, (c) ^{238}U, and (d) dose rate

The minimum values in R^2 and the high standard deviation of the soil depth functions for SM showed that the soil depth functions could not depict the vertical trend in some soil profiles (Table 3). This is the case for Profiles 2 and 10, where the SM was 0.22, 0.20, 0.23, and 0.21 and 0.25, 0.21, 0.22, and 0.24, respectively. These profiles had a local maximum or minimum between 15 and 45 cm that could not be modeled with the exponential function, which cannot be explained with the geophysical measurements or additional knowledge about the field. In both cases, the polynomial function of second degree had a lower error than for all other profiles. To solve this, other functions are required that can reproduce vertical distributions with local minima and maxima (minimax; Minasny, Stockmann, Hartemink, & McBratney, 2016).

TABLE 3. Summary of the model validation results with the coefficient of determination (R^2) and RMSE (in %) of the polynomial and exponential depth functions for soil organic C (SOC) and soil moisture (SM). Bolded values are referred to in the text

Trait	Statistic	Function	Min.	Median	Mean	Max.	SD
SOC	R^2	Polynomial	.93	.98	**.98**	1.00	.02
		Exponential	.83	.95	.94	1.00	.04
	RMSE	Polynomial	0.02	0.15	**0.14**	0.29	0.08
		Exponential	0.08	0.27	0.27	0.51	0.11
SM	R^2	Polynomial	.13	.99	**.92**	1.00	.18
		Exponential	.00	.88	.77	.99	.26
	RMSE	Polynomial	0.00	0.00	**0.00**	0.01	0.00
		Exponential	0.00	0.01	0.01	0.02	0.01

3.3 3D predictions

The independent validation with the validation set of 10 randomly located profiles with the same sampled depth increments showed a high overall explained variation and low errors for both polynomial and exponential functions and for both Cubist and random forests. The R^2 of Cubist models for SOC and for SM was .86 and .88 with the polynomial function and .86 and .87 with the exponential function (Table 4). Random forest models showed a similar R^2 except for SM with the polynomial function (R^2 = .84). The CCC of all Cubist models was slightly higher than the CCC of the random forests models. Cubist models had a CCC of .91 for SOC and .91 for SM with polynomial function. The CCC for SM with exponential function was slightly higher (CCC = .93). The error of all four models for SM was identical (RMSE = 0.02). For SOC, the error of the Cubist and random forests models with polynomial function was about 0.02–0.03% lower than the error of models with exponential function. The difference in RMSE between Cubist and random forests was <4% (Table 4).

TABLE 4. Results of the independent model validation with the explained variation as coefficient of determination (R^2), Lin's concordance correlation coefficient (CCC), and RMSE (in %) of the polynomial and exponential soil depth functions for soil organic C (SOC) and soil moisture (SM). Bolded values are referred to in the text

		Cubist			Random forests		
Trait	Function	R^2	CCC	RMSE	R^2	CCC	RMSE
SOC	Polynomial	.86	.91	**0.56**	**.89**	**.92**	**0.54**
	Exponential	**.87**	.91	0.58	.86	.90	0.61
SM	Polynomial	**.88**	.91	0.02	.84	.90	0.02
	Exponential	.87	**.93**	0.02	**.86**	**.92**	0.02

The minimum values in R^2 and the high standard deviation of the soil depth functions for SM showed that the soil depth functions could not depict the vertical trend in some soil profiles (Table 3). This is the case for Profiles 2 and 10, where the SM was 0.22, 0.20, 0.23, and 0.21 and 0.25, 0.21, 0.22, and 0.24, respectively. These profiles had a local maximum or minimum between 15 and 45 cm that could not be modeled with the exponential function, which cannot be explained with the geophysical measurements or additional knowledge about the field. In both cases, the polynomial function of second degree had a lower error than for all other profiles. To solve this, other functions are required that can reproduce vertical distributions with local minima and maxima (minimax; Minasny, Stockmann, Hartemink, & McBratney, 2016).

3.3 3D predictions

The independent validation with the validation set of 10 randomly located profiles with the same sampled depth increments showed a high overall explained variation and low errors for both polynomial and exponential functions and for both Cubist and random forests. The R^2 of Cubist models for SOC and for SM was .86 and .88 with the polynomial function and .86 and .87 with the exponential function (Table 4). Random forest models showed a similar R^2 except for SM with the polynomial function (R^2 = .84). The CCC of all Cubist models was slightly higher than the CCC of the random forests models. Cubist models had a CCC of .91 for SOC and .91 for SM with polynomial function. The CCC for SM with exponential function was slightly higher (CCC = .93). The error of all four models for SM was identical (RMSE = 0.02). For SOC, the error of the Cubist and random forests models with polynomial function was about 0.02–0.03% lower than the error of models with exponential function. The difference in RMSE between Cubist and random forests was <4% (Table 4).

TABLE 5. Results of the independent model validation for each individual sampled depth (as the midpoint of the depth increment) with the coefficient of determination (R^2), Lin's concordance correlation coefficient (CCC), RMSE, and the normalized RMSE (nRMSE) for soil organic C (SOC) and soil moisture (SM). For SOC as well as SM, Cubist with polynomial functions had the lowest error. Bolded values are referred to in the text

		SOC				SM			
		Cubist		Random forests		Cubist		Random forests	
Statistic	Depth	Polynomial	Exponential	Polynomial	Exponential	Polynomial	Exponential	Polynomial	Exponential
	cm								
R^2	7.5	**.76**	.76	**.83**	.82	.77	**.83**	.70	**.75**
	22.5	.64	**.80**	.76	**.77**	.84	**.92**	.87	**.89**
	37.5	.49	**.76**	.63	**.64**	.89	**.90**	.83	**.87**
	52.5	.27	**.65**	**.55**	.51	**.89**	.86	.85	**.90**
CCC	7.5	**.84**	.83	.86	**.88**	**.85**	.83	**.85**	.83
	22.5	**.64**	.55	**.65**	.52	.89	**.92**	**.90**	.86
	37.5	.53	**.62**	**.60**	.55	.89	**.94**	.89	**.92**
	52.5	.47	**.72**	**.65**	.62	.92	**.93**	.90	**.94**
RMSE, %	7.5	**0.38**	0.39	0.38	**0.35**	0.02	0.02	0.02	0.02
	22.5	**0.58**	0.77	**0.61**	0.81	**0.01**	0.02	**0.01**	0.02
	37.5	0.71	**0.67**	**0.67**	0.73	0.02	0.02	0.02	0.02
	52.5	0.54	**0.38**	0.47	**0.43**	0.03	0.03	0.03	0.03
nRMSE	7.5	**0.17**	0.17	**0.16**	0.15	**0.14**	0.14	**0.16**	0.15
	22.5	**0.23**	0.31	**0.25**	0.33	**0.15**	0.15	**0.14**	0.21
	37.5	**0.22**	0.21	**0.21**	0.23	**0.12**	0.10	**0.12**	0.12
	52.5	**0.14**	0.19	**0.12**	0.22	**0.06**	0.06	**0.06**	0.05

More important is that the nRMSE of Cubist and random forest models with the polynomial function did vary least with depth in absolute values. This showed that the model could predict SOC and SM with low error throughout the sampled interval of the soil profile (Table 5). Both Cubist and random forests with the exponential function for SOC and SM had high errors (nRMSE) in the depth increment ranging from 15 to 30 cm. Therefore, we conclude that the exponential function could not depict the vertical trend of SOC and, to a lesser extent, of SM within the sampled profile. We ascribe this to the 30-cm-deep plough horizon, which needs to be accounted for with a less uniformly decreasing soil depth function. The flexibility of polynomial functions of third degree or higher is potentially capable of depicting local variations in the soil better than exponential functions. We recommend that this be investigated in more detail.

Further, the R2 of the SOC models decreased from around .80 to .50 on average with increasing depth and increased from .76 to .88 with increasing depth for SM. Lin's CCC showed a similar pattern. These differences in explained variability indicate differences in explanatory power of the geophysical measurements for SOC and SM modeling for the depth intervals used in this study. On the one hand, geophysical measurements and especially EMI measurements are influenced by SM, whereas SOC content is related indirectly through SM content and influenced by other soil and environmental processes. This may not be covered by EMI and gamma-ray sensors, where covariates of the latter have little influence on depths >30 cm. On the other hand, this may refer to the decreasing range of SOC content and the increasing range of SM (Figure 3). The lower SOC content variability in depth may not be represented by the covariates. Therefore, these complex interactions need be investigated in more detail to make more precise conclusions about the use of geophysical measurements as covariates

for 3D modeling with soil depth functions. The final predictions are sketched in Figure 6 and shown in detail in the Supplements 1–4.

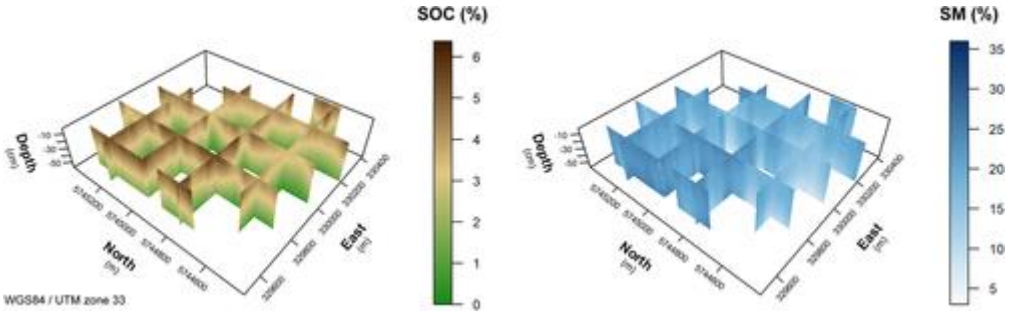

FIGURE 6

Three-dimensional (3D) predictions of soil organic C (SOC) and soil moisture (SM) with polynomial depth function and Cubist (see Supplements 1–4 for detailed animated cross sections)

Analyzing the interaction of spatial prediction of SOC and SM and the geophysical covariates, one can see that the highest SOC values were located in areas with high EC_a values (compare Figure 1). Figure 5 shows topsoil SOC contents of up to 6% in the western and central part of the site (lower left side) and ≈3% in the south (lower right side). This range of SOC content at this particular agricultural field is similar to the range of SOC in most agricultural fields in central Europe (Tóth, Jones, & Montanarella, 2013). A similar pattern can be seen in the SM prediction. In the western part, SM is distributed uniformly, with 20–25% in the whole profile, and in the south, there is much less SM in the deeper subsoil (5%) than in the topsoil (15–20%). These patterns can also be found in the sampled soil profiles (Figure 3).

In the central part of the field, pillar-like patterns of higher SOC content values were visible. These pillars are well described and linked to old meanders of the rivulet

Fließgraben or the river Elbe. In these areas, a farmer can expect better growing conditions for field crops, as SOC affects nutrient availability and SM retention. Thus, these areas need less additional fertilizer than the areas with less SOC and lower EC_a. Using the proposed framework can therefore contribute to a sustainable agricultural approach (e.g., precision agriculture that applies fertilizer according to soil requirements). Three-dimensional mapping is highly suitable for informing farmers, as sampling based on wecLHS is fast (only few profiles are required) and the model development based on the geophysical measurements is computationally efficient, relatively fast compared with conventional soil mapping, as well as potentially extendable to other soil properties such as pH, cation exchange capacity, and texture (Cassiani et al., 2012; Doolittle & Brevik, 2014).

4 CONCLUSION

In this case study, we predicted SOC and SM in the vertical as well as horizontal domain (i.e., in 3D using geophysical covariates derived from EMI and gamma-ray sensors with different intercoil spacings and thus different penetration depths and footprints of the signal). A weighted cLHS design was applied for calculation of the locations of the calibration samples. We hypothesized that the used sensor setup will lead to predictions of SOC and SM with high explained variation throughout the soil profile as well as in the spatial domain.

We showed that coefficient of determination and model error of the polynomial and exponential functions modeled and predicted with Cubist and random forests were stable over all depth increments. Thus, the data from two EMI sensors with depth-dependent sensitivity and gamma-ray spectrometry are well suited for the 3D prediction of SOC and SM despite the reduced number of samples. In general, the

differences between the models' error were rather small. The differences between the used machine learning methods are smaller compared with the differences between the used soil depth functions. This demonstrates the suitability of the sampling design approach for modeling with Cubist and random forests. Therefore, we conclude that the choice between soil depth functions is more important than the choice of the machine learning method for spatial prediction, if both methods are well established in DSM. The flexible polynomial function is capable of depicting local variation, which is not limited to plow horizons but also comprises clay-enriched horizons, pH drops with decreases in $CaCO_3$ content, and others. We recommend the combination of second-degree polynomial soil depth function with Cubist for 3D mapping of SOC and SM with two EMI sensors and gamma-ray spectrometry covering a wide range of environmental covariates representing the horizontal and vertical domain of SOC and SM variation on the field scale. Within the scope of precision agriculture, this approach is suitable for SOC and SM estimation in similar environmental conditions, as it offers a spatial evaluation that incorporates the whole soil continuum. Thus, the 3D mapping of SOC and SM with high spatial and vertical resolution can help to optimize sustainable management strategies on the field scale with respect to fertilization, irrigation, and liming and subsequently to increase food and biofuel productivity.

For future investigation and to simplify the approach for field application, the contribution and importance of the individual sensors and sensor settings are of great interest. Since both orientations of the CMD-Explorer showed similar interpolation results, these measurements may be strongly cross-correlated and redundant. This can be evaluated and solved with the feature importance calculated within random forests, but it requires comprehensive and complex analysis of the interaction of the modeled depth function coefficients and the geophysical measurements (e.g., by using

different slices of the target variable related to a specific depth increment compared to the depth sensitivity of the sensors). Further, the extension of the modeled depth may be of interest, since plants can uptake water from greater depth. This depends on the crop and also extends to forestry. For that purpose, other soil properties such as texture, water-holding capacity, permeability, horizontation, or the extension of the modeled depth to the depth of bedrock may be of interest. More complex soil depth functions such as polynomials of higher degree may be beneficial, when a tradeoff between soil sampling costs and model benefits is found. In our study, we successfully integrated depth-dependent EC_a data; however, we refrained from inversion of the data because we did not want to introduce additional uncertainties and ambiguities into the data analysis. As recently shown by von Hebel et al. (2019), an enhanced processing chain can provide accurate and quantitative EMI data. This offers interesting possibilities to extend the presented approach by depth-true electrical conductivity values.

REFERENCES

Abdu, H., Robinson, D. A., Seyfried, M., & Jones, S. B. (2008). Geophysical imaging of watershed subsurface patterns and prediction of soil texture and water holding capacity. *Water Resources Research*, 44(4). https://doi.org/10.1029/2008WR007043

Aldana Jague, E., Sommer, M., Saby, N. P. A., Cornelis, J.-T., van Wesemael, B., & Van Oost, K. (2016). High resolution characterization of the soil organic carbon depth profile in a soil landscape affected by erosion. *Soil and Tillage Research*, 156, 185– 193. https://doi.org/10.1016/j.still.2015.05.014

Binley, A., Hubbard, S. S., Huisman, J. A., Revil, A., Robinson, D. A., Singha, K., & Slater, L. D. (2015). The emergence of hydrogeophysics for improved understanding

of subsurface processes over multiple scales. *Water Resources Research*, 51, 3837– 3866. https://doi.org/10.1002/2015WR017016

Bouma, J. (2014). Soil science contributions towards Sustainable Development Goals and their implementation: Linking soil functions with ecosystem services. *Journal of Plant Nutrition and Soil Science*, 177, 111– 120. https://doi.org/10.1002/jpln.201300646

Bouma, J., & McBratney, A. (2013). Framing soils as an actor when dealing with wicked environmental problems. *Geoderma*, 200–201, 130– 139. https://doi.org/10.1016/j.geoderma.2013.02.011

Breiman, L. (2001). Random forests. *Machine Learning*, 45, 5– 31. https://doi.org/10.1023/A:1010933404324

Breiman, L., Friedman, J. H., Stone, C. J., & Olshen, R. A. (1984). *Classification and regression trees*. New York: Chapman and Hall.

Brus, D. J., Kempen, B., & Heuvelink, G. B. M. (2011). Sampling for validation of digital soil maps. *European Journal of Soil Science*, 62, 394– 407. https://doi.org/10.1111/j.1365-2389.2011.01364.x

Callegary, J. B., Ferre, P. A., & Groom, R. W. (2012). Three-dimensional sensitivity distribution and sample volume of low-induction-number electromagnetic-induction instruments. *Soil Science Society of America Journal*, 76, 85– 91. https://doi.org/10.2136/sssaj2011.0003

Cassiani, G., Ursino, N., Deiana, R., Vignoli, G., Boaga, J., Rossi, M., … Werban, U. (2012). Noninvasive monitoring of soil static characteristics and dynamic states: A case study highlighting vegetation effects on agricultural land. *Vadose Zone Journal*, 11(3). https://doi.org/10.2136/vzj2011.0195

Castrignanò, A., Wong, M. T. F., Stelluti, M., de Benedetto, D., & Sollitto, D. (2012). Use of EMI, gamma-ray emission and GPS height as multi-sensor data for soil characterisation. *Geoderma*, 175–176, 78– 89. https://doi.org/10.1016/j.geoderma.2012.01.013

Cho, Y., Sudduth, K. A., & Chung, S.-O. (2016). Soil physical property estimation from soil strength and apparent electrical conductivity sensor data. *Biosystems Engineering*, 152, 68– 78. https://doi.org/10.1016/j.biosystemseng.2016.07.003

Cook, S. E., Corner, R. J., Groves, P. R., & Grealish, G. J. (1996). Use of airborne gamma radiometric data for soil mapping. *Australian Journal of Soil Research*, 34, 183– 194.

Dexter, A. R., Richard, G., Arrouays, D., Czyż, E. A., Jolivet, C., & Duval, O. (2008). Complexed organic matter controls soil physical properties. *Geoderma*, 144, 620– 627. https://doi.org/10.1016/j.geoderma.2008.01.022

Dierke, C., & Werban, U. (2013). Relationships between gamma-ray data and soil properties at an agricultural test site. *Geoderma*, 199, 90– 98. https://doi.org/10.1016/j.geoderma.2012.10.017

Doolittle, J. A., & Brevik, E. C. (2014). The use of electromagnetic induction techniques in soils studies. *Geoderma*, 223–225, 33– 45. https://doi.org/10.1016/j.geoderma.2014.01.027

Ekstrøm, C. T. (2018). *MESS: Miscellaneous esoteric statistical scripts*. Comprehensive R Archive Network. Retrieved from https://CRAN.R-project.org/package=MESS

Fan, J., McConkey, B., Wang, H., & Janzen, H. (2016). Root distribution by depth for temperate agricultural crops. *Field Crops Research*, 189, 68– 74. https://doi.org/10.1016/j.fcr.2016.02.013

Godfray, H. C. J., Beddington, J. R., Crute, I. R., Haddad, L., Lawrence, D., Muir, J. F., … Toulmin, C. (2010). Food security: The challenge of feeding 9 billion people. *Science*, 327, 812– 818. https://doi.org/10.1126/science.1185383

Govers, G., Merckx, R., van Wesemael, B., & van Oost, K. (2017). Soil conservation in the 21st century: Why we need smart agricultural intensification. *SOIL*, 3, 45– 59. https://doi.org/10.5194/soil-3-45-2017

Hengl, T., de Jesus, J. M., MacMillan, R. A., Batjes, N. H., Heuvelink, G. B. M., Ribeiro, E., … Gonzalez, M. R. (2014). SoilGrids1km: Global soil information based on automated mapping. *PLOS ONE*, 9(8). https://doi.org/10.1371/journal.pone.0105992

IAEA. (2003). *Guidelines for radioelement mapping using gamma ray spectrometry data*. International Atomic Energy Agency. Retrieved from https://www-pub.iaea.org/mtcd/publications/pdf/te_1363_web.pdf

Jenny, H. (1941). *Factors of soil formation: A system of quantitative pedology*. New York: Dover Publications.

Jobbágy, E. G., & Jackson, R. B. (2000). The vertical distribution of soil organic carbon and its relation to climate and vegetation. *Ecological Applications*, 10, 423– 436.

Krige, D. G. (1951). A statistical approach to some basic mine valuation problems on the Witwatersrand. *Journal of the Southern African Institute of Mining and Metallurgy*, 52, 119– 139.

LAGB. (2014). *Bodenbericht Sachsen-Anhalt 2014: Grundlagen, parameter und hintergrundwerte*. Halle (Saale), Germany: Mitteilungen zu Geologie und Bergwesen von Sachsen-Anhalt 18.

Liu, F., Rossiter, D. G., Song, X.-D., Zhang, G.-L., Yang, R.-M., Zhao, Yu-G., … Ju, B. (2016). A similarity-based method for three-dimensional prediction of soil organic matter

concentration. *Geoderma*, 263, 254– 263. https://doi.org/10.1016/j.geoderma.2015.05.013

Martini, E., Werban, U., Zacharias, S., Pohle, M., Dietrich, P., & Wollschläger, U. (2017). Repeated electromagnetic induction measurements for mapping soil moisture at the field scale: Validation with data from a wireless soil moisture monitoring network. *Hydrology Earth System Sciences*, 21, 495– 513. https://doi.org/10.5194/hess-21-495-2017

McBratney, A., Whelan, B., Ancev, T., & Bouma, J. (2005). Future directions of precision agriculture. *Precision Agriculture*, 6, 7– 23. https://doi.org/10.1007/s11119-005-0681-8

McBratney, A. B., Mendonça Santos, M. L., & Minasny, B. (2003). On digital soil mapping. *Geoderma*, 117, 3– 52. https://doi.org/10.1016/S0016-7061(03)00223-4

McNeill, J. D. (1980a). *Electrical conductivity of soils and rocks*. Mississauga, ON, Canada: Geonics Limited. Retrieved from http://www.geonics.com/pdfs/technicalnotes/tn5.pdf

McNeill, J. D. (1980b). *Electromagnetic terrain conductivity measurement at low induction numbers*. Mississauga, ON, Canada: Geonics Limited. Retrieved from http://www.geonics.com/pdfs/technicalnotes/tn6.pdf

Minasny, B., & McBratney, A. B. (2006). Latin hypercube sampling as a tool for digital soil mapping. In P. Lagacherie, A. B. McBratney, & M. Voltz (Eds.), *Digital soil mapping. An introductory perspective* (pp. 153– 606). Amsterdam: Elsevier.

Minasny, B., McBratney, A. B., Mendonça-Santos, M. L., Odeh, I. O. A., & Guyon, B. (2006). Prediction and digital mapping of soil carbon storage in the Lower Namoi Valley. *Australian Journal of Soil Research*, 44, 233– 244. https://doi.org/10.1071/SR05136

Minasny, B., Stockmann, U., Hartemink, A. E., & McBratney, A. B. (2016). Measuring and modelling soil depth functions, in: In A. E. Hartemink & B. Minasny (Eds.), *Digital soil morphometrics*, Vol. 163. Progress in soil science (pp. 225– 240). Cham, Switzerland: Springer International Publishing.

Moghadas, D., Taghizadeh-Mehrjardi, R., & Triantafilis, J. (2016). Probabilistic inversion of EM38 data for 3D soil mapping in central Iran. *Geoderma Regional*, 7, 230– 238. https://doi.org/10.1016/j.geodrs.2016.04.006

Pebesma, E. J. (2004). Multivariable geostatistics in S: The gstat package. *Computers & Geosciences*, 30, 683– 691. https://doi.org/10.1016/j.cageo.2004.03.012

Pohle, M., & Werban, U. (2019). *Near surface geophysical data (electromagnetic induction—EMI, gamma-ray spectrometry)*. Selbitz (Elbe), Germany: PANGAEA. https://doi.org/10.1594/PANGAEA.910272

Probst, P., & Boulesteix, A.-L. (2018). To tune or not to tune the number of trees in random forest. *Journal of Machine Learning Research*, 18.

Quinlan, J. R. (1992). Learning with continuous classes. In A. Adams & L. Sterling (Eds.), *Proceedings of the 5th Australian Joint Conference On Artificial Intelligence* (pp. 343– 348). Singapore: World Scientific Publishing Company.

Quinlan, J. R. (1993). Combining instance-based and model-based learning. In P. Utgoff (Ed.), *Proceedings of the Tenth International Conference on International Conference on Machine Learning* (pp. 236– 243). San Mateo, CA: Morgan Kaufmann.

R Development Core Team. (2017). *R: A language and environment for statistical computing*. Vienna: R Foundation for Statistical Computing.

Ramirez-Lopez, L., Schmidt, K., Behrens, T., van Wesemael, B., Demattê, J. A. M., & Scholten, T. (2014). Sampling optimal calibration sets in soil infrared spectroscopy. *Geoderma*, 226–
227, 140– 150. https://doi.org/10.1016/j.geoderma.2014.02.002

Rawls, W. J., Pachepsky, Y. A., Ritchie, J. C., Sobecki, T. M., & Bloodworth, H. (2003). Effect of soil organic carbon on soil water retention. *Geoderma*, 116, 61– 76. https://doi.org/10.1016/S0016-7061(03)00094-6

Rentschler, T., Gries, P., Behrens, T., Bruelheide, H., Kühn, P., Seitz, S., … Schmidt, K. (2019). Comparison of catchment scale 3D and 2.5D modelling of soil organic carbon stocks in Jiangxi Province, PR China. *PLOS ONE*, 14(8). https://doi.org/10.1371/journal.pone.0220881

Schmidt, K., Behrens, T., Daumann, J., Ramirez-Lopez, L., Werban, U., Dietrich, P., & Scholten, T. (2014). A comparison of calibration sampling schemes at the field scale. *Geoderma*, 232–
234, 243– 256. https://doi.org/10.1016/j.geoderma.2014.05.013

Schmidt, K., Behrens, T., & Scholten, T. (2008). Instance selection and classification tree analysis for large spatial datasets in digital soil mapping. *Geoderma*, 146, 138– 146. https://doi.org/10.1016/j.geoderma.2008.05.010

Steyerberg, E. W., & Harrell, F. E. (2016). Prediction models need appropriate internal, internal-external, and external validation. *Journal of Clinical Epidemiology*, 69, 245– 247. https://doi.org/10.1016/j.jclinepi.2015.04.005

Tóth, G., Jones, A., & Montanarella, L. (2013). The LUCAS topsoil database and derived information on the regional variability of cropland topsoil properties in the European Union. *Environmental Monitoring and Assessment*, 185, 7409– 7425. https://doi.org/10.1007/s10661-013-3109-3

Veronesi, F., Corstanje, R., & Mayr, T. (2014). Landscape scale estimation of soil carbon stock using 3D modelling. *Science of the Total Environment*, 487, 578– 586. https://doi.org/10.1016/j.scitotenv.2014.02.061

Viscarra Rossel, R. A., Chen, C., Grundy, M. J., Searle, R., Clifford, D., & Campbell, P. H. (2015). The Australian three-dimensional soil grid: Australia's contribution to the GlobalSoilMap project. *Soil Research*, 53, 845– 864. https://doi.org/10.1071/SR14366

von Hebel, C., van der Kruk, J., Huisman, J. A., Mester, A., Altdorff, D. et al. (2019). Calibration, conversion, and quantitative multi-layer inversion of multi-coil rigid-boom electromagnetic induction data. *Sensors*, 19(21). https://doi.org/10.3390/s19214753

Acknowledgements

Funded by the State Postgraduate Fellowship Programme by the Research Funding Baden-Württemberg.

Finanziert durch ein Promotionsstipendium nach dem Landesgraduiertenförderungsgesetz im Rahmen der Förderprogramme Baden-Württemberg.